STIFFNESS AND STRENGTH OF TAPERED COMPOSITE RISER TUBES

A thesis submitted to the University of Manchester Institute of
Science and Technology for the degree of Doctor of Philosophy

by

Luiz Cláudio de Marco Meniconi

Department of Mechanical Engineering
Applied Mechanics Division

1999

To my parents, Márcio and Rosina.
In memory of my grandfather, Mozart.

DECLARATION

No portion of the work referred to in this thesis has been submitted in support of an application for another degree or qualification of this or any other university, or other institution of learning.

ABSTRACT

The application of composite tubes in production risers of tension leg platforms is considered. The main advantages of composite materials in this application are weight reduction (inclusive of the platform) and corrosion resistance. The tube studied is of a hybrid construction, made of glass fibre/epoxy resin mixed with carbon fibre/epoxy. The specific objects of the research are the *stress* or *tapered joints*. These are tubes of varying thickness designed to support the high bending moments developed at the top and at the base of the riser. The thickness variation is obtained by terminating, or dropping, some internal plies. The edge of the dropped plies are a source of out-of-plane stresses. The change in thickness constitutes a stress concentration for the in-plane stresses. There are two different failure modes possible at the thickness transition region: viz. delamination, triggered by the high out-of-plane stresses or over-stressing in the in-plane stress components. The experimental work carried out showed that the latter failure mode prevailed, mainly due to the high fracture toughness of the carbon/epoxy composite used in the assembly of the tubes. Finite element analysis of the specimens tested were performed to evaluate the resulting stresses. Two methods are applied for the design of composite riser tubes. The first one is suitable for thick laminated tubes with constant thickness. The second method applies to thick laminated tubes with varying thickness. Both methods are used as design tools for the analysis of a composite production riser. A steel riser is also analysed for comparison purposes. The study ends with the design of two composite tapered joints, placed at the extremities of the risers. The adoption of a composite riser precludes the use of tensioners, which introduces an important simplification into the production system.

ACKNOWLEDGEMENTS

CONTENTS

CHAPTER 1 INTRODUCTION

CHAPTER 1 INTRODUCTION

The objective of this research is to explore the design of a composite production riser for a tension leg platform (TLP), used for oil exploitation offshore. The proposed composite riser is of a hybrid construction. The hoop layers are made of a glass fibre/epoxy matrix composite. The main purpose of the glass sub-laminate is to resist the internal and external pressures. The axial strength of the riser is given by a carbon fibre/epoxy matrix sub-laminate, where the carbon fibres are positioned at a shallow angle to the axis. The carbon/epoxy laminae constitute the main load bearing layers for the axial forces and the bending moments to which the riser is subjected during operation.

Particular emphasis is placed on the design of the *tapered joints* of the riser. These are composite tubes of varying thickness placed at the extremities of the riser with the purpose of resisting the high bending moments developed there. The two main characteristics of the tapered joints are their considerable thickness and the interruption of some internal layers, to obtain the variation in thickness.

Accordingly, the models used to determine the stress generated by the operational loads have to be appropriate for the analysis of thick laminated tubes. The termination, or dropping, of some internal plies generates out-of-plane stresses that can trigger delaminations. A design methodology is needed to address this possibility.

The body of the thesis begins with a literature review of three different areas which are dealt with in Chapter 2. Firstly, failure by delamination is investigated with special emphasis on a fracture mechanics approach. Some discussion on the strength of laminates under compressive loads is also presented. Next the models available for the analysis of thick laminated tubes are introduced and discussed. Finally, the specific aspects of the design of a production riser for a floating platform are addressed.

Chapter 3 describes the experimental tests executed as part of the research. The tests started with the determination of the fracture toughness of the carbon/epoxy sub-laminates. This information is essential for analysing the possible occurrence of delaminations. A programme

of tests was then conducted on dropped ply composite tubular specimens. Carbon fibres aligned at two angles to the axis were examined: +/- 20° and 0°. The basic load conditions tested were internal pressure and four point bending. Some specimens were tested under different combinations of internal pressure and bending moment. The experimental work ended with internal pressure and bending tests on plain (i.e. constant thickness) tubes, to address the effect of the ply drop-off on their strength.

Chapter 4 contains results from finite element analysis (FEA) models of the specimens which were developed to determine the stresses due to the test loads. There were some preliminary tasks for the calibration of the FEA parameters. First a comparison was made with an exact solution for thick laminated tubes available in the literature. Following this, the validity of the "smearing" approach, that considers the angle-ply sub-laminate as an equivalent specially orthotropic material, is addressed. Finally it is demonstrated that the stresses present in a pure bending load condition can be obtained from an axisymmetric analysis. This greatly simplifies the models required.

After the FEA parameters had been settled, the analysis of the specimens tested was performed. The effect that the ply drop-off has on the stress fields was investigated. The FEA was also employed to calculate the *strain energy release rates* (SERRs) associated to the test loads. These are the fracture mechanics properties used to verify the possible onset of delaminations. The stress and SERR FEA models provide the information needed to explain the observed experimental results.

Chapter 5 describes the development of two methods for the stress analysis of thick laminated tubes. Both methods provide axisymmetric stress analyses. The first method is suitable for plain tubes and renders an exact solution for the internal and external pressure and axial load cases. The stresses generated by a bending moment can be obtained from the latter case. The second method is intended for thick laminated tubes with varying thickness. It is based on a variational principle and is approximate, the finite difference method being employed to represent the partial derivatives. The results of both methods are checked against the FEA results obtained in Chapter 4.

After the failure behaviour of the dropped ply tubes had been verified experimentally and the

design tools developed, a composite riser analysis was performed and the results are given in Chapter 6. The study starts with the analysis of a steel riser to supply the basis for comparison. The need for a tapered joint in the riser is demonstrated. The analysis proceeds with the design of a composite riser, including the establishment of a suitable design criterion. The characteristics of the composite riser are compared with those of the steel riser. The analysis ends with the outline design of two composite tapered joints for the top and the bottom of the composite riser.

Chapter 7 contains a list of conclusions drawn from the different phases of the research. In general, the feasibility of designing and manufacturing a composite production riser for a TLP is demonstrated. This includes tapered joints made of composites. The chapter ends with recommendations for the continuation of the research in this field.

CHAPTER 2 LITERATURE REVIEW

CHAPTER 2 LITERATURE REVIEW

2.1 INTRODUCTION

This literature review covers three main areas. The first aspect considered was the experimental program. Because the tapered composite tubes which are the object of the present research can develop delaminations, special attention was given to this type of defect. The taper effect is produced by varying the wall thickness of the tube. This is done by simply terminating, or dropping, some internal plies. The tip of the discontinuous plies constitutes preferential spots for the occurrence of voids. There is also the development there of through-thickness stresses.

These factors can lead to the occurrence of delaminations that are very deleterious to the performance of laminates. A fracture mechanics approach is adopted for the investigation of both static and fatigue behaviour of the tube. Consequently, the experimental tests proposed for the determination of the delamination fracture toughness of a composite are analysed. Following this, the ultimate strength of laminates is considered, due to the possibility of material failure by modes other than delamination.

Secondly, a range of available analytical and numerical models for the analysis of thick composite tubes is discussed. The aim is to define the methods capable of describing the behaviour of tapered composite tubes. The aspects covered are the 3D stress field present in a thick composite tube and the stress concentration effect caused by the terminating plies.

Finally, the procedures used for the analysis of a composite production riser are described. Once the failure process is identified and a proper model is adopted, the design of a composite riser can be accomplished. The emphasis is on the behaviour of the tapered composite tubes that are the object of the present research. These tubes are used at the extremities of the riser, where there are severe gradients in the bending moments. The tubes have increased thicknesses to resist these rapidly increasing bending moments.

2.2 EXPERIMENTAL ANALYSIS

2.2.1 DELAMINATION: FRACTURE MECHANICS APPROACH

The composite tapered tubes can be manufactured by using discontinuous internal carbon plies. The drawback is that ply drop-off generates out-of-plane stresses which are deleterious for laminates. Moreover, the resin-rich spots in front of the terminating plies are regions that tend to display defects in the matrix, like voids and microcracks. These defects, combined with the out-of-plane stresses, favour the development and propagation of delaminations.

Delaminations are sharp-edged defects that from an elasticity perspective possess stress singularities at their tips. The study of delaminations can thus be approached using fracture mechanics methods, principally through the investigation of the strain energy released during their propagation. This section provides some insight into the behaviour of laminates that are prone to develop delaminations, such as tapered ones. The fracture mechanics parameters involved are presented and discussed.

The major feature associated with internal discontinuous plies are the out-of-plane (or interlaminar) stresses that arise from their extremities, even in the case of in-plane loads. Internal dropped plies are one of the details that can generate this kind of stress. Trethewey [1] gave other examples, such as free edges, holes, bonded and bolted joints. All these features introduce stress-free surfaces which in their turn cause the development of high stresses in other planes. Figure 2.1 displays those details.

As shown by Pipes and Pagano [2], the behaviour of the stress field near the free edges can be demonstrated by the theory of elasticity. The three stress equilibrium equations are:

$$\frac{\partial \sigma_x}{\partial x} + \frac{\partial \tau_{xy}}{\partial y} + \frac{\partial \tau_{xz}}{\partial z} = 0 \tag{2.1}$$

$$\frac{\partial \tau_{yx}}{\partial x} + \frac{\partial \sigma_y}{\partial y} + \frac{\partial \tau_{yz}}{\partial z} = 0 \tag{2.2}$$

$$\frac{\partial \tau_{zx}}{\partial x} + \frac{\partial \tau_{zy}}{\partial y} + \frac{\partial \sigma_z}{\partial z} = 0 \tag{2.3}$$

Now consider a strip of a balanced and symmetrical laminate pulled along the x direction which lies along its length. The width of the strip is $2b$ and the thickness is $4h_0$, as figure 2.2 shows. Assuming σ_x is constant along the length, it follows that $\partial\sigma_x/\partial x=0$ and from equation 2.1 the interlaminar shear stress $\tau_{xz}(z)$ is given by:

$$\tau_{xz}(z) = - \int_{-\frac{t}{2}}^{z} \frac{\partial \tau_{xy}}{\partial y} dz \tag{2.4}$$

The in-plane shear stress τ_{xy} has a constant value in the interior region of each lamina, given by the classical laminate theory (CLT). As we move from the interior to the boundary, however, τ_{xy} should decrease to zero at the stress free surfaces where $y=\pm b$. Equation 2.4 implies that τ_{xz} must increase from zero in the interior to a large value at the boundary. The region where these alterations take place is called the interlaminar stress boundary layer. The same reasoning applies to the other out-of-plane stresses, τ_{yz} and σ_z.

Pipes and Pagano [2] applied a finite difference method to solve the three-dimensional equations for stress equilibrium, the stress-strain constitutive laws and strain-displacements relationships. Their example used a four layer $\pm 45^\circ$ graphite/epoxy laminate under uniform axial strain ε_x. The equations were solved for stress-free boundary conditions at the edges. Figure 2.3 displays the complete stress solution. In the central portion of the laminate, the in-plane stresses σ_x and τ_{xy} agreed well with the CLT. Both stresses drop in the boundary layer region near the edge. The interlaminar stresses σ_z, τ_{xz} and τ_{yz} were all nil in the central region of the laminate, but changed to some value near the edges. The largest effect was related to the τ_{xz} stress, which showed the largest increase.

A dropped-ply region is displayed schematically in figure 2.4. The thicknesses t_0, t_d and t_i are related to the outer continuous plies, discontinuous plies and inner continuous plies, respectively. The development of high interlaminar shear stresses near the front edge of the terminating plies can be demonstrated intuitively. There has to be a region where the in-plane loads carried by the discontinuous plies are transferred to the continuous ones. The way this is achieved is by interlaminar shear between the layers, defining a "shear-in" distance, as shown by Trethewey [1].

8

As Cui et al. [3] pointed out, there are two basic approaches to assess the static strength of tapered laminates. The first and more conventional one is through stress based failure criteria. To overcome the difficulty posed by the high stress gradients near the ply drop-off, solutions based on stress averaged over a distance or taken at characteristic distances are proposed.

Another possible approach is to use the strain energy release rate, based on linear elastic fracture mechanics (LEFM) theory. A prerequisite for the application of this later method is the existence of a sharp, crack-like defect. Several authors [1, 3-6] agree that delaminations can start in the matrix-rich region ahead of the terminating plies. This region contains defects like voids and microcracks due to limitations of the manufacturing process. The thickness transition region makes it difficult to apply sufficient pressure to maintain consolidation of the laminae during the cure of the resin. The combination of high out-of-plane stresses and initial defects provide the conditions for delaminations to start there. Larger interlaminar macrocracks can appear, between the continuous and the discontinuous plies. As a result, the basic assumption for a LEFM approach is fulfilled. That will be the approach used in this study.

Cui et al. [3] also stated that very often a small amount of stable delamination occurs, with steadily increasing loads. Then a sudden, unstable propagation spreads along the whole length of the component. A study of the stability of the process is then needed. Trethewey [1] performed some simulations to verify the influence of several parameters on the strength of tapered laminates. He found that the dropped plies thickness t_d produces a major effect. The strength of the laminate diminishes with increasing thickness of the dropped plies. This is because the eccentricity of the load path increases, causing higher and higher local moments. He also investigated the influence of the stiffness of the dropped plies (by varying the reinforcement fibre angle) and concluded that stiffer dropped plies show lower failure loads. The reason is that a stiffer discontinuous sublaminate carries a larger portion of the axial load than a more complaint one. Consequently, higher loads have to be transmitted to the continuous plies, causing a higher stress concentration. Cui et al. [3] arrived at the same conclusions.

One aspect of major concern relating to the design of composite tapered riser tubes is the effect of ply drop-offs spacing. A short tapered region may be desirable, but if the step spacing

is too small, interaction may occur. Cui et al. [7] performed an experimental investigation in which six plies of E-glass/epoxy laminates were dropped in groups of two plies, with a step spacing of 0, 1.0, 1.5 and 2.0 mm. They found differences of up to 27% in the loads that cause the onset of delamination. Considering a shear transfer mechanism, they arrived at a simple formula to estimate the critical distance S_c between dropped plies :

$$S_c = \frac{\sigma\, t_d}{2\tau_y} \qquad (2.5)$$

where σ is the normal stress in the loading direction and τ_y is the interlaminar shear yield stress.

As mentioned before, laminates containing internal discontinuous plies are prone to a concentration of defects in the resin pocket ahead of the ply drop-off. This is due to pressure gradients during the hot curing process, when the resin is molten. Voids tend to migrate to the lower pressure zone in the thickness transition region. During cool down or under in-service loads, those voids can originate microcracks. The combination of interlaminar loads and microcracks make the ply drop-off a critical spot in terms of delamination.

The design of the component has to consider the presence of defects from the very beginning of its life. This is done via a damage tolerance methodology. As defined by Gillespie [8], damage tolerance is the ability of the structure to resist failure in the presence of flaws, cracks or other defects for a specified period of time. A certain amount of damage always exists inside the structure. During cyclic loading that damage may propagate. The residual stiffness and strength are progressively reduced. A quantitative relationship between residual strength and the amount of damage is required to assess the remaining lifetime of the component. Design loads are established from the knowledge of damage growth rates over time. The methodology is illustrated in figure 2.5.

LEFM concepts are applied in order to address the strength of components that have sharp, crack-like defects. There are two possible approaches. The first one is by means of the *Stress Intensity Factor* (SIF) and the second is through the use of *Strain Energy Release Rate* (SERR). Both concepts are related as will be shown later. The origin of LEFM is due to the fundamental work of Griffith [9], who used an energy balance approach to explain the

strength of glass.

As shown by Gibson [10], consider a through-thickness crack in the uniaxially stressed, homogeneous, isotropic and linear elastic infinite plate, with thickness t, shown in figure 2.6. The presence of a crack of length $2a$ is assumed to cause stress relief in an elliptical cylinder around it. The ellipsis has a major axis of length $4a$ perpendicular to the crack plane and a minor axis which coincides with the crack length.

As the plate was assumed to be uniformly stressed to a value σ before the introduction of the crack, the strain energy U_r released due to the relaxation of stress is:

$$U_r = \frac{1}{2}\sigma\,\varepsilon\,V = \frac{1}{2}\frac{\sigma^2}{E}V \tag{2.6}$$

where ε is the uniform strain away from the crack and E is the modulus of elasticity of the material. Moreover, V is the volume of the elliptic region:

$$V = \pi\,(2a)\,(a)\,(t) = 2\pi a^2 t \tag{2.7}$$

from expressions (2.6) and (2.7), we get:

$$U_r = \frac{\pi\sigma^2 a^2 t}{E} \tag{2.8}$$

Griffith stated that the creation of two crack surfaces of length $2a$ and width t required the absorption of energy U_s given by:

$$U_s = S\,\gamma_s = 4at\gamma_s \tag{2.9}$$

where U_s is the energy absorbed during the creation of new crack surfaces, S is the total surface area of the crack and γ_s is the surface energy per unit area.

Considering a growing crack, the process is stable if the rate at which energy is absorbed by the creation of new surfaces is greater than the rate at which strain energy is released. As the thickness t is constant the increment in crack area is proportional to the increment in crack length a and we can write:

$$\frac{\partial U_s}{\partial a} > \frac{\partial U_r}{\partial a} \qquad (2.10)$$

On the other hand, crack growth is unstable if the strain energy is released at a rate that can not be totally absorbed:

$$\frac{\partial U_s}{\partial a} < \frac{\partial U_r}{\partial a} \qquad (2.11)$$

The threshold of stability or condition of neutral equilibrium is given by

$$\frac{\partial U_s}{\partial a} = \frac{\partial U_r}{\partial a} \qquad (2.12)$$

or, from (2.8) and (2.9):

$$\frac{\pi \sigma^2 a}{E} = 2\gamma_s \qquad (2.13)$$

This equation can be rearranged to the form:

$$\sigma \sqrt{\pi a} = \sqrt{2 E \gamma_s} \qquad (2.14)$$

The term on the left-hand side of this last expression depends only on the loading and crack geometry and it is called the *Stress Intensity Factor* (SIF). The term on the right-hand side depends only on material properties and is known as its *Fracture Toughness*. At the threshold of crack growth stability, they are equal. If the stress is high enough or, conversely, if the crack is big enough, the SIF surpasses the critical value and the crack propagation becomes unstable.

From the point of view of local behaviour of stresses at the crack tip, there are three possible modes of crack propagation. They are the well-known mode I (opening), mode II (in-plane shearing) and mode III (anti-plane shearing or tearing), displayed at figure 2.7.

Referring back to the basic experiment performed by Griffith, Westergaard [11] used a complex stress function approach to write down the expressions for the stress field in the

vicinity of the crack tip. He used a local polar co-ordinate system (r, θ) with origin at the crack tip, as shown in figure 2.8. Assuming plane stress conditions, he developed the following relationships:

$$\sigma_x = \frac{K_I}{\sqrt{2\pi r}} f_1 (\theta) \qquad\qquad (2.15)$$

$$\sigma_y = \frac{K_I}{\sqrt{2\pi r}} f_2 (\theta) \qquad\qquad (2.16)$$

$$\tau_{xy} = \frac{K_I}{\sqrt{2\pi r}} f_3 (\theta) \qquad\qquad (2.17)$$

Note the singularity in each stress component as r tends to zero. K_I is the stress intensity factor for the crack opening mode, already defined:

$$K_I = \sigma\sqrt{\pi a} \qquad\qquad (2.18)$$

Expression (2.14) states that when K_I reaches a critical value K_{Ic}, it corresponds to the fracture toughness of the material.

The $f_i(\theta)$ terms are trigonometric functions of the angle θ. Once K_I is determined, the whole stress field in the vicinity of the crack tip is known. Similar expressions were developed for other types of loading and crack geometries, together with the corresponding SIFs. For the cases of pure shear loads, we have, for instance:

$$K_{II} = \tau\sqrt{\pi a} \qquad \text{and} \qquad K_{III} = \tau\sqrt{\pi a} \qquad (2.19)$$

It is possible to develop similar expressions for the stress field near the crack tip in anisotropic materials, although they are more complicated than the corresponding expressions for isotropic materials. This discourages the use of the SIF approach in the analysis of cracks in composite materials. As explained by Rybicki et al. [12], the SERR concept is much easier to apply, as a detailed knowledge of the stress field around the crack tip is not needed. The energy perturbations caused by the crack growth can be evaluated from the global behaviour of the structure. This is true as long as the strain energy is only absorbed in the crack growing

process.

Broek [13] explained the SERR concept by first stating the Griffith criterion for fracture: "crack growth can occur if the energy required to form an additional crack of size da can just be delivered by the system". He considered a plate with a lateral crack as shown in figure 2.9. Note that in this case the crack length is a, and not $2a$ as it is in the case of an internal crack as shown in figure 2.6. If the ends of the plate are free to move during crack extension, work is done by the external load P. The balance of energy states that:

$$W = U + U_s \Rightarrow W - U = U_s \qquad (2.20)$$

where W is the work done by the external force, U is the elastic strain energy stored in the plate and U_s is the energy for the formation of a crack with a total surface area of S. The condition for crack growth becomes:

$$\frac{d}{dS}(W - U) = \frac{d}{dS}(U_s) \qquad (2.21)$$

the term on the left-hand side of this equation is the *Strain Energy Release Rate* (SERR), denoted by the symbol G. It is the rate of change of the strain energy released per unit area of crack growth. The term on the right-hand side is called the *Crack Resistance Force* R.

As shown in the graph at figure 2.10, under the action of the force P, the load application points undergo a relative displacement v. As the crack length increases by an amount da, the displacement increases by an amount dv. It follows from the definition above:

$$G_I = \frac{d}{dS}(W - U) \qquad (2.22)$$

The SERR is more specifically named G_I because this case deals with a pure opening mode. We have, due to the crack growth:

$$dU = \frac{(P + dP)(v + dv)}{2} - \frac{Pv}{2} = \frac{Pdv}{2} + \frac{vdP}{2} + \frac{dPdv}{2} \qquad (2.23)$$

and:

$$dW = \frac{2P + dP}{2}dv = Pdv + \frac{dvdP}{2} \qquad (2.24)$$

Using these expressions for dU and dW in equation 2.22 leads to:

$$dS.G_I = dW - dU = \frac{Pdv}{2} - \frac{vdP}{2} \qquad (2.25)$$

but:

$$v = CP \Rightarrow dv = CdP + PdC \qquad (2.26)$$

where C is the compliance of the cracked plate. The use of the relationship 2.26 in 2.25 results in:

$$G_I = \frac{P^2}{2}\frac{dC}{dS} = \frac{P^2}{2t}\frac{dC}{da} \qquad (2.27)$$

Thus, one can determine G_I by plotting the compliance C as a function of the crack length a and then calculating the slope of the curve. At the onset of unstable fracture the critical SERR G_{Ic} for this mode I crack propagation corresponds to the values P_c and $(dC/da)_c$ at fracture. Similar approaches can be applied to determine the critical SERRs G_{IIc} and G_{IIIc}. The advantage of expression 2.27 is that it does not require knowledge of material properties or stress distributions at the crack tip. All parameters can be measured from the behaviour of the whole specimen. The method applies either to isotropic or anisotropic materials.

The relationship between G_I and K_I can be easily demonstrated by referring back to the classical example of an infinite plate under uniaxial stress, introduced by Griffith. As G is defined as the rate of change of the strain energy released per unit area of crack growth, we have, from equation 2.8:

$$G_I = \frac{dU_r}{dS} = \frac{1}{2t}\frac{d}{da}\left(\frac{\pi\sigma^2 a^2 t}{E}\right) = \frac{\sigma^2 \pi a}{E} \qquad (2.28)$$

The number 2 appears in the denominator because in this case we have two crack fronts. Comparing this result with expression (2.18), it turns to be:

$$G_I = \frac{K_I^2}{E} \qquad\qquad \text{(plane stress)} \qquad (2.29)$$

As Broek [13] shows, there are similar expressions for a state of plane strain and for the other modes of crack propagation:

$$G_I = (1-\nu^2)\frac{K_I^2}{E} , G_{II} = (1-\nu^2)\frac{K_{II}^2}{E} \quad and \quad G_{III} = (1+\nu)\frac{K_{III}^2}{E} \quad \text{(plane strain)} \qquad (2.30)$$

where ν is Poisson's ratio. In real structures an existing crack can be stressed in more than one mode at the same time. To address the possibility of failure of the component with a defect, a mixed-mode criterion based on SERR can be applied. According to Trethewey [1], the most utilised criterion has the form:

$$\left(\frac{G_I}{G_{Ic}}\right)^l + \left(\frac{G_{II}}{G_{IIc}}\right)^m + \left(\frac{G_{III}}{G_{IIIc}}\right)^n = f \qquad (2.31)$$

Where f is a failure index that equals unity at the onset of delamination propagation. The most common form is a linear criterion ($l=m=1$), restricted to the first two modes of crack propagation ($n=-\infty$). This is how the criterion is adapted by Song and Wass [14], for instance.

Another possible feature is that during the crack growth process the relative participation of each mode changes. This is due to geometry changes of the crack as it propagates or to perturbations to the near field stresses caused by the propagation. Salpekar et al. [15] studied delaminations growing along tapered regions and found that initially the SERR was all mode I but this component decreased with increasing delamination size until it was all mode II.

Chatterjee et al. [16] examined another interesting case. They studied the behaviour of circular and elliptic delaminations under transverse shear stress. For such disbonds, the mode I component of the SERR is absent and fracture is due to modes II and III.

In order to apply the SERR criterion, one must determine the critical values, or fracture toughnesses, G_{ic} , $i=I,II,III$. Unfortunately, for a typical fibre/epoxy composite, the interlaminar fracture toughnesses are very low. They are one order of magnitude lower than the in-plane fracture toughnesses. The reason is that the fibres hardly play any role in

strengthening the material along the through-laminae direction. This is shown by Wilkins [17], in terms of the SIF, through the graph that is displayed in figure 2.11. This fact also helps to explain the general tendency of composite materials to delaminate.

There are several test methods proposed in the literature for the measurement of the most important fracture toughnesses, G_{Ic} and G_{IIc}. The most widely used are the double cantilever beam (DCB) test for G_{Ic} and the end-notched flexure (ENF) for G_{IIc}. Both tests use a flat specimen with a lateral crack at one side, previously generated. The basic lay-outs of those two tests specimens are shown in figure 2.12.

The data reduction for the DCB test is carried out by considering each half of the cracked specimen as a cantilever beam. As shown by Gibson [10], we have, from beam theory:

$$\frac{\delta}{2} = \frac{P\,a^3}{3E_{fx}I} \tag{2.32}$$

where $\delta/2$ is the tip deflection of each cantilever beam, P is the load, a is the crack (or beam) length , E_{fx} is the Young's modulus in bending of the cracked half of the DCB along its axial direction and I is its second moment of area about the centroidal axis. The compliance C is then given by:

$$C = \frac{\delta}{P} = \frac{2\,a^3}{3E_{fx}I} = \frac{64\,a^3}{E_{fx}t\,h^3} \tag{2.33}$$

where t is the specimen (or crack) width and h is the total depth of the specimen. The SERR is then found by substituting equation 2.33 in equation 2.27 and differentiating with respect to crack length a:

$$G_I = \frac{96\,P^2a^2}{E_{fx}\,t^2\,h^3} = \frac{3\,P\delta}{2\,t\,a} \tag{2.34}$$

The critical value G_{Ic} is calculated using the values P_c, δ_c and a_c at the onset of crack growth. Keary et al. [18] stated that the DCB specimen is very convenient from an experimental point of view because crack growth can be controlled when using a constant displacement testing machine. They suggested that the machine should be stopped to allow for the crack growth to

self arrest, following an initial crack jump. The history of load versus crack length is assessed by means of successive loading and unloading cycles. The displacement is zeroed between cycles to remove any possible permanent (plastic) effect. Although a single specimen permits a collection of a great amount of data, caution should be taken in verifying whether the basic assumptions are obeyed throughout or not. The crack front must remain perpendicular to the load direction, for instance.

Ivens et al. [19] mentioned four different methods for the measurement of the initiation (of crack growth) fracture toughness. The methods are: 5% increase of the initial compliance, visual detection, onset of non-linear load-displacement behaviour and acoustic emission. The relative positions of these criteria on the load versus displacement curve are shown in figure 2.13.

The 5% increase of the initial compliance method considers the crack to have started propagating when the plot of compliance against length reaches that value, somewhat arbitrarily. There is not relation between this point on the curve and the onset of crack propagation. Visual detection is enhanced by applying a white, contrasting coating to the lateral surfaces of the specimen. But crack propagation often starts in the middle of the specimen. Visual detection can thus overestimate the initiation fracture toughness.

The onset of non-linear behaviour is a good detection method, provided the material does not shown inherent non-linear elastic characteristics. Ivens et al. [19] considered acoustic emission a very accurate method to pinpoint the start of crack propagation. Threshold signal amplitudes can be established beforehand, by loading the specimen to a level where there is no crack growth.

The accuracy of the DCB method was investigated by Hashemi et al. [20]. They developed correction factors that account for some departures from the simple beam theory used for the basic data reduction. The first issue is the effective shortening of the beams due to large displacements, if the specimen is slender. Secondly, the end blocks used for the application of the load stiffen the beams at the extremities and this effect is taken into account when calculating the compliance.

The DCB method was originally conceived for testing unidirectional laminates, with 0° fibre angle with respect to the specimen length. When testing other orientations, different fracture phenomena can occur. Bazhenov [21] described tests performed in cross-ply glass/epoxy laminates in which he observed two fracture modes. The first one is an intralaminar mode, characterised by the appearance of bridging fibres between the crack faces. The fracture process is stable and the fracture toughness is relatively higher. The second mode is interlaminar fracture, without bridging fibres, showing unstable growing of the crack and smaller toughness values. The author suggests that both fracture modes are part of a single process. The crack initiates inside one ply and gradually approaches the interlaminar plane.

Robinson and Song [22] also agreed that the DCB test produces a complex fracture behaviour when applied to interfaces other than those of unidirectional laminates. They observed fibre bridging and crack front deviations from the intended mid-plane when testing $+45^\circ/-45^\circ$ carbon/epoxy laminates. If this complex fracture behaviour is due to the peculiarities of the test, it must be eliminated. They proposed an edge delaminated DCB specimen to keep the crack in the desired region. The principle is similar to the one behind the side grooved fracture specimen used to control the direction of crack growth in isotropic materials.

There is some controversy among the standardisation bodies on the way that the necessary starter crack is introduced into a DCB specimen, as discussed by Brunner et al [23]. The American Society for Testing and Materials, ASTM [24] favour the use of film inserts, on the grounds that this provides a well-defined and repeatable initial defect. On the other hand, The European Structural Integrity Society, ESIS [25] adopts a pre-crack, reasoning that this represents better a defect in a real structure. The pre-crack method usually gives conservative values of the fracture toughness G_{Ic}.

Referring again to figure 2.12, the SERR G_{II} can be obtained from the ENF test data by means of the following expression shown by Gibson [10], also derived from elementary beam theory:

$$G_{II} = \frac{9 P^2 a^2 C}{2t(2L^3 + 3a^3)} \qquad (2.35)$$

where P, a, t and L are defined in figure 2.12. $C = \delta/P$ is the midspan compliance. The critical SERR G_{IIc} corresponds to the critical load P_c and the associated compliance C_c. The

compliance can be obtained from beam theory as:

$$C = \frac{(2L^3 + 3a^3)}{8E_{fx}th^3}$$

(2.36)

where E_{fx} is now the Young's modulus of a beam of depth $2h$. Equations 2.35 and 2.36 can be modified to include the effects of shear deformation. The discussion on the establishment of a standard mode II fracture test is less mature than it is for mode I, as Davies et al. [26] explain. Important aspects remain to be clarified, concerning the type of starter defect (as it is in mode I test), the dimensions of the specimen and the influence of friction. There are several candidate test specimens for the measurement of G_{IIc}, although the ENF is still the preferred geometry.

One of those alternative geometries was introduced by Maikuma et al. [27], called the centre notch flexural (CNF) test specimen. Their experiments have demonstrated that the residual properties (after impact) of laminates show good correlation with mode II fracture toughness. The CNF specimen tries better to represent the defect geometry and loading situation that arises in real structures after such events.

Table 2.1 shows the critical SERR for modes I and II as listed by several investigators. The results listed are for common carbon/epoxy unidirectional laminates with approximately 60% fibre volume fraction. References to mode III fracture mode are more scarce in the open literature. From all the authors surveyed, only Gillespie [8] provided G_{IIIc} values.

During the present research, the G_{Ic} test was conducted in conformity to the directions of the ASTM D5528 standard test method [24]. The G_{IIc} test, for which no standard method is still available, was performed according to the procedures outlined by Carlsson and Pipes [28], for the ENF test configuration introduced by Russell and Street [29].

Previous research on angle-ply laminates (Shi et al. [30]) and cross-ply laminates (Bazhenov [21]) have shown some departures from the ideal crack morphology, as mentioned. Those authors detected crack deviations from the mid-plane of the specimens and fibre bridging between crack faces. Those perturbations indicated an intralaminar cracking process, as well as an interlaminar fracture. Robinson and Song [22] and Foster et al. [31] proposed modified

specimens to maintain the crack within the interlaminar region of angle-ply laminates. Teflon inserts were used to create edge delaminations along the whole length of the specimens, as shown in figure 2.14. This modification was adopted in the present work both for mode I and for mode II tests on angle-ply laminates.

The data reduction for mode I tests of specimens having edge delaminations is the same as that for specimens without them. This is because both the cracked central portion and the edge delaminated region of the specimen can be considered as cantilever beams of about the same length. Also, the fracture toughness G_{Ic}, given by expression 2.34, is a function of the load per width ratio P/t, which is the same for the two regions. So, if the total load imposed to the specimen is used in the computations, the total width (central portion plus delaminated edges) should also be used.

The data reduction for mode II tests must consider the influence of the edge delaminations. For the basic ENF specimen, without them, the compliance C is given by expression 2.36. The edge delaminations can be considered as two simply supported beams added to the previous ENF specimen. Their span is the same, $2L$, the thickness of each one is h, their width is t_e and every one is submitted to a central load of $P_e/2$. The central deflection of the delaminated edge portion δ, is then given by:

$$\delta = \frac{(P_e/2)(2L)^3}{48EI} \qquad (2.37)$$

and the edge beams compliance C_e results:

$$C_e = \frac{\delta}{P_e} = \frac{L^3}{Et_e h^3} \qquad (2.38)$$

As the central deflection δ is the same for both the central and edge regions and the total load P_T is the sum of the loads P and P_e, the total compliance C_T results:

$$\frac{1}{C_T} = \frac{1}{C} + \frac{1}{C_e} \qquad (2.39)$$

but from (2.36) and (2.38), $1/C_e$ can be written in terms of $1/C$:

$$\frac{1}{C_e} = \frac{1}{C}\frac{t_e}{t}\frac{\left(2L^3 + 3a^3\right)}{8L^3} \qquad (2.40)$$

and finally it is possible to obtain the cracked beam compliance, C, that is needed for the calculation of G_{IIc}, in terms of the total compliance C_T that is measured during the test,

$$C = C_T\left[\frac{2L^3\left(4t + t_e\right) + 3t_e a^3}{8tL^3}\right] \qquad (2.41)$$

2.2.2 DELAMINATION: FATIGUE

The previous section addressed the problem of delamination propagation under static loading conditions. In addition to the static behaviour, fatigue must also be considered for the production riser application, given the inherent dynamic nature of the environment. In this way, even when a given tapered tube geometry is proven safe from delaminating under static conditions, it still may not be so under fatigue loading.

Mohlin et al. [33] showed that the delamination growth under fatigue loading has similarities with the way that fatigue cracks grow in metals. There is a long initiation phase, followed by a rapid propagation once the delamination reaches a critical size. The Paris' law of fracture mechanics is used to quantify the rate of the propagation phase, adopting the SERR as the loading parameter:

$$\frac{dS}{dN} = K\left(\Delta G\right)^m \qquad (2.42)$$

where S is the delamination area, N is the number of cycles, ΔG is the range of the strain energy release rate, K and m are constants. The author tested T300/1034E graphite/epoxy laminates with 28 plies and a stacking sequence of $[\pm 45/0_2/\pm 45/90/0_3/\pm 45/0_2]_s$. A circular hole was drilled in the centre of each specimen, to provide the stress raising detail that leads to delamination. The specimens where loaded in compression with a R ratio $(=\sigma_{min}/\sigma_{max})$ of $-\infty$ and with several different values of σ_{min}, ranging from 50% to 80%, approximately, of the

static compressive strength, σ_{sc}. The delamination sizes were measured by means of X-ray radiation, at certain intervals.

In order to calculate the SERR for a given delamination size under a known loading condition, a 3D finite element program was used. Two analyses were undertaken, with increasing defect sizes. The variation in the total strain energy of the model between the two analysis gives the energy released. The drawback of this approach is that only the total G is obtained. It is not possible to separate it into the different propagation modes. Figure 2.15 shows a log-log diagram with some results. As can be seen, the Paris' law, expression 2.42, is satisfactorily obeyed.

Rybicki and Kanninen [34] introduced the *virtual crack closure* (VCC) method to calculate the SERR from FEM results. They started from the statement of Irwin that the energy absorbed when a crack extends by an amount Δa is equal to the work required to close it to its original length. Referring to the mesh of plate elements of thickness t as shown in figure 2.16, the expressions for the evaluation of the SERRs are:

$$G_I = \lim_{\Delta a \to 0} \frac{1}{2t\Delta a} F_{yc}(v_c - v_d) \quad and \quad G_{II} = \lim_{\Delta a \to 0} \frac{1}{2t\Delta a} F_{xc}(u_c - u_d) \qquad (2.43)$$

where F_{yc} and F_{xc} are the vertical and horizontal forces respectively, at node c, needed to bring nodes c and d together again. The vertical and horizontal displacements of node c are v_c and u_c. Similar nomenclature applies to node d. The nodes defining the delamination surfaces were duplicated, with stiff springs placed between them. The delamination progress is simulated by deleting the spring elements placed behind the crack front, in relation to the propagation direction. The forces and displacements necessary for the application of the method can be obtained from two subsequent analysis. In the first one, the forces developed at the springs are recorded. Then, those springs are deleted, allowing the crack faces to open a little more. The relative displacements of the nodes that were originally coincident at the crack tip are obtained. The interesting aspect of the method is that it can separate the different propagation modes. The method showed good correlation with reference values if constant strain elements were used. The authors [34] even declared that the mesh does not need to be very refined. On the other hand, poorer results were obtained when higher order elements

were adopted.

Murri et al. [35] tested symmetric tapered laminates with internally dropped plies in fatigue. The application of composite materials in their case was for the hubs of helicopter rotor blades. They tested both graphite/epoxy and glass/epoxy prepregs, with two different lay-ups. The fatigue loading was done in tension, with an R factor of 0.1 and a frequency of 5 Hz. In some of the 1" wide by 10" long specimens a tough thermoset interleaf was added to improve the resistance to delamination. The lay-ups consisted of sequences of $0°$ and $\pm45°$ layers, with the taper being created by dropping the latter ones. The taper angle was $5.7°$. Figure 2.17 shows the configuration of their specimens.

The authors conducted the tests until the onset of delamination, which was unstable, audible and visible. Figure 2.17 also shows some typical delamination locations reported. The maximum load varied between 60 and 120 kN for the various tests, but the authors did not mention the percentage of the ultimate load associated with each result. The number of cycles for unstable delamination onset ranged roughly from 10^4 to 10^6 cycles. An SERR approach was used in the analysis of the results, with the G values being obtained by means of the VCC method. The SERR associated with each test were compared to G values for the delamination onset of a group of DCB specimens also tested in fatigue. It is worth reproducing here the graph that showed the results of these last tests. The graph, displayed at figure 2.18, correlates the maximum G_I achieved during the cyclic loading with the number of cycles for the onset of delamination for a graphite/epoxy laminate.

Hojo et al. [36] also tested several different laminates in fatigue using the DCB test configuration. They utilised unidirectional carbon fibre prepregs, with matrices of different toughnesses, including several epoxies, a thermoplastic modified epoxy and PEEK. They reported changes in basic fatigue behaviour, depending on the toughness of the resin. In laminates with brittle matrices, the maximum load achieved during the cycle controlled the process. Laminates with toughened matrices showed the major influence of the load range. These former laminates also showed a higher growth threshold and lower crack growth rates.

Concerning the estimation of delamination growth under cyclic loading, Dahlen and Springer [37] introduced a model of the form:

$$\Delta a \frac{\sigma_f^2}{E_y G_{crit}} = A \left(U \frac{G_{max}}{G_{crit}} \right)^b \tag{2.44}$$

where Δa is the delamination growth during one cycle, σ_f and E_y are the ply strength and stiffness, respectively. G_{max} is the strain energy associate to the maximum stress achieved in the cycle and G_{crit} is the critical SERR. A and b are constants whose values depend on the percentile participation of modes I and II in the fatigue process. The form of the function U depends on whether or not there was shear reversal during mode II propagation. The authors argued that delamination grows faster when there is a shear deformation reversal at its tip.

Wisnom et al. [38] applied the simpler Paris' model (expression 2.42) to the investigation of the fatigue behaviour of a rapidly tapered composite helicopter blade. For a XAS/913 carbon/epoxy prepreg they determined values of 2.14 m/J and 6.77 for the constants K and m, respectively. In their case the delaminations started very early during the tests. There were two types of terminating plies in a given specimen, the first type with $\pm\,45^\circ$ and the second with 0° fibre angles. The delaminations always developed at the end of the stiffer, nought degree ones.

In another paper, Wisnom et al. [39] described static and fatigue tests on asymmetrically tapered composites, loaded in tension. The specimens were made up of blocks of eight plies with a lay-up of $(0_4/+45_2/-45_2)$ each. The taper in thickness was obtained by terminating one out of four blocks, as shown in figure 2.19. The specimens were made of Fibredux T300/914C carbon/epoxy prepreg tapes. During the static tests, the delamination onset loads were determined from the change in slope of strain gauge readings against the load. Figure 2.19 also shows a typical delamination observed during the static tests.

Fatigue tests followed the static ones. The R ratio was 0.1, the frequency was 2 Hz and the maximum load corresponded to 80% of the mean static delamination load. Delaminations appeared quickly, and propagated into the thin section. The crack layouts were similar to those observed during the static tests. The delamination lengths ranged from 2 to 20 mm, after 1000 to 6000 cycles.

Petrossian et al. [40] also performed cyclic load tests on unidirectional glass/epoxy and carbon/epoxy specimens. The introduction of high local interlaminar stresses was achieved by

simply cutting widthwise 4 plies out of the 32 plies of each specimen. The loading arrangement was a three-point bending. The cuts were made at the mid-length of the 40 mm long specimens. The beams consisted of 22 continuous plies, 4 cut plies and 6 continuous plies, counting from the compressed side to the tensioned one.

The authors applied Paris' law (equation 2.41) with the same modification given in expression 2.44, i.e., to normalise the cyclic SERR with respect to the critical static value, G_c. The SERR values were obtained from FEA models by means of the VCC method. The authors reported a change in mode mix, depending on the delamination size. For delamination lengths under 0.5 mm, the propagation had characteristics of both modes I and II. Beyond that length, the fracture progression was mainly by in-plane shear, mode II.

2.2.3 LAMINATE STRENGTH

In the previous two sections we have been concerned with the failure of the tapered tube by delamination, both under static and fatigue conditions. This type of failure was observed in many previous investigations done on tapered thickness composites, mainly due to the interlaminar stresses that the dropped plies cause. Nevertheless, the occurrence or not of delaminations depends on the severity of the stress concentration detail and on the toughness of the material. There can be further consequences of the dropped ply configuration that lead to the preferential occurrence of other failure modes.

The next failure mode to be considered is laminate failure by compressive stresses along the direction of the fibres. The composite tapered tubes have the main purpose of resisting the large bending moments developed at the extremities of a production riser, as mentioned in the introduction of this chapter. In pure bending loads, to a given extreme fibre tensile stress corresponds an opposite extreme fibre compressive stress of the same magnitude. It is well known that composite laminates tend to show lower longitudinal compressive strengths, compared with the tensile ones. These facts lead one to the conclusion that, if the tapered tube does not delaminate under a bending load, it will probably fail by compression at the concave side.

Apart from the bending load, the tapered tube can also be subjected to pressure, configuring a biaxial load case. The issue of the strength of composite tubes under biaxial load conditions was addressed by Hinton et al. [41]. They gathered a large database of experimental results related to +/-75°, +/-55° and +/-45° filament wound GRP tubes. The load cases were various combinations of circumferential tension and axial tension or compression. The authors applied five of the most well known failure criteria for composite laminates to their experimental results. The criteria utilised were the following:

- Maximum stress;
- Maximum strain;
- Hill;
- Tsai-Wu and
- Schneider.

In addition, they proposed a model of their own, which is an incremental version of the maximum stress criterion.

Their analysis is progressive, with the lamina stresses being compared with the lamina strengths at every step. The non-linear shear behaviour of composite laminae is taken into account, by decreasing the shear modulus at each load step. If a failure is detected, the elastic constants of the lamina involved are modified, as shown in table 2.2, and the new laminate stiffness is determined. The load is increased further, until another failure occurs. The laminate is considered to have failed when two modes of failure were detected in any given lamina.

The authors showed that their proposed incremental progressive failure model gave the best correlation with the experimental results, despite some observed discrepancies. All the other proposed criteria showed excessively conservative results for the initial failure envelopes of the +/-55° and +/-45° GRP tubes. Further, those criteria are related to initial failure only, and do not recognise the ability of the laminate to support loads beyond the first failure event. As Hart-Smith [42] discussed, some of the most used criteria, such as the Hill and the Tsai-Wu models, are mathematical formulations mixing different phenomena, which are not physically correlated. The basic assumption implied is the same "smearing" simplification adopted for the determination of the elastic constants. In reality, it is not the lamina that fails, but the

matrix, the fibres or the interface between them, with different mechanisms in each case.

Another question, common to all failure criteria, relates to the figures adopted for the strength values. As Hinton et al. [41] and also Piggott and Rai [43] noted, the strength values are obtained from simple load cases of unidirectional specimens. The strengths obtained are used to assess the behaviour of complex laminate geometries, often under 3D stress states. There are strong indications that the strength of a lamina depends on the lay-up arrangement of which it is part. This will determine, in the end, the real stress field that the lamina is subjected to.

Focusing now on the issue of the longitudinal compressive strength, Hull [44] gave a general picture of the behaviour of carbon/epoxy systems. He stated that there is no satisfactory general account of the question, so many are the factors involved. There are two basic failure mechanisms, depending on the shear modulus of the matrix and the shear strength of the fibres. The laminate can fail either by shear or by buckling of the fibres. To show the transition from one mode to the other the author displayed a plot of the compressive strength against temperature, see figure 2.20. This graph was obtained by Ewins and Potter [45].

The temperature rise diminishes the matrix shear modulus rapidly. For low temperatures and hence stiff matrices, the shear mode prevails. A schematic view of that failure mode is displayed at figure 2.20. A steady decrease of the compressive strength with the temperature is observed. At a very well defined transition point, the fibre buckling mode, also sketched in figure 2.20, becomes predominant. The rate of loss of compressive strength with temperature is much increased. The up-take of water has the same plasticising effect on the matrix, and similar reductions in the compressive strength of the laminate should be expected.

Hull [44] stressed that any factor which leads to a reduction in the support provided by the matrix and by the surrounding fibres will favour fibre buckling. The compressive strength will thus be greatly reduced in:
- Resin rich regions;
- Regions with a large number of voids;
- Regions where the fibres are misaligned or preferentially oriented for easy buckling;
- Regions where the fibres are debonded from the matrix;

• Regions where the matrix shows viscoelastic deformation.

It is evident that the thickness transition region of a tapered laminate can display at least the first three of the listed characteristics.

Effendi et al. [46] performed experimental evaluations of the compressive failure of several unidirectional laminates. They tested three carbon/epoxy systems: T300/914, T800/5245C and M40J/913, among other materials. The specimen configuration used was proposed by the French company Aerospatiale. A word of caution was given that no universally accepted compression test method exists today, so the results can vary according to the method used. The common feature of all test methods proposed is a high lateral constraint of the specimen to avoid its gross buckling failure under compressive load.

For the carbon/epoxy systems, the failure mode was reported to be fibre kinking, resulting in a deformation pattern as shown in figure 2.21. Different values were given to the geometric parameters α, β and d of the kink bands, according to the material tested. The reason for this failure mode, said the authors, was the initial waviness of the fibres. The load increment caused amplification of the waviness the fibres, resulting in fracture at the points with maximum stress in the fibres. The authors also reported a non-linear elastic behaviour of the load *versus* deformation curve, before failure. They attributed this behaviour to the intrinsic properties of the carbon fibres, and not to geometric effects like the initial fibre waviness.

The influence of the initial waviness of the fibres on the compression strength of unidirectional composites was also investigated by Hsiao and Daniel [47]. They considered three forms of waviness: uniform, localised and graded, all with a sinusoidal geometry. Models were developed for the reduction in stiffness and strength for each case, based on the CLT and on the Tsai-Wu failure criterion. A limited number of experiments were performed to verify the model. Figure 2.22 shows the results of their model for the uniform waviness case, applied to a IM6G/3501-6 carbon/epoxy system. The rate of reduction in compressive strength is quite drastic for amplitude over length ratios of the waviness under 5%.

Barbero and Tomblin [48] confirmed that the prediction of the compression strength of composites is divided into two schools: fibre micro-buckling models and kink band formation models. They proposed a model of the first group, relating the compression strength with the fibre misalignment. Their paper displayed a graph showing the reduction in compressive

strength that is very similar to the one displayed in figure 2.22. The authors went further, arguing that in reality, fibre misalignment follows a probability distribution, rather than having a single value. They proposed a damage mechanics model in which the random nature of fibre misalignment is considered.

The experimental investigation performed during the present research is described in Chapter 3. It started with tests for the determination of the toughness of the carbon/epoxy laminates. After that, several tubular specimens of different configurations were tested in pure internal pressure and in four point bending. There were some combined internal pressure and bending tests, as well. A few fatigue tests were also performed.

2.3 THICK COMPOSITE TUBE MODELS

The models available to describe composite tubes are classified in the review paper of Noor and Burton [49]. Two major groups are the three-dimensional and the two-dimensional models. Two-dimensional models account exactly (in the context of elasticity) for the stresses and strains at the surface of the lamina, whilst adopting some simplifying hypothesis for the out-of-plane (or transverse) ones. Three-dimensional models are appropriate to predict the values of the transverse stresses and deformations for thick laminates. 3D solutions are exact within the realm of linear elasticity, and so exempt of the simplifications imposed by 2D methods, like the CLT.

Several methods were proposed within the scope of the two-dimensional models to calculate the transverse shear deformations of thin to medium thick laminates. The objective was to improve the accuracy beyond the Kirchoff-Love hypothesis of straight inextensional normals, and hence null shear deformations, which is adopted in the CLT. The low transverse shear stiffness of laminated materials gives rise to significant shear deformations even for relatively slender members in bending. Most of the 2D methods are based on a hypothesis which assume quadratic or cubic variation of displacements, strains and stresses through the thickness. An intermediate approach between 2D and full 3D methods is to assume a piecewise variation of those quantities. Naturally, this discrete layer methodology allows a more flexible description of arbitrary displacement and stress fields.

As Reddy and Robbins [50] pointed out, two factors can lead to the necessity of a three-dimensional analysis. Firstly comes the inherent complexity of the stress field in a multi-layer, thick tube. In addition to that, there can be regions of potential damage initiation, requiring detailed assessment. These regions are usually associated with stress concentrations due to material or geometric discontinuities. Transverse stress fields are generated as a result. Features such as holes, ply drop-offs or free edges are typical examples. As the tapered composite tube has both characteristics, a full 3D modelling approach is mandatory.

Before discussing the available thick composite tube models, the nomenclature to be adopted in the study is defined. Figure 2.23 shows the cylindrical coordinate system used and the displacement and stress symbols and conventions. The average radius of the tube is r_o and its total thickness is h. The definition of what is considered "a thick composite tube" is somewhat arbitrary but it will be considered here as the one with an aspect ratio $S=r_o/h$ smaller than 4. The tapered tubes of a composite production riser from previous calculations [51] had S values between 1.9 and 4.7.

Pagano [52] studied the range of validity of the CLT by comparing the results provided by it with those given by the 3D linear elasticity theory. The analysis was concerned with flat, bi-directional ($0°/90°$) laminated plates in bending, with varying span-to-thickness ratios. He began by stating some of the restrictions of the CLT:

- Linear variation of in-plane displacements with thickness, even for drastic stiffness changes from layer to layer.
- Edge effects are neglected.
- Null transverse shear deformations, due to the Kirchoff-Love hypothesis (normals remain straight and normal).
- Constitutive relations based on a state of plane stress, not allowing precise determination of inter-laminar stresses.

Whitney [53] proposed a method to calculate the transverse shear stresses, overcoming one of the limitations of the CLT. The transverse shear stresses are obtained from approximate, piecewise functions. Those functions are adjusted to vanish at the free surfaces and to be continuous at the interfaces between two distinct layers. The results are still approximate for

thick laminates as they are obtained under the other assumptions of the CLT.

Pagano considered a state of plane strain, as figure 2.24 shows. The distributed load $q(x)$ is of the form:

$$q(x) = q_o \ sin\left(\frac{n\pi x}{L}\right) \qquad (2.45)$$

where q_o is a constant, L is the length of the plate and n is an integer. The loading in this form is common place in several methods derived for the analysis of thick laminates, as any load function can be expressed reasonably by a Fourier series. The span-to-thickness ratio is defined by him as $S=L/h$, where h is the total thickness of the plate.

Figure 2.25 shows some results for a three-ply laminate. The stresses were normalised by dividing them by the load amplitude q_o. The displacements were normalised as well, considering the geometry of the plate, the load and the Young modulus of the material. The normalised vertical displacement w is taken at the middle of the span. The normalised σ_x stresses are evaluated at mid-span, as well. The normalised shear stresses τ_{xz}, obtained for the CLT case as proposed by Whitney [53], are the ones at $x=0$. The normalised coordinate z is given by $z=y/h$. The load case shown corresponds to $n=1$. The CLT values are indicated by the dashed lines. The results confirm that the elasticity solutions converge to the CLT ones as the span-to-depth ratio increases. Generally the stresses converged more rapidly to the CLT results than the deflections. It should be noted that the definition of "thick" or "thin" laminates is also dependent upon material properties and laminate geometry.

In a later paper Pagano [54] extended the analysis to bi-directional, finite, laminated rectangular plates with pinned edges. The same conclusions were drawn regarding the convergence of 3D results to the CLT ones as the plates became thinner. Conversely, Pagano showed how the results of a full 3D analysis can differ from the CLT ones, for thick laminates.

Concerning thick, circular cylindrical composite shells, we will discuss some available models in the same chronological order that they have appeared in the literature. We begin with the work of Srinivas [55], published in 1974. The author proposed an approximate theory for

thick composite tubes, with general boundary conditions. He argued that an exact 3D analysis was only computationally viable (at that time) for a few cases. He developed both approximate and exact 3D models, together with a thin shell approach, in order to see how their results compared.

The author's approximate theory considers the displacements to be piecewise linear across the thickness. The displacements of the *jth* ply are given by:

$$u_j = r_e \sum_{k=0}^{j} U_k \ \zeta(j,k)$$

$$v_j = r_e \sum_{k=0}^{j} V_k \ \zeta(j,k) \tag{2.46}$$

$$w_j = r_e \sum_{k=0}^{j} W_k \ \zeta(j,k)$$

where *j=1,2,...p* (layer number) and

$$\zeta(j,k) = \begin{cases} 1 & \text{for } k \neq j \\ \dfrac{r - r_j}{h_j} & \text{for } k = j \end{cases} \tag{2.47}$$

In equations 2.46 U_k, V_k and W_k are functions of θ and z and are independent of r. These functions are the differences between the displacements of the inner and the outer surfaces of the *kth* ply at a given θ and z. The constant r_e is the external radius of the tube, r_j is the inner radius of the *jth* ply and h_j is its thickness.

The governing differential equations and boundary conditions are obtained by a variational approach. It states that the variation in strain energy U equals the work done by the applied forces due to virtual displacements, W_e (Hamilton's principle):

$$\delta U = \delta W_e \tag{2.48}$$

The strains are obtained from the displacements given by 2.46 through the strain-

displacements relations in cylindrical co-ordinates. The stresses are derived from the strains by means of the constitutive relations for orthotropic materials. The boundary conditions at the edges are obtained by equating the applied forces to the corresponding stress resultants.

Concerning the exact 3D analysis of laminated circular cylindrical shells, Srinivas pointed out that the simply-supported case is one of the few cases where an exact elastic analysis is possible. That is because the simply-supported boundary condition is naturally obtained if one chooses the displacements and stresses to be written as double trigonometric series. That seems to be another reason why several methods available in the literature for the analysis of thick laminated tubes adopt those kind of functions to represent displacements and stresses.

Pagano [56] proposed a theory to define completely the stress in a generic composite laminate. It was based on the variational principle proposed by Reissner, which stated that the governing equations of elasticity can be obtained from the variational equation:

$$\delta J = 0 \qquad\qquad (2.49)$$

where:

$$J = \int_V F \, dV \quad - \quad \int_{S'} \bar{\tau}_i u_i dS \qquad\qquad (2.50)$$

and

$$F = \frac{1}{2} \sigma_{ij} \left(u_{i,j} + u_{j,i} \right) - W \qquad\qquad (2.51)$$

In the above W is the strain energy density, V is the volume of the body, S is its total surface, τ_i are the prescribed tractions, u_i are the displacement components and S' is the portion of the surface where the tractions are prescribed. From this equation the author arrived at expressions for the stresses written in terms of stress resultants.

In a following paper Pagano [57] applied that formulation to study the elastic response of laminated axisymmetric bodies of revolution. The variations of stresses with the thickness were assumed to be of a given polynomial form in the r co-ordinate. This allows the integration of the expressions derived from the energy functional along the thickness, resulting in ordinary differential equations in the z co-ordinate. The differential equations were then

solved by a finite difference numerical scheme. He applied the methodology to involute bodies of revolution, but a tapered composite tube is also a possible target for his method.

Reddy and Liu [58] mentioned another aspect of the Kirchoff-Love assumptions. That is to consider the transverse displacement to be independent of the thickness coordinate. The authors argued that this simplification can lead to errors of up to 30% in the results for layered anisotropic shells.

The researchers proposed a method based on the hypothesis of a parabolic distribution of shear strains. The method is thus accurate in the prediction of the gross response characteristics (like deflections and fundamental frequencies) of thin and medium thick laminated shells. As already mentioned, such methodologies are unsuitable to detect the intricate variation of the stress field in thick laminated tubes. However, the authors proposed two parameters that could help to identify the possible need of a more sophisticated analysis. They stated that for a laminated shell panel the transverse normal stress is roughly of the order h/r_o while the transverse shear stress is of the order h/L, times the bending stresses.

Ren [59] derived an exact solution for laminated cylindrical shells in cylindrical bending. His basic assumption was that the shell length was infinite, so a state of plane strain held in the $r\text{-}\theta$ plane. Considering each layer to be composed of orthotropic materials with cylindrical anisotropy, the constitutive equations are given by:

$$\varepsilon_r = R_{11}\,\sigma_r + R_{12}\,\sigma_\theta \qquad \varepsilon_\theta = R_{12}\,\sigma_r + R_{22}\,\sigma_\theta \qquad \gamma_{r\theta} = R_{44}\,\tau_{r\theta} \qquad (2.52)$$

where R_{ij} are the reduced compliance coefficients for plane strain:

$$R_{ij} = S_{ij} - \frac{S_{i3}S_{j3}}{S_{33}} \qquad (i,j = 1,2,4) \qquad (2.53)$$

and S_{ij} are the compliance coefficients with respect to the axes of material symmetry which, in this case, coincide with the axes of shell symmetry. The normal stress along the axial direction is written as:

$$\sigma_z = -\frac{1}{S_{33}}\left(S_{13}\,\sigma_r + S_{23}\,\sigma_\theta\right) \qquad (2.54)$$

All the strains, stresses and displacements are independent of z. The load is a distributed radial force at the upper surface of the shell that can be written in the form of a Fourier series with respect to the angular coordinate θ:

$$q_r = \sum_{n=1}^{\infty} q_n \sin\left(\frac{n\pi\theta}{\phi}\right) \qquad (2.55)$$

The angle ϕ is the angular span of the shell, that equals to 2π in the case of a tube. The author showed that in this case a stress function in r and θ does exist that satisfies the partial differential equation resulting from the conditions of compatibility of displacements.

Roy and Tsai [60] also developed a model for a thick composite cylinder in a state of plane strain. They considered load cases of internal and external pressure and axial force. The filament-wound cylinders are considered as an assembly of orthotropic units. Each orthotropic unit is made of adjacent +/-α lay-ups, where α is the angle between the axis of the tube and the fibre direction. The assembly can be considered as a specially orthotropic tube. That is also the case for the carbon layers of the composite tapered tube.

Noor and Peters [61] agreed that analytical 3D solutions can be obtained for simply-supported orthotropic cylinders. However, they made the point that lengthy algebraic manipulations are involved. They proposed a semi-analytical procedure in which the displacements and stresses in the r-θ surface are obtained by a double Fourier series, combined with a numerical discretization through the thickness. They also stated that their method needed only a few pairs of Fourier harmonics to find the solution. Two dimensionless co-ordinates were used:

$$\xi = \frac{z}{L}\,; \qquad \rho = \frac{r - r_o}{h} \qquad (2.56)$$

and the displacements were written as:

$$\begin{Bmatrix} u \\ v \\ w \end{Bmatrix} = N^i \sum_{m=1} \sum_{n=0} \begin{Bmatrix} u_{mn} \cos m\pi\xi \cos n\theta \\ v_{mn} \sin m\pi\xi \sin n\theta \\ w_{mn} \sin m\pi\xi \cos n\theta \end{Bmatrix} \qquad (2.57)$$

The shape functions N^i are used in approximating the displacements along the thickness direction. Similar expressions apply to the surface loads and to the stresses. The method is based on three procedures, as explained by Noor and Peters:

- Mixed (flexibility/stiffness matrices) finite elements in the thickness direction. Stress components can be discontinuous at interfaces.

- Operator splitting to show the effects of different Fourier harmonics in the longitudinal and circumferential directions.

- Successive application of the finite element method and the Rayleigh-Ritz technique.

In a following paper [62], Noor and Peters introduced a first order shear deformation method to calculate the response of multilayered composite cylinders. Because the transverse shear stress is assumed to vary linearly with the thickness, some correction is necessary. The authors proposed to make the correction after a first two-dimensional appraisal of stresses and strains. This is done by comparing some gross response parameter indicated by the first order method with the full 3D value. The shear strain energy was chosen to be that parameter. A shear correction factor is obtained at the end.

To have a 3D solution, the authors estimated the out-of-plane stresses (σ_r, $\tau_{r\theta}$ and τ_{rz}) from the in-plane ones (σ_θ, σ_z and $\tau_{\theta z}$) by the integration of the 3D equilibrium equations:

$$\tau_{rz} = -\frac{1}{\alpha} \int_{-\frac{h}{2}}^{r} \left[\frac{1}{r_o} \frac{\partial}{\partial\theta} \tau_{\theta z} + \alpha\left(\frac{\partial}{\partial z} \sigma_z \right) \right] dr + c_z$$

$$\tau_{r\theta} = -\frac{1}{\alpha} \int_{-\frac{h}{2}}^{r} \left[\frac{1}{r_o} \frac{\partial}{\partial\theta} \sigma_\theta + \alpha\left(\frac{\partial}{\partial z} \tau_{\theta z} \right) \right] dr + c_\theta \qquad (2.58)$$

$$\sigma_r = -\frac{1}{\alpha} \int_{-\frac{h}{2}}^{r} \left[\frac{1}{r_o}\left(-\sigma_\theta + \frac{\partial}{\partial\theta} \tau_{r\theta} \right) + \alpha\left(\frac{\partial}{\partial z} \tau_{rz} \right) \right] dr + c_r$$

where

$$\alpha = 1 + \frac{r - r_o}{r_o} \qquad (2.59)$$

In another paper from Ren [63], he introduced an elasticity solution for a laminated circular cylindrical roof. The structure was of finite extent in both angular and length dimensions and is simply-supported on all the edges. The load considered was a distributed force acting on the outer surface, expressed as a double Fourier series.

Ren assumed the displacement fields to be similar to those shown by expression 2.57. The loads distribution along the θ and z directions were written as double Fourier series, as well. The procedure transformed the partial differential equations in r, θ and z that govern the problem into ordinary differential equations, in r. This is perhaps the strongest reason for adopting Fourier series for the solution of the problem.

Noor and Peters [61] had a semi-analytical approach, through the consideration of shape functions in the radial coordinate. Ren preferred power series in r. For a given Fourier pair (m,n) he wrote:

$$u_{mn} = \sum_{k=0}^{\infty} u_k r^{k+\lambda+1} \qquad v_{mn} = \sum_{k=0}^{\infty} v_k r^{k+\lambda+1} \qquad w_{mn} = \sum_{k=0}^{\infty} w_k r^{k+\lambda} \qquad (2.60)$$

where λ is an unknown constant and u_k, v_k and w_k are the coefficients.

Varadan and Bhaskar [64] adopted the same type of solution as Ren. They only wrote the expressions for the displacements in a slightly different way. They mentioned the fact that the solutions in the form of power series are associated with the classical method of Frobenius for solving the homogeneous coupled ordinary differential equations obtained. Those authors also wrote the conditions of continuity at any interface:

$$\begin{aligned} \left(\sigma_r, \tau_{r\theta}, \tau_{rz}, u, v, w \right) \quad & for\ layer\ (i-1) \quad = \\ \left(\sigma_r, \tau_{r\theta}, \tau_{rz}, u, v, w \right) \quad & for\ layer\ i \end{aligned} \qquad (2.61)$$

Varadan and Bhaskar repeated the comparative exercise made by Pagano [52], now in relation

to laminated tubes. They analysed several tube geometries by means of their exact elasticity solution. The load is an internal pressure given in terms of trigonometric functions both in co-ordinates θ and z, as it is common place. Figure 2.26 shows their results, in terms of normalised stresses. The tube in this case was made of three layers of equal thickness. The material was specially orthotropic, in a (90°/0°/90°) arrangement. This is quite similar to the tapered tube construction. They considered three different thicknesses, with aspect ratios S of 4, 10 and 100.

The authors showed with their results that the variations of in-plane stresses through the thickness of the tubes had patterns similar to those of a laminated plate. However, two differences arose concerning the stresses developed normally to the θ - z plane. The transverse normal stress in plates decreases monotonicaly from a maximum at the loaded face to zero at the free face. In the present case the maximum σ_r occurs inside the wall, there being greater differences from the loaded face value the thinner is the shell. Further, refined shell theories assume the transverse shear stresses to vary with the square of thickness. Figure 2.26 shows that σ_{rz} distribution for a thin shell (S=100) is far away from that assumption.

In another paper, Bhaskar and Varadan [65] proposed a piecewise higher-order theory for laminated composite cylindrical shells. They used a mixed stress-strain law for the kth layer, as introduced by Reissner, of the form:

$$
\begin{Bmatrix} \sigma_\theta \\ \sigma_z \\ \tau_{\theta z} \end{Bmatrix}^k = \begin{bmatrix} Q_{22} & Q_{23} & 0 \\ Q_{32} & Q_{33} & 0 \\ 0 & 0 & Q_{66} \end{bmatrix}^k \begin{Bmatrix} \varepsilon_\theta \\ \varepsilon_z \\ \gamma_{\theta z} \end{Bmatrix}^k + \begin{bmatrix} C_{12} \\ C_{13} \\ 0 \end{bmatrix}^k \left(\sigma_r \Big/ C_{11} \right)^k
$$

$$
\begin{Bmatrix} \varepsilon_r \\ \gamma_{r\theta} \\ \gamma_{rz} \end{Bmatrix}^k = \left(\frac{-1}{C_{11}^k} \right) \begin{bmatrix} C_{12} & C_{13} & 0 \\ 0 & 0 & 0 \\ 0 & 0 & 0 \end{bmatrix}^k \begin{Bmatrix} \varepsilon_\theta \\ \varepsilon_z \\ \gamma_{\theta z} \end{Bmatrix}^k + \begin{bmatrix} 1/C_{11} & 0 & 0 \\ 0 & 1/C_{44} & 0 \\ 0 & 0 & 1/C_{55} \end{bmatrix}^k \begin{Bmatrix} \sigma_r \\ \tau_{r\theta} \\ \tau_{rz} \end{Bmatrix}^k
$$

(2.62)

where C_{ij} and Q_{ij} are the three-dimensional and plane strain reduced stiffness coefficients, respectively. The authors assumed the shell to be loaded only by distributed forces on the inner and outer surfaces. The edges were free from any traction. The governing equation for the problem was then written using the principle of minimum potential energy.

Bhaskar and Varadan recalled that their previous paper [64] had shown that the in-plane displacements varied in a zig-zag manner through the thickness. These displacements are continuous across the interfaces, as the layers are perfectly bonded. Their first derivatives are discontinuous because of the abrupt change in elastic properties from layer to layer. The variation of w with r was very small for moderately thick shells. For these reasons, they wrote:

$$
\begin{aligned}
u^k &= u_0 + r\left(\phi_1\right) + \psi_k\left(S_1\right) + r^3\left(T_1\right) \\
v^k &= v_0 + r\left(\phi_2\right) + \psi_k\left(S_2\right) + r^3\left(T_2\right) \\
w^k &= w
\end{aligned}
\tag{2.63}
$$

The unknowns u_0, v_0, ϕ_1, ϕ_2, S_1, S_2, T_1, T_2 and w are functions of θ and z only. The term ψ_k is a piecewise, zig-zag linear function of r. Its value alternates between +1 and -1 for successive interfaces. There is no quadratic term in r in this proposed approximate displacement field. The authors argued that this is because its effect is small for symmetric laminated shells, which are the most common type.

Lagrange polynomials of the fourth degree were used to approximate the transverse shear stresses. They were chosen in order to satisfy the stress continuity conditions 2.61. However, the results showed that this approximation for the transverse shear stresses led to somewhat erroneous values when compared with the exact ones given in [64]. Much better agreement was obtained if the transverse shear stresses were evaluated from the equilibrium conditions.

Wu and Liu [66] introduced a mixed approximate displacement field for the case of a simply supported laminated cylindrical shell subjected to a sinusoidal internal pressure. The expressions for the kth layer incorporate both the piecewise polynomial approach and Fourier harmonics:

$$
\begin{aligned}
u_k &= \sum_{m=1}^{\infty}\sum_{n=1}^{\infty}\left[\left(a_0\right)_{mn}^k + r_k\left(a_1\right)_{mn}^k + r_k^2\left(a_2\right)_{mn}^k + r_k^3\left(a_3\right)_{mn}^k\right]\cos m\pi\xi\cos n\theta \\
v_k &= \sum_{m=1}^{\infty}\sum_{n=1}^{\infty}\left[\left(b_0\right)_{mn}^k + r_k\left(b_1\right)_{mn}^k + r_k^2\left(b_2\right)_{mn}^k + r_k^3\left(b_3\right)_{mn}^k\right]\sin m\pi\xi\sin n\theta \\
w_k &= \sum_{m=1}^{\infty}\sum_{n=1}^{\infty}\left[\left(c_0\right)_{mn}^k + r_k\left(c_1\right)_{mn}^k + r_k^2\left(c_2\right)_{mn}^k\right]\sin m\pi\xi\cos n\theta
\end{aligned}
\tag{2.64}
$$

The adoption of a polynomial expression permitted the minimum potential energy principle to be written in terms of stress resultants. The use of Fourier series allowed the unknown coefficients a_i^k, b_i^k and c_i^k to be obtained from a system of algebraic equations.

Returning to the basic Fourier series expansion of the displacement field, Ye and Soldatos [67] introduced a recursive solution for the laminated tube under sinusoidal pressure. Their approach was to consider the tube as an assembly of several fictitious thin cylinders (much more in number than the layers). By doing so they avoided the variable term $(1+r/r_o)$ of the governing differential equations written in terms of displacements. If that term is considered to be equal to unity, the coefficients of the differential equations turn out to be constant, allowing a much easier solution. Appropriate continuity conditions are imposed at all interfaces.

In a more recent paper, Ren [68] continued his research on elasticity formulations for laminated tubes. He focused now on axisymmetric problems, pursuing solutions by means of power series, as he did before. Interestingly he stated that this kind of solution is not easy to find in the case of transversely isotropic materials with elastic symmetry with respect to the r-θ plane. This is the case for several important problems including the composite riser tapered tube. He proposed a stress function approach instead, which looked possible due to the simplifications brought in by the axisymmetry.

Di and Rothert [69] used a zig-zag function to express the r-θ displacement field as Bhaskar and Varadan [65] did. They also used a third degree polynomial in r, including the quadratic term. The parameter ϕ that defines the slope of the segments of the zig-zag function was kept constant. This allowed an approximate solution to the laminated tube problem, with the number of variables being independent of the number of layers. Their method, however gave good results only for thin and medium thick tubes, simply-supported and subjected to sinusoidal pressure.

Harrison and Johnson [70] applied the full 3D method proposed by Pagano [57] to evaluate the stress field in laminated plates with an abrupt thickness taper. The functions that describe the dependence of stresses on the thickness direction were modified for the plane strain case. The method is layerwise: the compatibility and equilibrium equations are solved for every

sub-laminate, with continuity conditions imposed between them. Special considerations were necessary for the definition of the boundary conditions to match their number with the number of differential equations.

A similar approach for the evaluation of three-dimensional stress fields was proposed by Iarve [71]. He studied singular stress distributions at the edges of an open hole in a laminated plate. Polynomial splines were used to approximate the displacement and stress fields and to solve the boundary value problem. A system of equations was obtained through the application of the minimum potential energy principle.

The analysis of a thick composite tube based on the Lamé solution for an axisymmetric problem was presented by Soden [72]. The consideration of a "generalised" plane strain state in which ε_z is constant allows a closed-form solution of the differential equations of equilibrium. Despite this simplificating hypothesis, the solution is very useful. It permits the analysis of the important cases of a plain (non-stepped) composite thick tube under loadings as internal/external pressure or axial force. The solution is of the form:

$$\sigma = C r^{\alpha} + K \tag{2.65}$$

where C, α and K are constants.

Finally, we mention the work of Liu and Li [73], who made a compilation of the available theories for laminates. They classified them into three categories:
- Shear deformation theories.
- Layerwise theories.
- Global-local superposition theory.

Concerning shear deformation theories, they mentioned polynomial approximations up to the seventh degree in the r coordinate. A single polynomial describes the in-plane displacement variations through thickness. They also verified the prevailing effect of the odd-order terms, for symmetric laminates. Due to their C^n continuity, however, shear deformation theories can not describe properly the abrupt changes of in-plane displacements between adjacent layers.

Layerwise (or piecewise) theories, which include the zig-zag formulation, are considered up to

the third degree in r. The displacement w is also considered to vary across the thickness, differently from shear deformation theories. The results are accurate but involve loss in computational efficiency due to the great number of variables (the polynomial coefficients of each layer). Local behaviour is correctly represented, such as the one associated to interlaminar stresses. The authors proposed a global-local theory. They reasoned that it takes advantage of the computational efficiency of the global (shear deformation type) approach with the accuracy of the local (layerwise) one.

Two thick laminated tube models are developed in Chapter 5 of the present thesis. The first model is applicable to plain (non-stepped) thick composite tubes. The second model address the effect of the thickness reduction on the stress fields of a thick laminated, dropped ply tube.

2.4 RISER ANALYSIS

The exploitation of hydrocarbons beneath the oceans has experienced a great development in the past five decades. As deeper and deeper reservoirs were discovered, adequate engineering solutions were proposed in order to exhaust the reserves. The challenge consists in controlling high pressure, flammable fluids and providing means to separate, evaluate and export them in a harsh environment.

For water depths not exceeding approximately 200 m, steel jackets fixed with piles to the ocean soil are the most common solution. For cost effectiveness, small reservoirs and/or early production, systems based on semi-submersible platforms with catenary mooring were introduced. They offer the advantage of easy removal and installation at other sites. This solution is considered viable even for water depths over 1000 m, but implies using wet christmas trees (as the control valves are called) and flexible production lines. These are expensive items and maintenance is a concern when they are installed in great water depths.

As described by the API [74], *Tension Leg Platforms* (TLP) are anchored to the sea floor by means of vertical tendons, which restrain the platform at a draft deeper than that required to displace their weight. Figure 2.27 shows the TLP concept. The platform basic motions are also shown in the figure. The tendons remain constantly in tension, limiting the heave, pitch

and roll movements of the platform to small amplitudes. This permits the adoption of dry christmas trees, installed at the platform deck, and rigid *production risers*, the tubulars that connect them to the subsea well and protect the production tubings inside them. Under the action of wind, waves and current, the surge, sway and yaw responses are kept within acceptable limits despite the greater transverse compliance of the platform.

A TLP is particularly suitable for deep water applications [74], and several platforms of this kind have been installed in the North Sea and in the Gulf of Mexico. As stated by Delgado, Erb and Moe [75], the cost of a TLP is relatively insensitive to water depth, in comparison to fixed structures. On the other hand, TLPs are very sensitive to the weight on deck, as is any other floating structure. Every reduction in the weigth of the riser corresponds to another reduction in the weight of the hull, due to the smaller buoyancy required. This characteristic encourages the use of composite risers. In a typical TLP, there are between fifteen and thirty production risers. There can be a considerable reduction in the weight hanging on the deck if composite pipes are substituted for the steel ones.

Petersen et al. [76] indicated that a production riser needs to work in tension. This prevents excessive bending at the sea floor, avoids interference with another riser and enhances the fatigue performance, by limiting the maximum stress range. Tensioner systems are huge pieces of equipment, designed to permit relative movement between the top of the riser and the platform deck, whilst maintaining almost constant tension on the pipe. Composite risers can remove the need for tensioners, due to their lower weight and axial stiffness, when compared to steel. This will lead to a simplification and cost reduction of the whole production system.

The French companies Aerospatiale and IFP have studied the subject of composite risers for more than ten years [77]. Reports of the progress on their research have appeared regularly in the literature [78,79,80,81,82,83]. Sparks [78] noted that composite materials are suitable for risers because of their good fatigue and corrosion resistance, apart from weight and stiffness considerations. There have been two joint industry projects, studying composite risers [83]. The first project addressed the qualification of a prototype 9" internal diameter (ID) tube to attain the basic requirements in terms of internal pressure, axial tension and fatigue. The second study concentrated on defect tolerance and NDT techniques.

The composite tube proposed by IFP and Aerospatiale is of a hybrid construction, composed of glass and carbon fibres in an epoxy matrix, as figure 2.28 shows. Sparks [78] reasoned that this leads to a pipe with better mechanical properties and price advantage. The internal diameter is 229 mm and the total thickness 17.4 mm. Those dimensions are compatible with the standard production riser size of 245 mm (9 5/8") outside diameter (OD) and minimum internal drift requirement of 217 mm. This latter characteristic defines the maximum allowable size of an internal string to move through the inside of the riser.

Epoxy resin is used because of its good mechanical properties, ease of processing and high temperature performance. The riser acts as a safety barrier in case of a failure of internal tubings or during a blow-out in the well, when the riser internal pressure could reach 34.5 MPa (5000 psi). To resist this loading the tube has two layers (internal and external) of 90° filament wound S-glass fibres, with a total thickness of 9.5 mm. Tamarelle and Sparks [79] explained that glass fibre was adopted because of its adequate stiffness and strength, together with its low price when compared to carbon.

Carbon fibres are wound at +/- 20° angles, 5.9 mm thickness, and so they are the major contributors to the axial strength and stiffness of the tube. These layers were designed to resist the tension at the top of the riser in a 1000 meters water depth. The carbon fibres have also to withstand the axial force of 1420 kN due to internal pressure. Additionally to these axial loads, the riser has to resist those generated by platform movement, waves and current. Carbon fibres were chosen because of their resistance to fatigue and high ultimate tensile strength, associated with good chemical resistance to sea water.

An elastomer internal liner, made of Buna-N nitrile rubber with a thickness of 1 mm is used to improve water tightness. It also isolates the glass fibres from the sea water, which can degrade them. Finally, a polyethylene external coating, 1 mm thick, protects the outer surface of the pipe from shocks and abrasion.

Sparks et al. [81] described several tests on such tubes. The strength specifications were a burst pressure of 103.5 MPa (15000 psi), ends closed, and an ultimate uniaxial tensile strength of 4415 kN. One tube was pressurised at ambient temperature and burst at a pressure of 111 MPa, 7% higher than the specification. Another tube was pulled to failure at a tension of 4660

kN, 5.5% greater than specified. This last test was performed at a temperature of 110° C. Two tubes were subjected to fatigue tests. The first was submitted to a +/- 734 kN load range about a mean tension of 981 kN, over nearly 1 million cycles, without failure in the composite layers. This is 3 times the endurance of a steel tube of equivalent static strength under axial loading. The tube then withstood a pressure test at 34.5 MPa without any leakage. The second test simulated the service loads and lasted 4 months. There were more than 40 million cycles over 5 different load ranges, from +/-61 kN to +/-273 kN, with the same mean load of 981 kN. Several pressure tests were executed at intervals during the test, with no leakage.

Karivar-Sadri and Ochoa [84] reported a somewhat different construction, with the carbon fibres wound at +/- 35°. Prototype tubes were manufactured by the Brunswick Corporation for testing purposes. Sparks and Schmitt [82] also arrived at different constructions as a result of optimisation processes. The purpose was to design the tubes to have zero axial strain due to temperature and internal pressure loading. The riser tube so designed had winding angles of +/- 59.9° in the glass fibre layers and +/- 16.9° in the carbon fibre layers.

Rasheed and Tassoulas [85] developed a numerical procedure for the strength analysis of composite risers which they applied to tube geometry proposed by Aerospatiale and the IFP. The model considered a linear elastic behaviour in the along-the-fibres and transverse directions and a cubic polynomial stress-strain relation for in-plane shear. The failure criteria were decoupled, addressing separately the following failure modes: fibre breakage, matrix cracking (both in-plane and through thickness) and delamination.

According to Fischer [86], the French projects were successful in demonstrating the technical feasibility of composite production risers. When a full scale sea trial was proposed in 1989, however, there was no enthusiasm by the offshore industry, who were concerned with the cost effectiveness and the reliability of the system. Since then, the cost of carbon fibre and other raw materials have declined significantly, as the suppliers look for new markets, due to the reduced demand for military and aerospace products.

Salama [87] pointed out that the industry will only invest in composite risers if they show great price benefits. There will be a cost related to gathering sufficient reliability data. It will be also needed to break the "emotional barrier" associated with using a new material in a

critical application. Unit prices of composite tubes are still higher than those of metallic ones, but potentially money is saved in the overall system, when one considers the reduction in platform displacement and the possible absence of tensioners.

Different from drilling risers, which have a gimbals connection with the wellhead, production risers have to provide a smooth profile to the well, in order to prevent "dog-legs" in the tubing inside them. This is achieved with a *stress* or *tapered joint* [88,89,90]. Figure 2.29 shows the generic configuration of a production riser. In offshore jargon a "joint" is a single tube. The stress joint is tapered in its thickness, which varies along the length of the element, while the same ID is maintained. The thickness departs from that of a normal riser tube and reaches values four to six times higher. This results in a steadily increasing bending stiffness.

Lim et al. [88] argued that the tapered joint withstands the high bending moments close to the base of the riser and transfers them effectively to the subsea wellhead. Due to the length of the high bending moment domain, the region of thickness variation is often long (10 to 20 m), to limit the maximum stress and thus achieve an acceptable fatigue life. The same reason dictated the adoption of a refined surface finish and tight dimensional tolerances. Chiu [90] mentioned that titanium has been used as constructive material for production risers stress joints over the past 10 years. Myers and Delgado [89] showed that the tapered joints of the Jolliet TLP were made of forged steel.

There has been a renewed interest in composite risers in recent times, mainly in the United States. Fischer et al. [91] described an on-going joint industry project, partially funded by the National Institute of Standards (NIST) Advanced Technology Program (ATP). The goals of the project are to design, develop, manufacture, test and qualify a composite riser for deep water (1000-1600 metres). The authors commented on the barriers to the use of composite materials for production risers:

- Cost - While safety issues, low maintenance and low life cycle costs are important factors favouring composites in relation to steel, the initial cost reduction they can provide is still the major driving force for their consideration in a platform project. The economic advantages must then be clearly demonstrated.

- Material and performance data base - Mainly concerning long term behaviour. Most of the

data existing today are proprietary information. The great number of possible combinations in terms of fibre and resin systems make the question more difficult.

- Liners - Both thermoplastic and elastomeric liners are proposed to make the riser pressure tight. The same consideration about performance on the long term applies. Another issue is the resistance of the liner to a sudden decompression that can happen during operation.

- Design methods - Standard design methodologies do not exist at this date. This would help the industry to perform a preliminary analysis within a reasonable time frame.

- Metallic connectors - These are very important components of any practical riser design. They must assure proper load transfer from one riser joint to another. They also must maintain the continuity of the pressure tight barrier. Their performance can have a great impact on the cost, weight and performance of the riser.

- Manufacturing process control - The performance of any composite component is very dependent on the quality of the manufacture process. Adequate control is needed to ensure product quality and uniformity.

- Inspection - Acceptance and qualification of a composite riser will depend on a well established inspection method, adapted for the application in the field.

Baldwin et al. [92,93] gave some information about the first tests performed on the composite production riser which was the object of the NIST/ATP project. The riser tube had a 255 mm (10.05") internal diameter and was also of a hybrid construction, with alternating low angle carbon plies and hoop glass plies. The metallic connector was a threaded Hydril MAC-II, attached to the composite tube by means of multiple traplock interfaces. Combined internal pressure and axial load tests on two prototypes using a first connector configuration failed at an average pressure of 48 MPa (7000 psi) and at an average load of 3.2 MN (720,000 pounds). The failures occurred at the composite-to-metal interface. Those values were smaller than the specified 62 MPa (9000 psi) of pressure and 3.4 MN (770,000 pounds) of axial load. The connector design was revised and much better figures resulted. Figure 2.30 displays some of the experimental results obtained.

The objective of the present research is to investigate the feasibility of a composite tapered joint. In early papers, Sparks [78] argued that a composite riser should include a composite stress joint, but there were no suitable fabrication techniques. In another reference Sparks et

al. [81] mentioned the use of a composite tube reinforced with metal shell pieces of variable bending stiffness. Later on, Sparks et al. [83] proposed a reinforced composite pipe that would perform as a tapered joint, without giving any further details. They emphasised that a steel stress joint in a composite riser would lead to a concentrated bending moment in the composite due to the lower bending stiffness of the riser. Salama [89] described a hybrid construction, made of a titanium pipe with a tapered outer filament wound wrap of glass and carbon fibre composite. Fischer [84] considered composite stress joints to be less commercially mature than the composite production riser tube and requiring additional development.

The design of a TLP production riser is not a simple issue. Goulart and Roveri [94], and Rooney and Engebretsen [95] provided a general over-view of the process. In what follows we will describe the riser analysis procedure that PETROBRAS envisaged for a TLP to be installed in the Marlim field at the Campos basin, off the south-east coast of Brazil [96]. First, a fatigue analysis is performed in the frequency domain, based on an assumed life of 20 years and a design coefficient (defined as the ratio of the fatigue strength to the applied stress) of 10, related to major structural components without access for inspection. The S-N curves do not assume endurance limit. A mean stress correction is applied. The features evaluated are the first order wave response, the low frequency TLP motion and the vortex induced vibration. A Campos basin scatter diagram of 26 linearized sea states is used. The procedure considers 8 wave directions. The computer program is DERP, from Stress Engineering Services Ltd.

Then, regular (or monochromatic) wave analysis is used for sensitivity and optimization purposes, addressing the influence of variations in :

- wave periods,
- current velocity,
- hydrodynamic parameters,
- annulus and tubing fluids,
- top tension and tensioner stiffness characteristics,
- TLP offsets,
- extension of marine growth,
- TLP hull influence on wave kinematics.

The third step is component design. The taper joint profile design involves both fatigue and extreme loading considerations and is very sensitive to tensioner stiffness, requiring significant optimisation effort. The riser connectors have to be defined. A choice has to be made from integrated threaded couplings, weld-on threaded couplings or bolted flanges.

The following evaluation is a fatigue analysis in the time domain, accomplished using ANFLEX, a proprietary (PETROBRAS) computer program. The program considers the variation in the axial stiffness of the riser. The damage in a 3-hour sea state is determined, using the rainflow stress cycles counting method. Time domain analysis calibrates the frequency domain results. It is not considered a practical tool for fatigue analysis because of the computer time requirements, but it is most appropriate for a reserach project.

The next step is the analysis of vortex induced vibrations, using the programs SHEAR, developed at MIT, and LIC22, from LIC Engineering. An interference study is also performed, considering a distance of 3 meters between risers. All risers should have similar natural frequencies to minimise relative motions. Frequency domain analysis is the algorithm used. The criterion for acceptability is no impact with another riser in a 100 year storm active for a period of 3 hours.

Finally, ANFLEX is used to provide an extreme stress responses analysis. The extremes are based on irregular (or random) wave analysis, although there is uncertainty in respect to statistical extrapolation. Data from a 30 minutes time simulation result in a 3 hours maximum based on a Rayleigh statistical distribution.

For the purposes of the present study, such a comprehensive analysis is not needed. As the objective is a first comparative appraisal of the behaviour of composite against steel risers, one can use a much simpler approach, limited to extreme cases. Rooney and Engebretsen [95] suggested a regular wave analysis for extreme responses analysis. This method overcomes the uncertainty in statistical extrapolation associated with irregular waves. It is an uncomplicated analysis, suitable for comparison purposes. The boundary conditions at the top of the riser are the TLP extreme motions in a 100 year storm. When considered in the analysis, tensioner systems are represented by springs of equivalent stiffness.

The wave and current loading on the riser can be computed by the well known equation due to Morison, as shown by Johnson [97]:

$$f = C_m.\rho.S.a - (C_m - 1).\rho.S.A + \frac{1}{2}.\rho.C_d.D.(u-U)|(u-U)| \tag{2.66}$$

where f is the force normal to the riser, per unit length, C_m is the tranverse inertia coefficient, ρ is the mass density of fluid, S is the cross section area of the tube, a is the normal fluid acceleration, A is the riser normal acceleration, C_d is the tranverse drag coefficient, D is the external diameter of the tube, u is the normal fluid velocity and U is the normal riser velocity. The first term of the equation is the inertia force component. The second term is related to the added mass effect. The last term is the drag force. As can be seen, the equation is non-linear in the fluid and structure velocities.

The analysis considers the centenary wave and the associated profile of the current. Platform surge and sway movements have the same period as the wave [99], albeit the heave period is smaller. There is a 90° delay in phase angle between lateral oscillation of the platform and the wave crest variations, due to inertial effects. Platform mean lateral displacement (static offset), wave and current forces are taken to be in the same direction.

This thesis deals with the design of composite production risers in Chapter 6. Steel production risers are also analysed, for comparison purposes. The comparative study makes use of the ABAQUS program [99], which, through its AQUA module, has full wave and current loading capability. Moreover, the code is particularly suitable for the geometrically nonlinear problem associated with the study of a marine riser.

SPECIFICATION	G_{Ic} [J/m^2]	G_{IIc} [J/m^2]	REFERENCE
AS4/3501-6	175	525	(1)
AS4/3501-6	200	450	(8) *
T-300/5208	88	-	(10)
AS4/3502	161	-	(10)
G40-800/977-1	350	-	(23)
AS4/3503	-	615	(26)
AS4/2220-3	-	510	(27)
AS4-G/TACTIX 556	343	768	(32)

* Note : also listed a value of 800 J/m^2 for G_{IIIc}.

Table 2.1 Fracture toughness of carbon/epoxy unidirectional laminates, vf ~ 60% .

MODE NO.	MODE	MODIFIED ELASTIC CONSTANTS	
1	Longitudinal tension	$E_L = 0$	$v_{LT} = 0$
2	Longitudinal compression	$E_L = 0$	$v_{LT} = 0$
3	Transverse tension	$E_T = 0$	$v_{TL} = 0$
4	Transverse compression	$E_T = 0$	$v_{TL} = 0$
5	Intralaminar shear	$G_{LT} = 0$	

Table 2.2 Modification of the elastic constants as proposed by Hinton et al. [41].
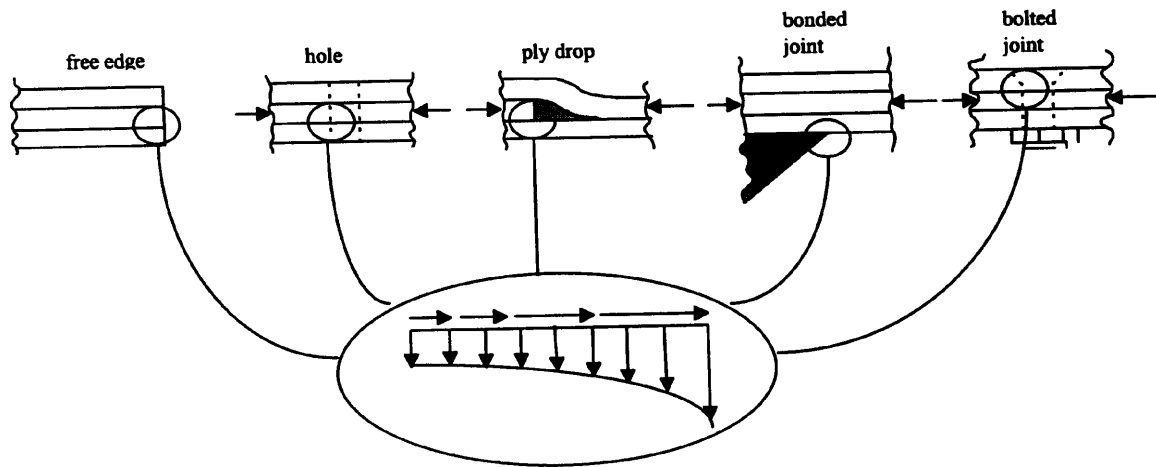
Figure 2.1 Details that cause out-of-plane stresses [1].
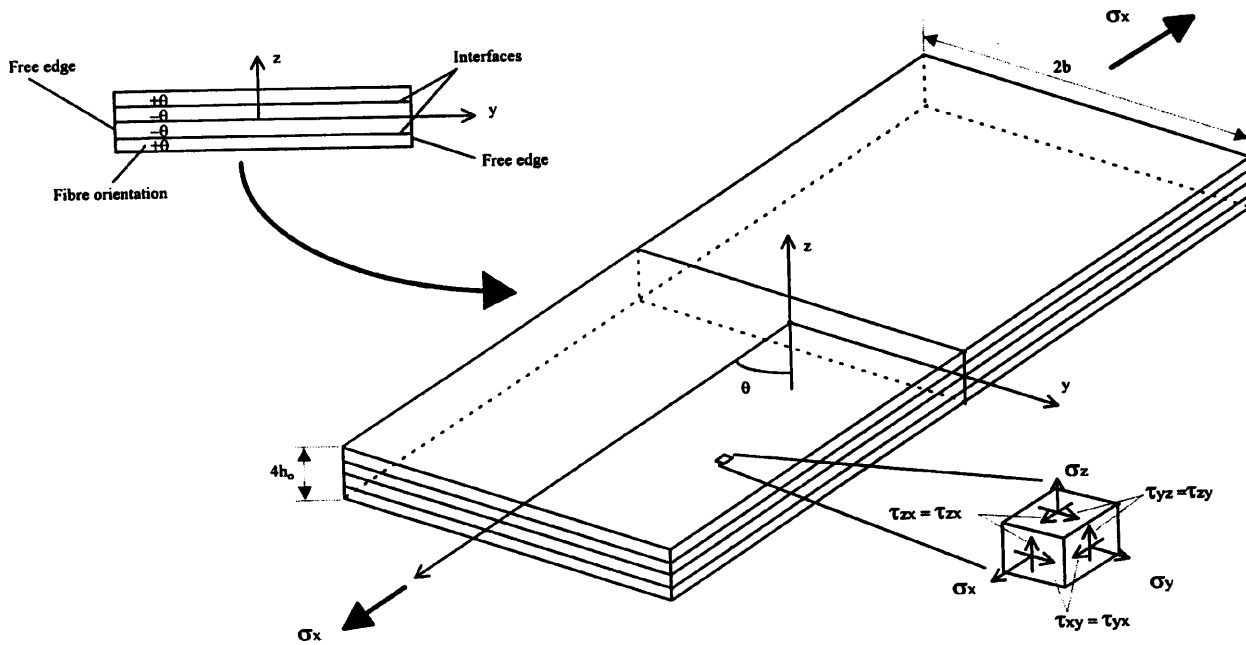
Figure 2.2 Model for the analysis of interlaminar stresses [2].
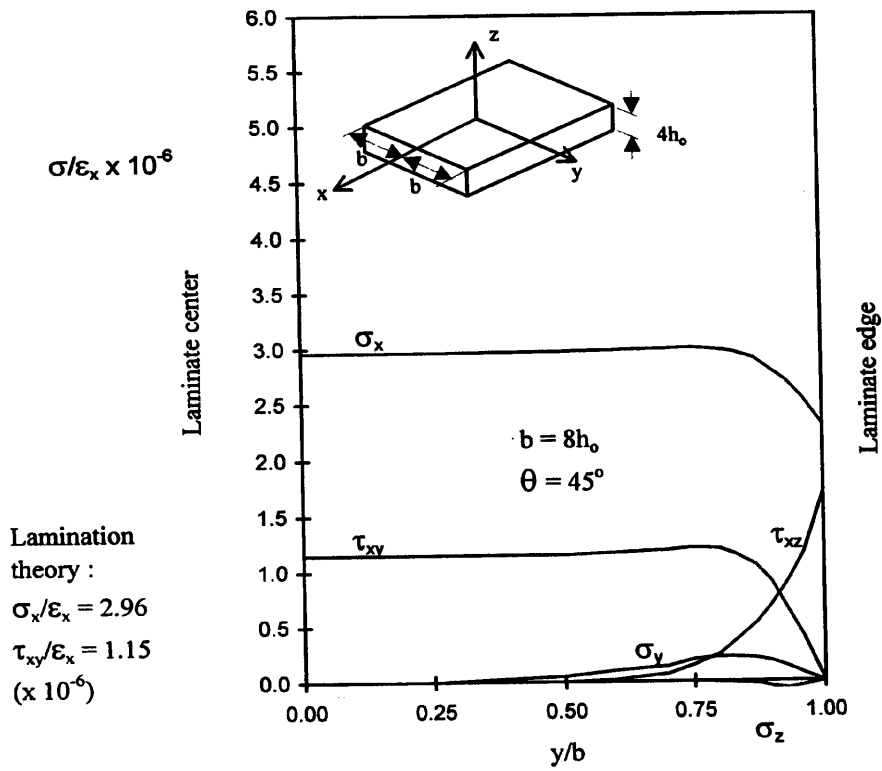
Figure 2.3 Distributions of stresses, according to Pipes and Pagano [2].
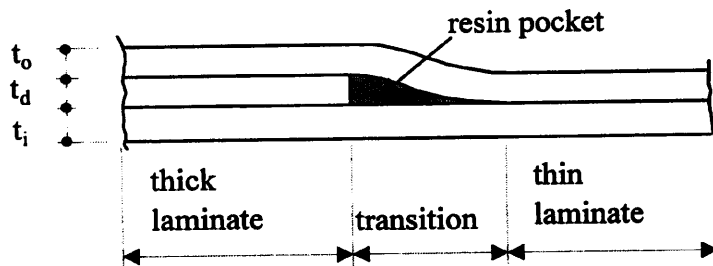
Figure 2.4 Features of the dropped ply region.
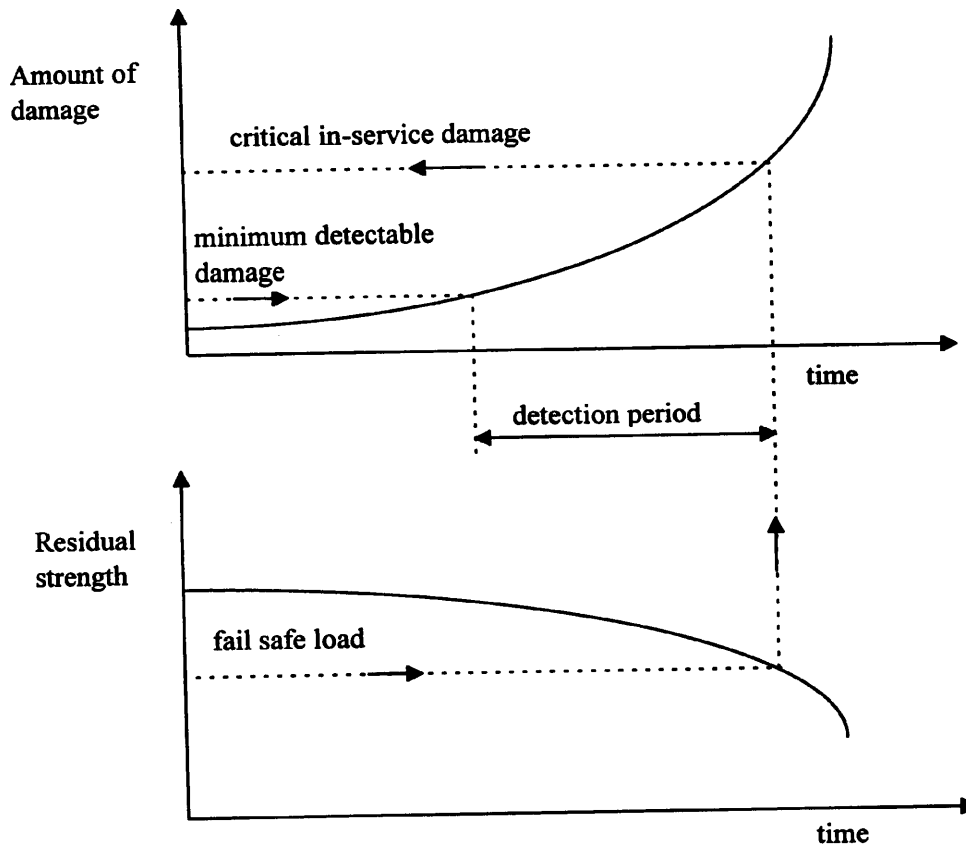
Figure 2.5 Damage tolerance methodology [8].
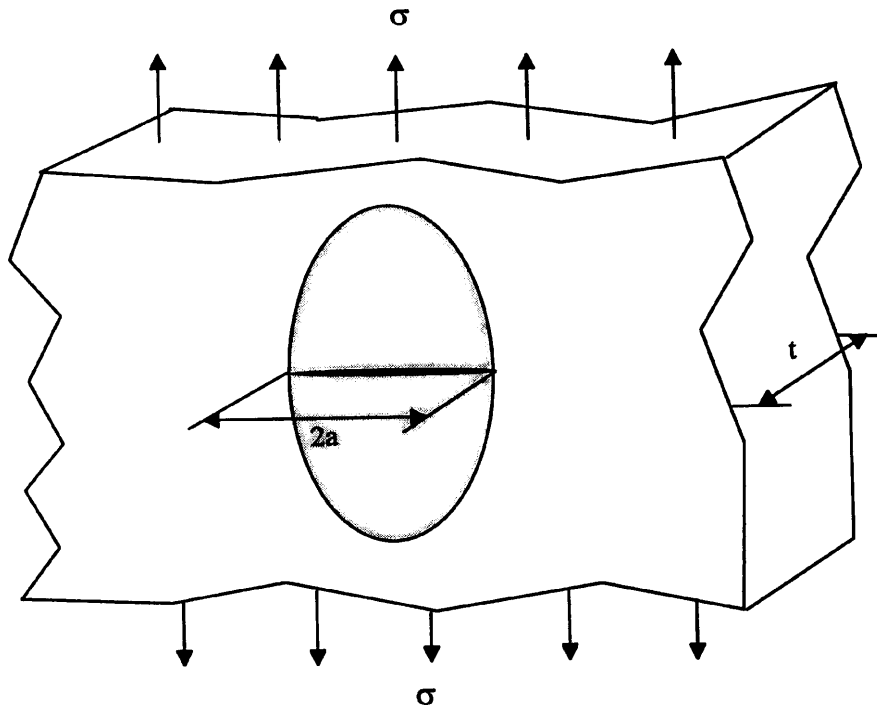
Figure 2.6 The Griffith crack.
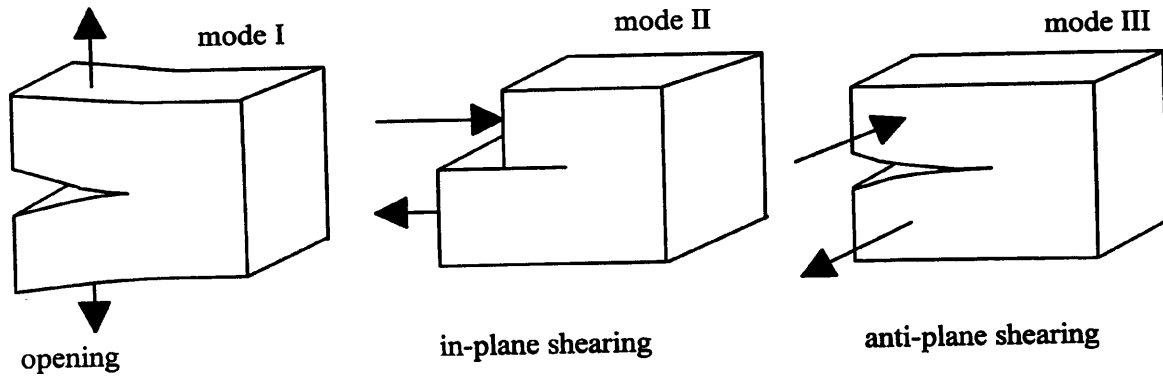
Figure 2.7 The three modes of crack propagation.
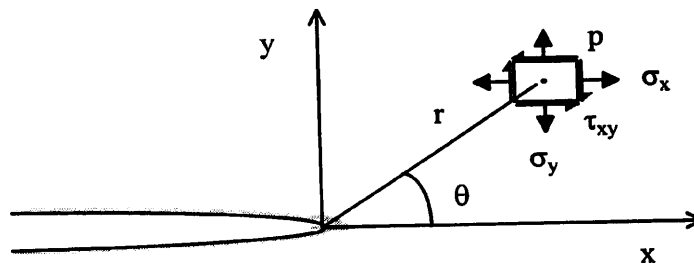
Figure 2.8 Stresses at point p, near the crack tip [11].
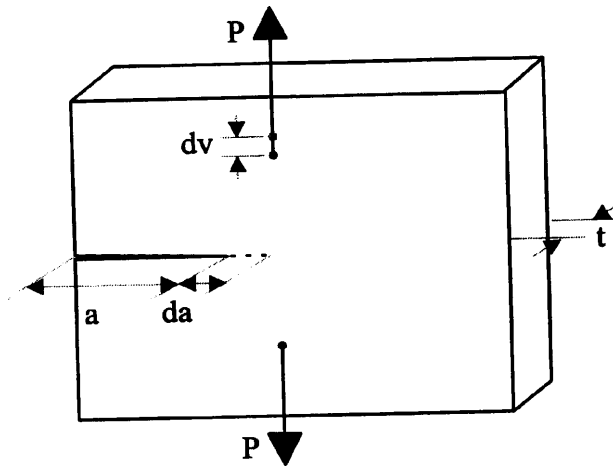
Figure 2.9 Plate with a lateral crack.
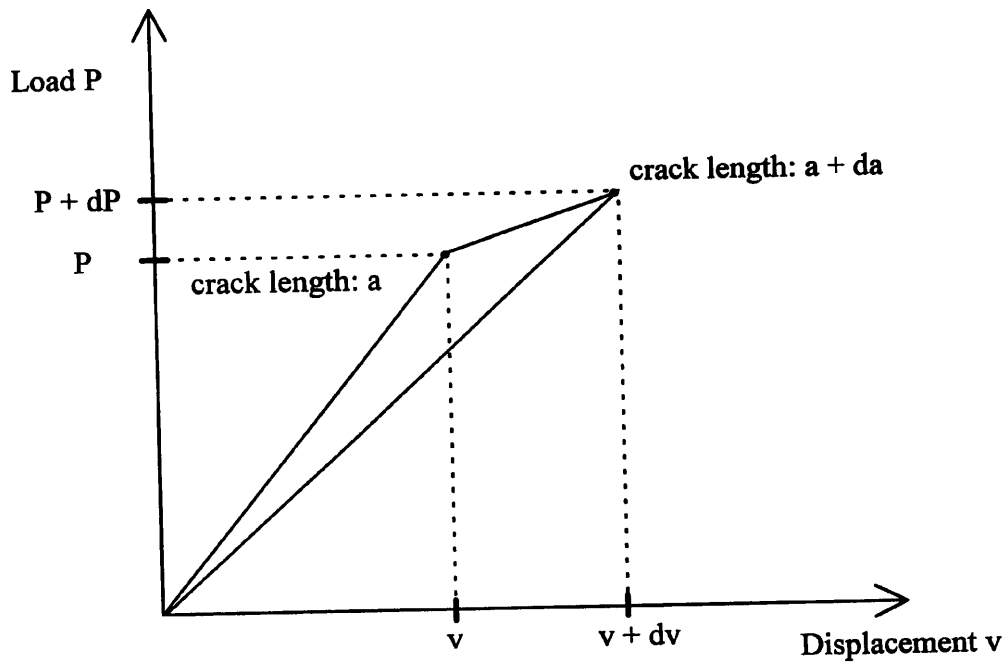
Figure 2.10 Graph of load *versus* displacement for a plate with a lateral crack.
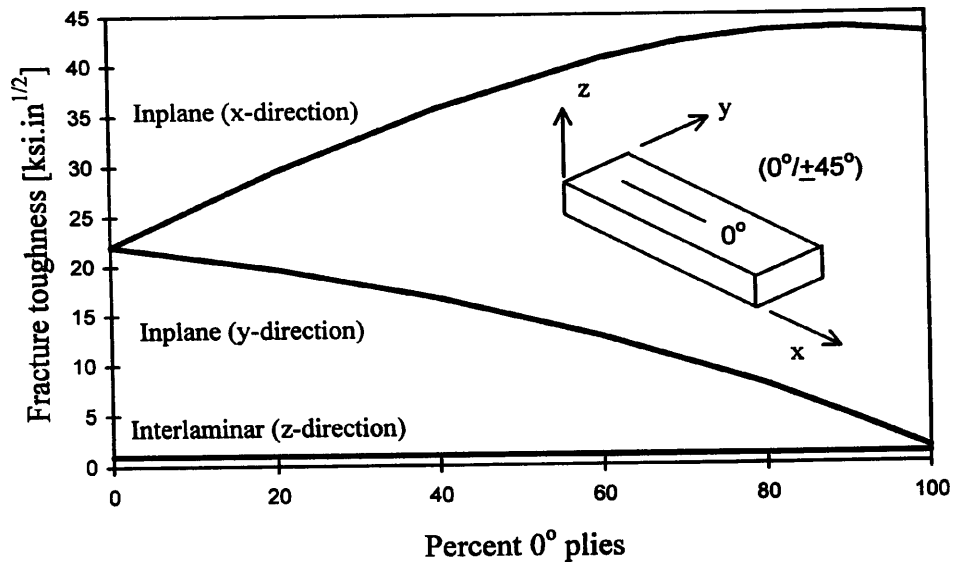
Figure 2.11 Fracture toughnesses of composite laminates [17].

double cantilever beam (DCB)   end-notched flexure (ENF)
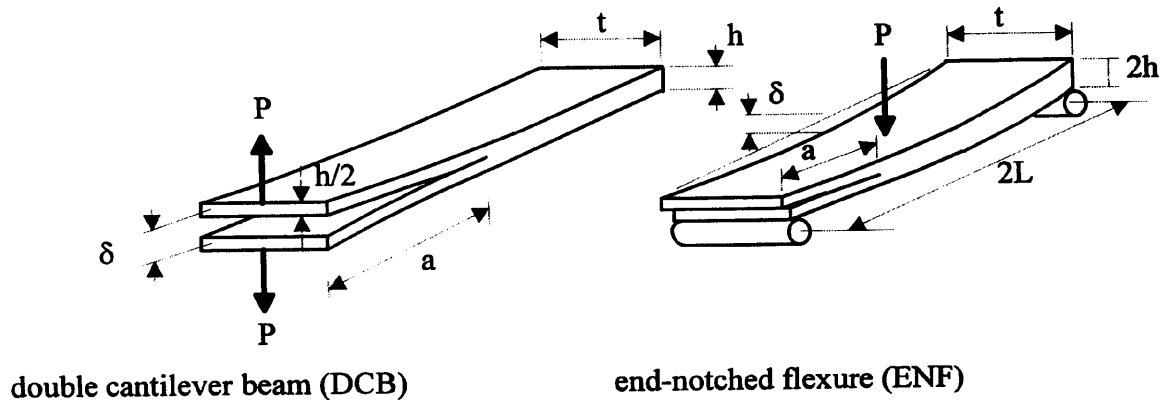
Figure 2.12 Tests for determination of critical values of SERR, according to Gibson [10].
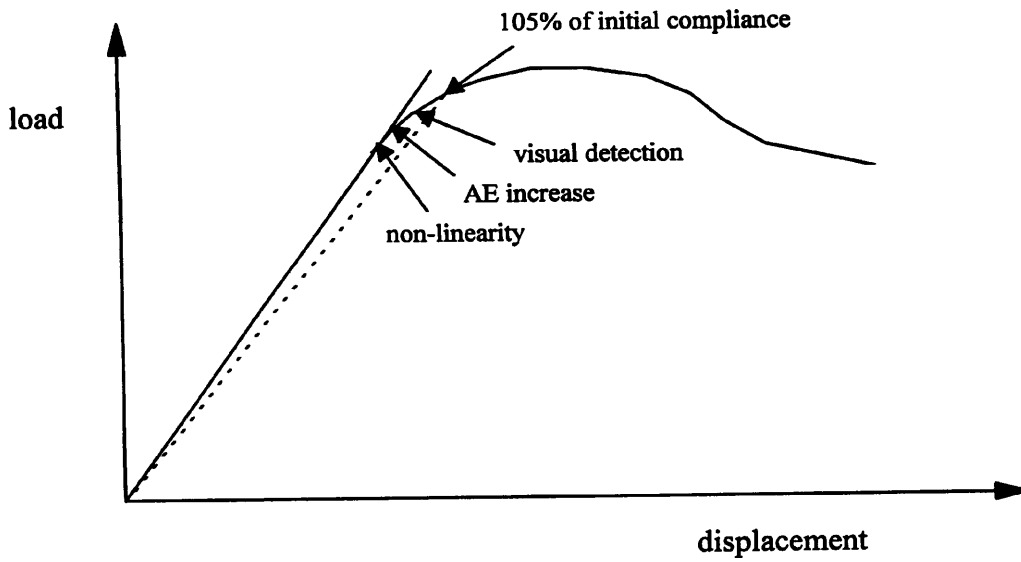
Figure 2.13 Relative position of the four initiation detection methods, after Ivens et al [19].
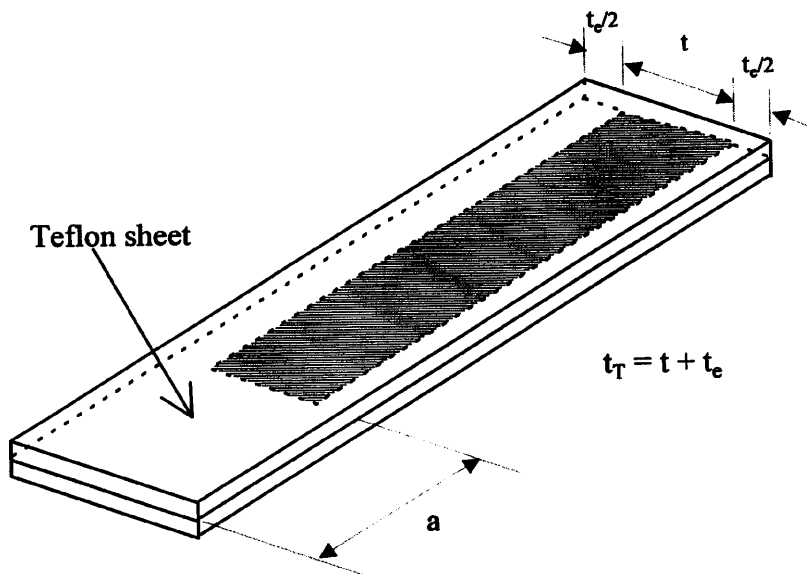
Figure 2.14 SERR specimens with edge delaminations at the mid-plane.
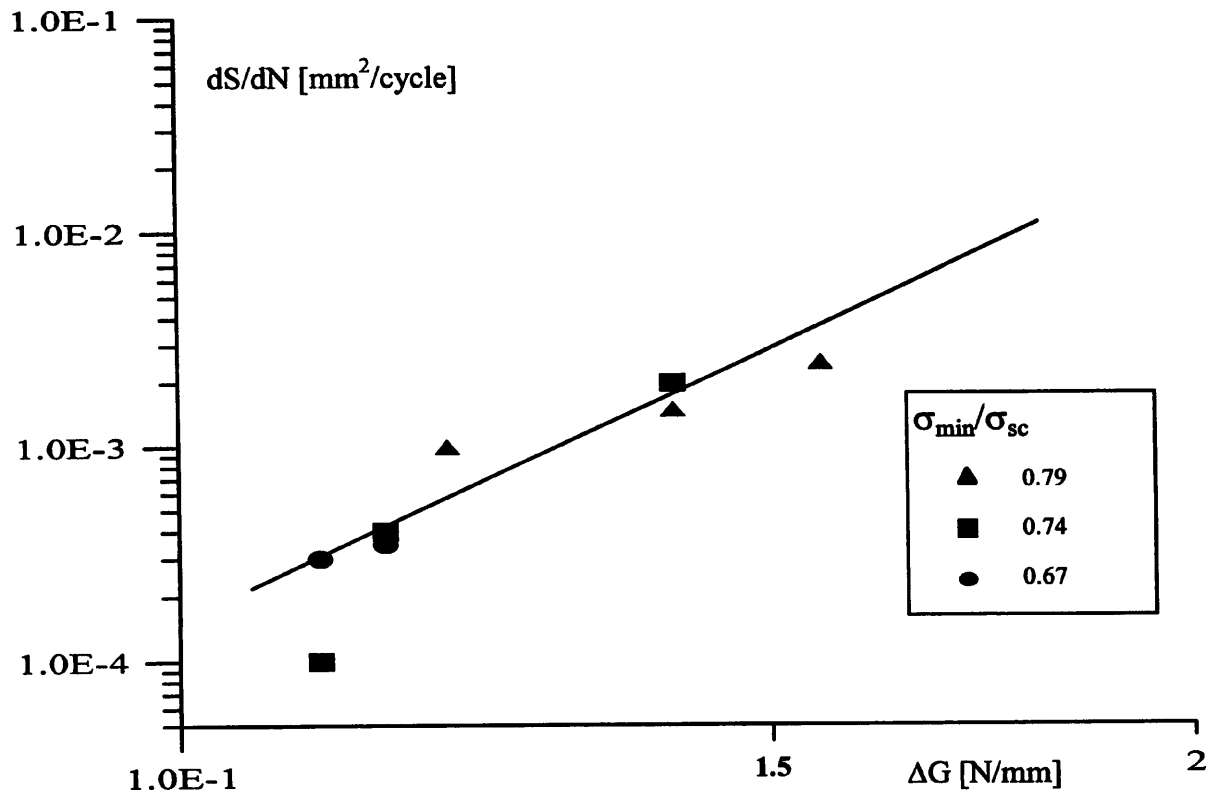
Figure 2.15 Graph of dS/dN *versus* ΔG [33].
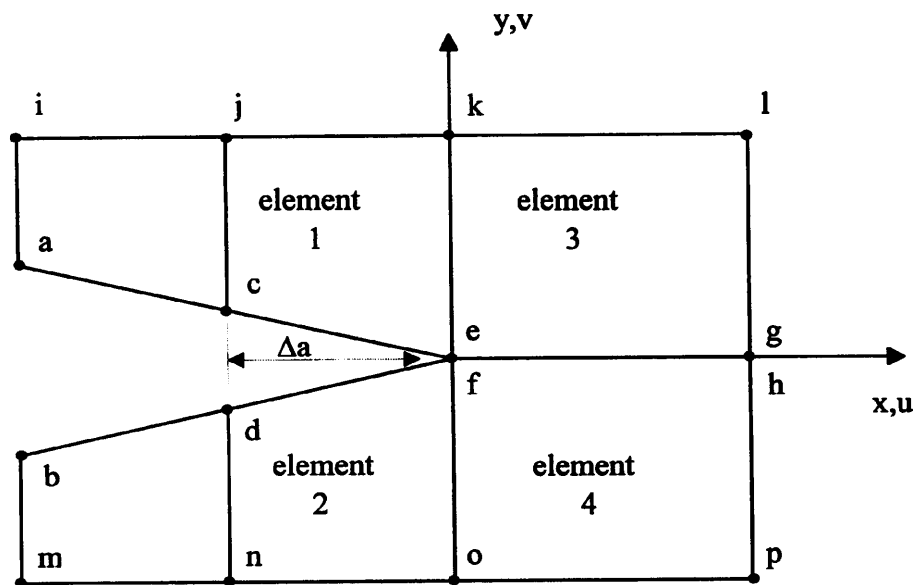
Figure 2.16 Plate finite element mesh near a crack tip, illustrating the VCC method [34].
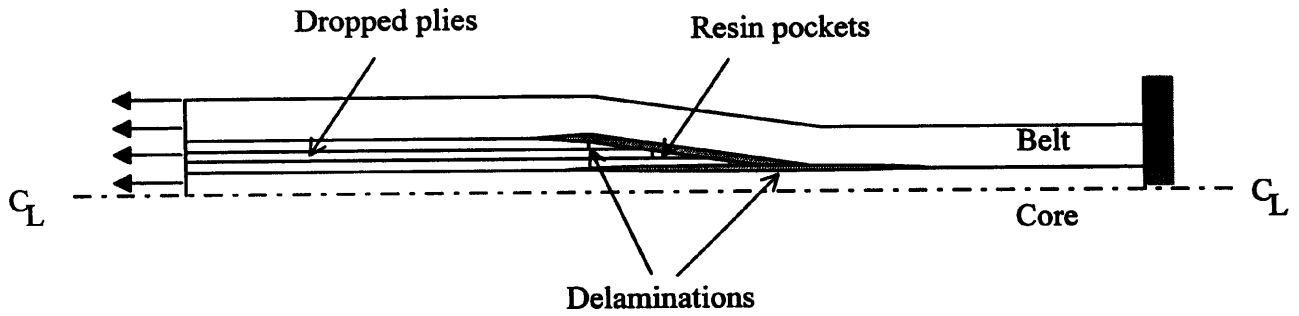
Figure 2.17 Fatigue specimens of tapered laminates for a helicopter rotor hub [35].
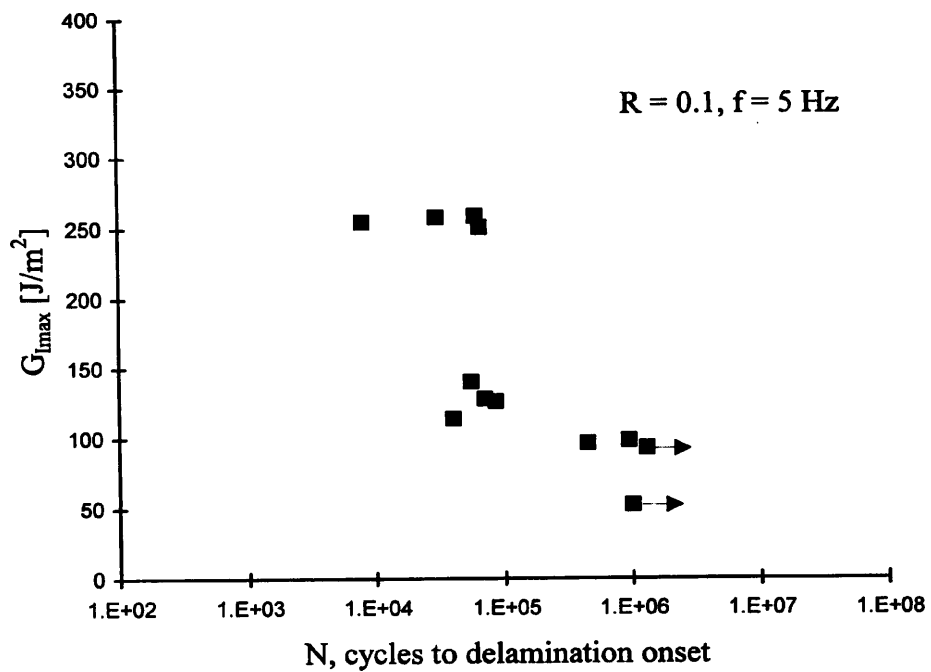

Figure 2.18 G_{Imax} as a function of cycles to delamination onset for IM6/1827I
graphite/epoxy laminate [35].
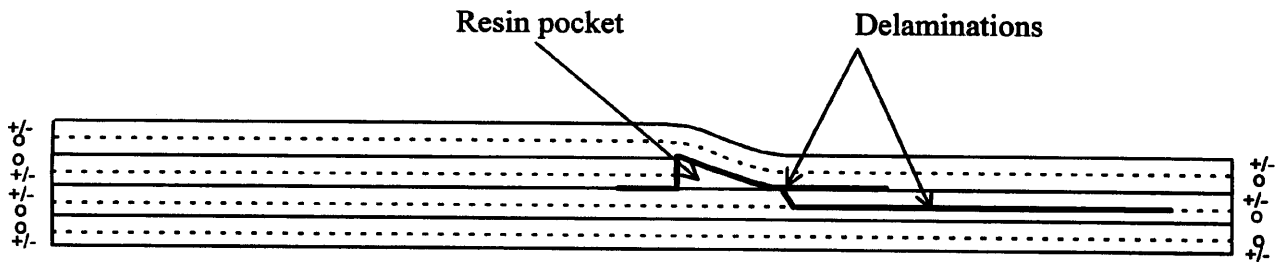
Figure 2.19 Asymmetrically tapered specimens [39].
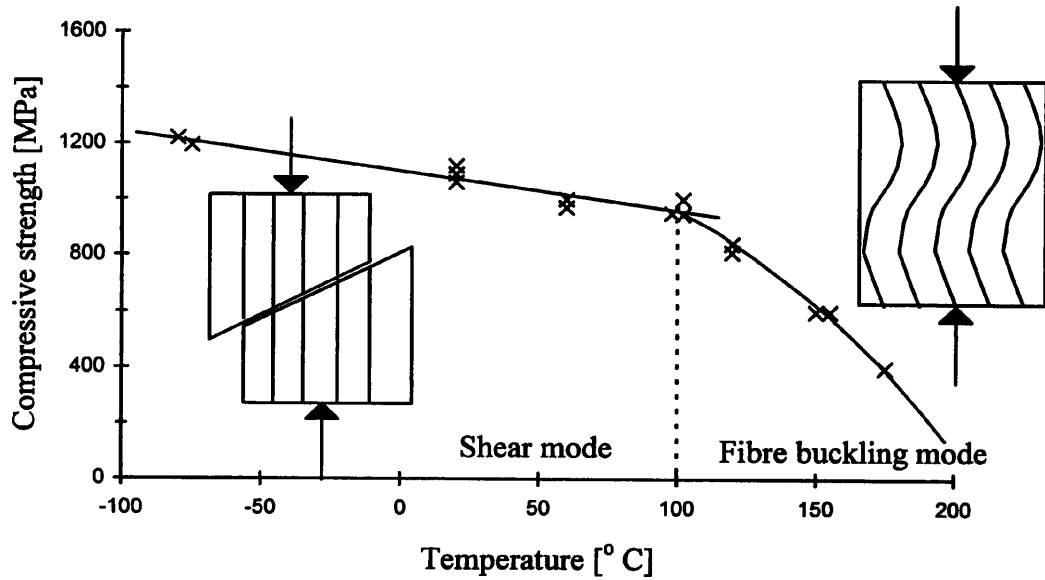
Figure 2.20 Variation of the longitudinal compressive strength of unidirectional carbon/epoxy laminae with temperature [44].
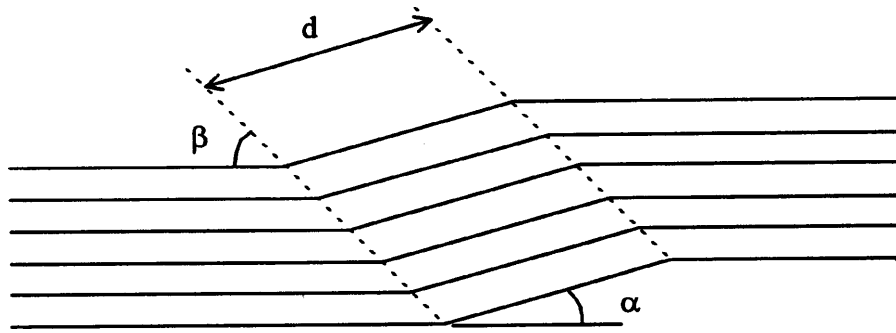
Figure 2.21 Geometric characteristics of the kink bands [46].
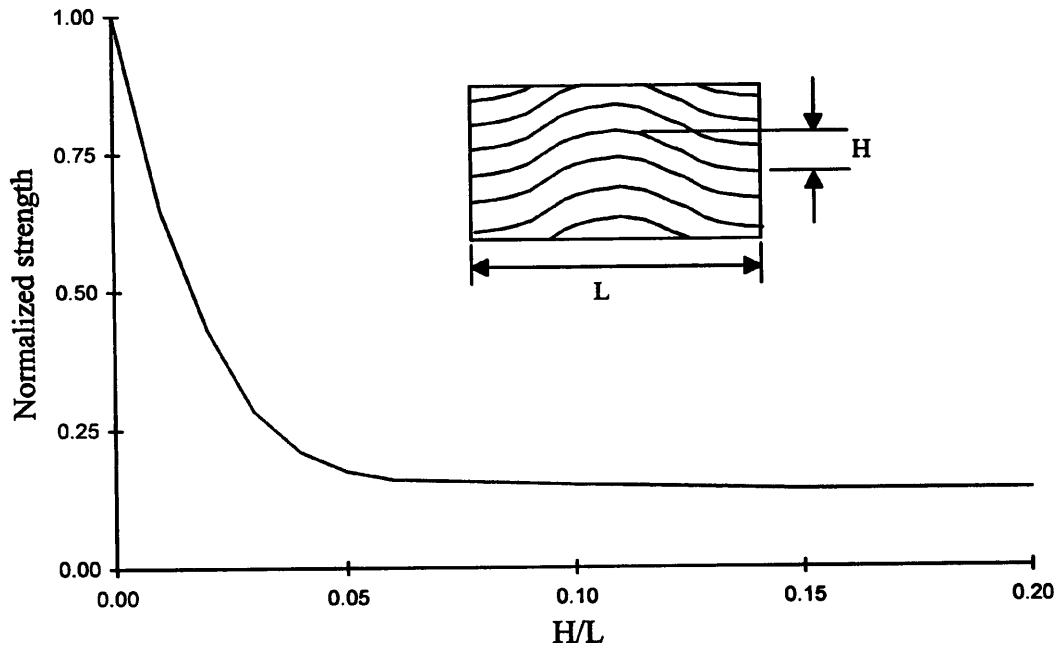
Figure 2.22 Predicted longitudinal compressive strength reduction with waviness, according to the model of Hsiao and Daniel [47].
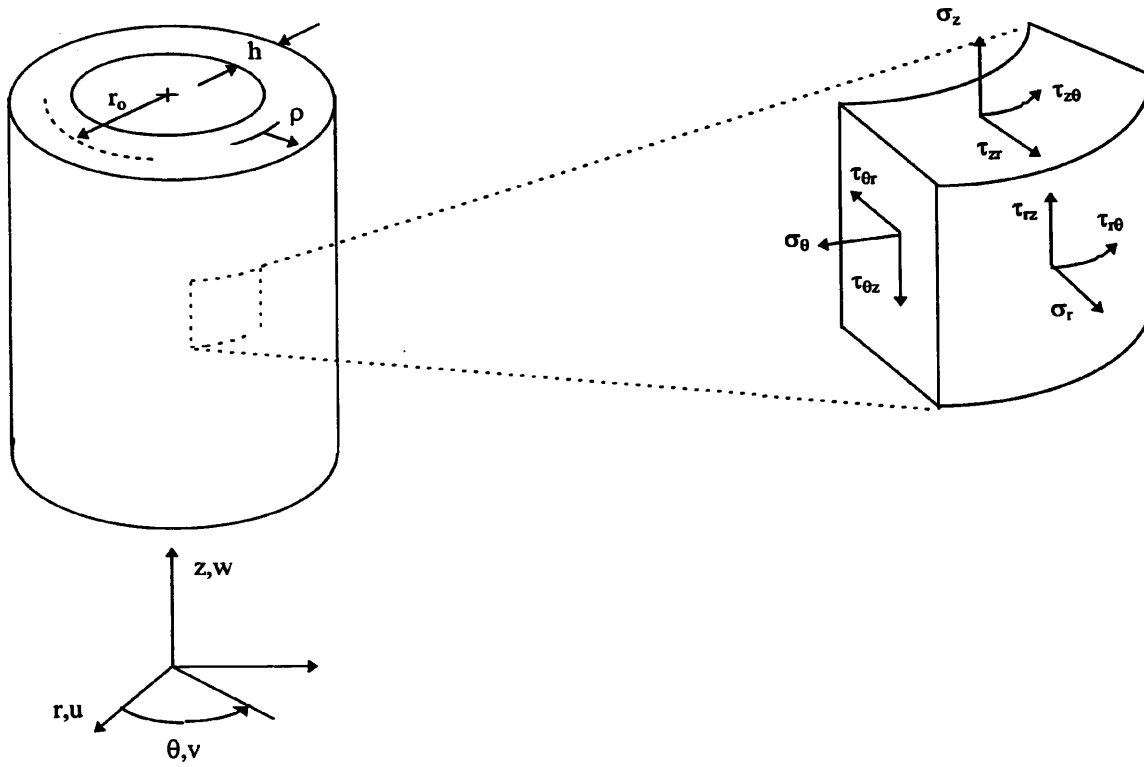
Figure 2.23 Cylindrical coordinates with associated displacements and stresses.
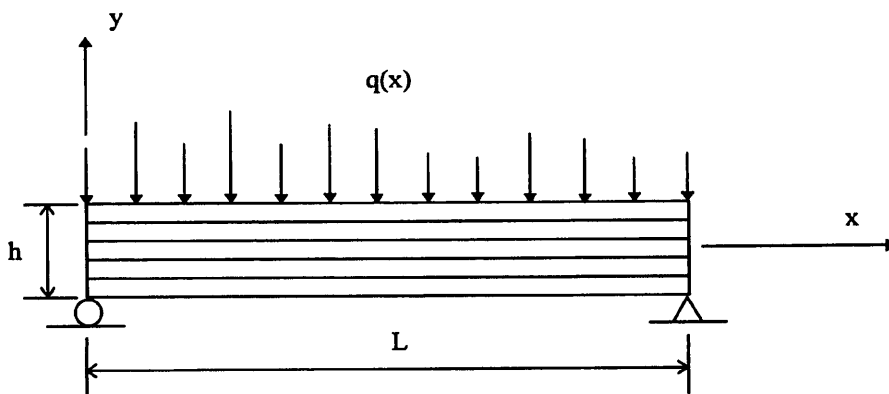
Figure 2.24 Laminated plate problem analysed by Pagano [52].
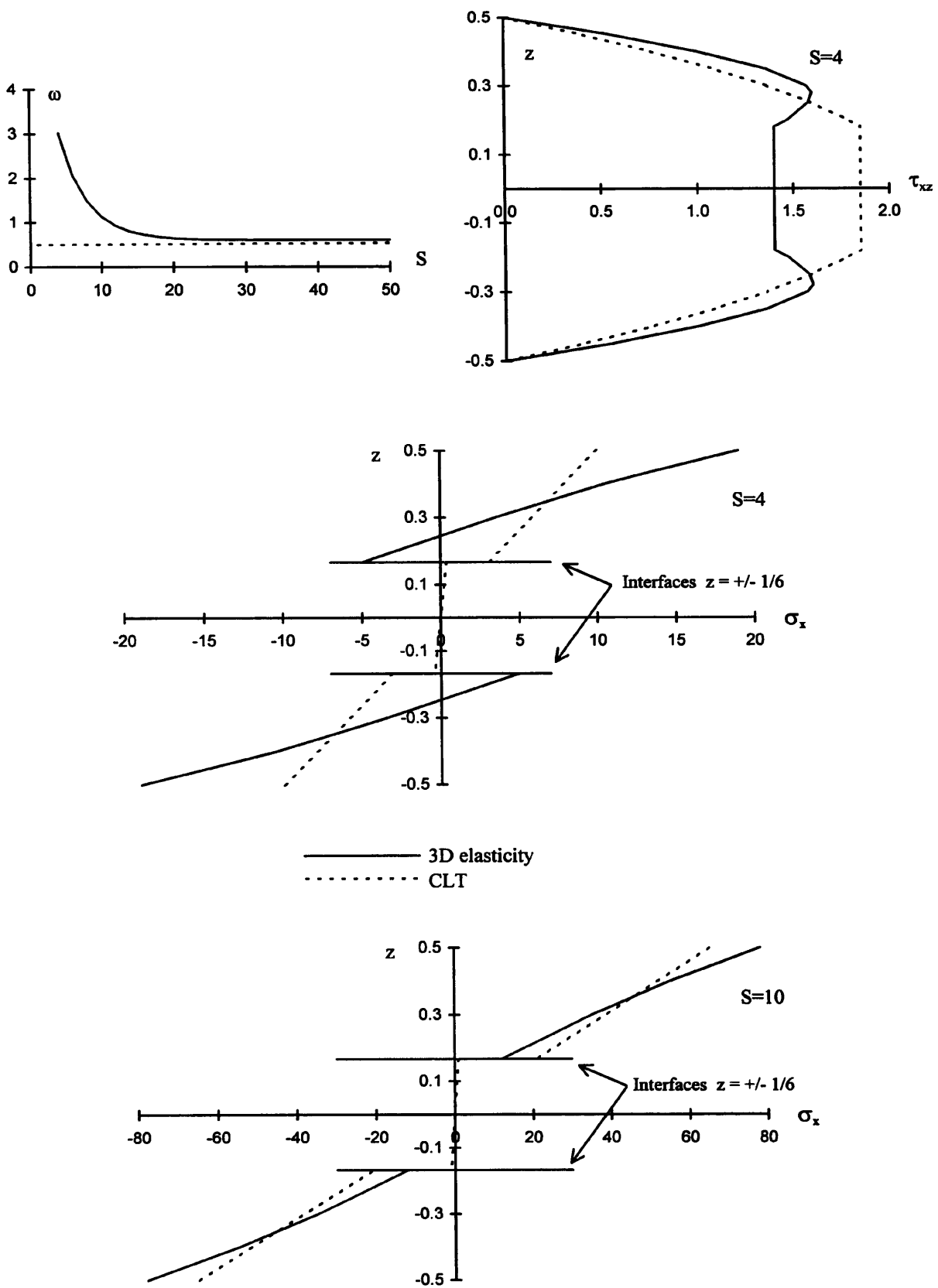
Figure 2.25 Comparison between 3D elasticity results and CLT, according to Pagano [52].
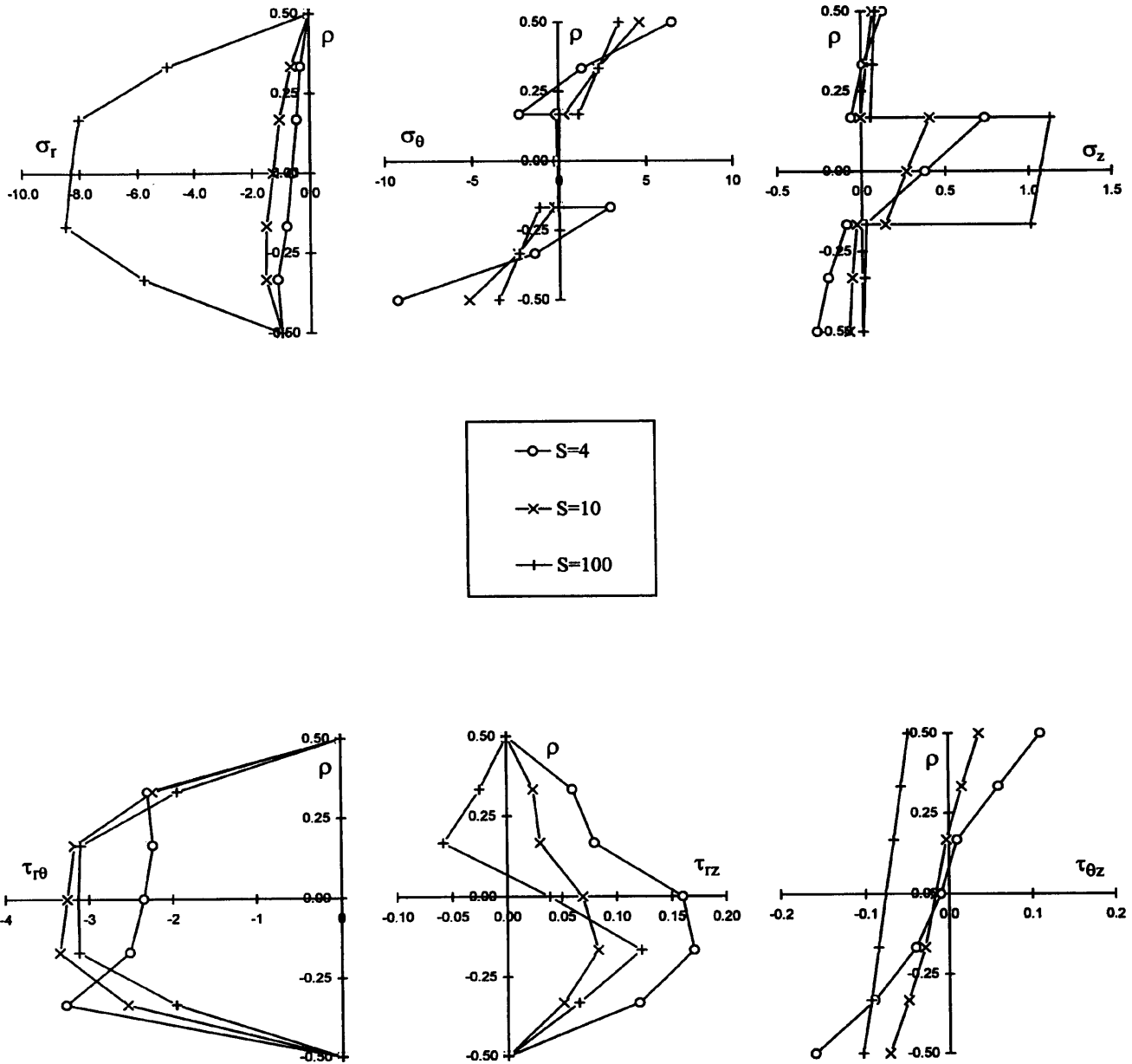
Figure 2.26 Stress distribution through the thickness of a (90°/0°/90°) laminated composite tube [64].
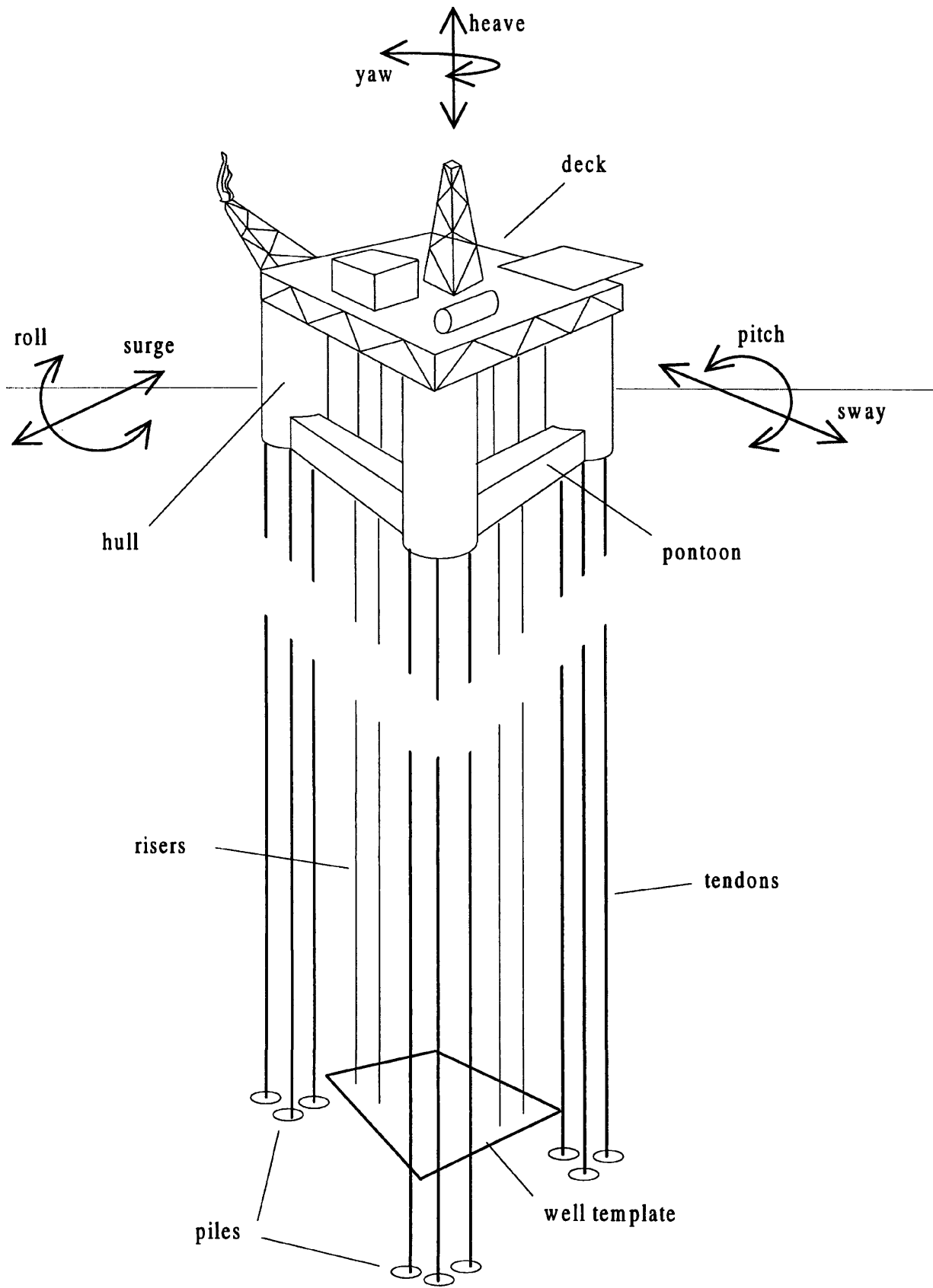
Fig 2.27 Tension leg platform concept and definition of motions.

External coating   +/- 20° carbon plies   Internal liner

90° glass plies
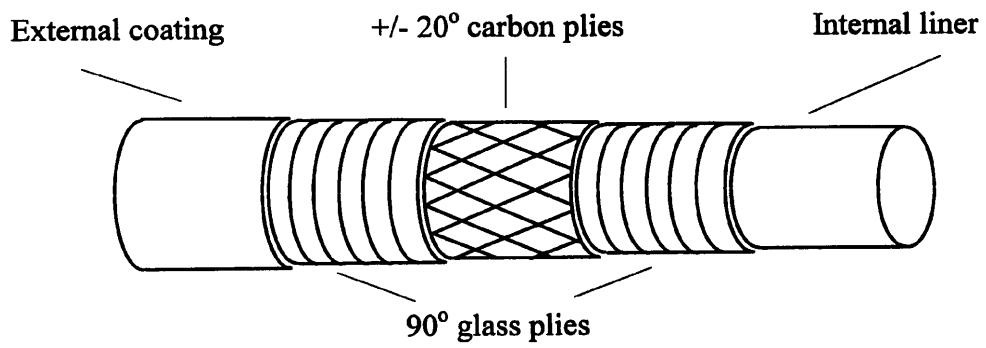
Figure 2.28 Composite riser tube configuration.
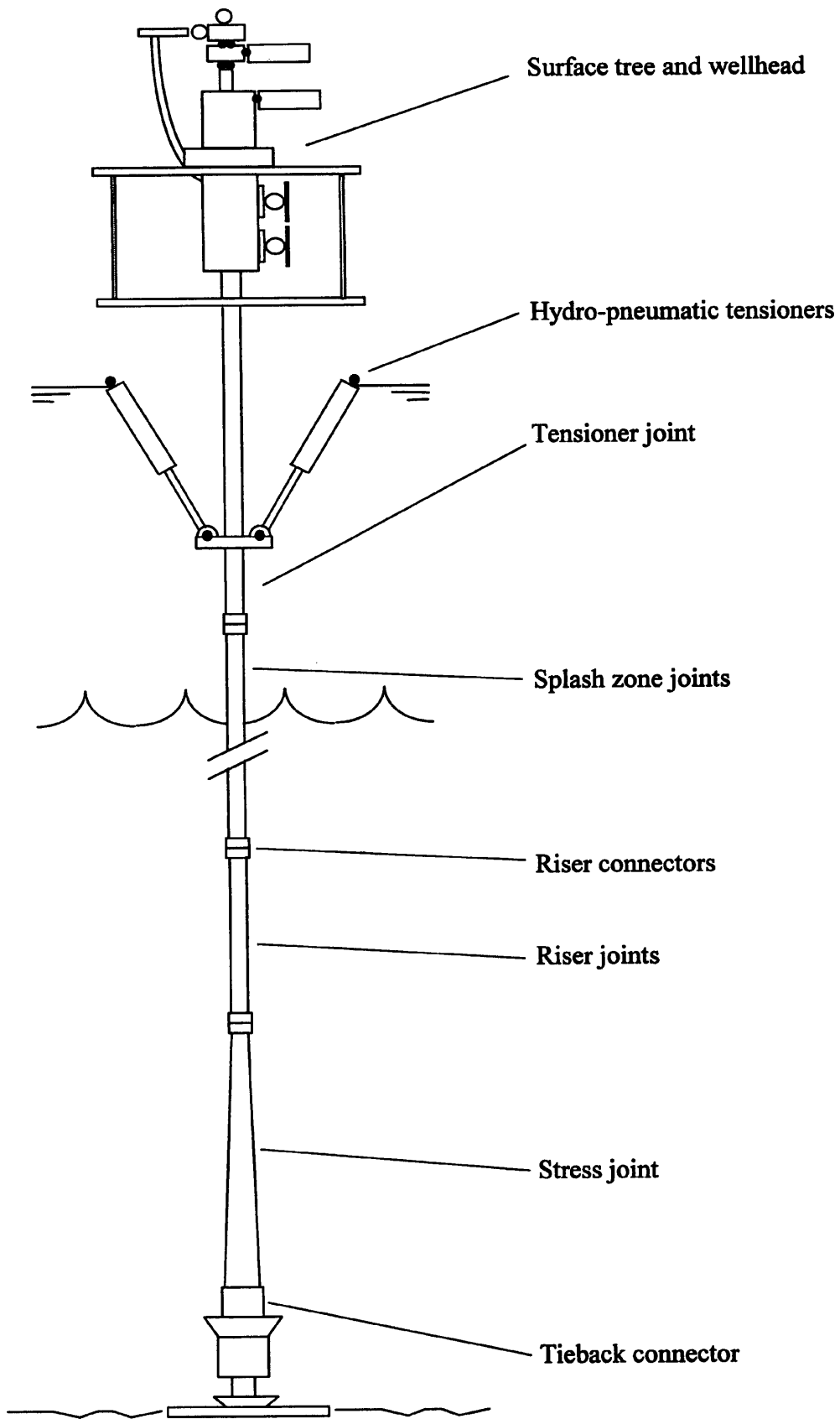
Figure 2.29 Production riser configuration [91].
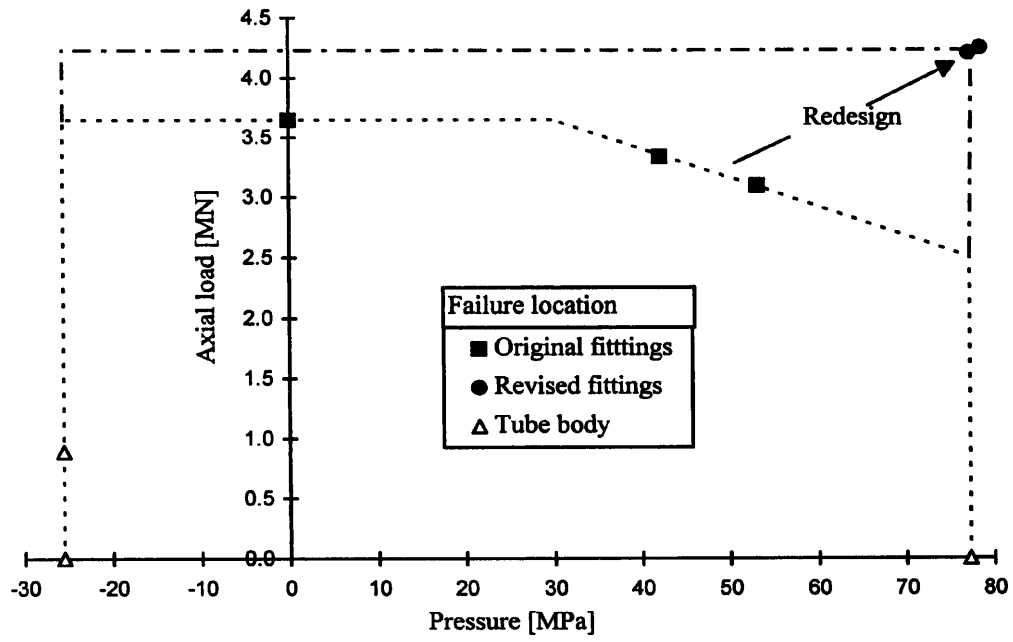
Figure 2.30 Experimental failure envelope for a prototype composite production riser [92].

CHAPTER 3 EXPERIMENTAL WORK

CHAPTER 3   EXPERIMENTAL WORK

3.1 INTRODUCTION

This chapter describes the experimental tests carried out during the research. On the the first set of tests the interlaminar fracture toughnesses of the carbon/epoxy composite were evaluated, in terms of critical Strain Energy Release Rates (SERR's). Flat specimens were assembled and cured for that purpose.

Later, angle-ply carbon/epoxy composite tubes with built-in ply drop-offs were tested. Given the measured interlaminar fracture toughnesses, the main objective of the carbon tube tests was to demonstrate whether or not the delamination type of failure was to prevailed. Some basic fatigue tests were performed, as a first appraisal of the behaviour of the dropped ply tubes under cyclic loading. These tests were only concerned with the carbon/epoxy composite, where the ply drop-off is due to be located in a tapered joint of a composite riser.

Following the all-carbon tubes experiments, hybrid glass/epoxy and carbon/epoxy tubes were tested. The tubes were subjected to four point bending tests, internal pressure tests and combinations of these two basic load conditions. Both +/-20° and 0° carbon fibre arrangements were considered. A set of plain, non-stepped, angle-ply tubes was tested in four point bending. The unidirectional carbon/epoxy system used in the tubes was the T300/MTM28 pre-pregs from Advanced Composites Group. According to the supplier, the pre-preg sheets have 50000 filaments per tow, a weight of 135 g/m^2 and a fibre volume fraction of 52%. The glass/epoxy pre-pregs were the GE 131, from Primco. This is a biased, 44 satin woven cloth, with an average glass content of 290 g/m^2 and a fibre volume fraction of 53%. The glass weight ratio between the warp and weft directions is 6.9:1. Accordingly, the warp direction was made the circumferential one, during the assembly of the tubes. The reason for using a woven cloth instead of a unidirectional pre-preg was simply that the manufacturers only supply the former, as there is not a market for the latter.

The carbon/epoxy SERR specimens were assembled by hand lay up. The tubes were made by the table rolling process. This process consists of two parallel flat surfaces that move over a cylindrical mandrel placed between them, rolling the pre-preg sheets one by one.

3.2 FRACTURE TOUGHNESS MEASUREMENTS

The critical SERRs G_{Ic} and G_{IIc} were obtained from the double cantilever beam (DCB) and the end notched flexure (ENF) tests, respectively. The specimens were cut from flat plates assembled by hand lay-up. The final thickness of the plates was approximately 3.3 millimetres, comprising 24 layers.

The manufacturing of the flat plates was achieved as follows. The stack of plies making up the plates were cured in a controlled temperature hydraulic press, according to the instructions of the pre-preg manufacturer. Vacuum was applied to the bagged plates before the press introduced a pressure of 0.3 MPa (40 psi). The vacuum was then released, to avoid dust and humidity entering the material in case of bagging failure. The temperature was raised at a rate of $1°$ C per minute up to $120°$ C, for a one hour cure dwell. The pressure of 0.3 MPa was maintained during the whole curing process. After the curing period, the plates were cooled down at a rate no greater than $3°$ C per minute. Figures 3.1 to 3.3 illustrate the lay-up and curing processes.

The plate dimensions were 160 X 200 mm and 5 specimens were cut from each plate, measuring 25 X 150 mm each. There were 20 specimens in total made up of four sets of 5 specimens. The first set was used for mode I tests on unidirectional $0°$ laminates. The second set was used for mode II tests, on $0°$ laminates. The third and fourth sets were similar to the first two but were performed on balanced $+/-20°$ angle-ply configurations. The initial defects required by the fracture toughness tests were obtained by placing a 10 μm thin Teflon sheet into the mid-thickness of the specimens.

For the angle ply material, each arm of the specimens had a balanced and symmetric stacking sequence, as follows: [(+20/-20)$_3$/(-20/+20)$_3$/Teflon/(-20/+20)$_3$/(+20/-20)$_3$]. It was preferred to have a bending/twisting coupling rather than a bending/shearing one. The shearing effect could introduce undesirable propagation modes during the mode I (peel) test. The twisting was constrained by the stiffness of the metallic hinges and supports of the test set-ups.

The G_{Ic} test was performed according to the directions of the ASTM D 5528 standard test method [24]. The G_{IIc} test, for which no standard method is available, was performed according to the procedures outlined by Carlsson and Pipes [28] for the ENF test configuration introduced by Russell and Street [29]. The edge Teflon insert proposed by Robinson and Song [22] was included for the tests of angle-ply laminates. The SERR values for modes I and II were obtained from expressions 2.34 and 2.35, developed in Chapter 2.

Figure 3.4 shows the experimental set-up for the mode I DCB test. Figures 3.5 and 3.6 plot the curves of load *versus* displacement obtained for mode I and mode II tests, respectively. The mode I tests required only small loads and were done on a screw driven INSTRON machine in the Paper Science Department at UMIST, fitted with a 500 N load cell. The mode II tests were performed on a screw driven INSTRON machine fitted with a 10 kN load cell.

The loading rate was 0.5 mm/min. for both tests. The mode I test displayed stable crack propagation, allowing several measurements of delamination length and respective load. The mode II test, on the other hand, was unstable. Once the delamination started to propagate, the load fell to zero immediately. Only one measurement of delamination length and associated load was possible.

Tables 3.1 and 3.2 display the resulting mode I and mode II fracture toughnesses. The values for the T300/MTM28 carbon/epoxy system were high, specially for the mode II toughness. The values were high when compared with table 2.1, Chapter 2, which displays some SERR values published in the open literature about carbon/epoxy laminates.

Epoxy resins are inherently brittle, due to the high degree of crosslinking. In recent times, however, there have been significant advances in toughening epoxy-based composites, as Woo and Mao [100] show. The blending of epoxy resins with thermoplastics like polysulfones, polyether sulfones and polyimides enhances fracture toughness without compromising other desirable properties, like the glass transition temperature. Those authors reported values up to 480 J/m^2 for G_{Ic} and up to 910 J/m^2 for G_{IIc}.

The MTM 28 carbon/epoxy pre-preg has a toughened epoxy matrix, intended to increase the impact resistance of the composite. The good toughness values are marketed as a special feature of the product in the supplier's catalogue. When consulted about the high SERR

values obtained experimentaly, the Advanced Composites Group technical director, Shahidi [101], confirmed the information. He informed that the toughning additive is a crosslinkable thermoplastic of molecular weight between 70,000 and 150,000.

Concerning the experimental results, there was no general trend regarding fibre orientation. Mode I thoughnesses were higher for the unidirectional laminates and mode II were higher for the angle-ply laminates. The scatter in the results was greater for the angle-ply laminates. The edge delaminated specimens performed well, with no apparent crack departure from the mid plane.

3.3 CARBON/EPOXY, STEPPED TUBE TESTS

The first tube made was called the prototype tube and was designated P1. After it was tested in bending and proved satisfactory, its dimensions were adopted for six other carbon/epoxy tubes, namely C1 to C6. Figure 3.7 shows the configuration and dimensions of the dropped-ply carbon tubes, which are listed in table 3.3. It shows a thickness reduction of the carbon/epoxy laminates from 3.85 mm to 3.0 mm, on average.

The steel sleeves were employed to resist the high concentrated loads imposed by the testing machine during the four point bending tests. The glass/epoxy reinforcements at the extremities helped to deliver the stresses to the carbon/epoxy tube more evenly. The making of the tubes by means of the table rolling process is shown in figure 3.8. The tubes were made by Custom Composites of Rochdale, Lancashire.

Every tube had two dropped-ply regions, in a symmetric arrangement in relation to the central section. The thickness reductions were obtained by terminating 3 pairs of +/- 20° layers, at the mid-thickness. The layup sequence was $(+20^{\circ}/-20^{\circ})_{13}$ for the thick part and $(+20^{\circ}/-20^{\circ})_{10}$ for the thin part. The dropped ply regions were 50 mm away from the glass sleeves and from the central section of the tube, as figure 3.7 shows. A preliminary evaluation of the length of the stress alteration caused by the dropped plies can be attained as indicated by Horgan [102], who examined the Saint Venant's principle for composite cylinders. He proposed a simple formula for the decay length λ (for reduction to the nominal load value), for tubes loaded

axially:

$$\lambda \approx \frac{R}{3.83}\sqrt{\frac{E_1}{G_{12}}}$$ (3.1)

where R is the external radius, E_1 is the longitudinal modulus of the laminate and G_{12} is its shear modulus. The values of those elastic constants provided by the suppliers, were 117 GPa and 5 GPa, respectively. For an external radius of roughly 35 mm this corresponds to an influence length of about 45 mm, 5 mm less than the distance adopted. This question was re-examined during the stress analysis of the tubes that followed the experimental investigation.

3.3.1 FOUR POINT BENDING TESTS

The carbon/epoxy tubes were instrumented with six strain gauges along the axial direction at the extreme fibre positions, i.e. along the top and the bottom generators. Strain gauges 1, 5, 7 and 11 were positioned over the thickness transition regions. Strain gauges 3 and 9 were placed at the central, thinner section. The numbering system used for the strain gauges, which was adopted for all the tubes used in the research is shown in figure 3.9. The odd numbered sensors were aligned with the axial direction, and the even numbered ones were positioned along the circumferential direction.

Tubes P1 and C1 to C4 were tested in four point bending on the 200 kN, screw driven INSTRON machine at a displacement rate of 0.7 mm/min of the moving head. Figure 3.10 shows all the measurements made using the strain gauges placed at the thickness transition regions. The graphs show the great scatter, +/- 35% of the average, of the strain readings. The reason for this was attributed to the high strain gradients at the "bumps". A little difference in axial position of the strain gauge would result in a large difference in the strain indicated. There was also some variation in the geometry of the transition region, from tube to tube.

Apart from one obvious strain gauge failure (sg 5, tube P1) and some small perturbations observed at mid-load by several sensors, the test data change smoothly to the end. There were not sensible changes in the readings, close to the failure point. We recall that Wisnom et al. [39] used the change in slope of the strain readings to detect the onset of delaminations, given

the opaqueness of the material.

The edge of the glass/epoxy reinforcement presented a stress concentration factor similar to the one at the ply drop-off region. The result was that only two tubes, C1 and C2, failed at the transition region. The other three, tubes P1, C3 and C4, displayed failures that started at the junction between the glass reinforcement and the carbon tube. Figures 3.11 and 3.12 show the two types of failure in tubes C2 and C3. The tubes were painted white for better contrast. Table 3.4 shows the bending moments at failure. All failures occurred at the compressed side of the tubes.

Regardless of the point of initiation of failure, the thickness transition regions were submitted to high strain values at the extreme bending fibres of the tubes, as indicated by figure 3.10. Small portions were cut from tubes P1 and C1, to perform a microscopic investigation of the cross section after the tests. Micrographs were taken both from the extreme fibre and from the neutral plane positions in bending. They are shown in figure 3.13, for tube P1, and in figure 3.14, for tube C1.

The micrographs show that the transition region is a preferred location for voids, due to the poor consolidation there during the curing process. The way that pressure is applied to the laminate during the cure of the resin is by means of a thermo-shrinkable tape wrapped around the tube. The slope of the transition region makes it difficult for the tape to work properly there. This created a zone of smaller pressure in the molten resin, where the voids tend to migrate to. It must be said, however, that the amount of voids in the transition regions became smaller as the manufacturer gained experience in making dropped-ply tubes.

Figures 3.13 and 3.14 also show that the manufacturing process did not have a good control of the geometry of the transition regions, given the obvious variations in their construction. Despite the occurrence of voids, no delamination was detected by micrography in any position of the transition regions. The investigation covered the tension side, the compression side and the neutral plane of tubes P1 and C1. This fact, together with the strain readings, led to the conclusion that the prevailing failure mode was by compressive collapse, and not by delamination.

Figure 3.15 displays the strain readings at the central, thinner section of the tubes. There were some small perturbations in the readings at the mid-load level, as well. The variation in the results was smaller, as one should expect, being of about +/- 10% of the average value. These readings were used to calculate the axial modulus E_z of the tube. It follows, from simple beam theory, that:

$$\varepsilon = \frac{R}{\rho} = \frac{M R}{E_z I} \quad \Rightarrow \quad E_z = \frac{M R}{\varepsilon I} \tag{3.2}$$

where ε is the measured strain, ρ is the curvature radius, R is the external radius of the tube, M is the applied bending moment and I is the second moment of area of the section. The results are shown in table 3.5.

3.3.2 FATIGUE TESTS

A full fatigue evaluation of the dropped ply tubes was not one the objectives of this present research. Nevertheless, the fatigue problem is important enough for the composite riser application to deserve at least a screening evaluation during the tests. This was done for tubes C5 and C6. They were cycled in four point bending at medium frequencies (up to 4 Hz), for 500,000 cycles. The stress ratio was 0.1. Tube C5 was cycled between 0.26 and 2.64 kNm. This maximum moment corresponds to 61% of 4.32 kNm, the average failure moment for tubes C1 and C2, that failed at the transition region. Tube C6 was submitted to higher loads, between 0.29 and 2.88 kNm maximum, that is 67% of the average failure moment. The tests were done on the 600 kN servo-hydraulic INSTRON machine. Figure 3.16 shows the experimental set-up.

The purpose of these fatigue tests was to verify whether the cyclic loading would cause the material to delaminate or not. The main variables monitored were the strains in the transition region, as was done during the quasi-static tests. For the tests of tube C5, the strain readings were taken manually, from the stored display of a KONTRON data logger, at some given numbers of cycles. The test was interrupted for the night and re-started the following day. Figure 3.17 shows the results.

The variables plotted are the absolute values of the strain range at the four thickness transition spots, in the extreme fibre positions. The vertical lines represent the end of the days, where the test was stopped. There was an accommodation period of about 30,000 cycles at the beginning of the test after which the readings reached a lower value. There were pronounced fluctuations later on, but they all started from the beginning of the next day. Thermal effects have to be considered, as well. In order to "filter out" these effects, other variables were plotted. These were the differences between the strain ranges. The idea was that any thermal or external effect of any kind would affect all the strain gauges equally. As it was very unlikely that delaminations would start simultaneously at two spots, the difference between the strain ranges in those two locations would serve to detect its onset.

The two differences, $\Delta1$-$\Delta5$ and $\Delta7$-$\Delta11$, were much more stable with the number of cycles. There was a pronounced change in the latter variable, at the beginning of the fourth day. The question was that the lines marked in the graph with an arrow represent the days where the specimen was taken off the machine, to replace fatigued screws in the jaws. The perturbation in strain pattern could be due to the repositioning of the specimen.

In an attempt to remedy this problem, tube C6 was tested continuously, with automatic strain readings by the data logging system. The results of that test are shown in figure 3.18. All the 6 axial strain gauges were installed. Unfortunately,another problem arose. There were several strain gauge failures. Strain gauge 11 failed at the beginning of the test, strain gauge 9 failed at 130,000 cycles, strain gauge 5 at 190,000 cycles and strain gauge 3 at 390,000 cycles. Strain gauges 1 and 7 remained operational till the end. The difference in their readings was plotted as well. It can be seen that in this case the accommodation period was longer, lasting about 75,0000 cycles. At 340,000 cycles there was an event that affected all the remaining strain gauges and changed the difference $\Delta7$ - $\Delta1$ from 500 $\mu\varepsilon$ to 600 $\mu\varepsilon$.

After the fatigue tests were concluded, small samples were cut from the four transition regions at the extreme fibres of both tubes. None of the micrographs showed any sign of delamination. Figures 3.19 and 3.20 display some of the results, for tubes C5 and C6, respectively. Despite some indications detected by the strain gauges, no delamination or cracking was observed at the ply drop-off regions. If there was any damage, it occurred elsewhere. There was the difficulty of separating strain gauge failure from a failure in the tube. The experimental

technique needs to be improved.

3.4 HYBRID, STEPPED, ANGLE-PLY TUBE TESTS

After the tests of the all-carbon/epoxy angle-ply, stepped tubes were completed, the work continued with the evaluation of hybrid tubes, that represented the real application. The configuration of the hybrid tubes was quite similar to the configuration of the carbon specimens, shown in figure 3.7. The axial dimensions and the internal diameter were the same. The differences were the addition of internal and external glass/epoxy sub-laminates, 1.5 mm thick each, and the consideration of a thicker +/- $20°$ carbon/epoxy sub-laminate, with thickness dropping from 5.8 to 5.0 mm. At the thicker section the S ratio (average radius over total thickness) was 34.5/8.8 = 3.9. Table 3.6 shows the dimensions of all the 15 specimens made. They were called HST tubes (hybrid, stepped, +/-$20°$ tubes). They also had glass/epoxy reinforcements at the ends.

3.4.1 FOUR POINT BENDING TESTS

The tubes were tested in four point bending on the 600 kN servo-hydraulic INSTRON machine. The steel sleeves were made thicker, to resist the higher concentrated loads. The steel tubes adopted were of specification 4" SCH 160, with an ID of 87 mm and a thickness of 13.5 mm. The load was applied under displacement control, at a rate of 1.5 mm/min. Six tubes were tested in pure bending, as shown by the results in figure 3.21. The bending moments at failure are listed in table 3.7.

The failures occurred at the compressed side. In all but one tube, tube HST03, the starting spot was the thickness transition region. Tube HSTO3 failed at a spot under the steel sleeve. The large scatter in the results is evident, with a coefficient of variation of 20%. Tube HST11, that attained the highest moment, was completely severed at failure. Figure 3.22 shows the failure state of tube HST01.

Figure 3.23 displays a close-up of a failure spot at the transition region. The outer glass/epoxy layer (that had a black pigment in the resin) was burst by the failure of the inner carbon/epoxy

sub-laminate. It is seen that the carbon fibres were cut by the compressive failure. Secondary (post-initial failure) cracks along the +/-20° fibre orientations are also visible.

3.4.2 INTERNAL PRESSURE TESTS

Tubes HST04, HST05 and HST06 were pressurised to failure inside the rig shown in figure 3.24. The tubes were lined with a latex membrane to make them pressure tight. The extremities were closed by aluminium plugs, where "u" rings provided the seals, as displayed in figure 3.25. The tests did not introduce any axial load in the tubes, as the thrust occasioned by the internal pressure was resisted by the rig's frame. The whole rig was surrounded by a polycarbonate enclosure.

Hydraulic oil was pumped inside the tubes by a high pressure, air-driven pump, at a low volumetric rate, until burst failure. The tubes were instrumented by three circumferential strain gauges each, at positions 2,4 and 6. The pressure values were taken at the pump. As all the strain gauges showed the same trend, figure 3.26 includes only strain gauge 4 readings against pressure.

Damage started to show in all tubes, at pressure values between 30 and 35 MPa. The latex membrane in tube HST04 tore apart at a high pressure, so that test had to be repeated. This showed clearly the reduction in circumferential stiffness due to the damage already present in the tube. The second test progressed linearly until the burst point.

There was a small variation in the ultimate pressure supported by the tubes, as table 3.8 shows. Figure 3.27 shows the failure state of tube HST06. The tube displayed a long opening along the axial direction of the tube, perpendicular to the broken circumferential glass fibres.

3.4.3 COMBINED TESTS

The final tests performed on the HST tubes were bending tests combined with internal pressure. To that purpose, a special rig was assembled, as shown in figure 3.28. it consisted of a "U" shaped reaction frame, designed to resist the thrust caused by the internal pressure. The frame was placed inside the 600 kN INSTRON machine, where the bending load was applied.

After the tube was bent, the internal pressure was increased, until failure. The aluminium plugs moved freely and were secured by circular stops on the reaction frame. This arrangement caused the reaction forces to be applied at the centre of the plugs, avoiding any local moment.

The "U" frame was put between two polycarbonate plates 10 mm thick, to allow visual inspection of the area whilst providing a safety barrier. The plastic plates were reinforced by a 5 mm thick steel plate lid and by 25 mm steel angles. Two rubber mats sealed the ends of the frame. A plastic sheet covered the space between the polycarbonate plates and the moving jaw of the INSTRON machine, in order to avoid oil spillage.

To make the tests safer, the bending load was applied first, under displacement control, at a rate of 1.0 mm/min. Two maximum bending moments were adopted: 5.20 kNm and 10.40 kNm. These values corresponded to 33% and 66%, respectively, of the average moment at failure for the pure bending tests (15.69 kNm). The higher bending level was applied first, for tubes HST07, HST08 and HST09. The tubes were instrumented at the central section, by means of strain gauges 3, 4, 9 and 10. Figure 3.29 shows the results for tube HST07. Due to the special characteristics of this test, the results require detailed explanation.

As the moment *versus* pressure graph shows, the indicated moment decreased linearly with the increase in pressure, until a sudden change in slope occurred at a pressure of 35 MPa. We recall that the tests were executed under displacement control by the INSTRON machine, for safety reasons. Once the maximum moment was reached, the moving head was stopped and was kept in position by the control loop of the machine. The pressure started to increase, with the tube already bent into a shallow "U", as displayed in figure 3.30. The figure shows the force equilibrium diagram for the system consisting of the tube plus the aluminium plugs.

During the pure bending phase the force applied by the machine actuator, $F_{INSTRON}$, was the force indicated by the load cell. Once the tube was bent, its curvature was kept constant by the machine, the pressure inside the tube then started to increase. That internal pressure caused reaction forces F_{plug}, to hold the aluminium plugs in position. As the diagram indicates, those reaction forces were normal to the plugs by virtue of the circular stops and so were inclined to the horizontal direction, due to the curvature of the tube. These were equal and opposite to the

forces applied to the reaction frame. The circular stops in the reaction frame then introduced a large horizontal force component and a smaller vertical component in it. The horizontal component of the force at the stops were reacted by the frame. The vertical component tried to raise the frame and hence the tube. The frame imposed a force back on the tube that is referred to as F_{pres1} in the diagram of figure 3.30. It was labelled this way to stress that it was a force due to the internal pressure in the tube.

In consequence of the additional force component, F_{pres1}, the applied bending moment, and thus the curvature radius of the tube, tended to increase. But the control loop of the machine would not allow that, as it kept the curvature radius constant. The result was that the force applied by the actuator and indicated by the load cell was diminished, in order to keep the sum $F_{INSTRON}+2F_{pres2}$ constant. Nevertheless, the bending moment that the tube "felt" was constant. The difference between F_{pres1} and F_{pres2} was the vertical component of F_{plug}. Because F_{pres1} and F_{pres2} had different values, a shear force was introduced in the tube. The shear force (the vertical component of F_{plug}) was not significant, however, due to the shallow angles of inclination of the extremities of the tube, which were smaller than $3°$. This situation persisted until the pressure of 35 MPa was reached, when damage in the tube started to change its stiffness and hence the applied moment.

The graph of moment against pressure in figure 3.29 displays both the apparent moment (due only to the load indicated by the load cell) and the corrected moment (the one caused by the sum of forces $F/2_{INSTRON} + F_{pres2}$). The first failure occurred at a moment of 10.4 kNm, but the ultimate moment at break was of about 8 kNm. The graphs of strain *versus* moment considered the corrected value. There was a linear increase of strains with moments during the application of the load. Then, the bending moments remained constant while the strains were affected by the increase in pressure. When the first damage occurred, the bending moment started to fall, as the stiffness of the tube became smaller.

The plots of strains against pressures showed that the strain gauges positioned at the compressed side (numbers 9 and 10) were the most affected once the damage started to show up. The final failure occurred at the thickness transition region, at the compressed side. That was the case for all the tubes tested in combined bending plus internal pressure. Figures 3.31 and 3.32 show the results of the combined tests on tubes HST08 and HST09. They display the

same general pattern observed for tube HST07.

Tubes HST13, HST14 and HST15 were tested at the lower bending moment, 5.2 kNm. For this bending moment level the first damage onset was less pronounced, but even so the point when the behaviour changed could be determined for all tests. Figures 3.33 to 3.35 display the results, for tubes HST13 to HST15, respectively. Figures 3.36 and 3.37 show the experimental set-up for the combined load tests. Figure 3.38 displays the failure of tube HST08. The damage after failure was more extensive in this case than it was for the pure bending and the pure internal pressure loads. The results of all the combined load tests, in terms of the initial damage and final failure points, are listed in table 3.9. The moments listed are the corrected ones.

3.5 HYBRID, STEPPED, UNIDIRECTIONAL TUBE TESTS

Some tubular specimens were made with the carbon/epoxy sub-laminate whose fibres were aligned with the axial direction. This was easily achieved by the table rolling manufacturing process. These specimens were called HSN tubes (from hybrid, stepped, nought 0° carbon fibres).

In order to keep the same magnitude of bending moment values at failure, the carbon/epoxy sub-laminate thickness was reduced. The thickness of the carbon sub-laminates was reduced from 4.6 to 3.9 mm, on average. The external and internal glass/epoxy sub-laminates had the same thickness as before, i.e. 1.5 mm each. Table 3.10 lists the measured dimensions of the HSN tubes. These tubes were tested in four point bending and internal pressure load conditions.

3.5.1 INTERNAL PRESSURE TESTS

Tubes HSN01 to HSN03 were tested under internal pressure until they burst. The test rig was the same as that used for testing HST tubes in pure internal pressure mode. The internal liner in this case was made of polyethylene. This proved to be more difficult to handle than the latex membrane used before. All the tests had to be repeated due to failure in the seals.

Eventually all the tubes were burst. Again, the strain gauges detected the onset of damage at pressures under the final pressures achieved. Table 3.11 shows the results. The final pressures achieved in this case were lower than they were for the HST tubes pressure tests.

3.5.2 FOUR POINT BENDING TESTS

The specimens HSN04 to HSN09 were submitted to four point bending tests, in the 600 kN INSTRON servo-hydraulic machine. The displacement ratio of the moving head was 1.0 mm/min. Figure 3.39 shows the results of the tests, in terms of the graph of bending moments *versus* strains. The strains values plotted were the average strains at the central section (the average of the absolute values indicated by strain gauges 3 and 9). All the failures were on the compressed side of the tubes. Tubes HSN04 and HSN08 failed under the glass reinforcement. Table 3.12 lists the bending moments at failure.

The much smaller variation in the results is noticeable, when compared with the four point bending tests for the angle-ply stepped tubes. Two factors may have contributed to this. The zero degree orientation of the carbon fibres could have lead to a more uniform thickness transition region. Secondly, the manufacturer improved his technique, as he learnt from the previous tubes he made.

3.6 HYBRID, PLAIN, ANGLE-PLY TUBE TESTS

3.6.1 FOUR POINT BENDING TESTS

This set consisted of 3 plain tubes, without any thickness change. Their dimensions are shown in table 3.13. The glass/epoxy sub-laminates had the usual thickness, 1.5 mm each. The +/-20°

carbon/epoxy sub-laminate was 3.9 mm thick, on average. These tubes were named HPT tubes (from hybrid, plain, +/- 20°). The tubes were tested only in four point bending, to provide a case with no ply drop-off detail.

The results of the tests are listed in table 3.14. In this case, all the failure occurred at the compressed side, but under the glass/epoxy reinforcement. This was to be expected, given the stress concentration factor that existed at the end of the glass reinforcements. Nevertheless, the results provided a verification of the influence of the ply drop-off detail on the bending strength of the tubes. Even though in this case the carbon fibres were arranged at +/- 20° with the axial direction, the failure moments were higher than they were in the previous case. We recall that in the previous case, where the smaller thickness of the 0° carbon/epoxy sub-laminate was also 3.9 mm, the average moment at failure was 12.63 kNm, compared with 16.48 kNm for the present case.

The results of the tests are shown in figure 3.40. For these tests no strain gauges were applied to the specimens. The graphs of figure 3.40 plot the displacement of the moving head of the INSTRON machine against the indicated bending moment.

3.7 HYBRID, PLAIN, UNIDIRECTIONAL TUBE TESTS

3.7.1 INTERNAL PRESSURE TESTS

The last set of tubes tested consisted again of 3 plain tubes, but now with the carbon fibres oriented at a 0° with the axis. Those were the HPN tubes (from hybrid, plain, zero degrees). The dimensions of the specimens are shown in table 3.15. The glass/epoxy sub-laminates were 1.5 mm each. The nought degree carbon/epoxy sub-laminate was 4 mm thick on average. The tubes were tested in pure internal pressure, using latex membranes as liners, as the polyethylene membranes proved problematic. The aim was to verify the reduction in burst pressures observed from the angle-ply tubes to the unidirectional ones.

The results of the tests are listed in table 3.16 and showed graphically in figure 3.41. The same

sort of initial failure and burst pressures observed for the dropped ply, unidirectional tubes (table 3.11) were also noted in this case. The dropped-ply detail did not affect the behaviour of the tubes under internal pressure load. The reduction in the final pressures achieved, in relation to the HST tubes, was confirmed. The tubes had different thicknesses and angles for the carbon sub-laminates, but the main load carrier under internal pressure were the hoop glass/epoxy layers. The glass sub-laminates were essentially the same for all the tubes tested. The only difference was that the glass/epoxy pre-pregs for the angle-ply and for the unidirectional tubes were from different batches. Even so, the reduction in final pressures looked excessive. The stress analysis, performed in the next Chapter, will help to clarify this issue.

| Sample	G_{Ic} [J/m^2]	Sample	G_{IIc} [J/m^2]
MI0-1	640	MII0-1	1351
MI0-2	503	MII0-2	1699
MI0-3	580	MII0-3	1276
MI0-4	477	MII0-4	1331
MI0-5	529	MII0-5	1302
average	546		1392
coefficient of variation	12%		13%

Table 3.1 Fracture toughness results for unidirectional (0°) T300/MTM28 carbon/epoxy laminates.

Sample	G_{Ic} [J/m^2]	Sample	G_{IIc} [J/m^2]
MI20-1	235	MII20-1	1891
MI20-2	292	MII20-2	1653
MI20-3	356	MII20-3	1384
MI20-4	333	MII20-4	1820
MI20-5	268	MII20-5	1139
average	297		1577
coefficient of variation	16%		20%

Table 3.2 Fracture toughness results for angle-ply (+/-20°) T300/MTM28 carbon/epoxy laminates.

TUBE	ID [mm]	OD$_1$ [mm]	OD$_2$ [mm]
P1	60.1	67.8	66.1
C1	60.1	67.7	66.1
C2	60.0	67.8	66.1
C3	60.0	67.7	66.0
C4	60.0	67.7	66.0
C5	60.0	67.6	66.0
C6	60.0	67.8	66.0

Table 3.3 Dimensions of the stepped carbon tube specimens.
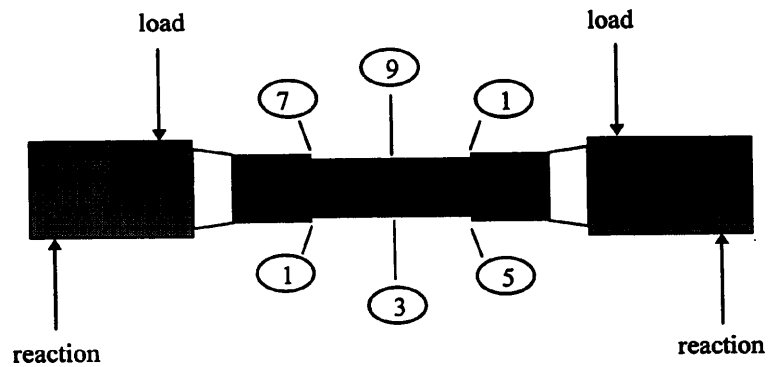
TUBE	MOMENT AT FAILURE [kNm]	FAILURE START SPOT
P1	4.02	toe of glass reinforcement
C1	4.50	position 11
C2	4.13	position 7
C3	4.23	toe of glass reinforcement
C4	4.53	toe of glass reinforcement

Table 3.4 Bending moments at failure: stepped, angle-ply, carbon/epoxy tubes.

TUBE	STRAIN GAUGE	AXIAL MODULUS IN BENDING E_z [GPa]
P1	3	69.6
	9	69.4
C1	3	61.7
	9	65.8
C2	3	76.3
	9	75.9
C3	3	77.2
	9	77.3
C4	3	81.6
	9	74.0
	average	72.9
	c.v.	8.4 %

Table 3.5 Axial moduli in bending: angle-ply, carbon/epoxy tubes.

TUBE	ID [mm]	OD_1 [mm]	OD_2 [mm]
HST01	60.4	78.0	76.2
HST02	60.2	77.8	76.3
HST03	60.3	78.0	76.4
HST04	60.3	77.6	76.0
HST05	60.3	77.9	76.4
HST06	60.3	77.7	76.2
HST07	60.3	77.8	76.3
HST08	60.3	78.0	76.5
HST09	60.2	78.0	76.4
HST10	60.2	78.1	76.5
HST11	60.3	78.0	76.4
HST12	60.3	78.0	76.5
HST13	60.3	77.8	76.4
HST14	60.3	78.0	76.4
HST15	60.3	77.7	76.0

Table 3.6 Dimensions of the hybrid, stepped, +/- 20° angle-ply tube specimens.

TUBE	MOMENT AT FAILURE [kNm]	FAILURE START SPOT
HST01	17.47	ply drop-off, compressed side
HST02	13.10	ply drop-off, compressed side
HST03	16.68	under the steel sleeve
HST10	16.23	ply drop-off, compressed side
HST11	19.56	completely severed, at drop-off
HST12	12.10	ply drop-off, compressed side
average*	15.69	
c.v.*	20%	

* not considering tube HST03

Table 3.7 Bending moments at failure: hybrid, stepped, +/- 20° angle-ply tubes.

TUBE	FIRST DAMAGE PRESSURE [MPa]	RUPTURE PRESSURE [MPa]
HST04	34.	46.8
HST05	35.	47.5
HST06	31.	45.4

Table 3.8 Internal pressure tests: hybrid, stepped, +/- 20° angle-ply tubes.

TUBE	INITIAL DAMAGE		FINAL FAILURE	
	Moment [kNm]	Pressure [MPa]	Moment [kNm]	Pressure [MPa]
HST07	10.4	35.	8.	44.7
HST08	10.2	24.	9.	34.2
HST09	10.4	32.	10.	36.0
HST13	5.2	26.	5.	41.4
HST14	5.2	29.	5.	46.5
HST15	5.2	26.	5.	41.5

Table 3.9 Combined tests results: hybrid, stepped, +/- 20° angle-ply tubes.

TUBE	ID [mm]	OD$_1$ [mm]	OD$_2$ [mm]
HSN01	60.3	75.6	74.2
HSN02	60.3	75.2	73.9
HSN03	60.3	75.3	73.9
HSN04	60.3	75.3	73.8
HSN05	60.2	75.4	74.1
HSN06	60.3	75.5	74.2
HSN07	60.3	75.5	74.1
HSN08	60.3	75.2	74.0
HSN09	60.3	75.3	73.9

Table 3.10 Dimensions of the hybrid, stepped, 0° carbon fibre tube specimens.

TUBE	FIRST DAMAGE PRESSURE [MPa]	RUPTURE PRESSURE [MPa]
HSN01	23.	35.9
HSN02	22.	31.6
HSN03	26.	36.9

Table 3.11 Internal pressure tests: hybrid, stepped, unidirectional tubes.

TUBE	MOMENT AT FAILURE [kNm]	FAILURE START SPOT
HSN04	12.50	under glass reinf., comp. side
HSN05	12.81	ply drop-off, compressed side
HSN06	12.99	ply drop-off, compressed side
HSN07	13.03	ply drop-off, compressed side
HSN08	12.96	under glass reinf., comp. side
HSN09	11.67	ply drop-off, compressed side
average*	12.63	
c.v.*	5%	

* not considering tubes HSN04 and HSN08

Table 3.12 Bending moments at failure: hybrid, stepped, unidirectional tubes.

TUBE	ID [mm]	OD [mm]
HPT01	60.3	74.0
HPT02	60.3	74.2
HPT03	60.3	74.2

Table 3.13 Dimensions of the hybrid, plain, +/- 20° carbon tube specimens.

TUBE	BENDING MOMENT AT FAILURE [kNm]
HPT01	17.90
HPT02	17.38
HPT03	14.17

Table 3.14 Four point bending tests: hybrid, plain, +/- 20° tube specimens.

TUBE	ID [mm]	OD [mm]
HPN01	60.3	74.2
HPN02	60.3	74.3
HPN03	60.3	74.4

Table 3.15 Dimensions of the hybrid, plain, 0^0 carbon tube specimens.

TUBE	FIRST DAMAGE PRESSURE [MPa]	RUPTURE PRESSURE [MPa]
HPN01	20.	34.2
HPN02	22.	37.1
HPN03	24.	34.1

Table 3.16 Internal pressure tests: hybrid, plain, unidirectional tubes.
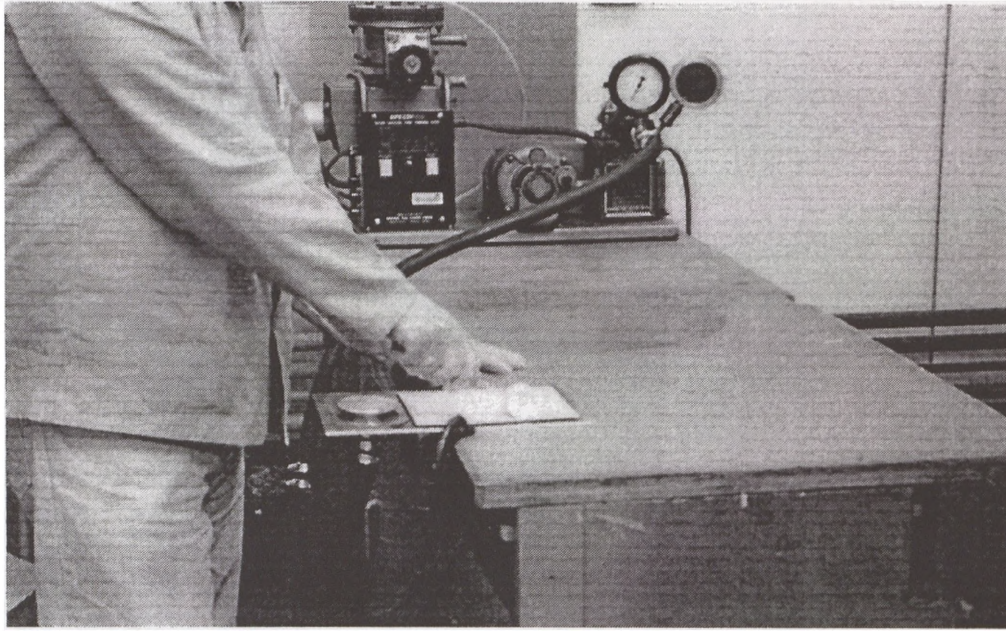
Figure 3.1 Assembling the flat plates from which the specimens were cut by hand lay up.
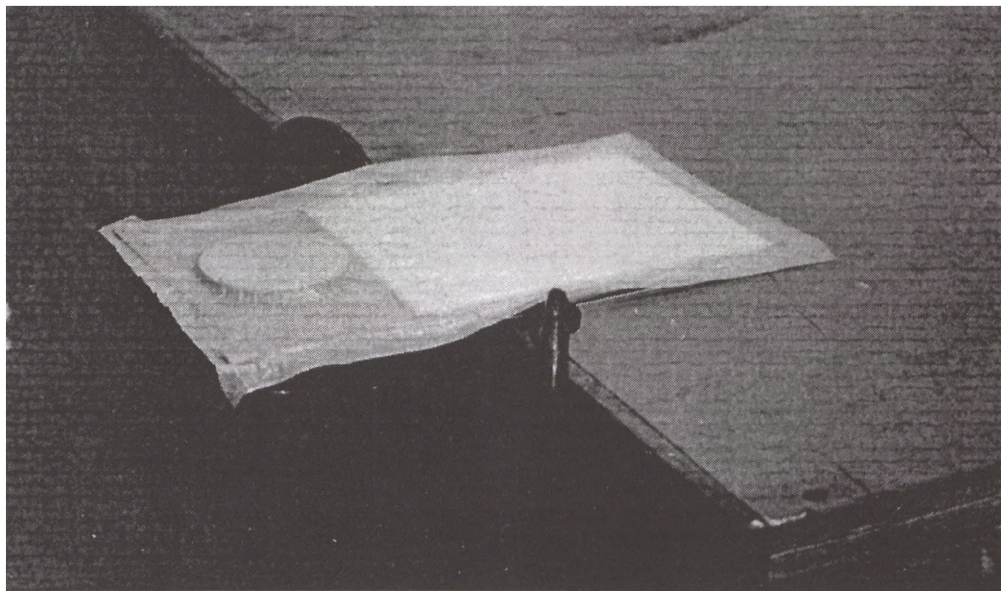
Figure 3.2 Application of vacuum to help debulk the pre-preg material.
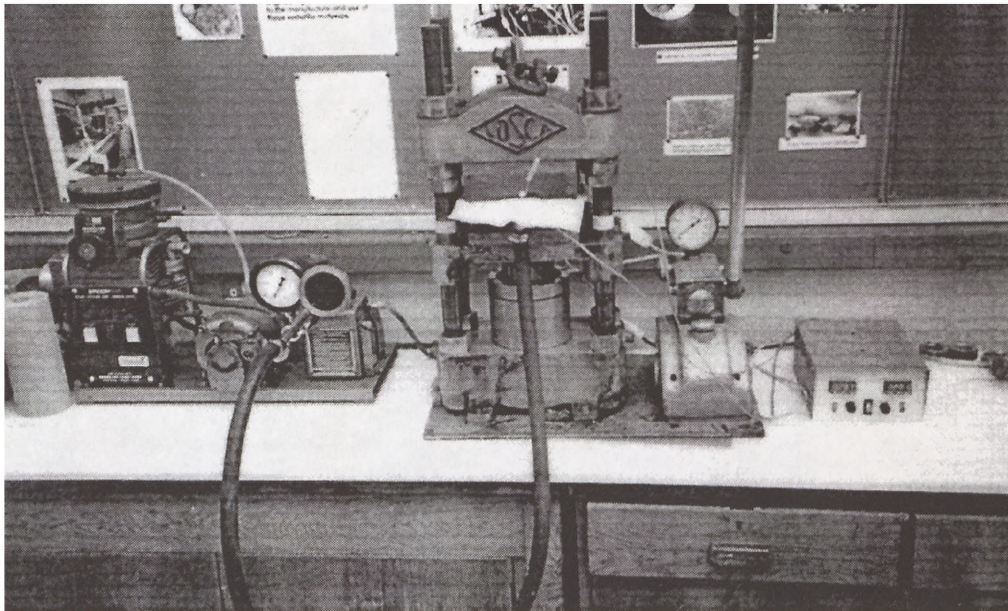
Figure 3.3 Cure in a controlled temperature press, assisted by vacuum.

Figure 3.4 Mode I fracture toughness test using the DCB specimen.
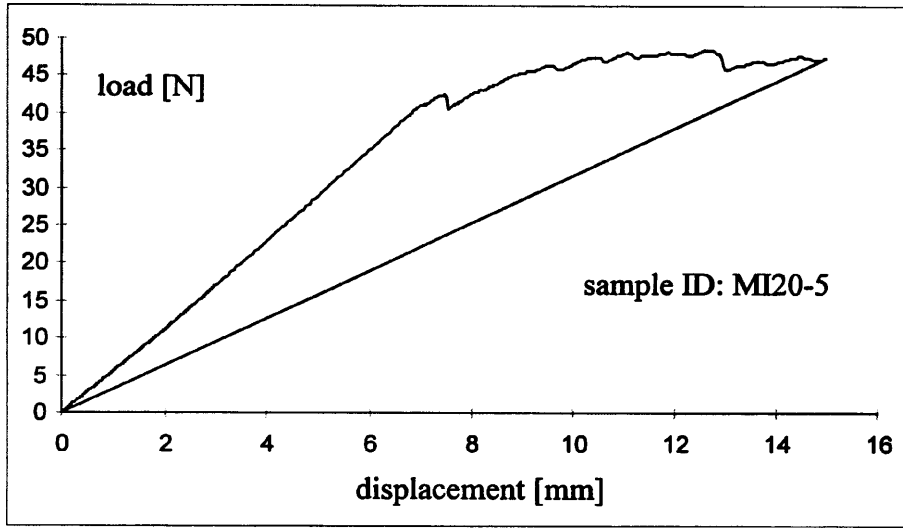
Figure 3.5 Load *versus* displacement curve for a mode I (DCB) fracture test.
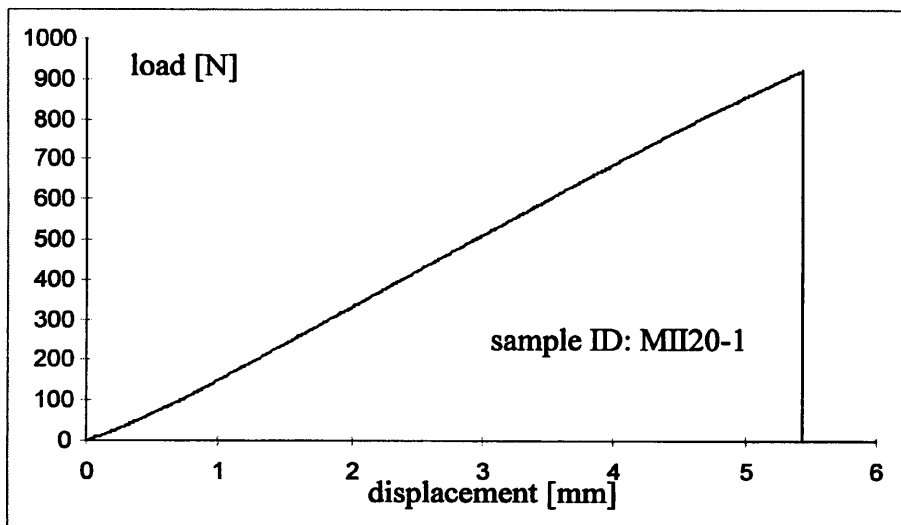
Figure 3.6 Load *versus* displacement curve for a mode II (ENF) fracture test.
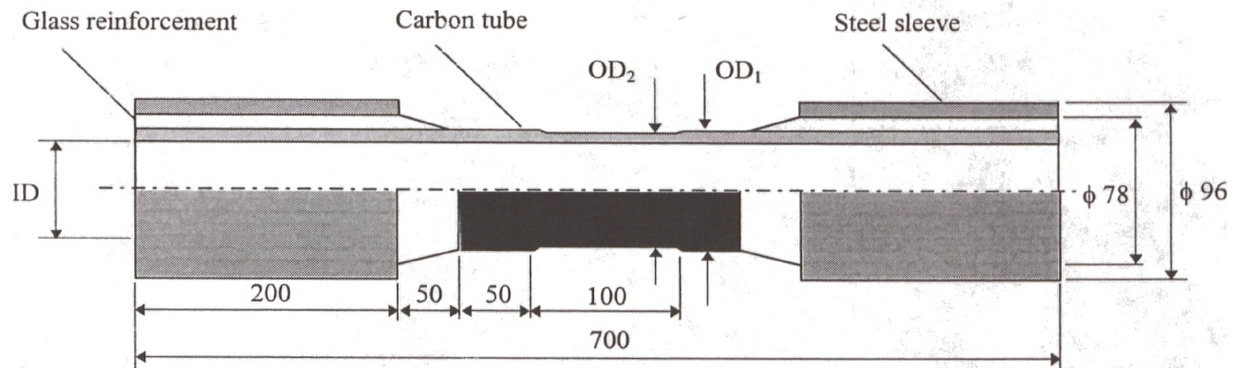
Figure 3.7 Geometry of the dropped ply carbon/epoxy tubular specimens.
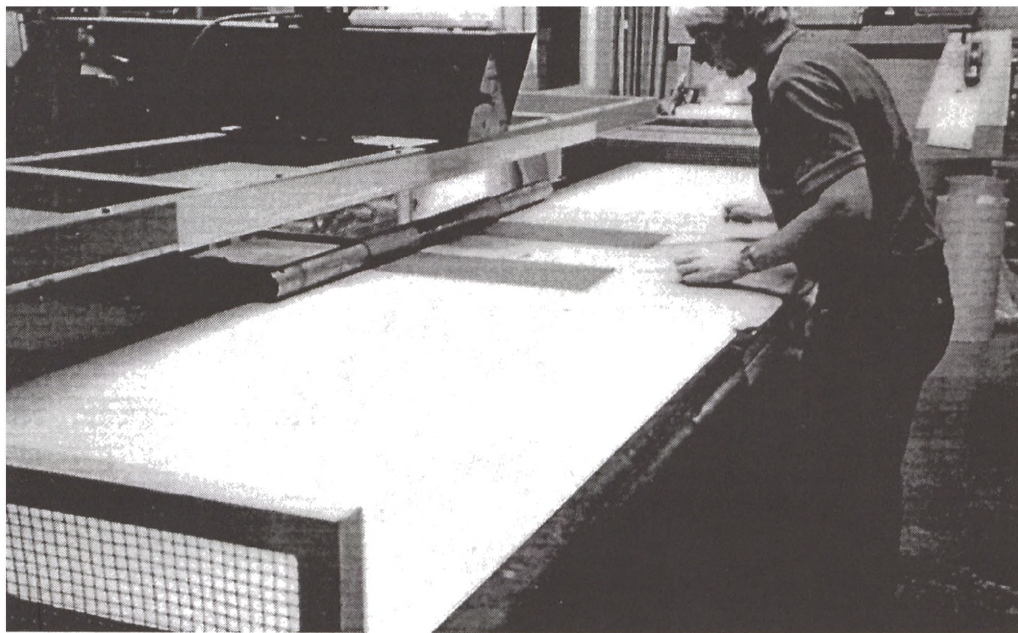
Figure 3.8 Assembling the tubes by means of the table rolling process.
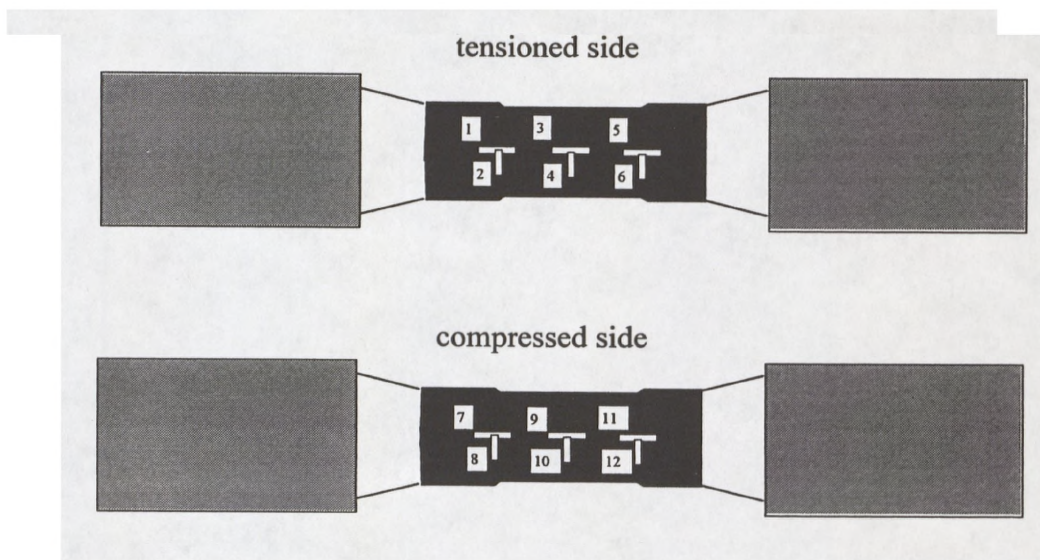
Figure 3.9 Identification of the strain gauges.
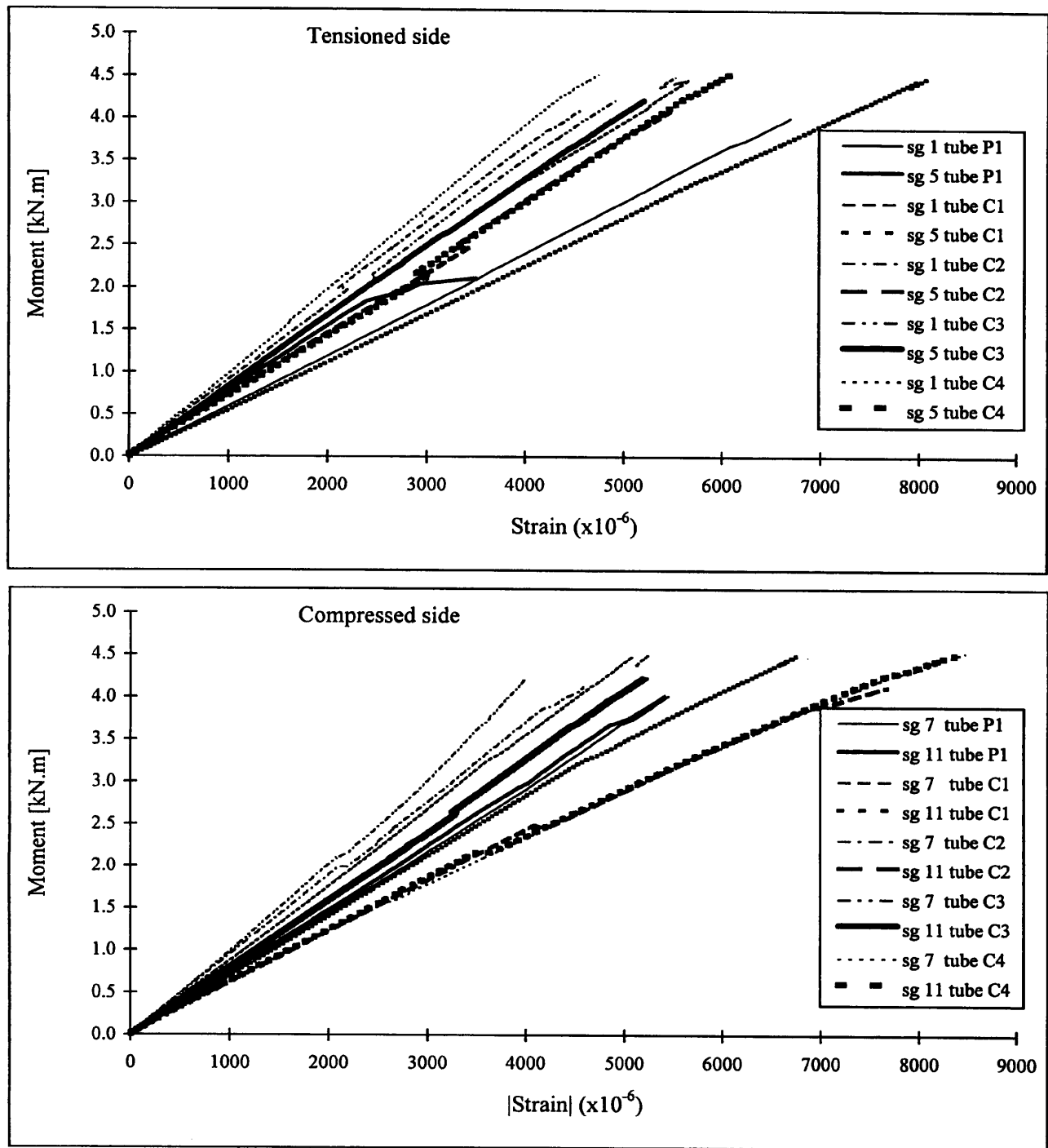
Figure 3.10 Strain measurements at the outer surface of the ply drop region.
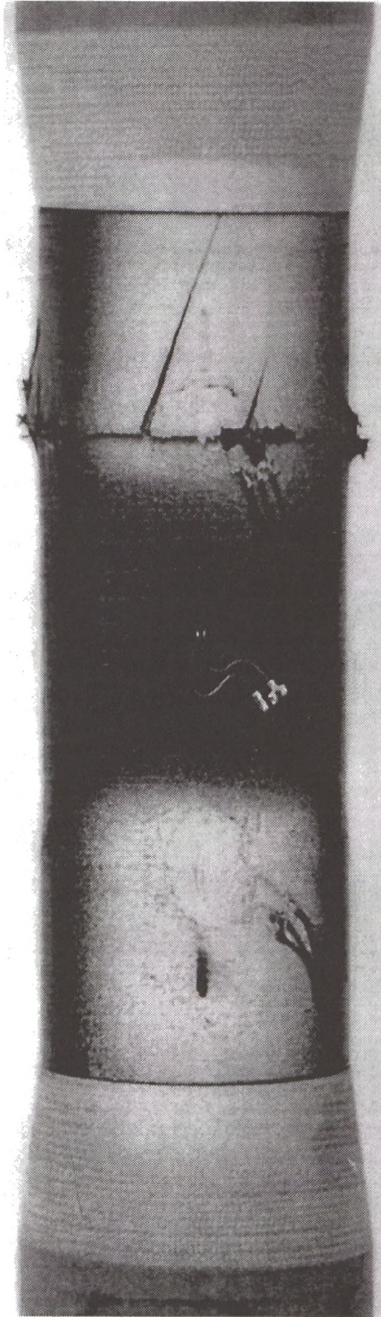
Figure 3.11 Failure aspect of tube C2.
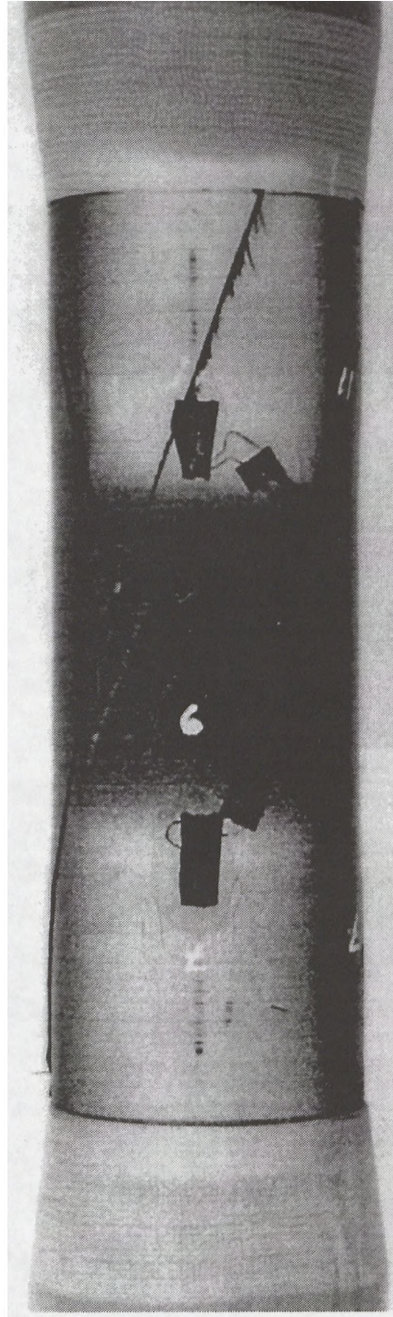
Figure 3.12 Failure aspect of tube C3.

2 mm

1 mm

0 mm
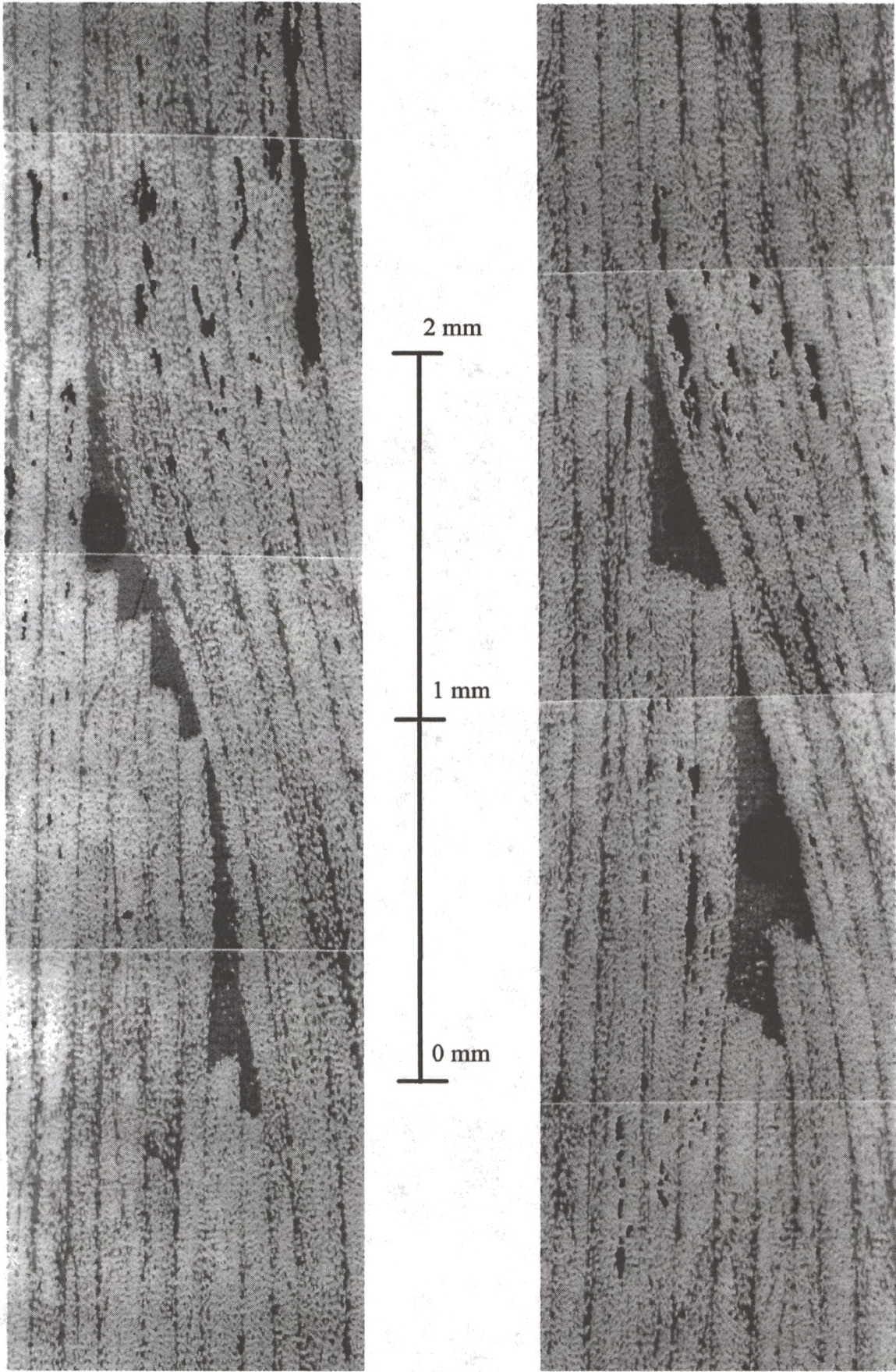
Neutral plane.

Position 11.

Figure 3.13 Micrographs of tube P1.

104

2 mm

1 mm

0 mm
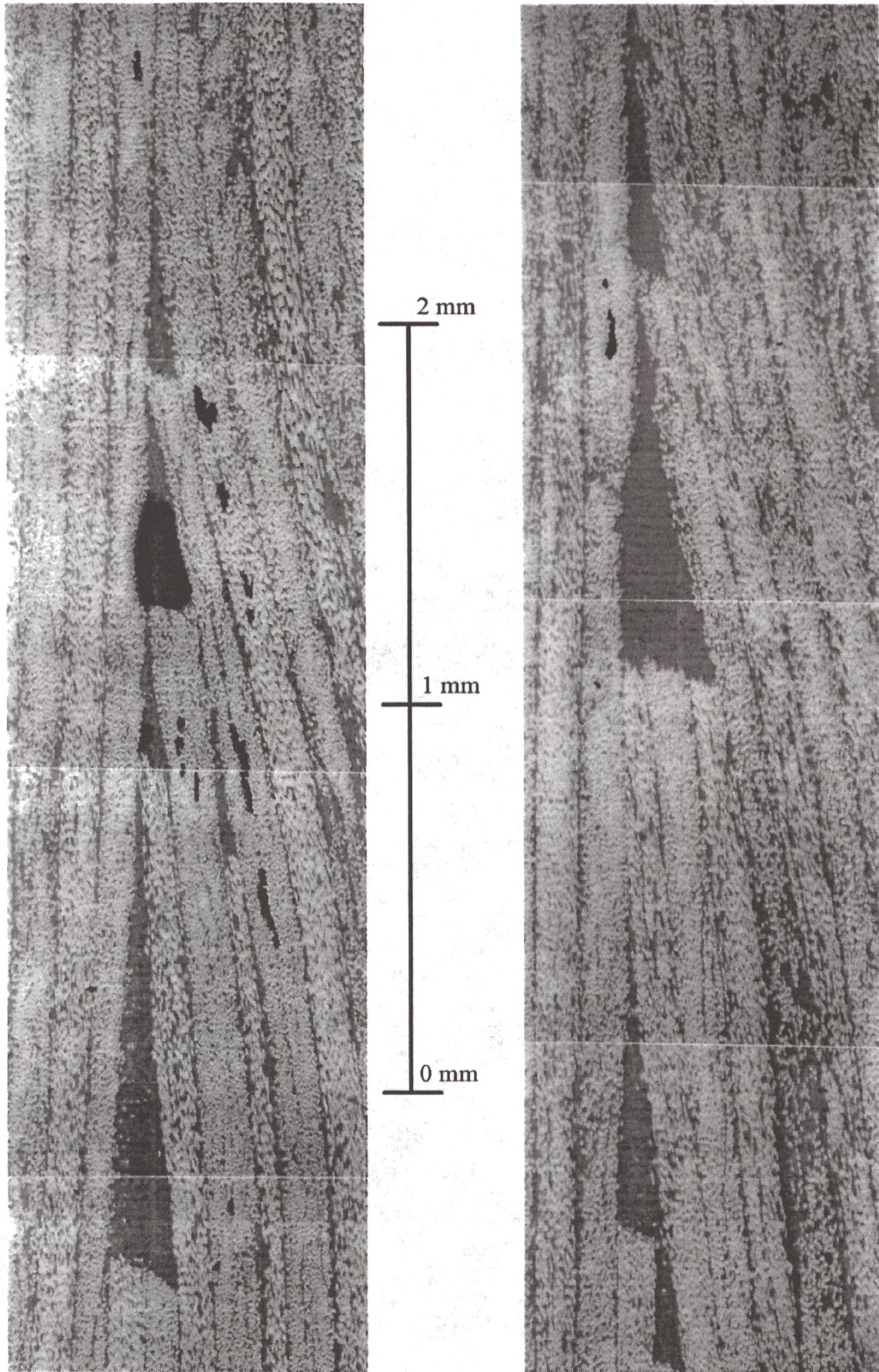
Neutral line.

Position 7.

Figure 3.14 Micrographs of tube C1.
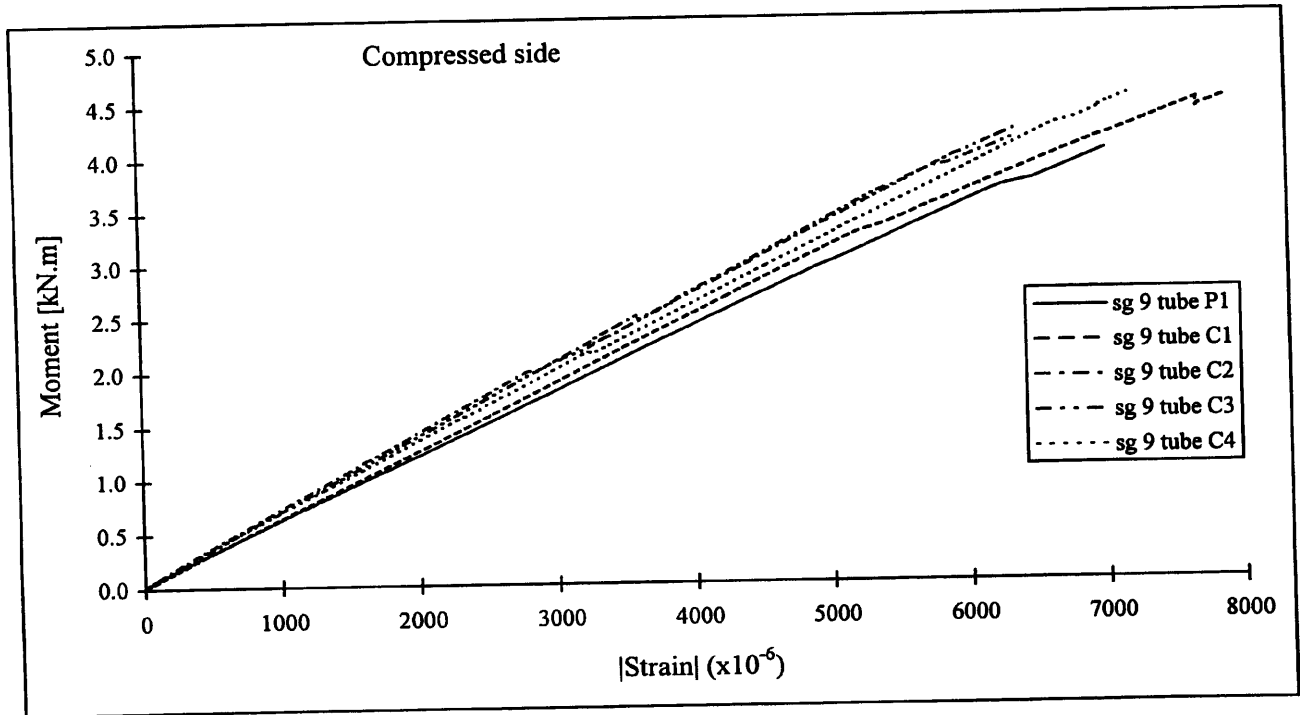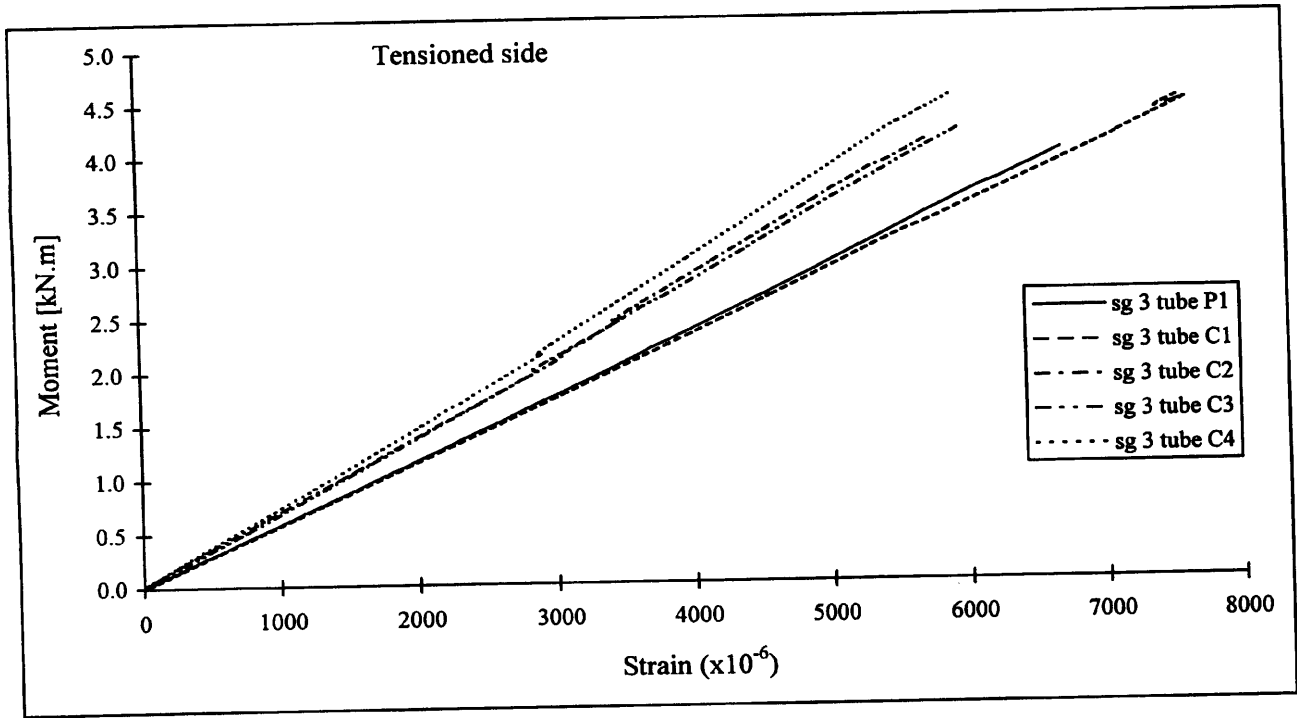
Figure 3.15 Strain measurements at the central section of the angle ply carbon/epoxy tubes..
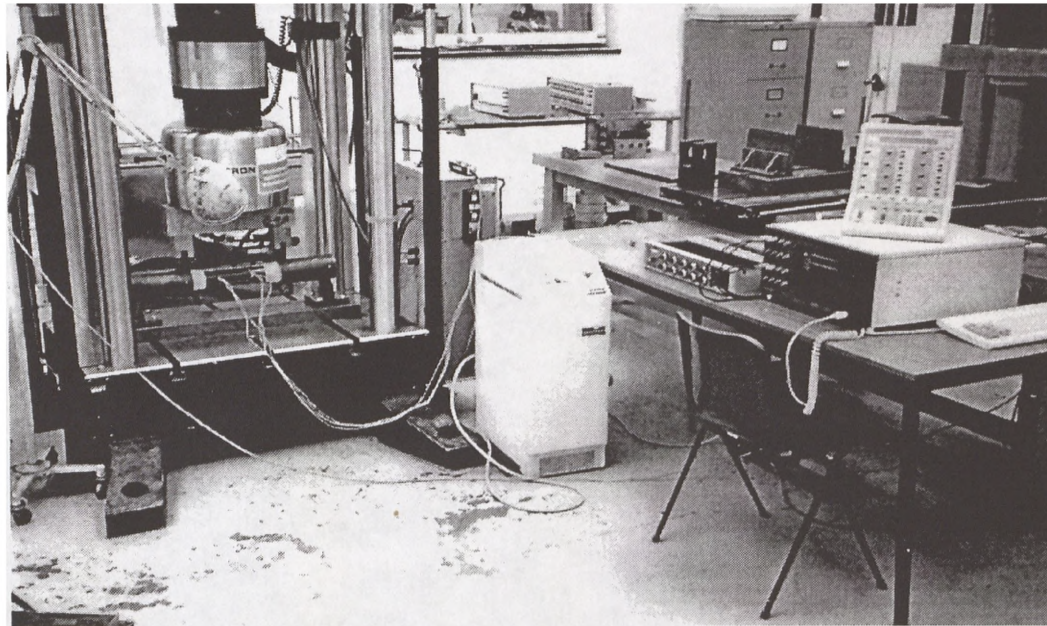
Figure 3.16 Experimental setup for the fatigue tests.
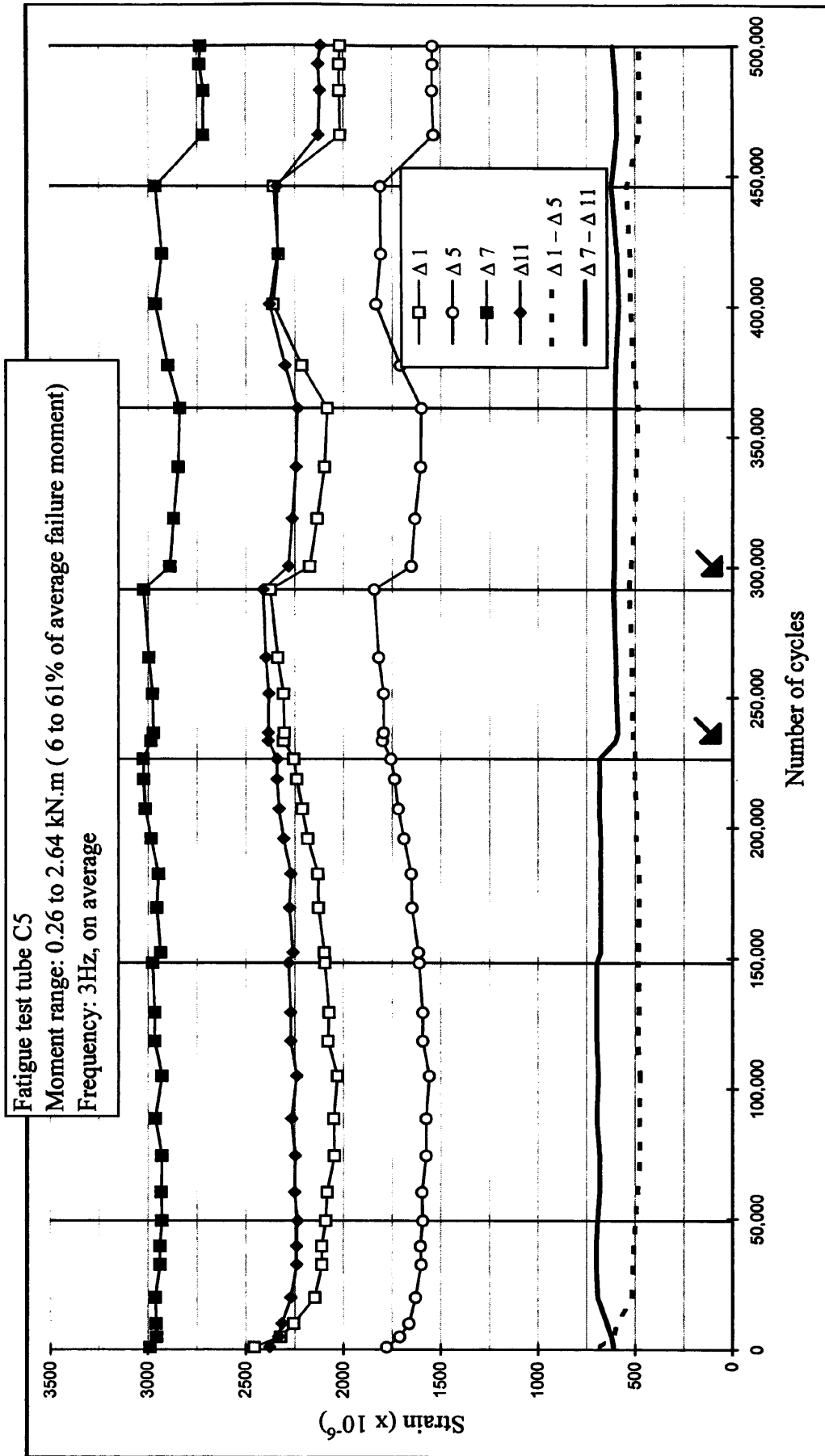
Figure 3.17 Fatigue test results for tube C5.
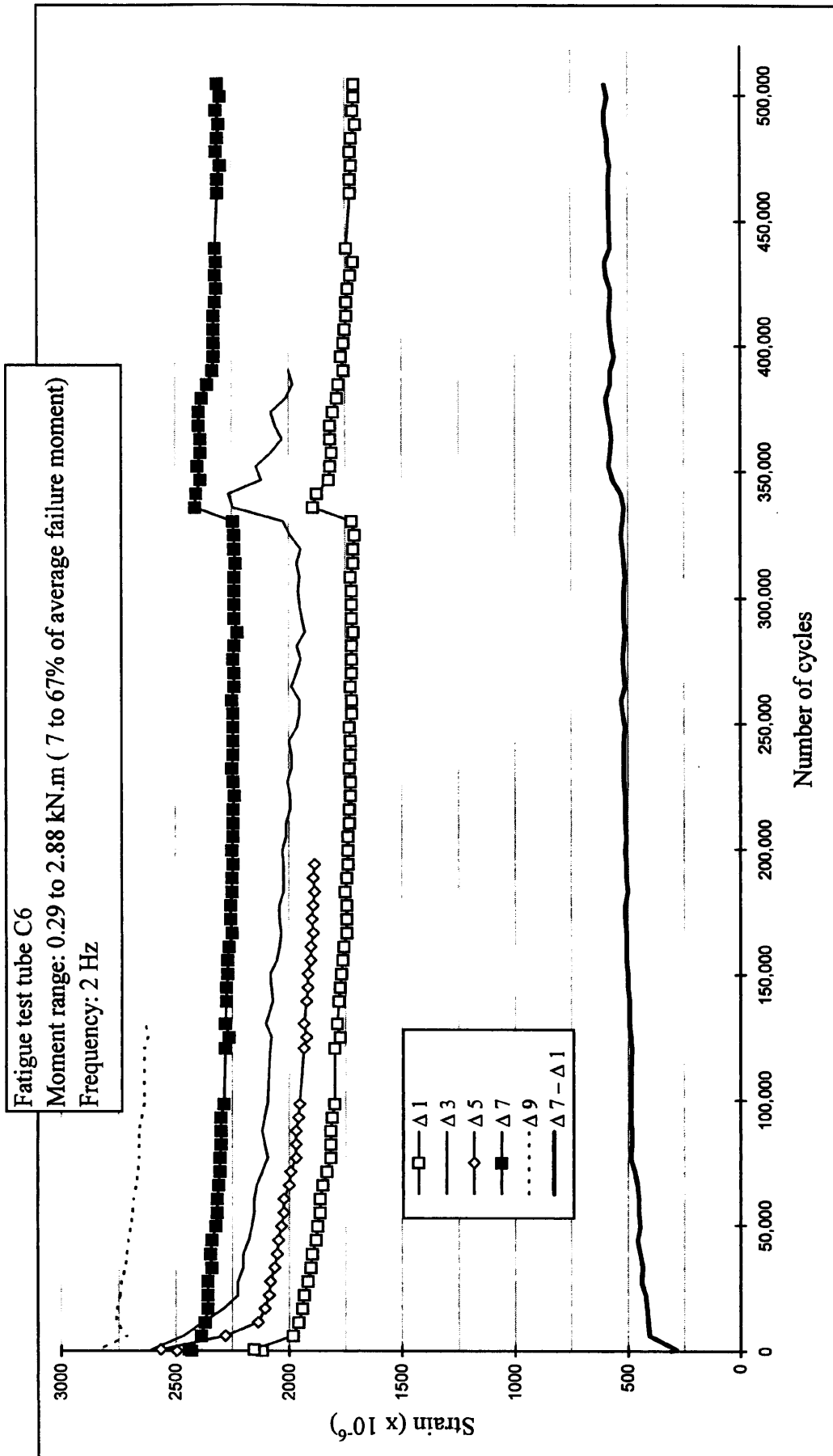
Figure 3.18 Fatigue test results for tube C6.

2 mm

1 mm

0 mm
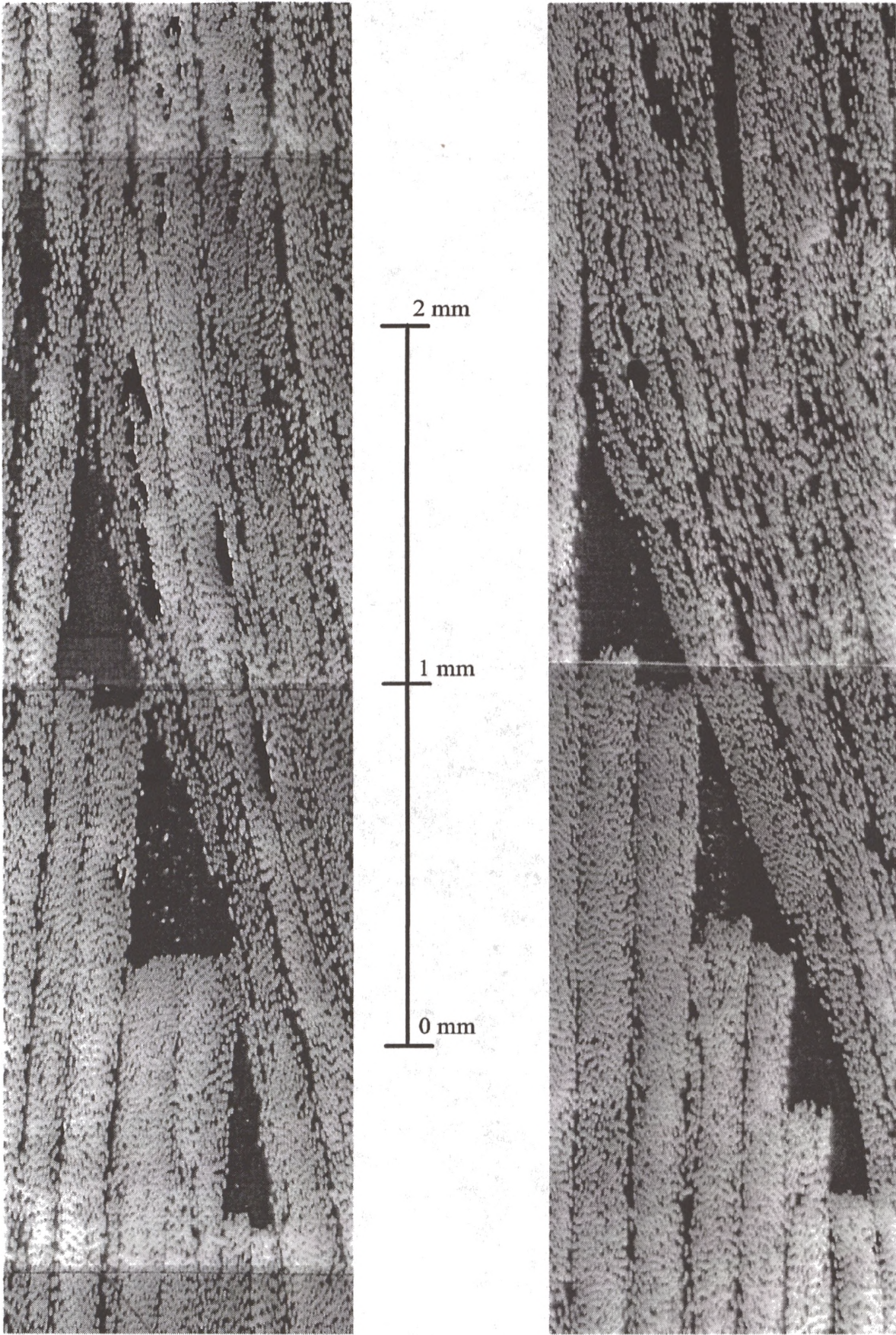
Position 5.

Position 11.

Figure 3.19 Micrographs of tube C5.

2 mm

1 mm

0 mm
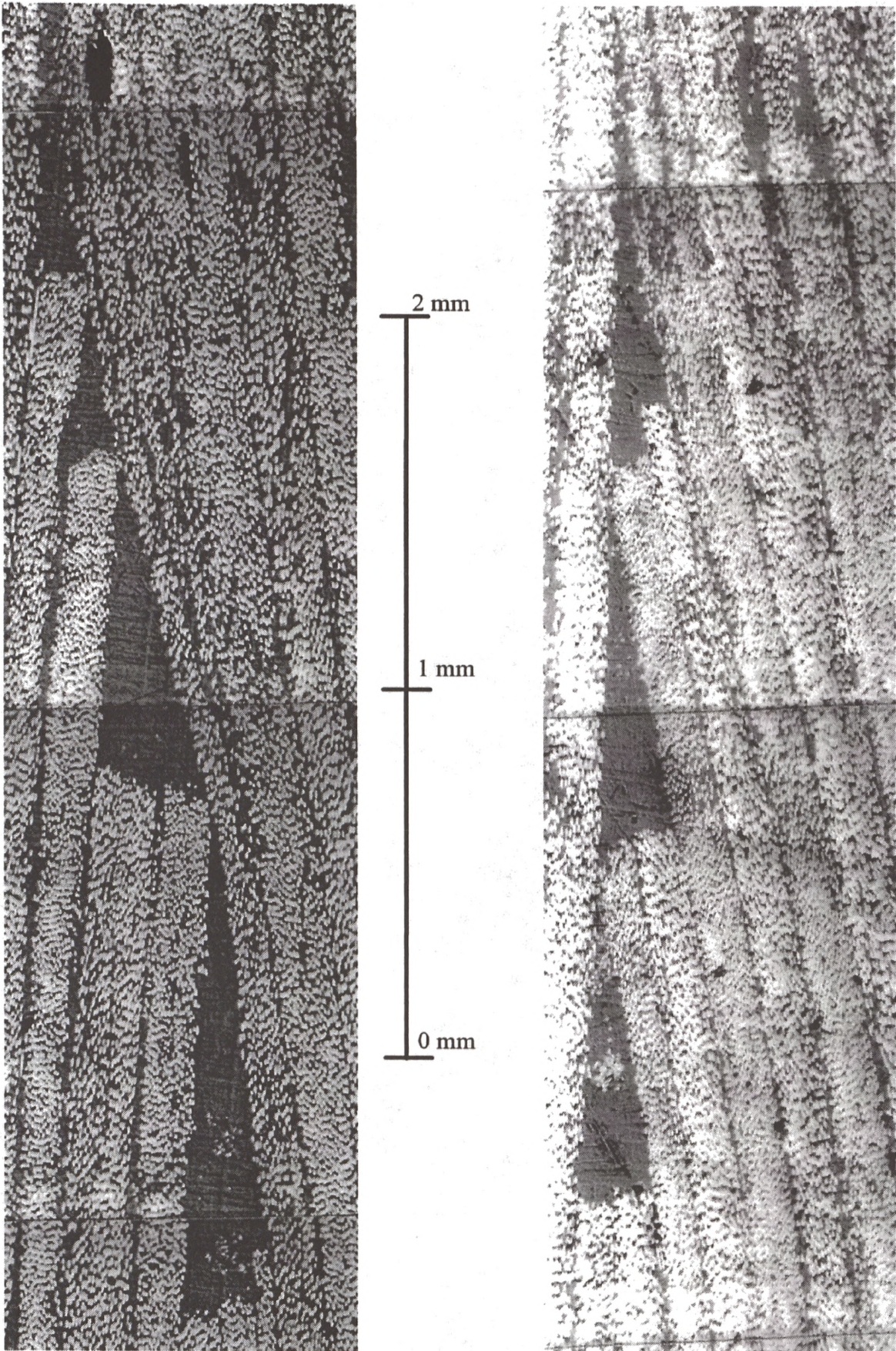
Position 1.

Position 11.

Figure 3.20 Micrographs of tube C6.

111
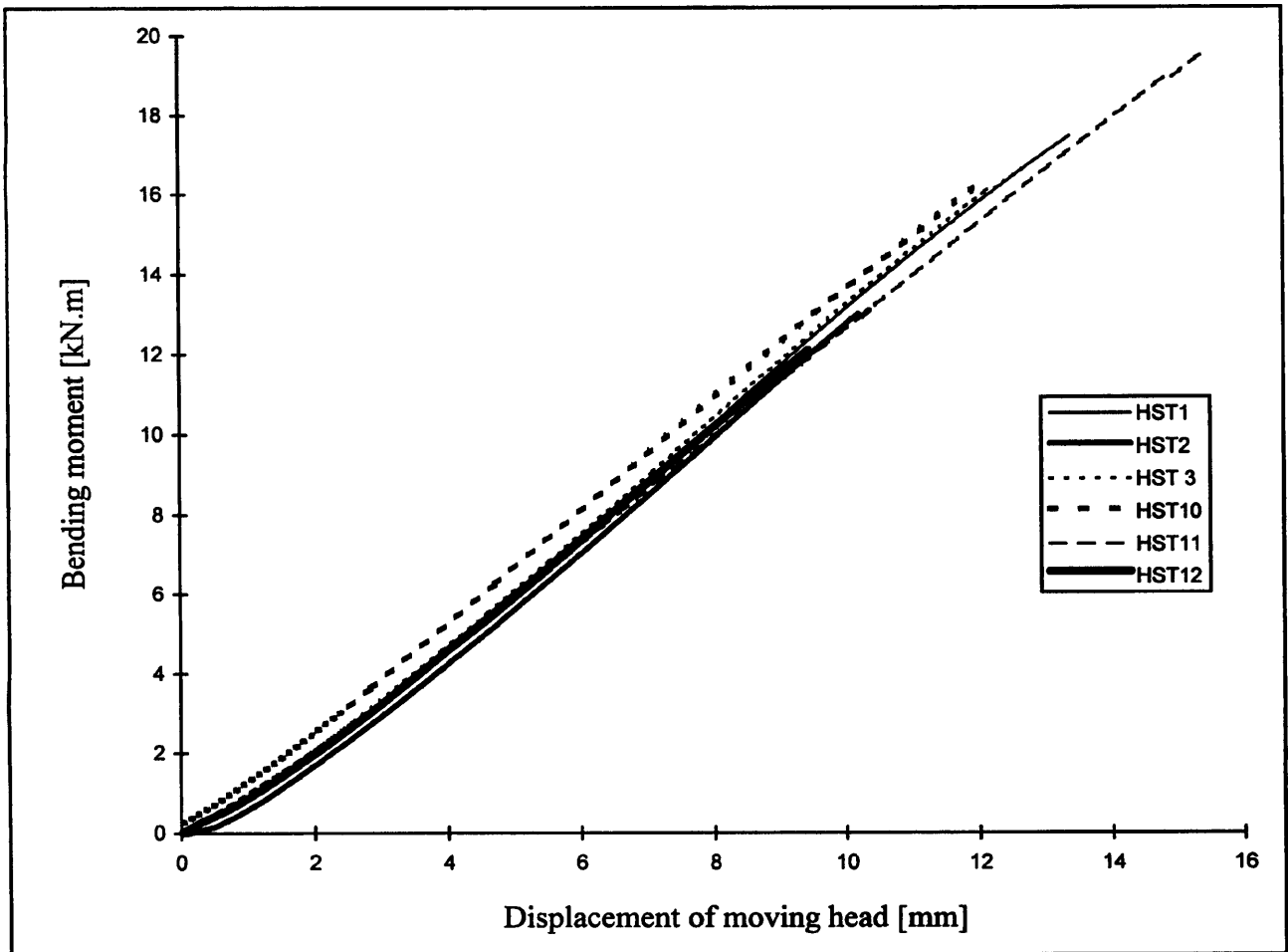
Figure 3.21 Four point bending test results for the hybrid, stepped, +/- 20° angle-ply tubes.
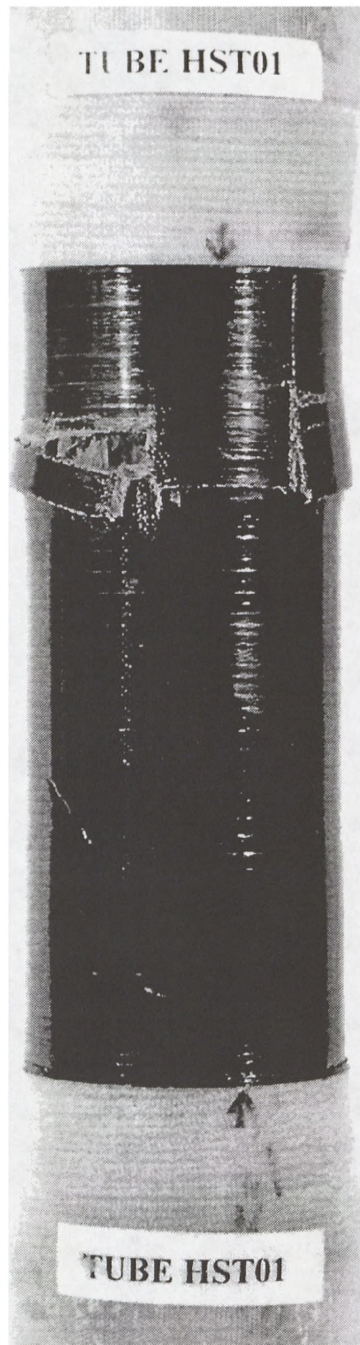
Figure 3.22 Tube HST01 after failure.
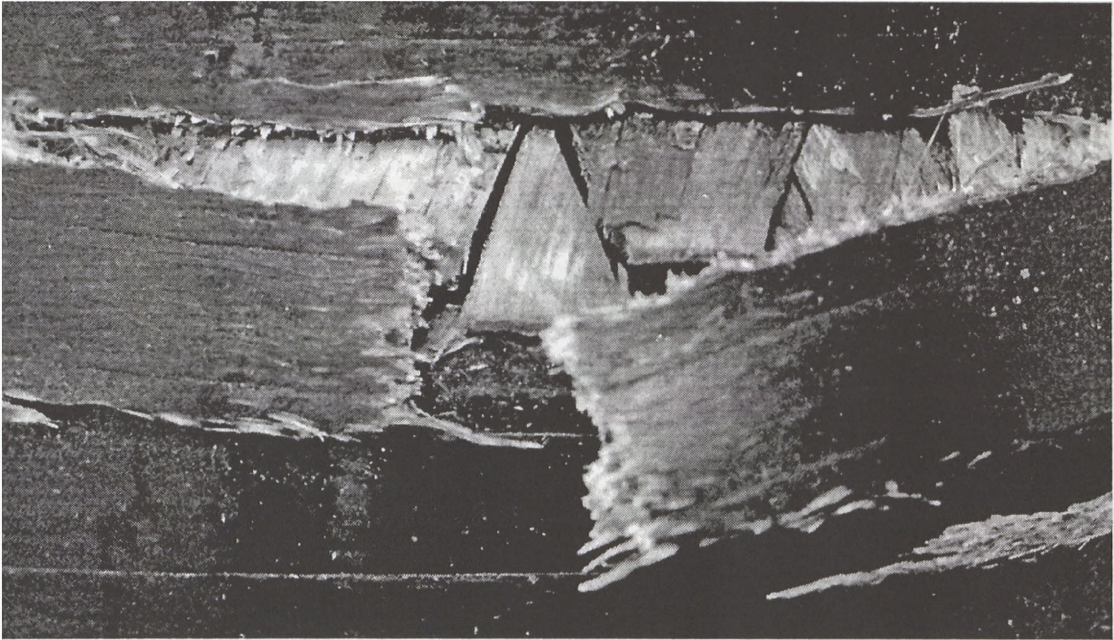
Figure 3.23 Close-up of a failure location.
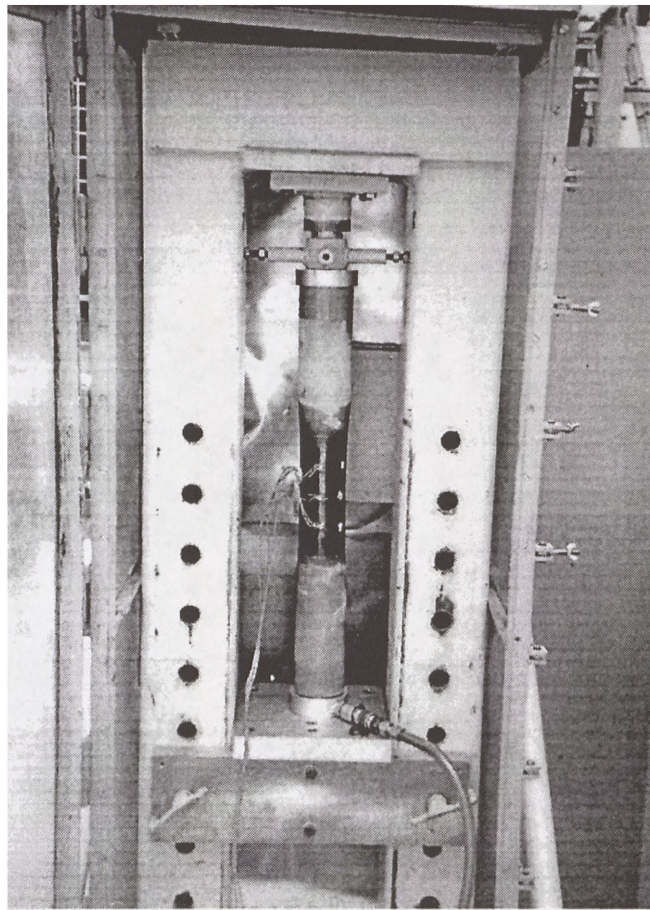
Figure 3.24 Internal pressure test rig.

15

r 3

U ring

100

1/4" NPT

15

30

30

80

30

20

r 30

30

50

Aluminium plug	
Design: Luiz Meniconi	
Scale: 1/1	16/02/98
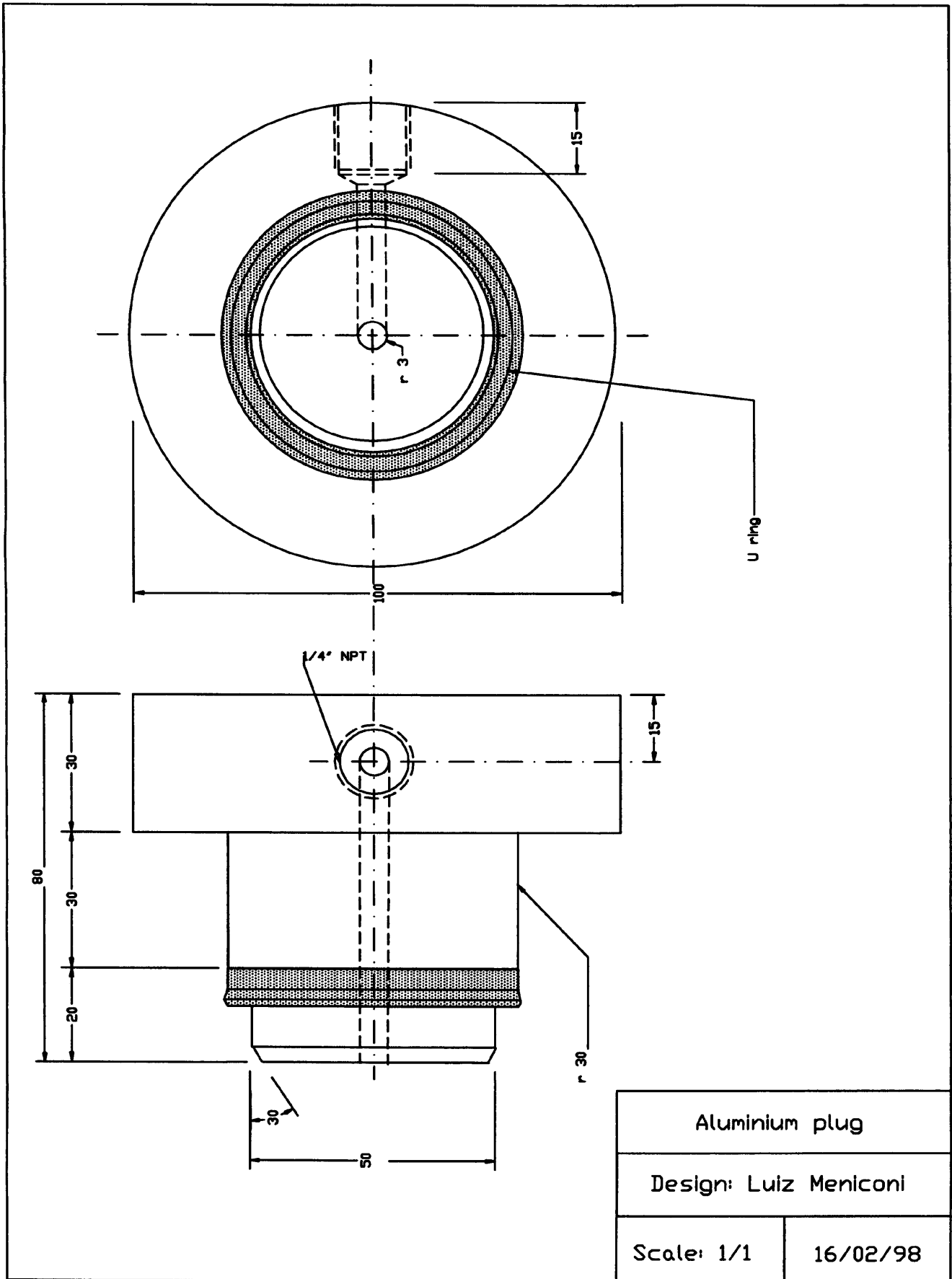
Figure 3.25   Aluminium plugs for sealing.

116
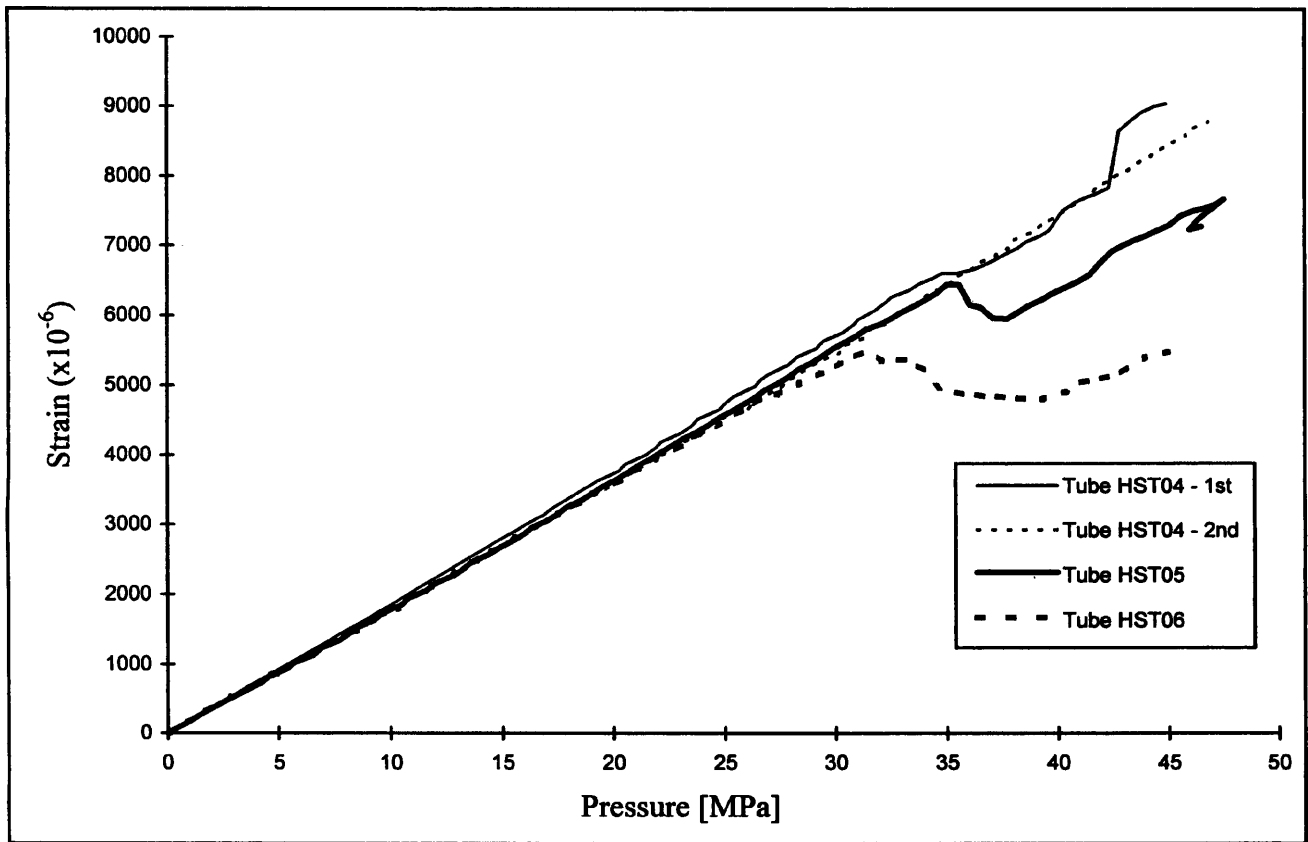
Figue 3.26 Internal pressure test: hybrid, stepped, +/- 20° angle-ply tubes.

117
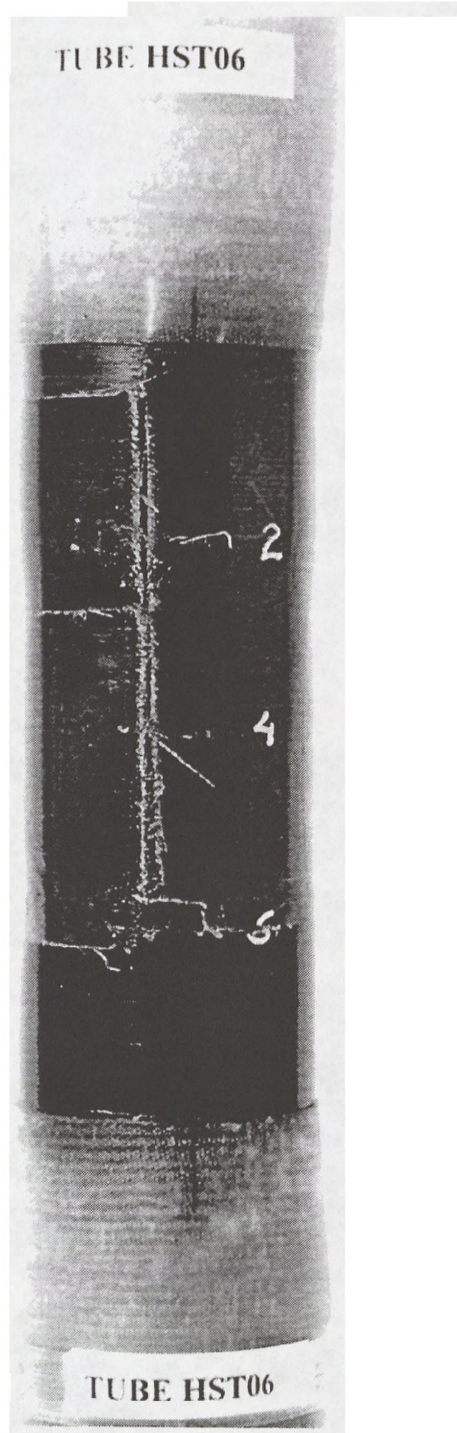
Figure 3.27 Tube HST06 at failure.
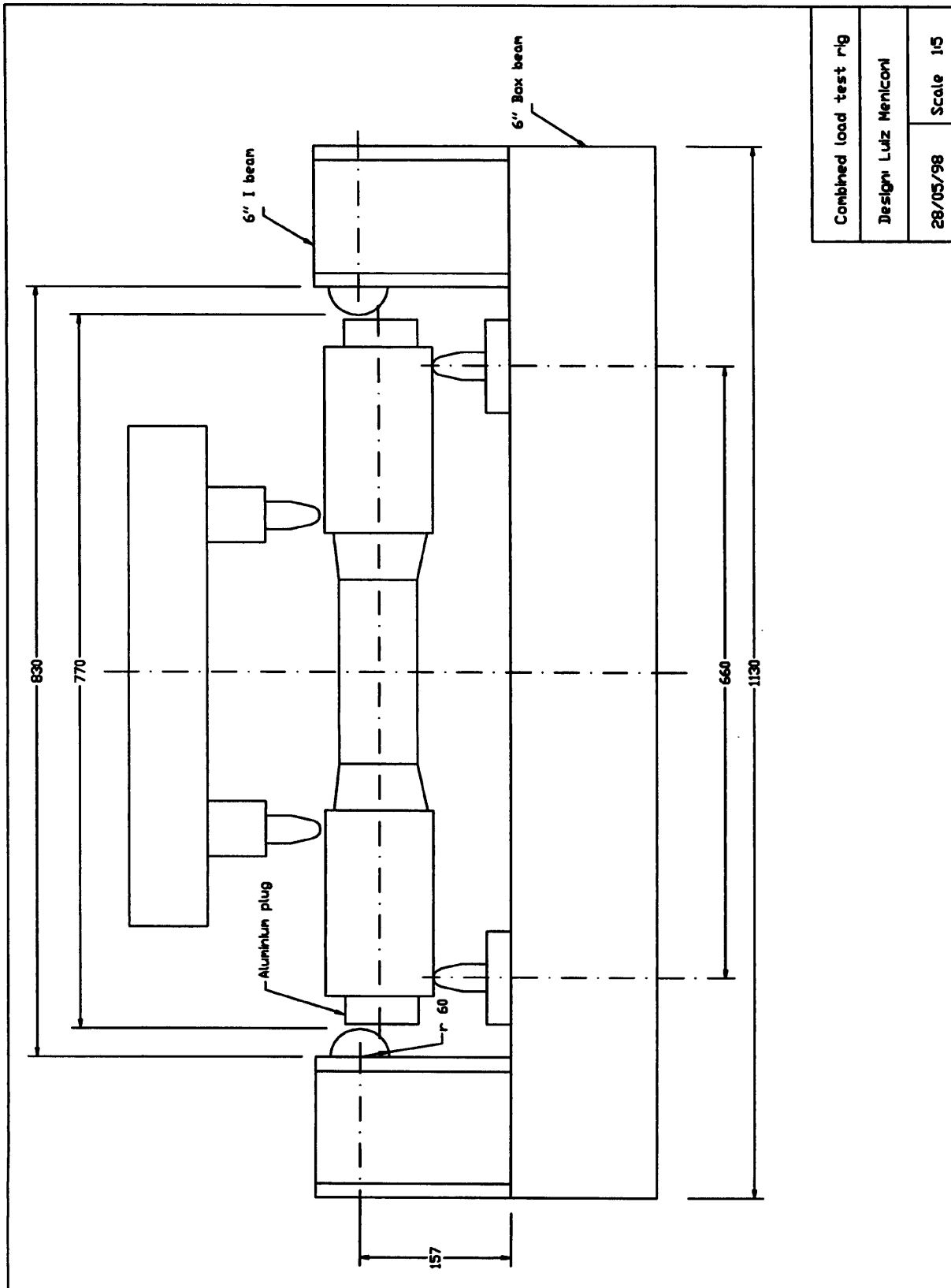
Figure 3.28   Reaction frame for the combined test.
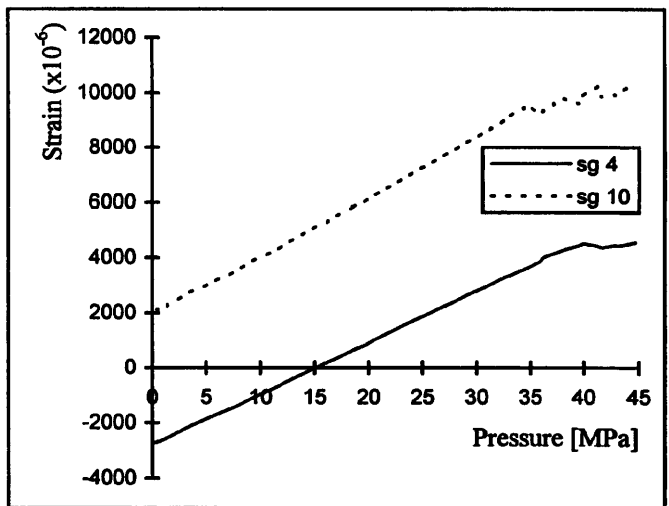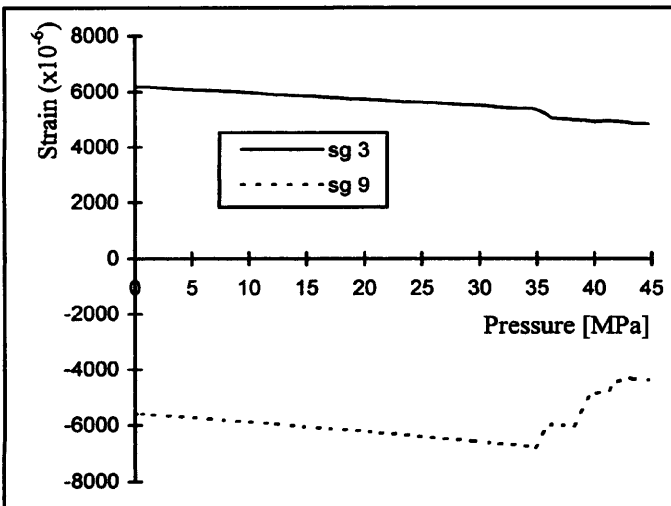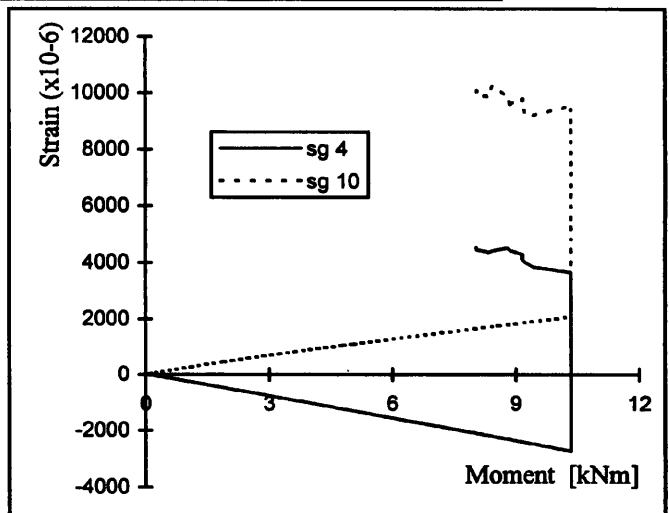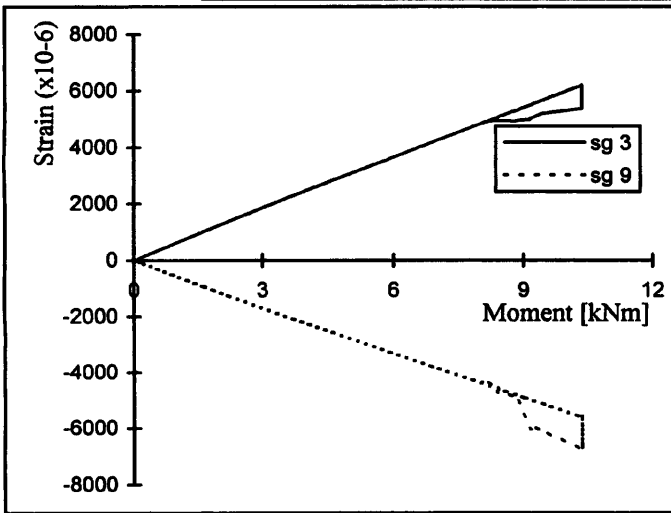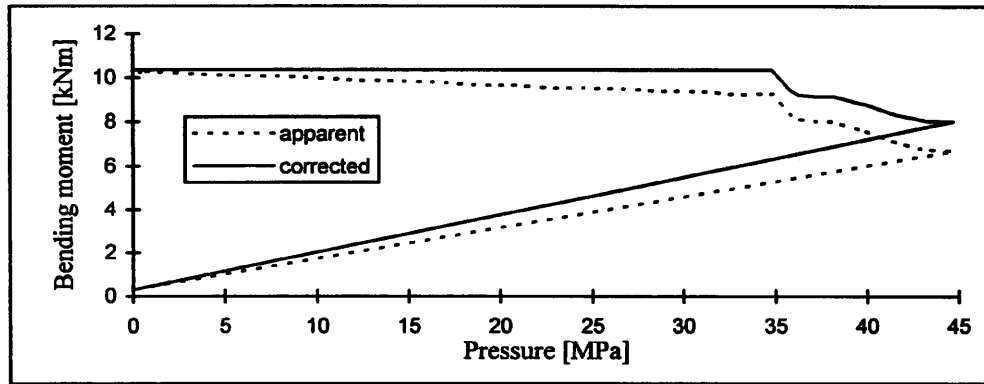
Figure 3.29 Combined test results for tube HST07.
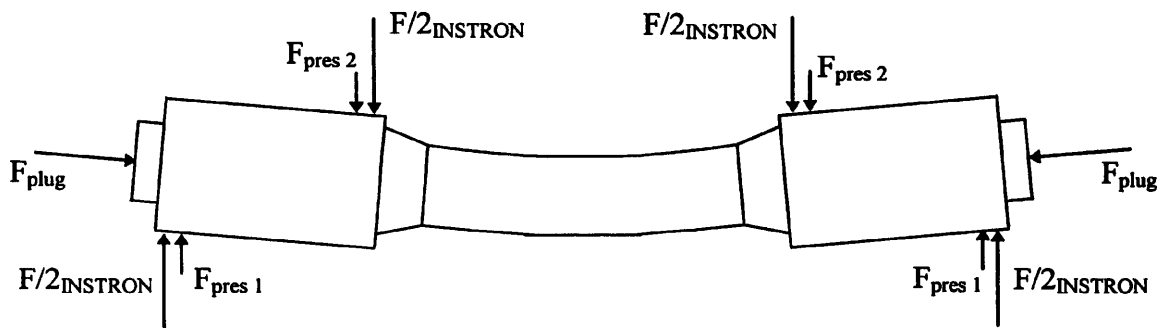
Figure 3.30 Equilibrium diagram for the tube plus aluminium plugs, combined test.
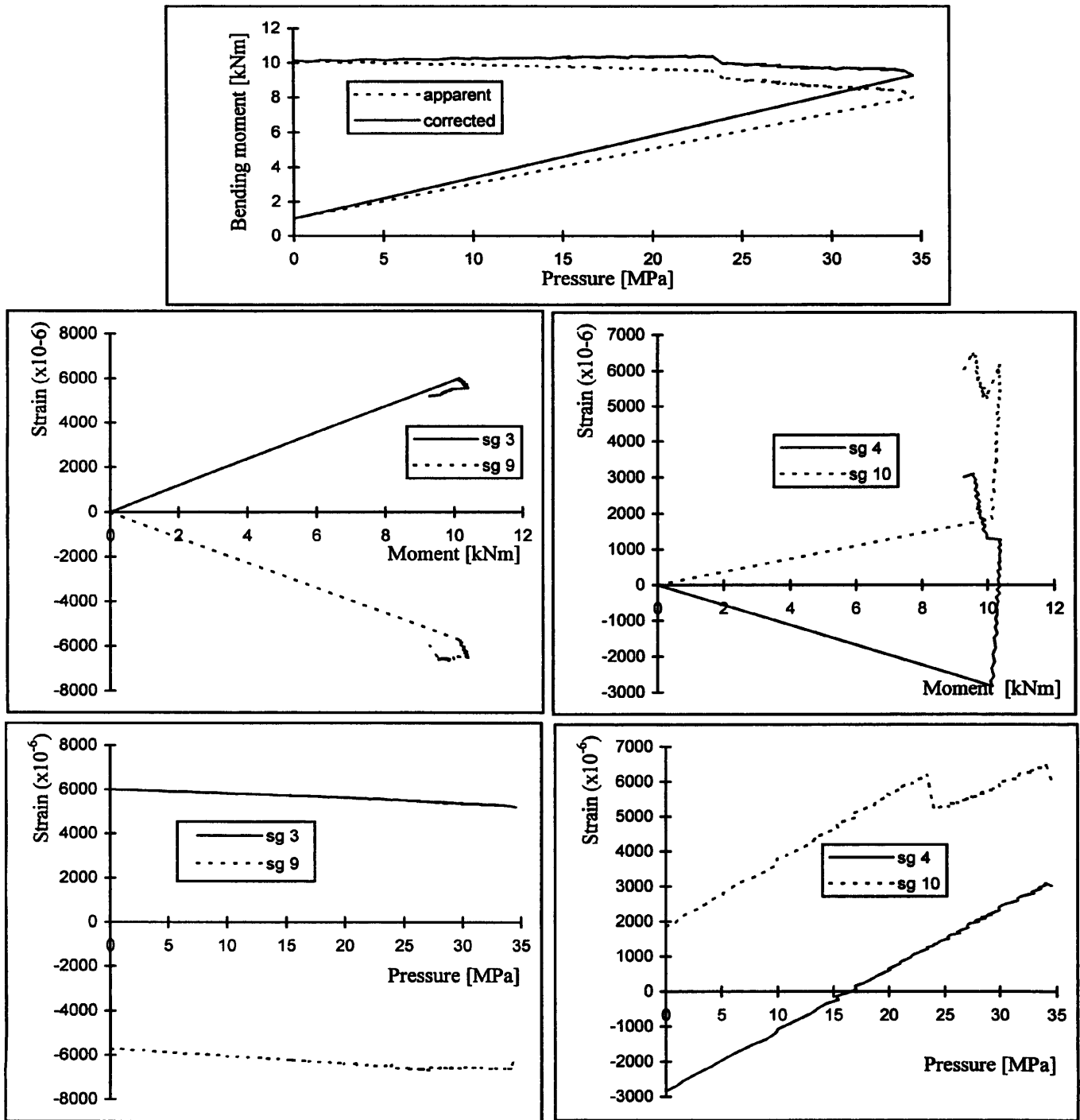
Figure 3.31 Combined test results for tube HST08.
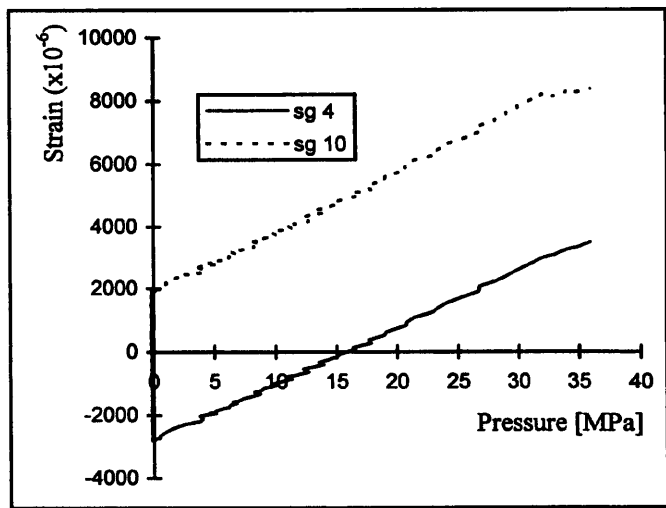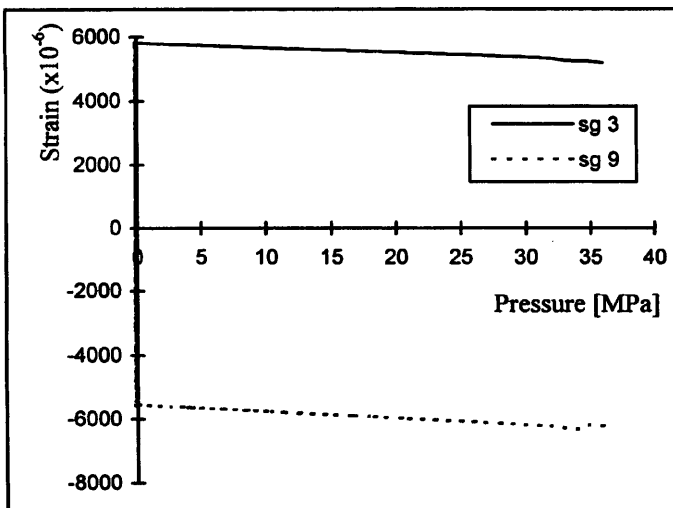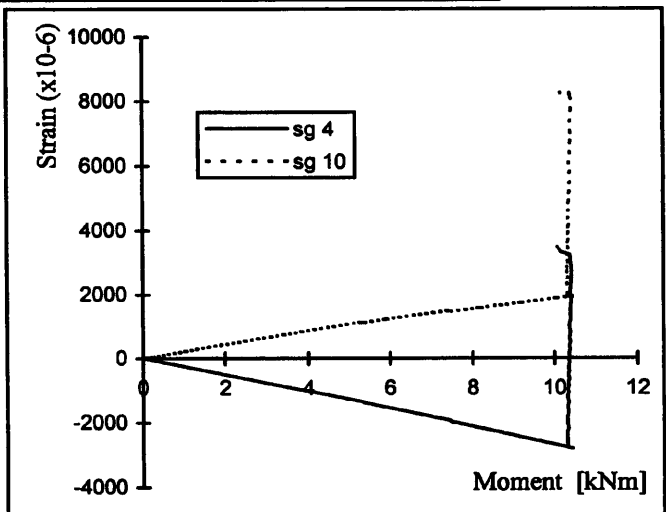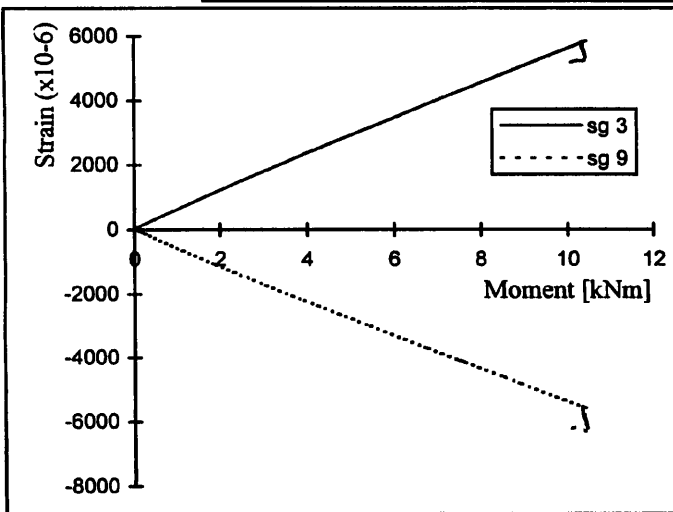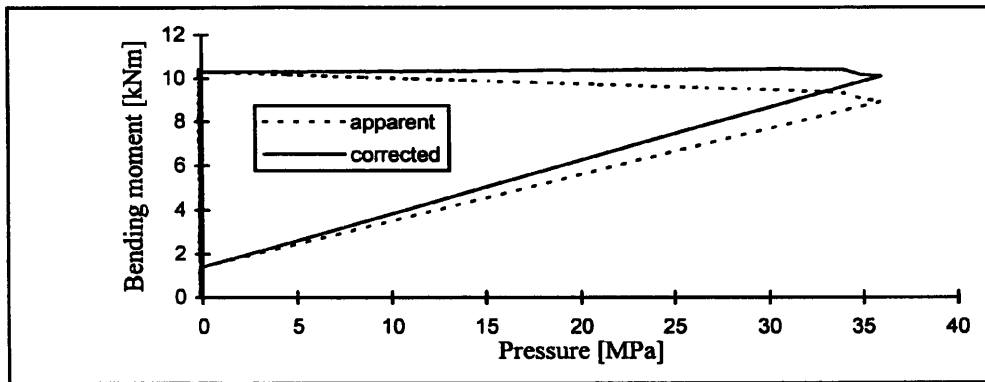
Figure 3.32 Combined test results for tube HST09.
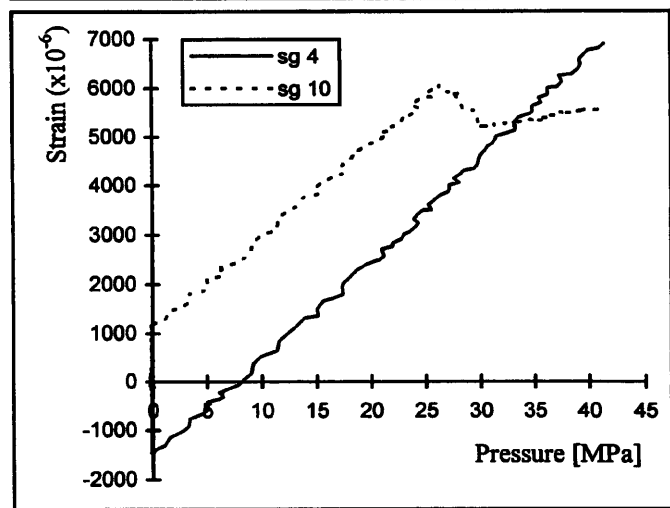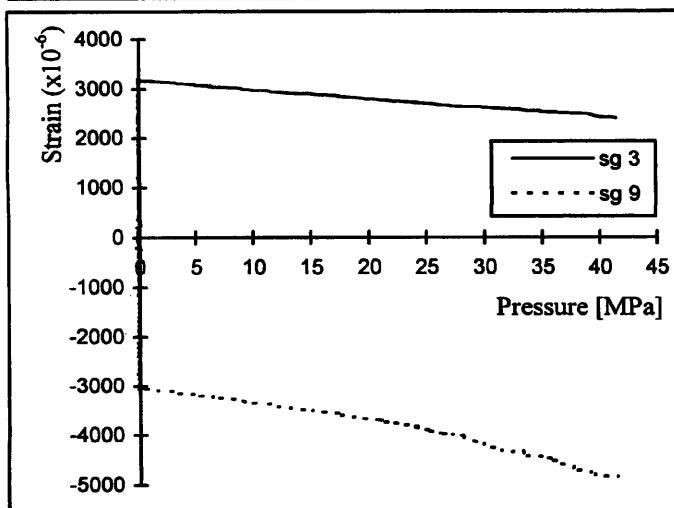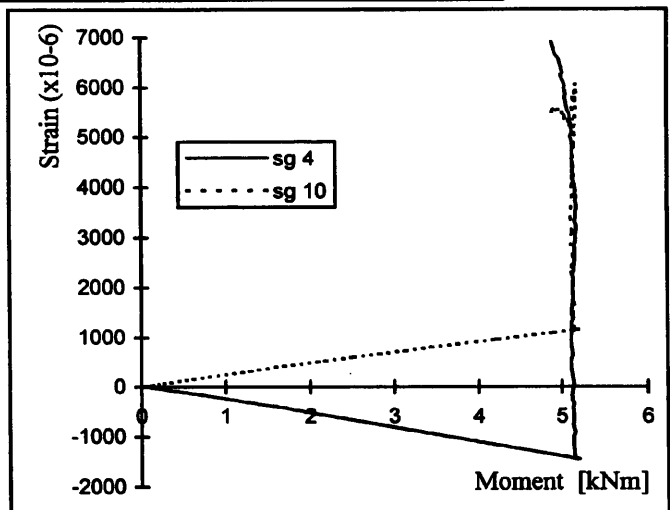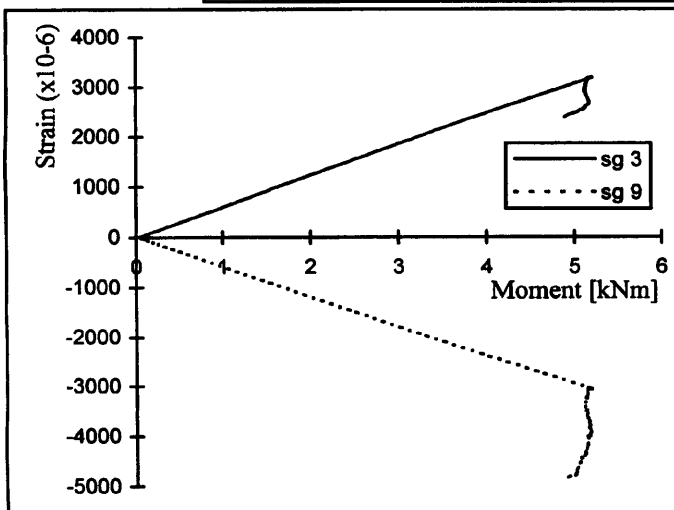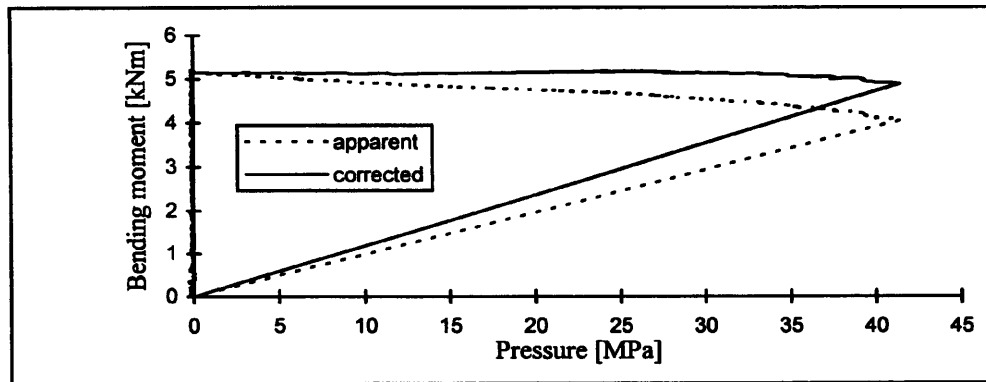
Figure 3.33 Combined test results for tube HST13.
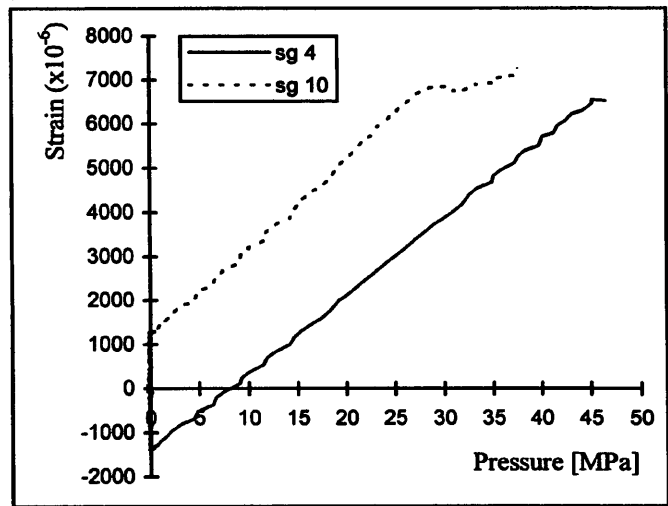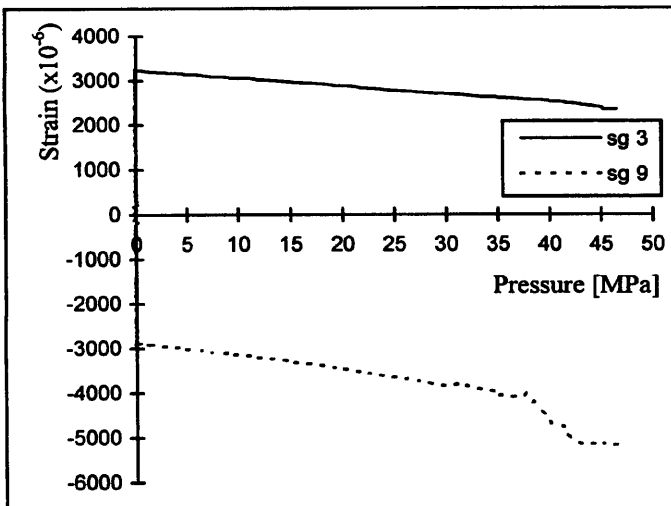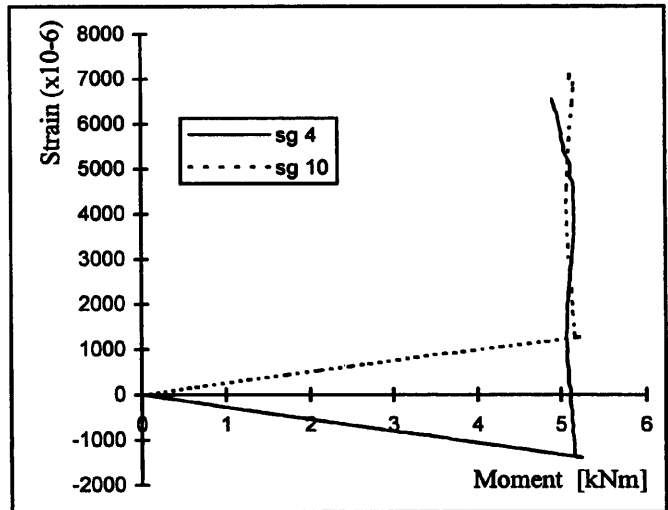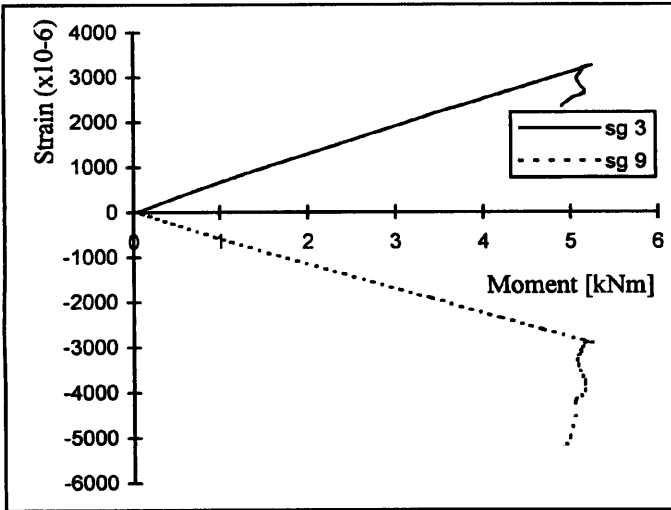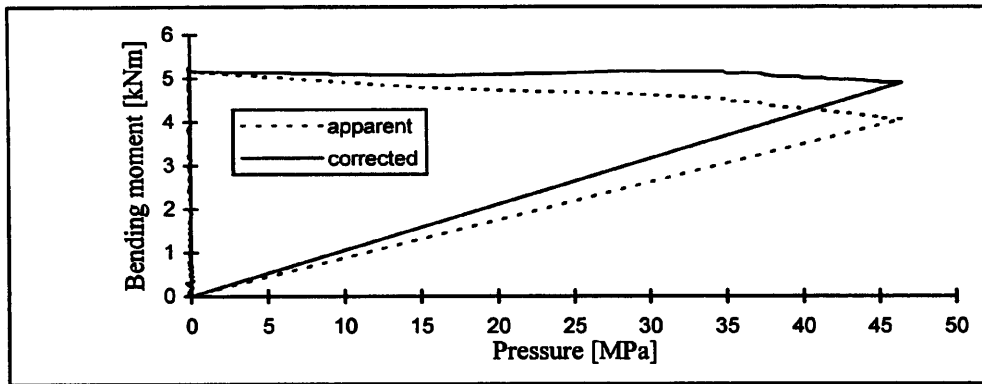
Figure 3.34 Combined test results for tube HST14.
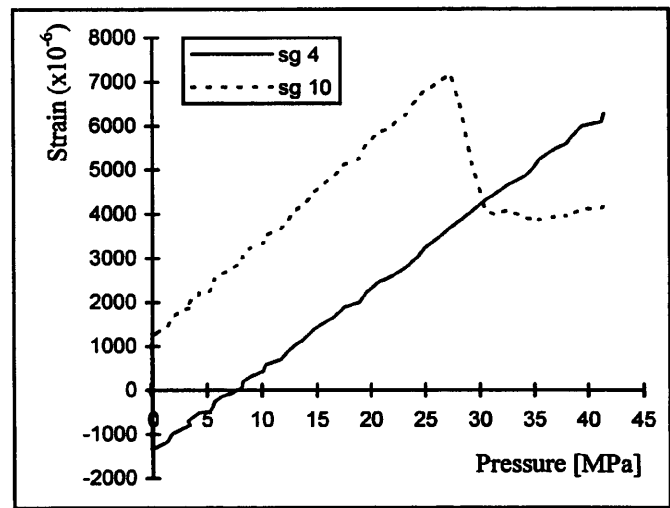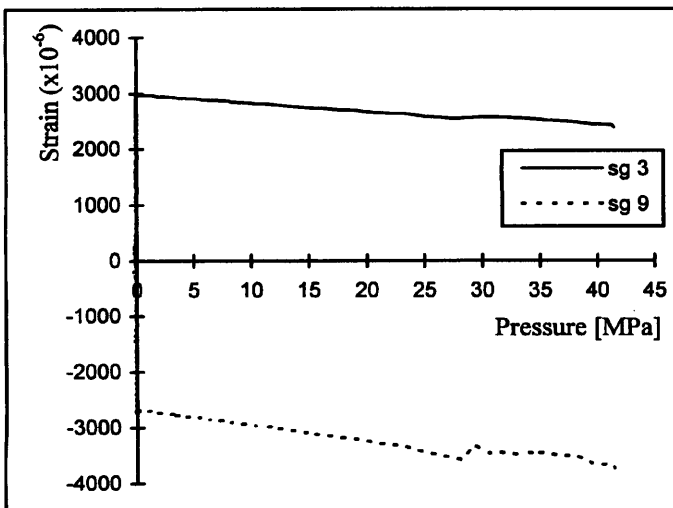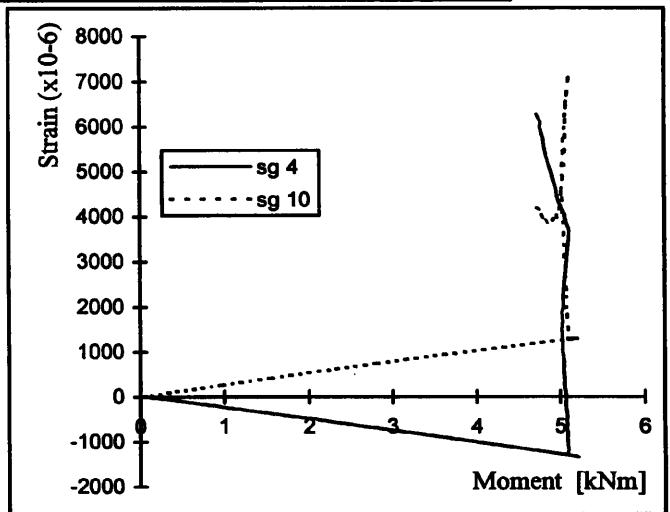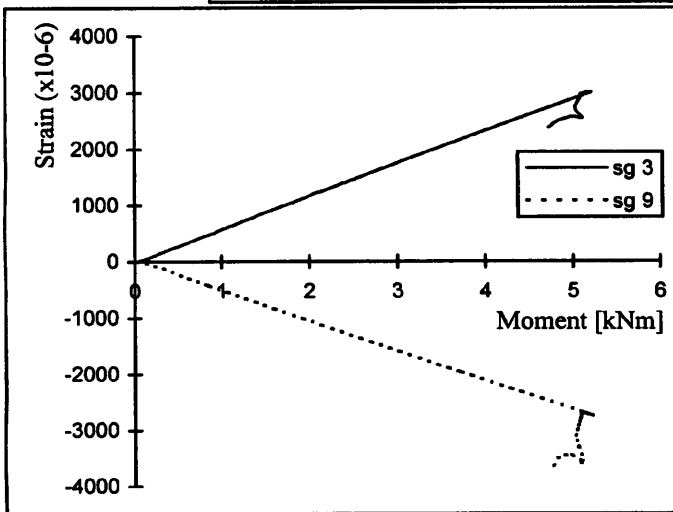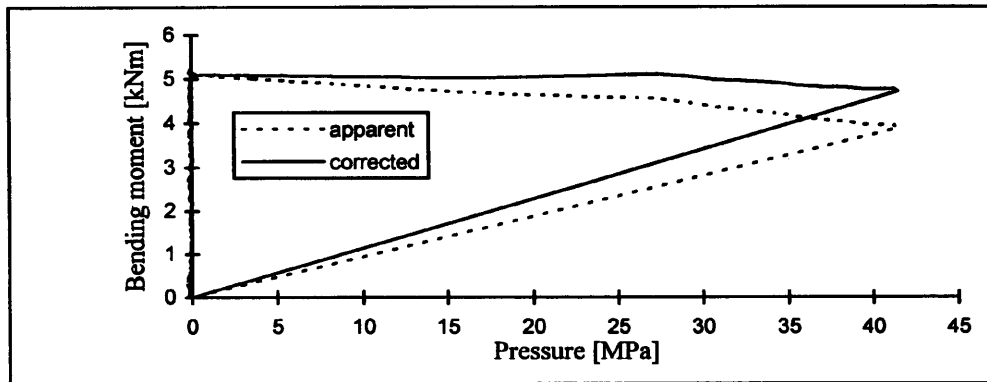
Figure 3.35 Combined test results for tube HST15.
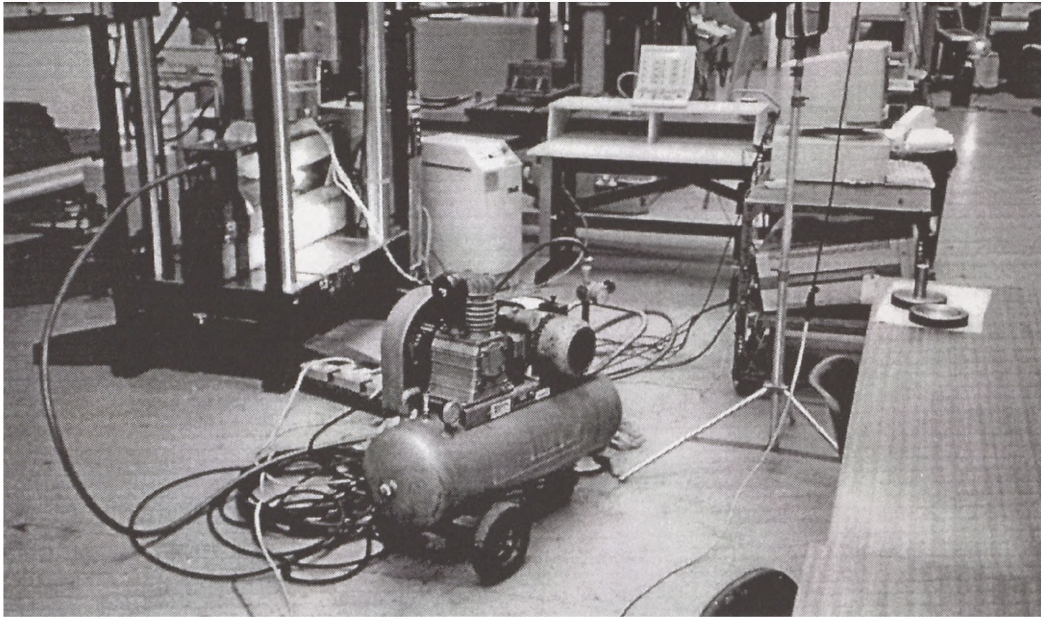
Figure 3.36 Experimental set-up for the combined tests.
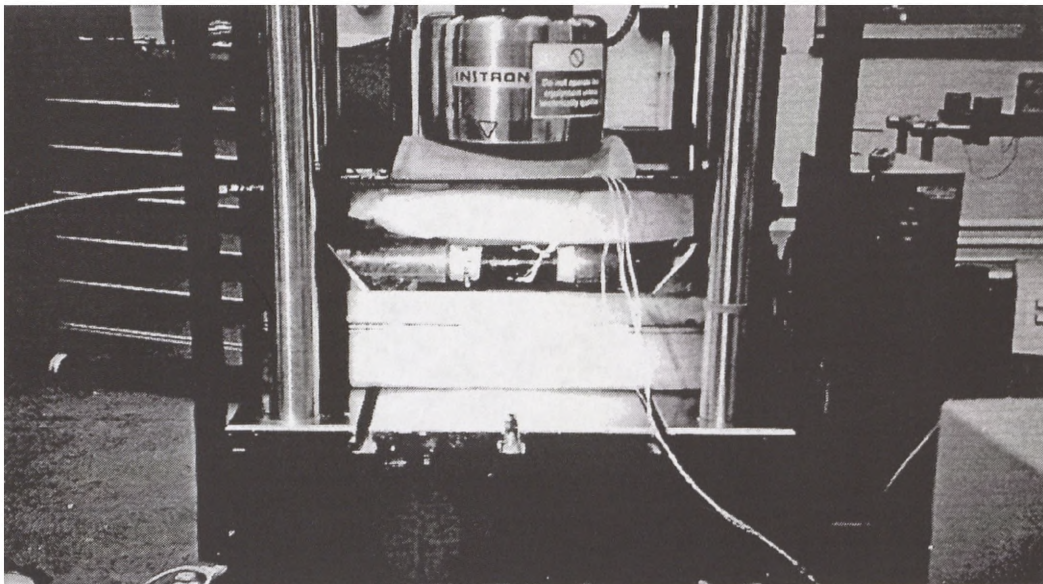
Figure 3.37 Test base, isolated by polycarbonate plates.

127
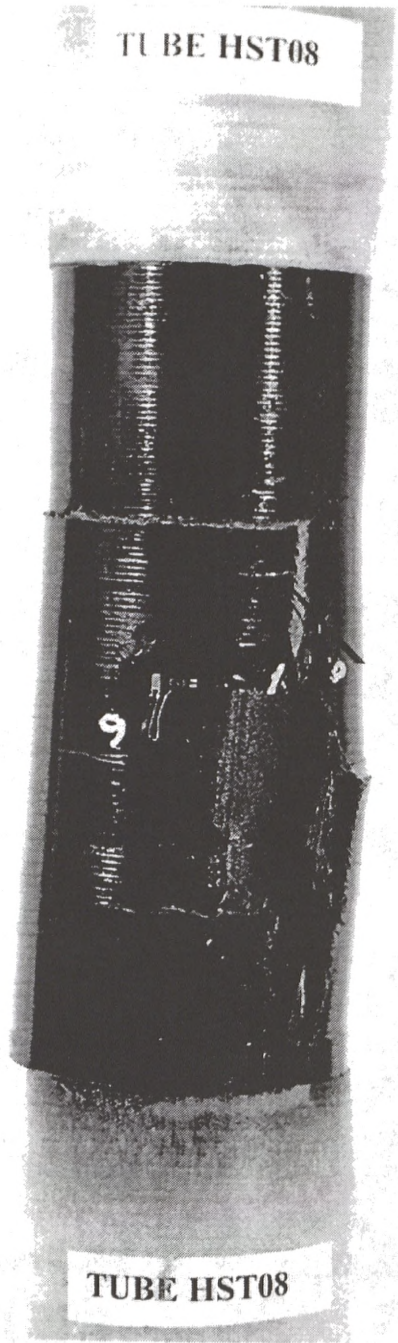
Figure 3.38 Failure aspect of tube HST08.
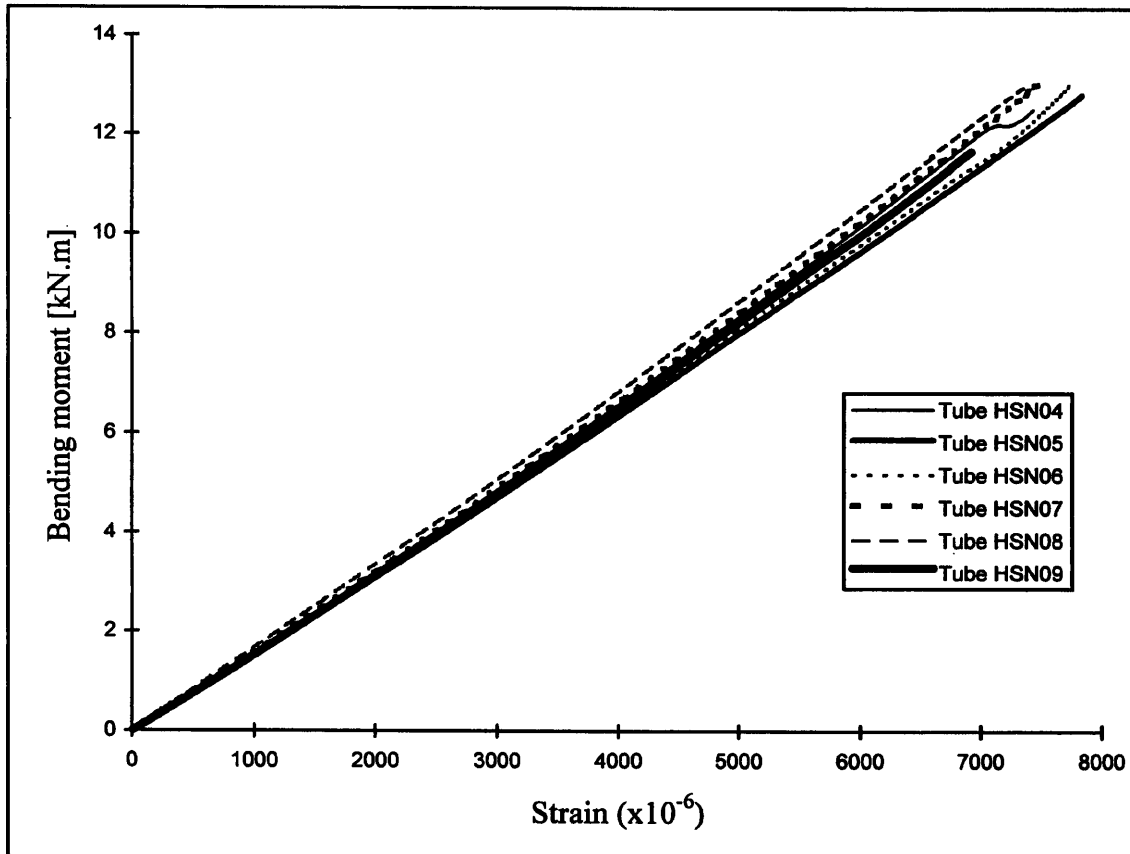
Figure 3.39 Four point bending test results: hybrid, stepped, unidirectional tubes.
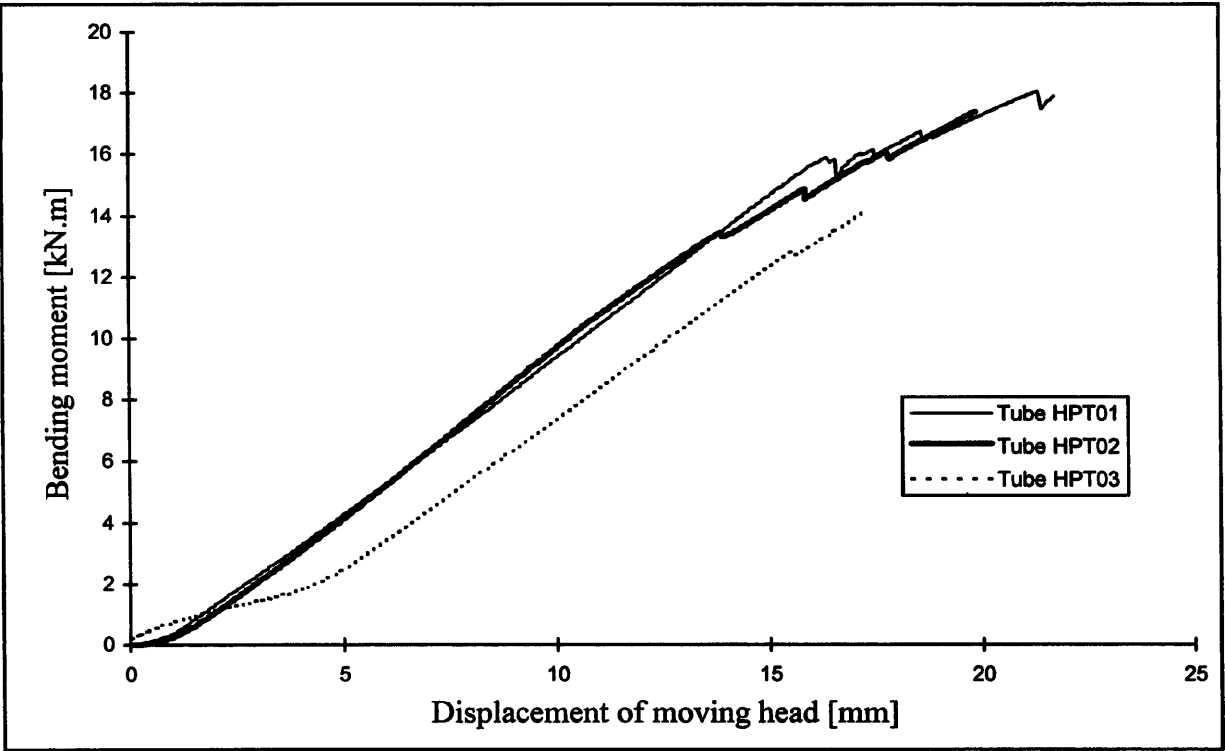
Figure 3.40 Four point bending test: hybrid, plain, +/-20° angle-ply tubes.
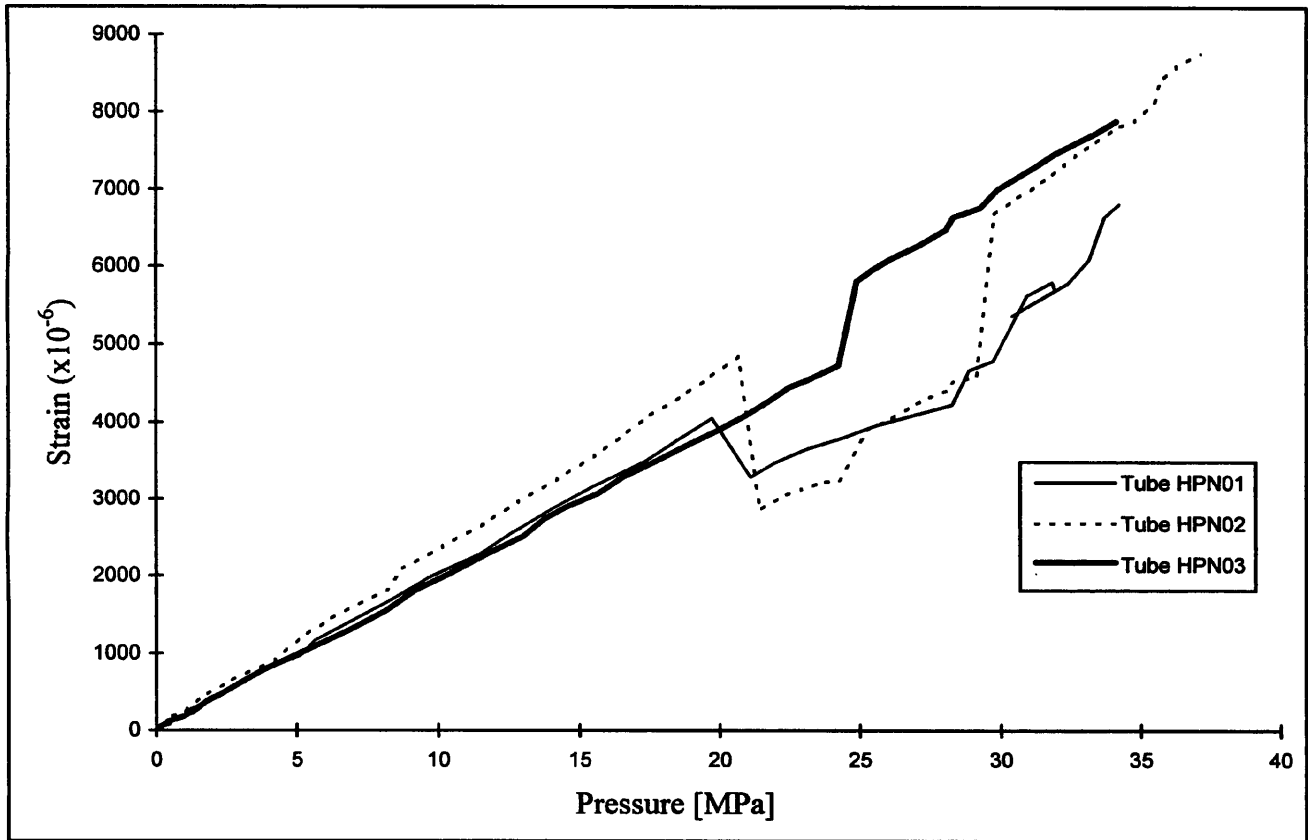
Figue 3.41 Internal pressure test: hybrid, plain, unidirectional carbon tubes.

CHAPTER 4 FINITE ELEMENT MODELS

CHAPTER 4 FINITE ELEMENTS MODELS

4.1 INTRODUCTION

The purpose of this chapter is to describe the results obtained from Finite Element Analysis (FEA) models of the tapered composite tubes. A first objective of these models was the determination of the stresses and SERRs associated to the experimental results reported in Chapter 3. Secondly, the models provide results with which those using thick tube models dealt with in the next chapter will be compared to.

A preliminary task was to calibrate of the FEA parameters (element type and mesh size) to reproduce with sufficient accuracy an exact solution available in the literature for thick composite tubes. Following this, the "smearing" approach was checked. This considers the assembly of several alternate angle-ply laminae to correspond to an equivalent specially orthotropic material. Then the possibility of using axisymmetric models was addressed. The objective was to define the simplest model that could still reproduce all the relevant characteristics of a thick composite tapered tube.

After the FEA parameters were settled, the all-carbon/epoxy stepped tube specimen was analysed. The influence of the thickness transition region geometry on the local stress field was investigated. Following this, a SERR analysis was performed, in order to understand better the behaviour observed during the tests.

The chapter ends with the analysis of hybrid composite tubes, addressing the load cases executed during the experimental investigation. The analysis surveyed the stresses for each experimental load case in Chapter 3 in order to define the strength values for the tubes. This information will be employed in the analysis of a composite riser that is performed in Chapter 6.

4.2 CALIBRATION OF FEA PARAMETERS

4.2.1 COMPARISON WITH EXACT RESULTS

An exact 3D solution was taken from Varadan and Bhaskar [64] for calibration purposes. They studied several configurations of layered tubes. We selected a case very similar to the composite riser construction. This was a $(90°/0°/90°)$ layered laminated tube. Each layer had the same thickness in their case. The loading was an internal pressure q_i of the form:

$$q_i = - Q_0 \, sin\left(\frac{m\pi z}{L}\right)cos(n\theta) \qquad (4.1)$$

where Q_0 is a constant positive pressure (resulting in a negative radial stress), z is the axial co-ordinate, L is the length of the tube and θ is the angular co-ordinate. The integers m and n were equal to 1 and 4, respectively. All the layers were made of the same material and the lamina properties were:

$$\frac{E_L}{E_T} = 25, \qquad \frac{G_{LT}}{E_T} = 0.5, \qquad \frac{G_{TT}}{E_T} = 0.2 \quad and \quad \nu_{LT} = \nu_{TT} = 0.25$$

where the subscript L refers to the longitudinal direction and the subscript T refers to the transverse direction. E are the Young's moduli, G are the shear moduli and ν are the Poisson's ratios. The results were given in terms of the following non-dimensional stresses:

$$\overline{\sigma}_r = \sigma_r \Bigg/ \left(Q_o \, sin\left(\frac{m\pi z}{L}\right)cos(n\theta) \right)$$

$$(\overline{\sigma}_\theta, \overline{\sigma}_z) = \left(\frac{10}{Q_0 S^2}\right)(\sigma_\theta, \sigma_z) \Bigg/ \left(sin\left(\frac{m\pi z}{L}\right)cos(n\theta) \right)$$

$$\overline{\tau}_{r\theta} = \left(\frac{10}{Q_0 S}\right)\tau_{r\theta} \Bigg/ \left(sin\left(\frac{m\pi z}{L}\right)sin(n\theta) \right) \qquad (4.2)$$

$$\overline{\tau}_{rz} = \left(\frac{10}{Q_0 S}\right)\tau_{rz} \Bigg/ \left(cos\left(\frac{m\pi z}{L}\right)cos(n\theta) \right)$$

$$\overline{\tau}_{\theta z} = \left(\frac{10}{Q_0 S^2}\right)\tau_{\theta z} \Bigg/ \left(cos\left(\frac{m\pi z}{L}\right)sin(n\theta) \right)$$

where r defines the radial direction of the tube and S is the average radius to thickness ratio, which was taken equal to 4.

As the layers were made from specially orthotropic materials, and, given the pressure distribution defined by equation 4.1, only one eighth of the tube was modelled, due to the existing symmetry. 20-node brick elements were used for that purpose, with a very fine mesh. There were six elements across the thickness. The FEA code used was ABAQUS [99]. Figure 4.1 shows the mesh that resulted, together with the internal pressure distribution.

At first, a full integration brick element, with 27 Gaussian points was adopted. Later a more economical reduced integration scheme, with 8 Gaussian points was tried. The results are shown in Figure 4.2, where they are compared with the exact solution. The parameter ρ is a non-dimensional radial co-ordinate, ranging from -0.5 at the inner surface to 0.5 at the outer one. The FEA results were taken at the integration points.

As can be seen, the agreement was very good, both for the full and the reduced integration elements. There were only some minor discrepancies in the σ_r and the $\tau_{r\theta}$ stress components. This result supported proceding to the analysis of a tapered tube with the same sort of mesh parameters.

4.2.2 ANGLE-PLY LAMINATED TUBE MODELS

Having defined the 3D solid element suitable to the study of thick composite tubes, it was necessary to consider possible simplifications, as a full 3D analysis is very demanding in terms of time and memory allocation. The first aspect to consider is the existence of symmetry planes. This is the case of the 90° glass layers, because they are specially orthotropic in the directions defined by the tube. The direction of the fibres (direction 1) is the circumferential direction (θ) of the tube. Direction 2 of the lamina is the axial (z) direction and direction 3 is the radial (r) direction of the tube.

The $+\phi$ and $-\phi$ carbon laminae do not possess the same symmetry properties as the 90° glass layers. Their 1 and 2 principal material directions do not coincide with any directions defined by the tube, albeit direction 3 is the same as the radial direction. But, because the carbon sub-laminate is balanced, it is possible to define an equivalent material that is also specially orthotropic in the tube directions. Then, symmetry considerations can be applied to the whole thickness of the composite tube. This substitution of the laminate by an equivalent smeared

material with suitable elastic constants was analysed by Khalil and Soden[103].

It was first necessary to define the 3D elastic constants for the linear elastic, specially orthotropic, equivalent material. We have, for a single lamina:

$$
\begin{Bmatrix} \sigma_1 \\ \sigma_2 \\ \sigma_3 \\ \tau_{23} \\ \tau_{13} \\ \tau_{12} \end{Bmatrix} = \begin{bmatrix} C_{11} & C_{12} & C_{13} & 0 & 0 & 0 \\ C_{21} & C_{22} & C_{23} & 0 & 0 & 0 \\ C_{31} & C_{32} & C_{33} & 0 & 0 & 0 \\ 0 & 0 & 0 & C_{44} & 0 & 0 \\ 0 & 0 & 0 & 0 & C_{55} & 0 \\ 0 & 0 & 0 & 0 & 0 & C_{66} \end{bmatrix} \begin{Bmatrix} \varepsilon_1 \\ \varepsilon_2 \\ \varepsilon_3 \\ \gamma_{23} \\ \gamma_{13} \\ \gamma_{12} \end{Bmatrix}
\tag{4.3}
$$

where σ_i and τ_{ij} are the direct and shear stresses, ε_i and γ_{ij} are the engineering strains. Direction 1 is parallel to the fibres. Directions 2 and 3 are perpendicular to them. Directions 1 and 2 are in-plane and direction 3 is through-thickness. The stiffness coefficients C_{ij} are:

$$
C_{11} = \frac{\left(1 - \upsilon_{32}\upsilon_{23}\right)}{R} E_1
$$

$$
C_{12} = C_{21} = \frac{\left(\upsilon_{21} + \upsilon_{23}\upsilon_{31}\right)}{R} E_1
$$

$$
C_{13} = C_{31} = \frac{\left(\upsilon_{31} + \upsilon_{21}\upsilon_{32}\right)}{R} E_1
$$

$$
C_{22} = \frac{\left(1 - \upsilon_{13}\upsilon_{31}\right)}{R} E_2
$$

$$
C_{23} = C_{32} = \frac{\left(\upsilon_{32} + \upsilon_{31}\upsilon_{12}\right)}{R} E_2
\tag{4.4}
$$

$$
C_{33} = \frac{\left(1 - \upsilon_{12}\upsilon_{21}\right)}{R} E_3
$$

$$
C_{44} = G_{23}
$$

$$
C_{55} = G_{13}
$$

$$
C_{66} = G_{12}
$$

where: $R = 1 - \upsilon_{12}\upsilon_{21} - \upsilon_{13}\upsilon_{31} - \upsilon_{23}\upsilon_{32} - 2\upsilon_{21}\upsilon_{13}\upsilon_{32}$

By considering reciprocal relationships one can derive the useful expression:

$$\frac{v_{ij}}{E_i} = \frac{v_{ji}}{E_j} \tag{4.5}$$

As the unidirectional layers are considered to be transversely isotropic in the 2-3 plane:

$$C_{22} = C_{33}, \quad C_{12} = C_{13}, \quad C_{55} = C_{66}, \quad C_{44} = G_{23} = \frac{E_2}{2(1+v_{23})} \tag{4.6}$$

The stresses are then referred to the directions r, θ and z. The fibre direction is at an angle ϕ to the axial direction. The result is:

$$\begin{Bmatrix} \sigma_r \\ \sigma_\theta \\ \sigma_z \\ \tau_{r\theta} \\ \tau_{rz} \\ \tau_{\theta z} \end{Bmatrix} = \begin{bmatrix} \overline{C}_{11} & \overline{C}_{12} & \overline{C}_{13} & 0 & 0 & \overline{C}_{16} \\ \overline{C}_{21} & \overline{C}_{22} & \overline{C}_{23} & 0 & 0 & \overline{C}_{26} \\ \overline{C}_{31} & \overline{C}_{32} & \overline{C}_{33} & 0 & 0 & \overline{C}_{36} \\ 0 & 0 & 0 & \overline{C}_{44} & \overline{C}_{45} & 0 \\ 0 & 0 & 0 & \overline{C}_{54} & \overline{C}_{55} & 0 \\ \overline{C}_{61} & \overline{C}_{62} & \overline{C}_{63} & 0 & 0 & \overline{C}_{66} \end{bmatrix} \begin{Bmatrix} \varepsilon_r \\ \varepsilon_\theta \\ \varepsilon_z \\ \gamma_{r\theta} \\ \gamma_{rz} \\ \gamma_{\theta z} \end{Bmatrix} \tag{4.7}$$

The rotated stiffness coefficients are as follows:

$$\overline{C}_{11} = C_{33}$$

$$\overline{C}_{12} = \overline{C}_{21} = n^2 C_{13} + m^2 C_{23}$$

$$\overline{C}_{13} = \overline{C}_{31} = m^2 C_{13} + n^2 C_{23}$$

$$\overline{C}_{16} = \overline{C}_{61} = mn C_{13} - mn C_{23}$$

$$\overline{C}_{22} = n^4 C_{11} + 2m^2 n^2 C_{12} + m^4 C_{22} + 4m^2 n^2 C_{66}$$

$$\overline{C}_{23} = \overline{C}_{32} = m^2 n^2 C_{11} + (m^4 + n^4) C_{12} + n^2 m^2 C_{22} - 4m^2 n^2 C_{66}$$

$$\overline{C}_{26} = \overline{C}_{62} = n^3 m C_{11} - (n^3 m - nm^3) C_{12} - nm^3 C_{22} + 2mn(m^2 - n^2) C_{66}$$

$$\overline{C}_{33} = m^4 C_{11} + 2m^2 n^2 C_{12} + n^4 C_{22} + 4m^2 n^2 C_{66}$$

$$\overline{C}_{36} = \overline{C}_{63} = m^3 n C_{11} - (m^3 n - mn^3) C_{12} - mn^3 C_{22} - 2mn(m^2 - n^2) C_{66}$$

$$\overline{C}_{44} = m^2 C_{44} + n^2 C_{55}$$

$$\overline{C}_{45} = \overline{C}_{54} = -mn C_{44} + mn C_{55}$$

$$\overline{C}_{55} = n^2 C_{44} + m^2 C_{55}$$

$$\overline{C}_{66} = m^2 n^2 C_{11} - 2m^2 n^2 C_{12} + m^2 n^2 C_{22} + (m^2 - n^2)^2 C_{66} \tag{4.8}$$

where $m = \cos\phi$, $n = \sin\phi$. It is noticeable that the cross terms with subscripts *16, 61, 26, 62,*

36, 63, 45 and *54* are odd powers of sinφ, what makes them odd functions of φ . The carbon sub-laminate of the tapered tube is balanced, i.e., every +φ layer has a -φ counterpart of the same thickness. The mentioned cross terms tend to vanish for the whole assembly when we add up the contribution of every lamina to the stiffness matrix of the carbon sub-laminate. The result is that the carbon fibre sub-laminate can be considered to be made of a specially orthotropic material which principal material directions coincide with the cylindrical coordinate directions. The constitutive equations for both sub-laminates (glass and carbon) are therefore of the form:

$$
\begin{Bmatrix} \sigma_r \\ \sigma_\theta \\ \sigma_z \\ \tau_{r\theta} \\ \tau_{rz} \\ \tau_{\theta z} \end{Bmatrix} =
\begin{bmatrix}
\overline{C}_{11} & \overline{C}_{12} & \overline{C}_{13} & 0 & 0 & 0 \\
\overline{C}_{21} & \overline{C}_{22} & \overline{C}_{23} & 0 & 0 & 0 \\
\overline{C}_{31} & \overline{C}_{32} & \overline{C}_{33} & 0 & 0 & 0 \\
0 & 0 & 0 & \overline{C}_{44} & 0 & 0 \\
0 & 0 & 0 & 0 & \overline{C}_{55} & 0 \\
0 & 0 & 0 & 0 & 0 & \overline{C}_{66}
\end{bmatrix}
\begin{Bmatrix} \varepsilon_r \\ \varepsilon_\theta \\ \varepsilon_z \\ \gamma_{r\theta} \\ \gamma_{rz} \\ \gamma_{\theta z} \end{Bmatrix}
\tag{4.9}
$$

Sometimes it is more convenient to work with the compliance matrix instead of the stiffness one. We have, at the lamina level, using the notation introduced in expression 4.3:

$$
\begin{Bmatrix} \varepsilon_1 \\ \varepsilon_2 \\ \varepsilon_3 \\ \gamma_{23} \\ \gamma_{13} \\ \gamma_{12} \end{Bmatrix} =
\begin{bmatrix}
S_{11} & S_{12} & S_{13} & 0 & 0 & 0 \\
S_{21} & S_{22} & S_{23} & 0 & 0 & 0 \\
S_{31} & S_{32} & S_{33} & 0 & 0 & 0 \\
0 & 0 & 0 & S_{44} & 0 & 0 \\
0 & 0 & 0 & 0 & S_{55} & 0 \\
0 & 0 & 0 & 0 & 0 & S_{66}
\end{bmatrix}
\begin{Bmatrix} \sigma_1 \\ \sigma_2 \\ \sigma_3 \\ \tau_{23} \\ \tau_{13} \\ \tau_{12} \end{Bmatrix}
\tag{4.10}
$$

The definitions of the lamina compliances referred to the directions defined by the fibres are given in terms of the basic elastic properties as:

$$
S_{11} = \frac{1}{E_1}
$$

$$
S_{12} = S_{21} = -\frac{v_{12}}{E_1}
\tag{4.11}
$$

$$
S_{13} = S_{31} = -\frac{v_{13}}{E_1}
$$

$$S_{22} = \frac{1}{E_2}$$

$$S_{23} = S_{32} = -\frac{v_{23}}{E_2}$$

$$S_{33} = \frac{1}{E_3}$$

$$S_{44} = \frac{1}{G_{23}}$$

$$S_{55} = \frac{1}{G_{13}}$$

$$S_{66} = \frac{1}{G_{12}}$$

and because of the transverse isotropy in the 2-3 plane:

$$S_{22} = S_{33}, \quad S_{12} = S_{13}, \quad S_{55} = S_{66}, \quad S_{44} = \frac{1}{G_{23}} = \frac{2(1+v_{23})}{E_2} \tag{4.12}$$

The lamina compliance coefficients S_{ij} can be rotated to give the compliances referred to the tube directions in a way similar to that for the stiffness coefficients (equations 4.8). The expressions can be found in the literature, see Tsai [104]. The problem is that, unlike the stiffness coefficients, the lamina compliance coefficients cannot be added up to form the total compliance of the laminate.

This is illustrated by means of a simple spring model, as figure 4.3 shows. The laminated tube, submitted to an axial force, can be considered as an array of parallel springs (every lamina) pulled together. Every spring is stretched by the same amount Δx (as every lamina develops the same strains). The stiffness of the assembly C_t is the sum of the individual stiffnesses C_i, but the total compliance S_t is not. The total force F_t is the sum of the contribution of every individual spring force F_i. The individual force at a given spring is a function of its stiffness, as the stress tensor for a given lamina is a function of its stiffness matrix.

If we recall that the equivalent material is specially orthotropic, the rotated compliance matrix is uncoupled in its normal and shear terms, as is the rotated stiffness matrix (relation 4.9). The expression of the rotated compliance matrix, obtained as the inverse of the rotated stiffness

matrix, is greatly simplified:

$$\overline{S}_{11} = \frac{\left(\overline{C}_{22}\overline{C}_{33} - \overline{C}_{23}^{\,2}\right)}{C}$$

$$\overline{S}_{12} = \overline{S}_{21} = \frac{\left(\overline{C}_{13}\overline{C}_{23} - \overline{C}_{12}\overline{C}_{33}\right)}{C}$$

$$\overline{S}_{13} = \overline{S}_{31} = \frac{\left(\overline{C}_{12}\overline{C}_{23} - \overline{C}_{22}\overline{C}_{13}\right)}{C}$$

$$\overline{S}_{22} = \frac{\left(\overline{C}_{11}\overline{C}_{33} - \overline{C}_{13}^{\,2}\right)}{C}$$

$$\overline{S}_{23} = \overline{S}_{32} = \frac{\left(\overline{C}_{12}\overline{C}_{13} - \overline{C}_{11}\overline{C}_{23}\right)}{C}$$

$$\overline{S}_{33} = \frac{\left(\overline{C}_{11}\overline{C}_{22} - \overline{C}_{12}^{\,2}\right)}{C}$$

$$\overline{S}_{44} = \frac{1}{\overline{C}_{44}}$$

$$\overline{S}_{55} = \frac{1}{\overline{C}_{55}}$$

$$\overline{S}_{66} = \frac{1}{\overline{C}_{66}} \qquad (4.13)$$

where C is the determinant of the normal components of the rotated stiffness matrix:

$$C = \begin{vmatrix} \overline{C}_{11} & \overline{C}_{12} & \overline{C}_{13} \\ \overline{C}_{12} & \overline{C}_{22} & \overline{C}_{23} \\ \overline{C}_{13} & \overline{C}_{23} & \overline{C}_{33} \end{vmatrix} = \overline{C}_{11}\overline{C}_{22}\overline{C}_{33} + 2\overline{C}_{12}\overline{C}_{13}\overline{C}_{23} - \overline{C}_{12}^{\,2}\,\overline{C}_{33} - \overline{C}_{13}^{\,2}\,\overline{C}_{22} - \overline{C}_{23}^{\,2}\,\overline{C}_{11} \qquad (4.14)$$

and, through analogy with expressions 4.11, one can derive the values of the equivalent elastic constants for $a + /\text{-}\phi$ balanced laminated tube, with a modification for E_r:

$$E_r = E_j \qquad \left(\neq \frac{1}{\overline{S}_{11}}\right)$$

$$\upsilon_{r\theta} = -\overline{S}_{12}\ E_r$$

$$\upsilon_{rz} = -\overline{S}_{13}\ E_r$$

$$E_\theta = \frac{1}{\overline{S}_{22}}$$

$$\upsilon_{\theta z} = -\overline{S}_{23}\ E_\theta$$

$$E_z = \frac{1}{\overline{S}_{33}}$$

$$G_{r\theta} = \frac{1}{\overline{S}_{44}}$$

$$G_{rz} = \frac{1}{\overline{S}_{55}}$$

$$G_{\theta z} = \frac{1}{\overline{S}_{66}}$$

(4.15)

The difference in the treatment for E_r is also explained by a spring model. The arrangement for the out-of-plane stiffness is in series, not in parallel. So, the stiffness coefficients in that direction do not add up. If E_r is taken as the inverse of the total rotated coefficient in the radial direction, its value will change slightly with the rotation angle ϕ in the θ - z plane, which is not physically acceptable. The solution is to consider E_r always to equal E_3 (that in a transversely isotropic material is the same as E_2), no matter what the value of the rotation angle ϕ.

It is now possible to investigate the feasibility of the smeared properties concept. The geometry of the all-carbon tubes tested during the research is used for that purpose. The 3D FE model of the tube is shown in Figure 4.4. The length of the model is 80 mm and the internal diameter is 60 mm. The ply drop-off is slightly closer to the base, to allow for an even load distribution, as the axial load is applied as a displacement of the top section. The 20-noded brick, reduced integration elements are used.

There are four elements across the thickness, that drops from 3.9 to 3 mm. The full circumference is modelled, divided in 40 elements, as the individual +/- θ laminae do not permit symmetry considerations. There are 16 elements along the axis, with only one element length at the thickness variation region. This is not suitable for defining the stress concentration effect entirely, but that is not the main objective however. The use of a very refined, full 3D model would be very costly. Some stress perturbation will be however detected.

Two material descriptions are adopted, using the same geometric model. In the first one, every element is composed of 6 layers, 0.14 mm thick each on average (the thickness of the real laminae). The elastic properties of the carbon epoxy pre-pregs utilised in this research are shown in table 4.1.

The average fibre content of the stepped tubes was determined by means of acid digestion, according to the standard method ASTM D-3171 [105]. The results were a fibre volume fraction v_f of 56%, a matrix fraction v_m of 41% and a void content v_v of 3%. The values provided by the pre-pregs suppliers correspond to a fibre volume fraction of 60%. The stiffness and strengths values are corrected by means of simple micro-mechanics models, as shown by Eckold [106]. In the end, the corrected figures are simply the results of a rule of mixtures on fibres and matrix, given the little difference between the measured and the reference v_f fraction.

The corrected lamina properties are used in the FEA model. There is a local orientation for every lamina, alternating $+20°$ and $-20°$ angles between the fibres and the axial direction, to reproduce the real situation. This first model is called the laminate model. The second model uses the smeared equivalent material, with principal directions coincident with those of the tube. The elastic properties associated to the $+/- 20°$ angle-ply arrangement of the same carbon/epoxy pre-pregs, given by expressions 4.15, are shown in table 4.2.

By way of comparison, it is recalled that during the four point bending tests of the all-carbon tubes, their axial elastic moduli E_z were determined. The average value was 72.9 MPa, with a coeficient of variation of 8.4% (table 3.5). The value of 78.4 MPa for E_z, obtained from the properties of the laminae informed by the manufacturer (corrected for v_f) and by means of expressions 4.15, is within this experimental range.

The stresses obtained from the smeared model are referred to the directions r, θ and z of the tube. These stresses have to be transformed to the lamina directions, in order to compare them with the associated strengths. To do that, we refer again to the parallel springs model. The smeared tube shares the same strain state with every lamina, as in the spring model the equivalent spring and every individual spring are stretched by the same amount. Tsai [104] gives the transformation matrix to rotate the strains from the tube directions to those associated with the lamina:

$$
\begin{Bmatrix} \varepsilon_1 \\ \varepsilon_2 \\ \varepsilon_3 \\ \gamma_{12} \\ \gamma_{13} \\ \gamma_{23} \end{Bmatrix} =
\begin{bmatrix}
0 & s^2 & c^2 & 0 & 0 & -cs \\
0 & c^2 & s^2 & 0 & 0 & cs \\
* & 0 & 0 & 0 & 0 & 0 \\
0 & 2cs & -2cs & 0 & 0 & c^2-s^2 \\
0 & 0 & 0 & -s & c & 0 \\
0 & 0 & 0 & c & s & 0
\end{bmatrix}
\begin{Bmatrix} \varepsilon_r \\ \varepsilon_\theta \\ \varepsilon_z \\ \gamma_{r\theta} \\ \gamma_{rz} \\ \gamma_{\theta z} \end{Bmatrix},
$$

$$c=\cos\phi \quad and \quad s=\sin\phi \tag{4.16}$$

$$* \, Note: \quad \varepsilon_3 = (\sigma_r - C_{31}\varepsilon_1 - C_{32}\varepsilon_2)/C_{33}$$

The original transformation matrix does not affect ε_3, which remains equal to ε_r, if the rotation is in the θ–z plane. But, as explained before, the arrangement in the transverse direction is in series, not in parallel. The forces (or the stresses σ_r and σ_3) are the same, but the deformations are not. To account for that, ε_3 is then determined from σ_r, ε_1 and ε_2, as indicated in expressions 4.16.

Once the lamina strains are defined, the lamina stresses are obtained by using the lamina stiffness matrix, expression 4.3. Two analyses were run, using both material considerations. The first one was an axial load on the tube that caused an axial strain ε_z of 1% at the thinner section. The second load case was an internal pressure of 100 MPa. The results are shown in figures 4.5 and 4.6, for the spot where the stress concentration was the greatest: in the transition region, close to the thinner portion of the tube.

The laminate and smeared models compare well, generally speaking. The scattered appearance of some stresses of the laminate model is due to the coarseness of the mesh and to the low value of those stresses. The laminate model really considers every lamina, with alternating angles, which generated discontinuities. The stresses τ_{12} and τ_{23} are taken in absolute value because they change from positive to negative from a $+\theta$ to a $-\theta$ layer. To conclude, it is possible to say that the smeared model captures the right average values well.

4.2.3 AXISYMMETRIC MODEL: BENDING LOADS

The use of the smeared carbon/epoxy material properties introduces a significant

simplification into the problem, as symmetry planes can be considered. The simplest model is the one that considers axial symmetry, of course. If the loads applied to the composite riser tube were only axial forces and internal pressures, the axis-symmetry could be considered straight away, as those loads display that form of symmetry.

The question that remains to be addressed concerns the bending load, which is not axisymmetric. On the other hand, elementary beam theory shows that the stress due to bending at a given point is proportional to the distance between that point and the neutral plane. If we consider the angle θ to take the values of $0°$ and $180°$ at the neutral plane, the distance between any point (r,θ) of the tube and the neutral plane is $r.sin\theta$. One obvious guess is to consider all 3D stresses due to bending to be proportional to $r.sin\theta$. The stresses associated with the bending load can then be obtained from an axisymmetric analysis with a uniform axial strain equal to the bending strain at the extreme fibre.

To verify this hypothesis, an axisymmetric FEA model of the tube is considered, with the same mesh geometry in an axial plane as the full 3D model. The bending load is applied to the full 3D model as a rotation of the top section. Both models used the smeared material properties. The extreme fibre axial strain at the thinner section is 1%. If the outside radius of the tube is r_{out}, the bending stresses σ_{bend} are obtained from the axisymmetric stresses σ_{ax}:

$$\sigma_{r,bend} = \sigma_{r,ax} \cdot \frac{r}{r_{out}} \cdot sin\theta$$

$$\sigma_{\theta,bend} = \sigma_{\theta,ax} \cdot \frac{r}{r_{out}} \cdot sin\theta$$

$$\sigma_{z,bend} = \sigma_{z,ax} \cdot \frac{r}{r_{out}} \cdot sin\theta \tag{4.17}$$

$$\tau_{rz,bend} = \tau_{rz,ax} \cdot \frac{r}{r_{out}} \cdot sin\theta$$

The axisymmetric model provides only 4 stress values (the ones that are axisymmetric). The stress are taken at the integration points of the elements. Figure 4.7 shows the comparison between the two models, for the point closest to the outer radius of the transition region. The variation of all stresses with θ is read directly from the 3D model and is calculated from expressions 4.17, for the axisymmetric model. In the spot investigated, $\tau_{r\theta}$ is identically zero, as the point is very close to the external surface of the tube. The $\tau_{\theta z}$ stress that the

axisymmetric model cannot provide is not zero. Nevertheless, that stress is generally the smallest, and is particularly small at the position where all the other stresses are greater, the $90°$ position.

Figure 4.8 shows further comparisons, now for integration points with different radius at the $90°$ angular position, at the thickness transition region, close to the thinner part of the tube. Again, the 3D results are read directly and the axisymmetric ones are given by relations 4.17. As before, stresses $\tau_{r\theta}$ and $\tau_{\theta z}$ for the full 3D model have very small values. The conclusion from the graphs shown in figures 4.7 and 4.8 is that it is possible to capture all the relevant features of the stress field generated at the dropped ply region with a simple axisymmetric model, even for bending loads.

4.3 ALL-CARBON TUBES ANALYSIS

After the FEA parameters are set, the analysis continues with the investigation of the stresses present in the tubes tested. We begin with the first set of specimens, the all-carbon/epoxy, stepped, angle-ply tubes. Direct comparison between applied stresses and material strengths are performed. An investigation on the possible onset of delaminations is also carried out.

4.3.1 STRESSES DUE TO BENDING

The average dimensions of the all-carbon specimens are adopted for the models. The internal diameter is 60 mm, the external diameter of the thinner portion of the tube is 66.0 mm and the external diameter of the thick part is 67.7 mm. The thickness drops from 3.9 to 3.0 mm. The length of the thickness transition region is 3.7 mm, the average length obtained from the micrographs shown in Chapter 3.

From the micrographs it was concluded that two basic configurations of the terminating plies are possible. Three pairs of +/- $20°$ layers are terminated to obtain the reduction in thickness. The first arrangement occurs when the outer layer is the shortest and the inner layer is the longest. This is termed the stepped model. The other case is when the outer layer is the longest and the inner layer is the shortest, resulting in an overlapping configuration. The

manufacturing process does not have the control to predict the geometry of the transition region. As the micrographs of the preceding chapter showed, both basic configurations occurred, with some mixed ones, as well.

Figures 4.9 and 4.10 show the meshes adopted for each models. The resin pockets are also modelled, treating the epoxy resin as an isotropic elastic material with elastic constants $E = 4$ GPa and $v = 0.4$ (Hull, [44]). Local coordinate systems are introduced for the elements at the curved portions of the laminae, to conform with the curves developed by the fibres. The elements used are 8-node iso-parametric quadrilaterals for the composite and the 6-node triangles for the resin. Due to the simplicity of the axisymmetric analysis, it is possible to use very small elements, with sides measuring 0.148 mm, which are comparable with individual lamina thicknesses.

Figures 4.9 and 4.10 also indicate the axial stress σ_z due to an extreme fibre bending strain of 1% in the thinner portion of the tube away from the transition region. The load is applied to the FEA model in the form of nodal displacements, to ensure good uniformity of stresses. The results highlight the effect of the thickness transition region on the stresses. There are three stress concentration spots observed. The first one is at the outer surface of the tube, at the thickness transition region, close to the thinner part of the tube. This stress concentration is due to the difference in thickness. There are also very small high stress spots at the points where the terminating plies touch the continuous ones. This effect is amplified by the FEA models, which consider the contact to be a line, when in reality there is a small surface contact. This effect is difficult to consider, due to the variability of the geometry of the terminating plies. The last stress concentration spot, which is the same irrespective of the geometry of the transition region, is the tip of the last resin pocket, where the continuous layers join. The analysis focused on the first and the last spots for the reasons explained above.

The cylindrical stress components developed at the outer surface and at the tip of the resin pocket locations are shown in figure 4.11, for the stepped and the overlapped models. The extreme fibre axial stress σ_z at the thinner part of the tube, away from the transition region, is 770 MPa. The maximum observed value of 1500 MPa defines a Stress Concentration Factor (SCF) of 1.95. The influence length at both sides of the stress hot spot is of about 20 mm, less

than half of the 45 mm length estimated in Chapter 3. The graphs show that the results do not differ that much, depending on the model adopted, apart from some discrepancy observed in τ_{rz}.

It is possible to check the accuracy of the models proposed, based on the experimental results. This is done by comparing the experimental strains with those indicated by the FEA model. As shown in Chapter 3, strain gauges were installed at the thickness transition regions and at the central section, during the four point bending tests of the all-carbon tubes. The gauge length of the sensors was 3 mm, so the strains indicated were the averages over that length. The axial strain ε_z at the outer surface has the same pattern as the axial stress σ_z. There is a pronounced gradient at the transition region, so any variation in the axial position of the strain gauge would result in a noticeable difference in the average value. There is also the influence of the different lengths of the transition regions from tube to tube.

Nevertheless, the comparison still provides some information about the consistency of the models. The average axial strains over a 3 mm length at the middle of the transition region are obtained from the FEA results, at the outer surface. Table 4.3 shows the comparison, in terms of the ratio between the average transition region strain and the nominal extreme fibre strain at the thinner portion of the tube. The results compare well, given the variability of the average strains at the step position. The small difference between the two FEA models allows the use of only one, so the stepped model is chosen.

Figure 4.12 shows the lamina stresses, obtained as explained in the previous sections, for the stepped model, considering the compressed side. Direction 1 is along the fibres and directions 2 and 3 are normal to them. Directions 1 and 2 lie on the surface of the laminae and direction 3 is the through-thickness direction. It is noticeable that the stress concentration at the outer surface affects the in-plane stresses (mostly σ_1). The stress concentration at the resin tip affects more the out-of-plane stresses σ_3 and τ_{13}. In order to compare the stresses with the strengths displayed in table 4.4 we recall the experimental results again.

All the failures observed during the bending tests of the all-carbon tubes were at the compressed side. Only two failures occurred at the thickness transition region, the others being at the toe of the glass/epoxy end reinforcements. The tubes that failed at the thickness transition region were tube C1 (at a bending moment of 4.50 kNm) and tube C2 (at a bending

moment of 4.13 kNm). The average bending moment at failure was then 4.32 kNm.

The bending moment associated with the axisymmetric FEA model is obtained from the axial reaction forces, considering that they obey the same transformation law 4.17, valid for the stresses. For a given nodal support with radius r, the ABAQUS axisymmetric analysis gives the reaction force F_{ax} related to the full circumference. In the axisymmetric model, every node represents a circle in the actual 3D specimen. The reaction force in bending per unit angle, f_{bend}, is given by:

$$f_{bend} = \frac{r}{r_{out}} \frac{F_{ax}}{2\pi} \sin\theta$$ (4.18)

where r_{out} is the outer radius of the tube. The resultant force for an infinitesimal arc $d\theta$ is $f_{bend}d\theta$. The moment caused by that resultant is its value multiplied by the distance to the neutral plane, $r \sin\theta$. The final moment M is obtained from the integration over the whole circumference:

$$M = 2 \int_0^\pi f_{bend}\, r \sin\theta\, d\theta = \frac{F_{ax} r^2}{\pi r_{out}} \int_0^\pi \sin^2\theta\, d\theta = \frac{F_{ax} r^2}{\pi r_{out}} \left| \frac{1}{4}(2\theta - \sin 2\theta) \right|_0^\pi$$ (4.19)

$$M = \frac{F_{ax} r^2}{2 r_{out}}$$

The total reaction moment is the sum of the moments M due to every support node. The resulting value is 6.93 kNm, so the experimental average failure moment (4.32 kNm) corresponds to 62.3 % of the FEA value. It is necessary to multiply the stresses obtained by the FEA (that refer to a maximum extreme fibre strain of 1%) by 0.623 in order to compare them with the strengths. The resulting stresses, considering the side under compression, are those plotted in figure 4.12.

At the outer surface position, the resulting maximum compressive stress along the fibres σ_1 is -1019 MPa, 80 % of the strength C_1. The in-plane σ_2 stress is slightly affected, being 40 MPa (50% of $T2$) at its peak position. The in-plane shear stress τ_{12} is also little changed, its peak being equal to 27 MPa (27% of S_{12}). At the resin pocket tip the out-of-plane σ_3 stress is -63 MPa (25% of C_2) and τ_{13} is -53 MPa (53% of S_{12}). So, all the indications are that the

prevailing failure is due to compression along the fibres at the outer surface of the transition region, close to the thinner section.

For the analysis to be complete, it is necessary to consider the possible onset of delaminations from the resin pockets, due to the high out-of-plane stresses there. To that end, a SERR, fracture mechanics approach, is needed. This is the subject of the next section.

4.3.2 STRAIN ENERGY RELEASE RATE (SERR) DETERMINATION

Quasi-static bending tests

The virtual crack closure method of Rybicki and Kanninen [34] was adopted for the determination of the SERRs. In the FEM mesh, the nodes defining the delamination surface are duplicated, with stiff springs placed between them. The delamination progress wis simulated by deleting the spring elements placed behind the crack front, in relation to the propagation direction.

Due to the simplicity of an axisymmetric model, the forces and displacements necessary for the application of the method can be obtained from two successive runs. In the first one, the forces developed at the springs placed at the crack front are recorded. Then, those springs are deleted, allowing the crack faces to open a little more. The relative displacements of the nodes that were originally coincident at the crack tip are obtained. The energy balance principle states that the work needed to close the crack is equal to the strain energy released. The SERR's for an axisymmetric load case are calculated from the following expressions, for a delamination in the θ-z plane:

$$G_{I,ax} = \frac{1}{2\Delta S_{ax}} F_{r,ax} \Delta u_{ax} \quad and \quad G_{II,ax} = \frac{1}{2\Delta S_{ax}} F_{z,ax} \Delta w_{ax} \tag{4.20}$$

where ΔS is the delamination area increment, F_r is the force indicated by the radial spring and F_z the force indicated by the axial spring. Δu is the relative radial displacements of the crack surfaces and Δw is their relative axial displacement. The subscript ax refers to axisymmetric

results. The axisymmetric analysis results from ABAQUS are related to a full circumferential delamination. In order to introduce the variation with $r \sin\theta$, to consider the bending case, it is necessary to obtain the forces per unit angle, f_i:

$$f_{r,bend} = \frac{r}{r_{out}} \frac{F_{r,ax}}{2\pi} \cdot \sin\theta \quad and \quad f_{z,bend} = \frac{r}{r_{out}} \frac{F_{z,ax}}{2\pi} \cdot \sin\theta \qquad (4.21)$$

The displacements with subscript *bend*, associated with the bending load, are also modified:

$$\Delta u_{bend} = \frac{r}{r_{out}} \Delta u_{ax} \cdot \sin\theta \quad and \quad \Delta w_{bend} = \frac{r}{r_{out}} \Delta w_{ax} \cdot \sin\theta \qquad (4.22)$$

where r is the radius at the position of the delamination being investigated and r_{out} is the outside radius at the same z coordinate. The SERR's for bending load are obtained by an integration along the semi-circumference (so ΔS_{bend} is half the ΔS_{ax}). This is done to account separately for the SERRs related either to the compressed side or the tensioned side of the tube. The need for the separate analysis comes from the fact that the mode I SERR is zero at the side of the tube with negative radial stress, as the defect is closed by it. It follows that:

$$G_{I,bend} = \frac{1}{2\Delta S_{bend}} \int_0^\pi f_{r,bend} \cdot \Delta u_{bend} d\theta = \frac{1}{\Delta S_{ax}} \left(\frac{r}{r_{out}}\right)^2 \frac{1}{2\pi} \int_0^\pi F_{r,ax} \, \sin\theta . \Delta u_{ax} . \sin\theta . d\theta$$

$$= \frac{1}{2\Delta S_{ax}} \left(\frac{r}{r_{out}}\right)^2 \frac{F_{r,ax} . \Delta u_{ax}}{\pi} \int_0^\pi \sin^2\theta . d\theta = \frac{F_{r,ax} . \Delta u_{ax}}{2\pi\Delta S_{ax}} \left(\frac{r}{r_{out}}\right)^2 \left|\frac{1}{4}(2\theta - \sin 2\theta)\right|_0^\pi \qquad (4.23)$$

$$G_{I,bend} = \frac{F_{r,ax} . \Delta u_{ax}}{4\Delta S_{ax}} \left(\frac{r}{r_{out}}\right)^2 \quad and, similarly, \quad G_{II,bend} = \frac{F_{z,ax} . \Delta w_{ax}}{4\Delta S_{ax}} \left(\frac{r}{r_{out}}\right)^2$$

One important consequence of expressions 4.23 and 4.20 is that the SERR's associated with pure bending loads are less than half of the SERR's related to the axisymmetric load that gives the same maximum absolute axial strain.

As discussed by Rybicki and Kanninen [34] and verified in the present work, the virtual crack closure method works better with constant strain, 4-noded axisymmetric elements. The convergence of the method was tested, using three different mesh sizes for these elements. The incremental length ΔS was varied, for the same initial defect length. The final ΔS size of about 0.15 mm is considered adequate.

The failure index was calculated according to the expression:

$$f.i. = \frac{G_I}{G_{Ic}} + \frac{G_{II}}{G_{IIc}}$$

(4.24)

where G_I and G_{II} are the SERR values applied to the tube and those with suffix c are the critical ones, also known as the fracture toughnesses of the material. The experimental evaluation of the toughness of the T300/MTM28 carbon/epoxy system, described in Chapter 3, indicated average values of 297 J/m^2 for mode I and of 1577 J/m^2 for mode II, for +20°/-20° angle-ply interfaces.

The literature review has shown that delaminations in tapered composites develop both between the layers and at the resin pocket (refer to figures 2.17 and 2.19). A crack initiated at a stress concentration spot would propagate along two fronts. The virtual crack closure method has to be applied to the two fronts simultaneously, dividing the total energy released by the total incremental area.

The micrographs in Chapter Three showed that the transition region is a preferred place for voids, due to the poor consolidation there, during manufacturing. If there is a void at the resin pocket, this will provide the starting defect. Two stress concentration locations are chosen in the stepped model to receive an initial defect. These are the resin tips located at the outer dropped plies and at the junction of the continuous plies.

Initial defects with 0.3 mm lengths (two elements) are introduced at both locations. The initial defects are then increased in both directions, in increments of about 0.15 mm to either side. Figure 4.13 shows the variation of the SERRs and failure indexes with defect size for both starting locations. The relative importance of modes I and II changed from one spot to the other.

The fracture toughnesses obtained experimentally were related to inter-ply cracks. In absence

of better information, the same values are used to investigate the cracks between a lamina and pure resin. For crack tip orientations out of the θ-z plane, the force and displacement components in the directions normal and parallel to the crack front have to be determined.

The results in figure 4.13 have to be discussed with the stress results in mind. For the bending case, the failure was at the compressed side. The direct stress σ_3 was negative at the continuous plies spot and positive at the dropped plies spot. This implies that a defect in the previous position tends to be closed (no mode I propagation). Further, the crack driving force in mode II in that location is diminished by the friction between the crack surfaces. So the critical spot for delamination onset, at the compressed side, is the one at the dropped plies.

The examination of the micrographs in Chapter 3 shows a maximum void size of about 0.5 mm. The failure index at the dropped plies spot for a 0.5 mm defect under bending load, is less than 0.5. The results shown correspond to the average bending moment of 4.32 kNm at failure. A defect 0.5 mm wide, even if it was circumferential, as considered in the model, would not start a delamination. The conclusion is that the failure in compression of the fibres at the outer surface of the transition region would indeed prevail over possible delamination at the dropped plies. This is consequence of two factors: the maximum defect size is not large enough and the fracture toughness of the material is high.

There can be a different situation during a tensile axial load case. The σ_1 stress at the outer surface hot spot, for a 1% (now uniform) nominal strain, is 1636 MPa. Table 4.4 shows that this is the T_1 strength of the laminae. At the continuous plies spot, now the relevant one, as σ_3 is positive, the failure index (scaled up to 1/0.623, for 1% nominal strain) is equal to 1.6, for a 0.5 mm defect. So, it is possible that a delamination could start there first, during a tension axial load situation. It is not possible to be certain because the failure index graphs were determined for a very severe defect that runs along the full circumference of the tube. If a delamination starts there, its growth will be stable with the load, as the slope of the curve failure index *versus* defect size is positive. The cases of axial load combined with bending moment have to be addressed individually. The resulting failure indices will be a function of the relative participation of the axial force and the bending moment.

Fatigue bending tests

In relation to the basic fatigue tests performed, we recall the graph in figure 2.18, Chapter

Two, obtained by Murri et al. [35]. The graph showed delaminations starting at 500,000 cycles for a maximum G_I of about 100 J/m^2. The results plotted were for a IM6/1827I graphite/epoxy laminate, for conditions very close to those used in the present research. The stress ratio R was 0.1, the same adopted here, and the frequency was 5 Hz, while we used a maximum frequency of 4 Hz. The tests performed here lasted 500,000 cycles. If we consider that the maximum moment for the fatigue tests performed was 67% of the average moment at failure, the results in figure 4.13 display a maximum G_I of about 80 J/m^2. This value is related to a circumferential defect with a size of 0.5 mm, at the junction of the continuous plies, at the tensioned side of the bent tube. So, the screening fatigue tests and the results available in the literature indicate that delamination due to bending was improbable also for dynamic fatigue conditions.

4.4 HYBRID, STEPPED TUBES ANALYSIS

4.4.1 ANGLE-PLY TUBES

The next tubes to be studied are the hybrid 90° glass/epoxy, stepped, +/- 20° carbon/epoxy specimens. The FEA model uses the average dimensions of the 15 specimens made. The internal diameter is 60.3 mm, the maximum external diameter is 77.9 mm and the minimum external diameter is 76.3 mm. The carbon sub-laminate thickness drops from 5.8 to 5.0 mm. The total thickness of the glass sub-laminates is 3.0 mm, equally divided between inner and outer layers. The side lengths of the smallest elements are of the order of the lamina thickness.

Bending tests

For the bending case the load (applied as nodal displacements) introduces an extreme fibre strain of 1%, at the thinner part of the tube, as in the previous model. That load corresponds to a bending moment of 15.67 kNm. This is practically the average value of 15.69 kNm (with a c.v. of 20%), obtained experimentally during the pure bending tests of the angle-ply hybrid tubes. Five out of six specimens broke at the ply drop region, at the compressed side of the tube. The other one broke under the glass reinforcement, at the end of the steel sleeve. Figure 4.14 shows the stress results for this case, and table 4.4 displays the strength values for both

carbon and glass sub-laminates. The reason for the "jagged" appearance of stress σ_2 along the transition region in figure 4.14 is that the local reference directions changed from element to element of the FEA mesh.

The comparison between lamina stresses and strengths, knowing that the failure was at the compressed side, points to a first failure due to transverse compression at the outer glass lamina. The minimum σ_2 stress indicated there is -218 MPa, well beyond the (estimated) C_2 value of 130 MPa. This failure is not catastrophic, though, as the carbon sub-laminate is the main load carrier during the bending load. The final failure is due to compression along the fibres at the outer carbon lamina, once the σ_1 stress indicated there (-1227MPa), is 96% of the tabulated C_1 value. All the other lamina stresses, in both sub-laminates, are less relevant.

Internal pressure tests

The lamina stresses associated with an internal pressure of 46.6 MPa are plotted in figure 4.15. Three different cross sections are considered, one at the thinner portion of the tube, one passing through the resin tip at the transition region and one at the thick part. The conclusion, supported by the experimental results, is that the dropped ply detail did not affect the strength of the tube, for an internal pressure load condition. The critical spot is the inner glass lamina.

The pure internal pressure tests of three hybrid angle-ply tubes, listed in table 3.8, indicated a final failure at an average pressure of 46.6 MPa. We can see from the graphs in figure 4.15 that they do not provide any explanation for those figures, bearing in mind the strengths listed in table 4.4. One possible cause is the stress concentration caused by the glass reinforcement, mainly on the carbon sub-laminate. The maximum circumferential stress at the innermost glass layer is presumably smaller, under the reinforcement. In order to verify this hypothesis, a model of the thick portion of the tube, including the glass reinforcement, was examined. The stresses in the carbon sub-laminate did not change substantially.

Further information is provided by the circumferential strain gauges placed at the central (thin) portion of the hybrid stepped tubes, during the pressure tests. The slopes of the elastic portion of the strain vs. pressure curves indicated an elastic modulus E_1 of 55 GPa for the carbon/epoxy sub-laminate. This was the average value for the three tubes tested, with a coefficient of variation of 2%. This value is 34% higher than the figure provideded by the pre-preg supplier, 41 GPa. If this value is considered in the analysis, the carbon/epoxy sub-

laminate will be subjected to smaller stresses and the peak stress at the inner glass layer will be higher. The results are plotted in figure 4.15, labelled as corrected values.

The maximum stress in the inner glass layer increases from 420 to 450 MPa. Even so, the woven roving strength is over-estimated. The T_l value observed experimentally is well under the value of 660 MPa given by the supplier. As the stresses on the carbon sub-laminate are even smaller, the preliminary damage indicated by the strain gauges during the internal pressure tests also happened at the glass/epoxy layers. Most probably, the early damage indications were related to matrix cracking parallel to the weft direction of the woven roving.

Combined tests

Next, a failure envelope is determined, according to the maximum stress criterion, in order to address the results of the combined tests. The incremental approach proposed by Hinton et al. [41], that reduces the elastic constants affected by early ply failure to zero, is not adopted at this stage. For the pure bending case, the C_2 strength of the glass sub-laminate was reached first, but the high stress spot was localised. It would be unreal to zero the corresponding elastic constants for the whole tube.

For the internal pressure case, early damage certainly affected the circumferential stiffness, as the experimental tests showed, but it did not vanish. The problem is that no other strength of the lamina was exceeded, other than the critical one.

The calculated failure envelope considers the corrected E_1 stiffness of 55 GPa for the glass/epoxy sub-laminate, as well as a revised T_1 strength of 450 GPa. Figure 4.16 displays the failure envelope for the hybrid, stepped, angle-ply tubes, in terms of the internal pressures and bending moments. The combined tests results are plotted, together with the pure load cases. The large dispersion observed for the pure bending load (with a c.v of 20%, for five valid tests) is evident. This is probably due to the lack of control on the geometry and void content of the thickness transition region. The pure internal pressure cases presented a much smaller coefficient of variation of 2%, related to three experiments. The combined load cases displayed a variation in between those extremes.

The failure envelope shows that the internal pressure does not affect the bending moment that causes the failure by fibre longitudinal compression at the outer carbon layer. This is explained by figure 4.15, that shows that the stress σ_1 at the outer carbon layer due to the

internal pressure is zero. It can be seen that the revised T_1 value for the glass sub-laminate and the C_1 value given by the manufacturer for the carbon sub-laminate resulted in a reasonable average failure envelope for the experimental tests.

SERR analysis

To finish the analysis of the hybrid, stepped, angle-ply tubes, an SERR analysis is performed for the pure bending case. The resulting graphs are displayed in figure 4.17. The critical spot is at the end of the dropped plies, where σ_3 is positive, as the failures occurred at the compressed side. The resin tip at the junction of the continuous plies shows negative σ_3 stress. The failure index at the critical spot, for a 0.5 mm wide circumferential defect is of about 0.8. So, failure by delamination is not expected to start before the axial collapse of the carbon fibres. The tube could fail by delamination under a uniform compressive axial load, as the failure index will be of around 2.0 for the same maximum compressive stress.

4.4.2 UNIDIRECTIONAL TUBES

The hybrid, stepped, $0°$ carbon tubes were tested in pure bending and pure internal pressure loads. The average dimensions of the nine HSN specimens made are used for the FEA model. These are an internal diameter of 60.3 mm, a maximum outer diameter of 75.4 mm and a minimum external diameter of 74.0 mm. The $90°$ glass/epoxy layers are 1.5 mm thick each, as before. The $0°$ carbon/epoxy sub-laminate was made thinner, to maintain the same load levels at failure. Its thickness drops from 4.6 to 3.9 mm.

Bending tests

The four point bending tests indicated an average moment of 12.63 kNm at failure, with a c.v. of 5% for four valid results. This was much better than the bending tests of the angle-ply tubes. The better control of the manufacturing process as more and more tubes were made may have contributed to that. The $0°$ orientation of the carbon sub-laminate could have caused less variation in the properties of the transition region as well. Figure 4.18 displays the results of the FEA for a bending moment of 12.63 kNm. The original E_1 value of 41 GPa is used for the glass/epoxy sub-laminate. We have to consider that the manufacturer produced the average

value from a much larger population of results.

All the specimens failed at the extreme fibre of the compressed side, so figure 4.18 displays the stresses there. The pattern is the same as that observed for the angle-ply tubes. There is a first failure due to transverse compression at the external glass layer, as the minimum stress there is -183 MPa, compared with a strength C_2 of 130 MPa (table 4.4). Following that the outer carbon layers fail by longitudinal compression of the fibres, given the minimum calculated stress of -1172 MPa (92% of the strength C_1). The maximum stress location is again at the end of the thickness transition region, close to the thinner part of the tube.

Internal pressure tests

The internal pressure tests of three HSN tubes indicated an average ultimate pressure of 34.8 MPa, with a coefficient of variation of 8%. There were also some early indications of damage. Figure 4.19 shows the lamina stresses for the internal pressure of 34.8 MPa, using the original E_1 stiffness of 41 GPa for the glass/epoxy sub-laminate. The results shown are those related to the thin section of the tube. The maximum σ_1 stress is 324 MPa, at the inner glass layer (this value would be 353 MPa if we had taken an E_1 value of 55 GPa for the glass/epoxy woven roven). This implies an even lower T_1 strength than that inferred from the tests on the HST tubes. The pre-pregs for the HSN tubes were from a different batch than those of the HST tubes. Even so, the reduction in the strength T_1 (that was low already) is excessive.

SERR analysis

To conclude the study of the HSN tubes, an SERR analysis in bending is performed. For the $0°$ carbon fibre orientation, the average experimental toughnesses were 546 J/m^2 for mode I and 1392 J/m^2 for mode II. Figure 4.20 shows the SERR values and the corresponding failure indices, for a bending moment of 12.63 kNm. The same behaviour observed for the previous cases occurs again.

Once it is known that the tubes failed at the compressed side, the critical spot for any delamination onset is at the end of the dropped plies. The failure index there is quite low, smaller than 0.4, reflecting the higher G_{Ic} value for the $0°$ carbon fibre orientation. As a consequence, the tubes failed in compression at the outer carbon layers before any delamination started at the dropped plies. Again, the tube could delaminate during a tensile axial load, when the failure index at the junction of the continuous plies (where σ_3 will be

positive) will be larger than one before the T_1 strength of the carbon fibres is reached. As before, the considerations about delamination onset are related to an initial axisymmetric defect 0.5 mm wide.

4.5 HYBRID, PLAIN TUBES ANALYSIS

4.5.1 ANGLE-PLY TUBES

This set consisted of the hybrid, plain, +/- 20° carbon specimens. The average dimensions of the three HPT tubes tested are similar to those of the thin part of HSN tubes. The ID is 60.3 mm and the average OD is 74.1 mm. The total glass/epoxy thickness is 3.0 mm and the carbon/epoxy sub-laminate is 3.9 mm thick. The tubes were tested in four point bending and failed at an average bending moment of 16.48 kNm, with a c.v. of 12%. As was to be expected, all the tubes failed at the compressed side, but under the glass reinforcement. That provided the only source of stress concentration in the absence of the thickness transition region.

The FEA of the HPT tubes indicates a minimum σ_1 stress of -1288 MPa (101% of strength C_1) at the outer carbon layer for a bending moment of 16.48 kNm. The model does not consider the glass reinforcement, so that value is related to a position far from the stress concentration location. Even so, that maximum compressive stress value, along the carbon fibres, is consistent with the previous bending tests results and with the tabulated strength of the material.

4.5.2 UNIDIRECTIONAL TUBES

The three HPN specimens were tested in internal pressure. The objective was to confirm the reduced final pressures achieved, in relation to what one would expect based on the strength figures provided by the supplier of the glass/epoxy woven roven. The average dimensions of the tubes are an ID of 60.3 mm and an OD of 74.3 mm. The carbon sub-laminate has a thickness of 4.0 mm. Once more, the listed E_1 stiffness value of 41 GPa is considered, for the glass/epoxy sub-laminate. Figure 4.21 shows the lamina stresses, related to the average failure

pressure of 35.1 MPa (c.v. of 5%).

It can be seen that the state of stress developed in this case is very similar to that related to an internal pressure at the thinner part of tubes HSN (figure 4.19). This is because the dimensions and properties of the tubes are practically the same. The average final pressures at failure are about the same too, 34.8 MPa for tubes HSN and 35.1 MPa for tubes HPN, now. The maximum σ_1 stress achieved by the inner glass layer for the present case is 347 MPa. The low T_1 strength of the glass/epoxy woven roving is confirmed.

Property	Carbon/epoxy ($v_f = 56\%$)	Glass/epoxy woven roving
E_1 [GPa]	117	41
E_2 [GPa]	8	9
G_{12} [GPa]	5	7 *
v_{12}	0.34	0.26 *
v_{23}	0.5 *	0.4 *
G_{23} [GPa]	2.67 **	3.21 **

* Estimated from literature.

** Equal to $E_2/2(1+v_{23})$ [103].

Table 4.1 Stiffness of the pre-pregs, according to suppliers.

Property	Value
E_r [GPa]	8.00
E_θ [GPa]	8.71
E_z [GPa]	78.35
$v_{r\theta}$	0.405
v_{rz}	- 0.013
$v_{\theta z}$	0.139
$G_{r\theta}$ [GPa]	2.94
G_{rz} [GPa]	4.73
$G_{\theta z}$ [GPa]	15.38

Table 4.2 Elastic properties of the equivalent,"smeared", carbon/epoxy material

for a +/- 20° angle-ply configuration.

TUBE	$\varepsilon_{trans}/\varepsilon_{nom}$ *	MODEL	$\varepsilon_{trans}/\varepsilon_{nom}$
P1	0.85	Stepped	0.84
C1	0.84		
C2	0.91	Overlapped	0.85
C3	0.80		
C4	1.00		

* Average of 4 values per tube

Table 4.3 Strain at the transition region over nominal strain: comparison between experimental results and FEA models.

Strength [MPa]	Carbon/epoxy (v_f =56%)	Glass/epoxy woven roving
Longitudinal tensile T_1	1640	660
Longitudinal compressive C_1	1280	400 *
Transverse tensile T_2	80	100
Transverse compressive C_2	250 *	130 *
Shear S_{12}	100	60 *

* Estimated from literature.

Table 4.4 Strengths of the pre-pregs, according to suppliers.

161
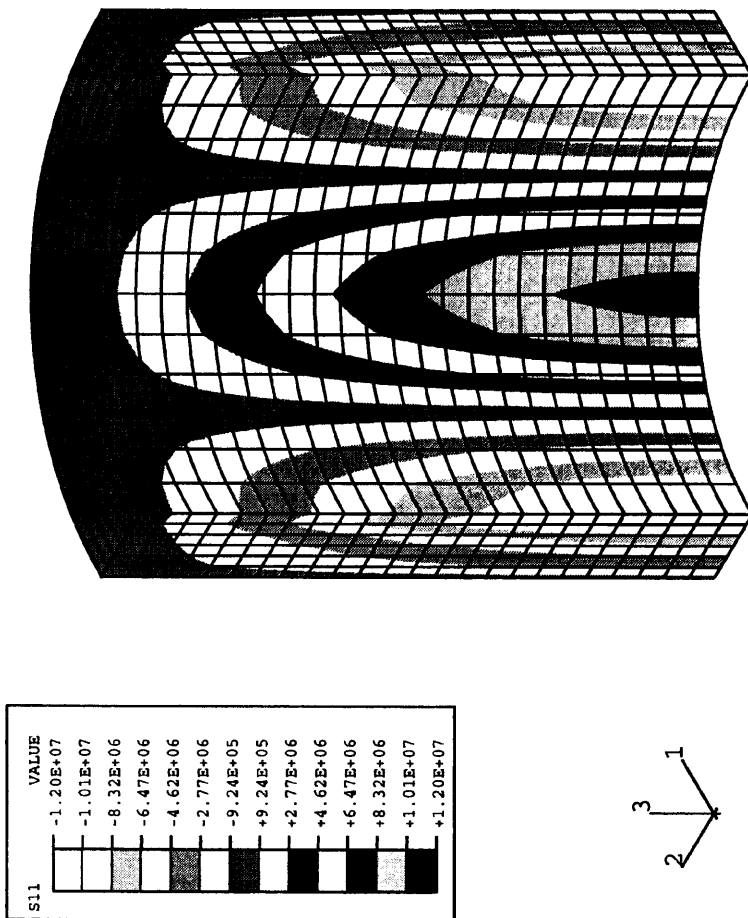
Figure 4.1 FEA mesh for the exact 3D solution and associated pressure distribution.

162
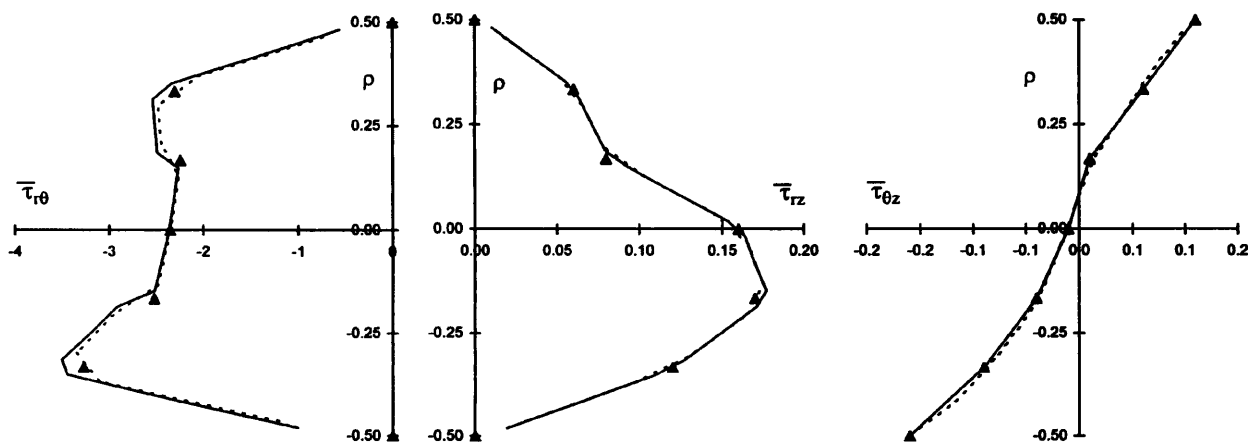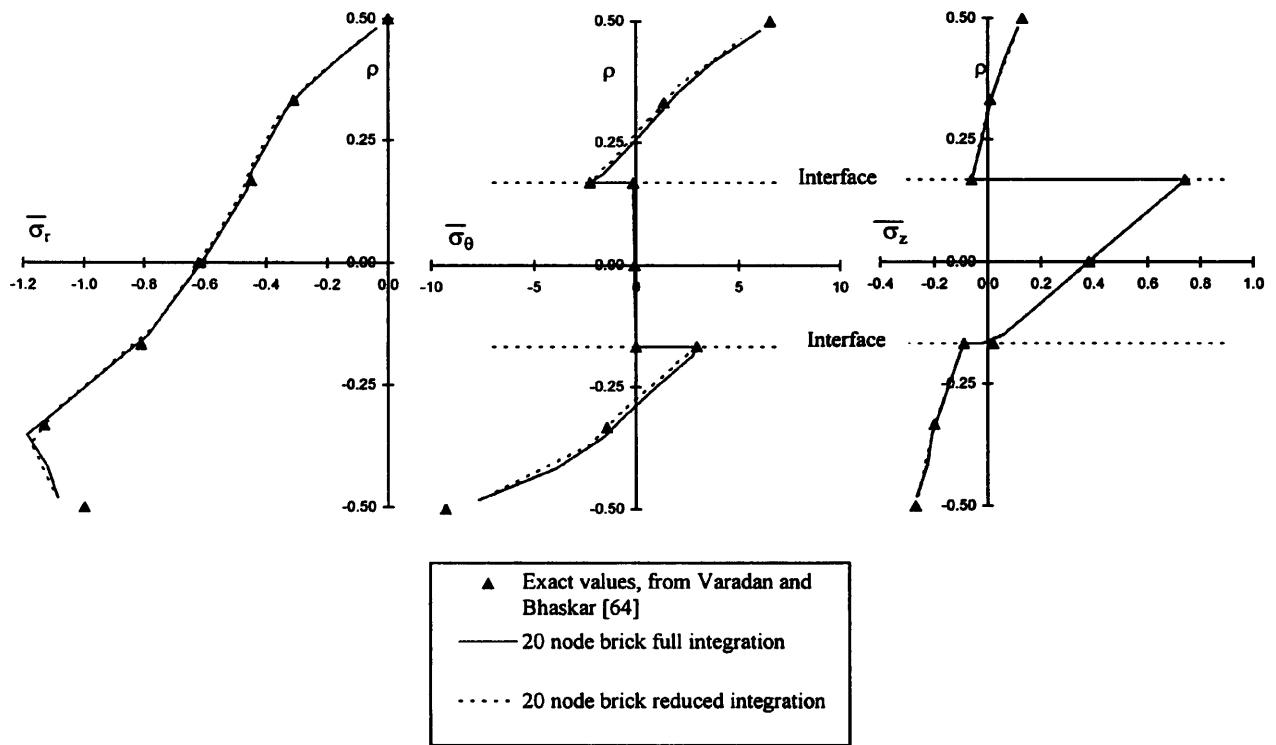
Figure 4.2 Comparison between FEA and exact values, for a $(90^\circ/0^\circ/90^\circ)$ laminated tube, S=4.
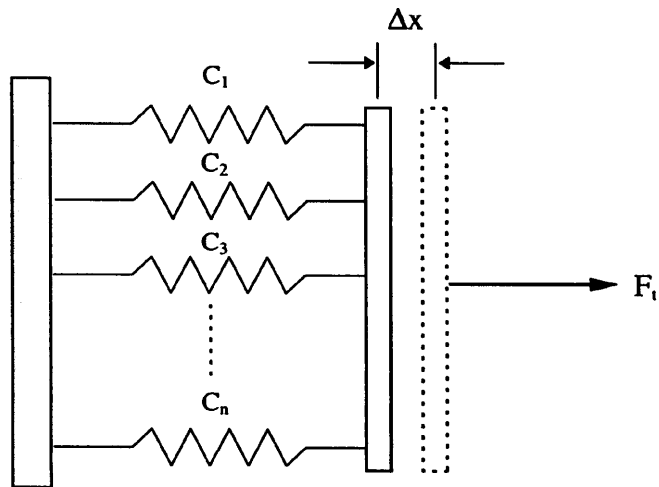
$$F = C.\Delta x \qquad\qquad C = 1/S$$

$$\Delta x_t = \Delta x_1 = \Delta x_2 = \Delta x_3 = \ldots = \Delta x$$

$$F_t = F_1 + F_2 + F_3 + \ldots + F_n$$

$$C_t = C_1 + C_2 + C_3 + \ldots + C_n$$

$$1/S_t = 1/S_1 + 1/S_2 + 1/S_3 + \ldots + 1/S_n$$
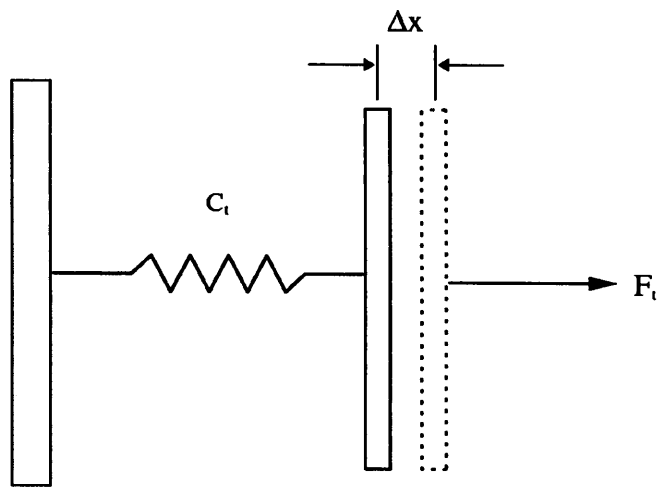
Figure 4.3 Array of parallel springs model.
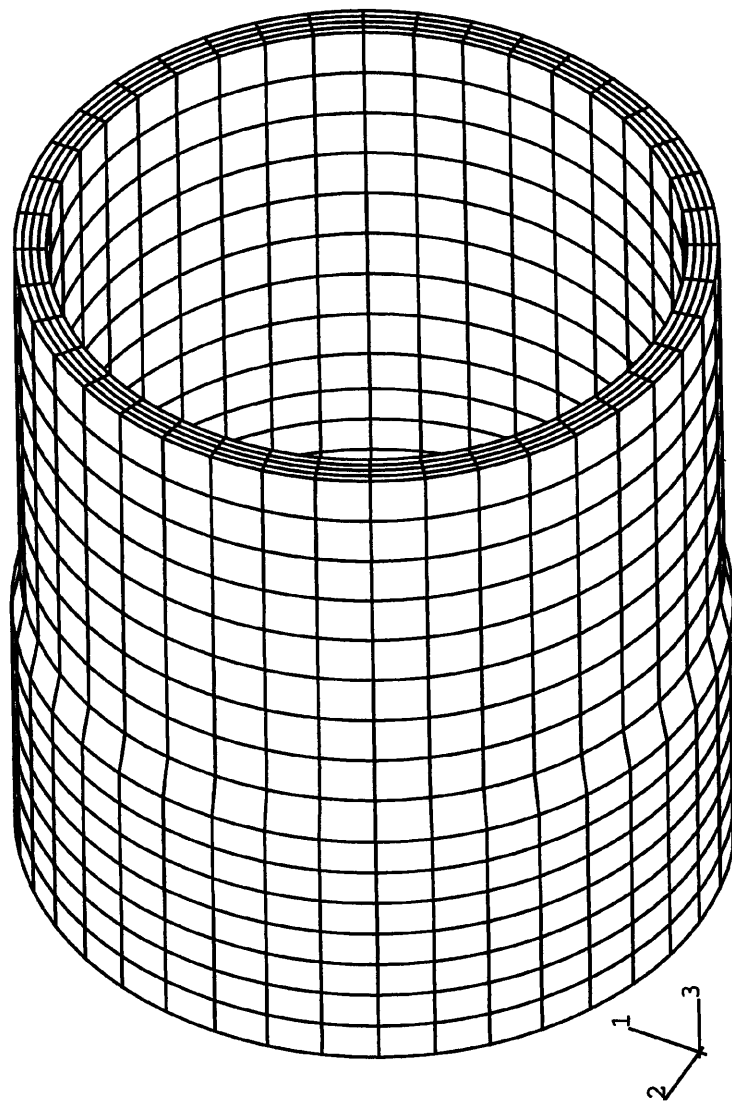
Figure 4.4 Full 3D model of the all-carbon, dropped ply tube.
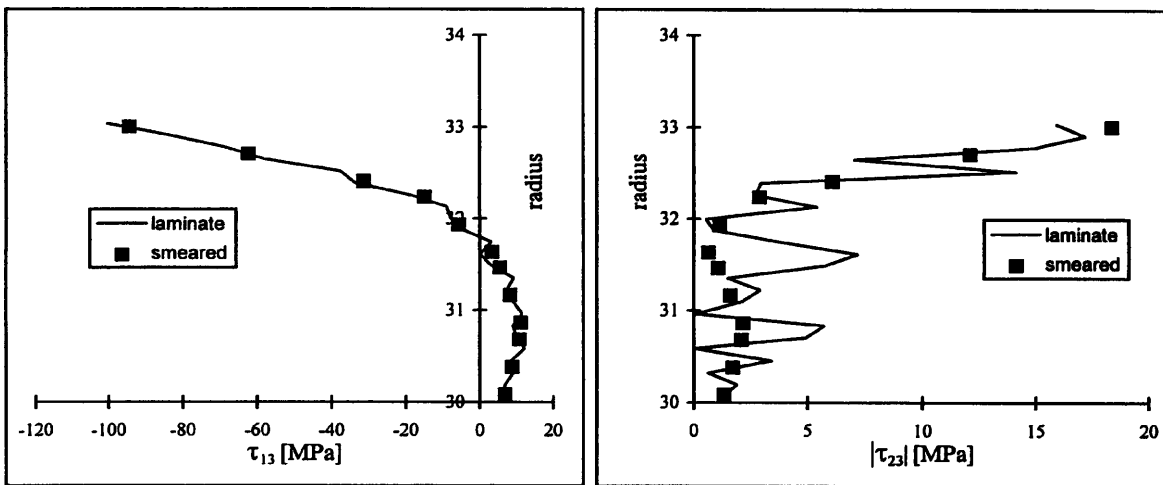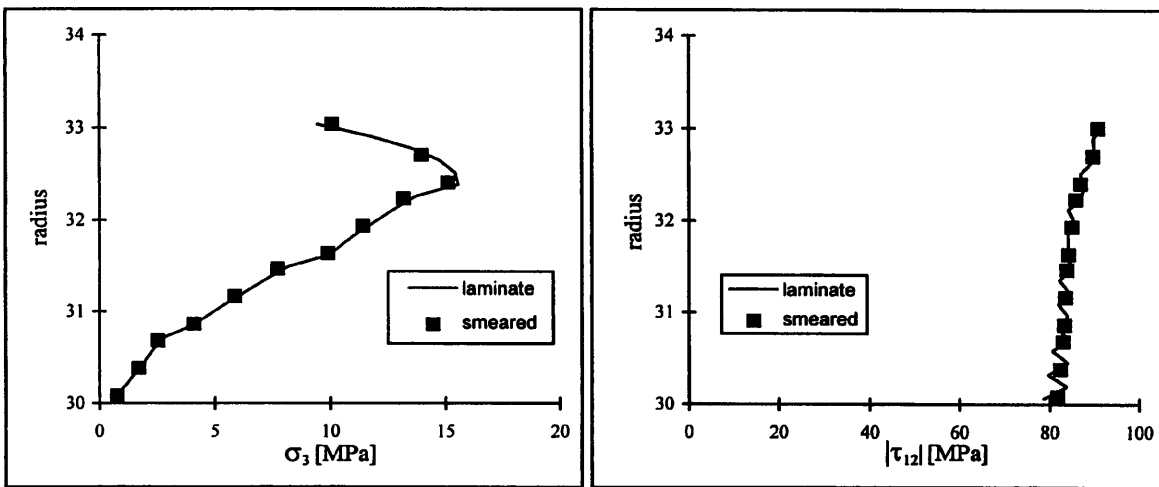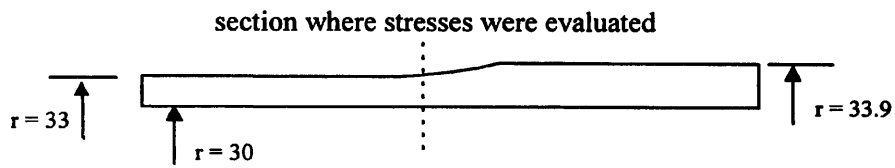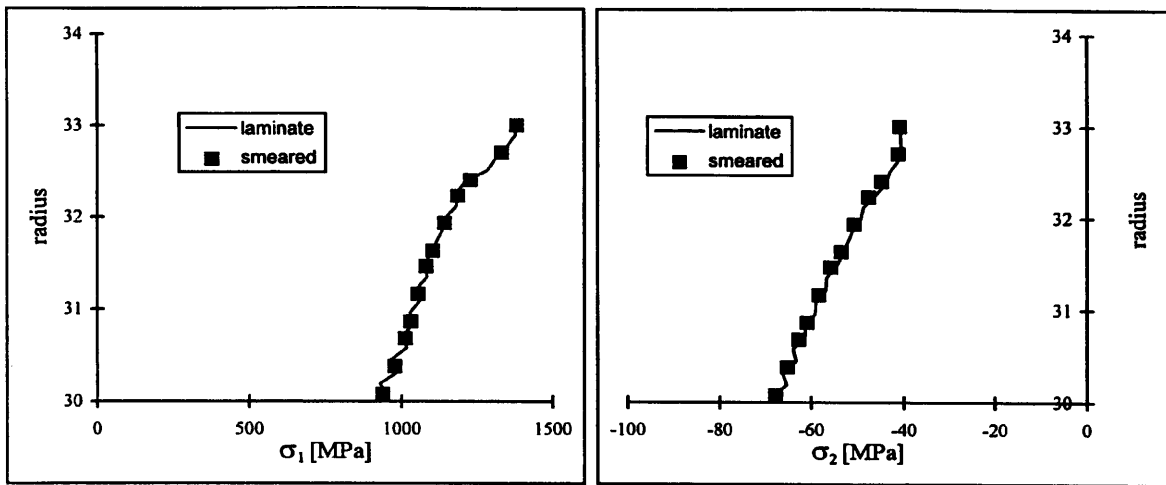
Figure 4.5 Comparison between smeared and laminate models, axial strain of 1%.
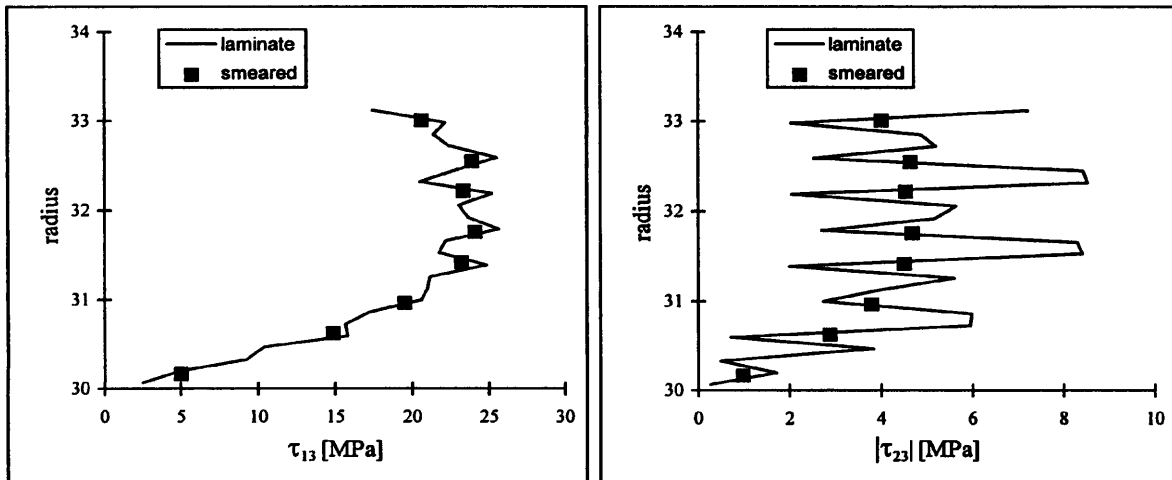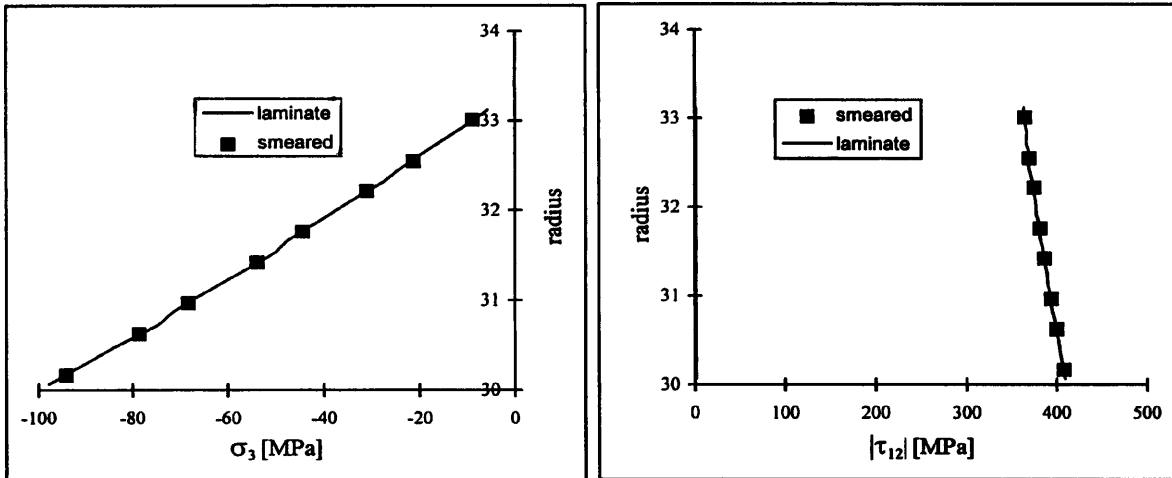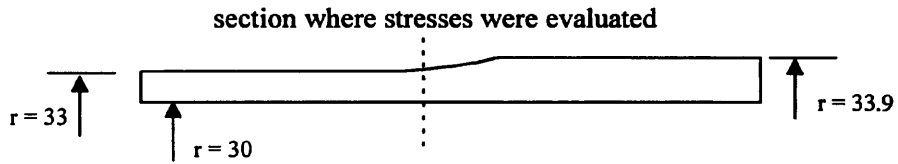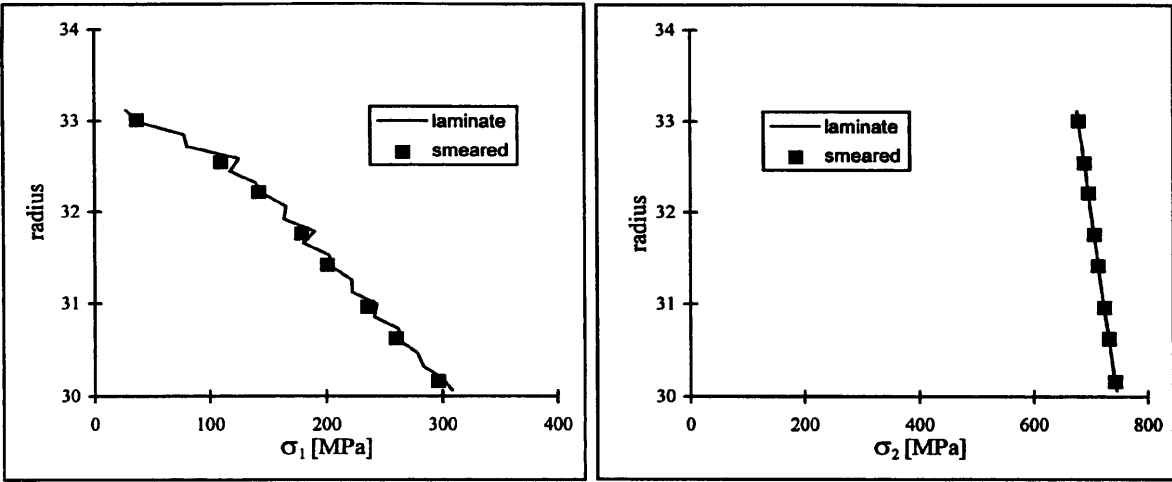
Figure 4.6 Comparison between smeared and laminate models, internal pressure of 100 MPa.
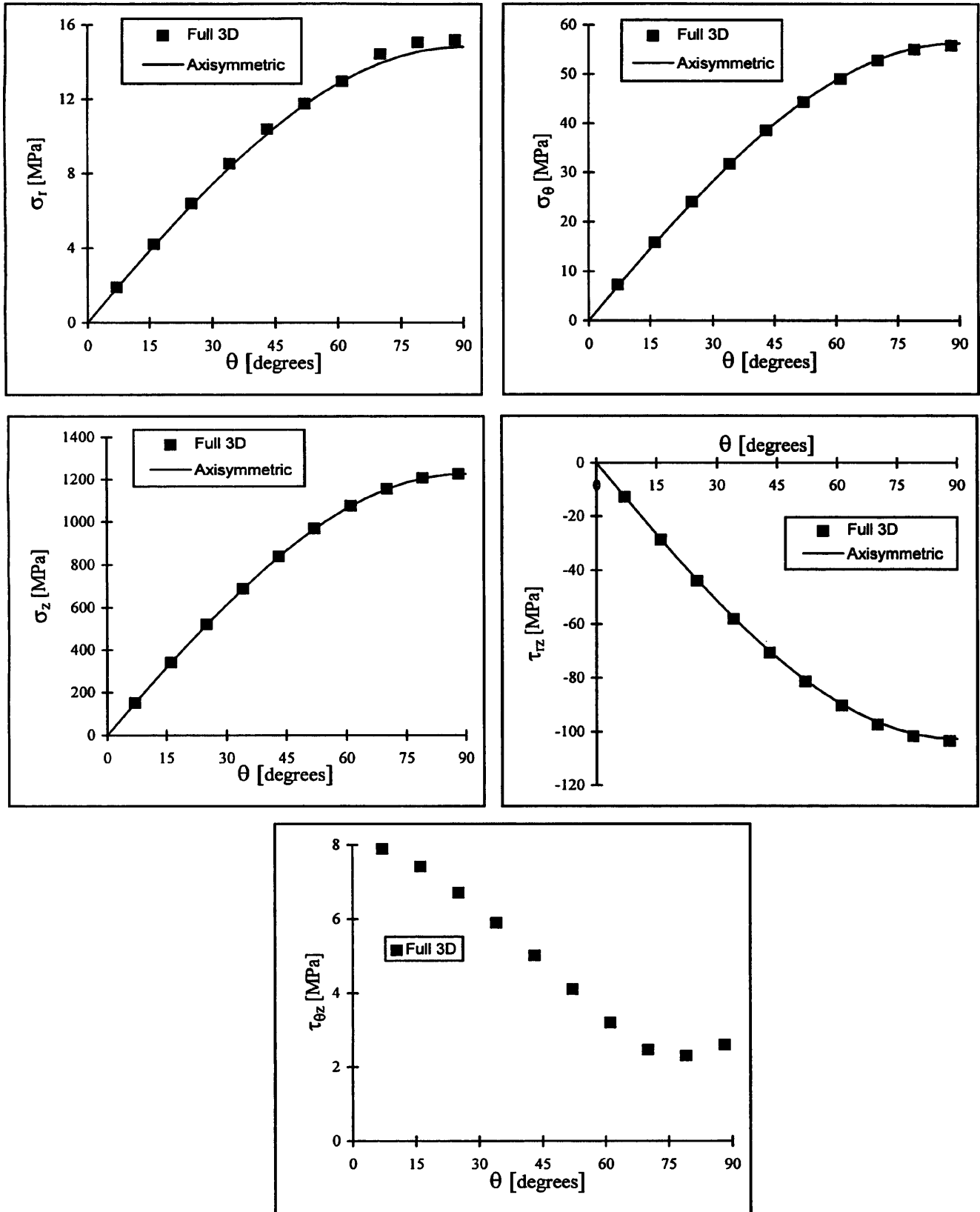
Figure 4.7 Smeared models in bending: comparison between full 3D and axisymmetric results, r ~ r_{out}.
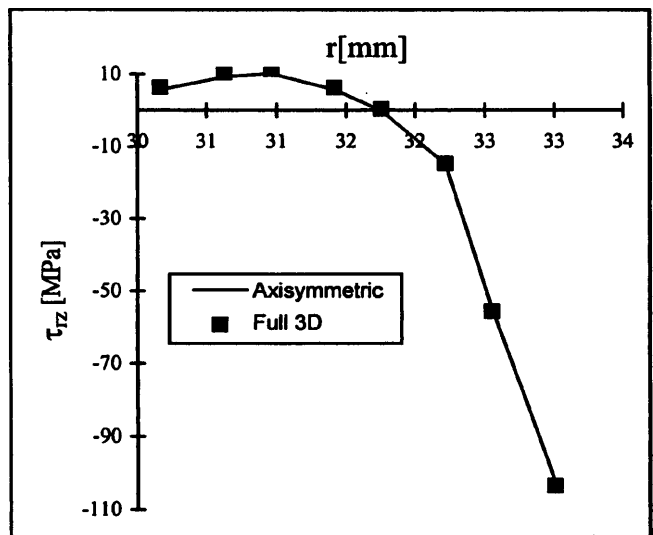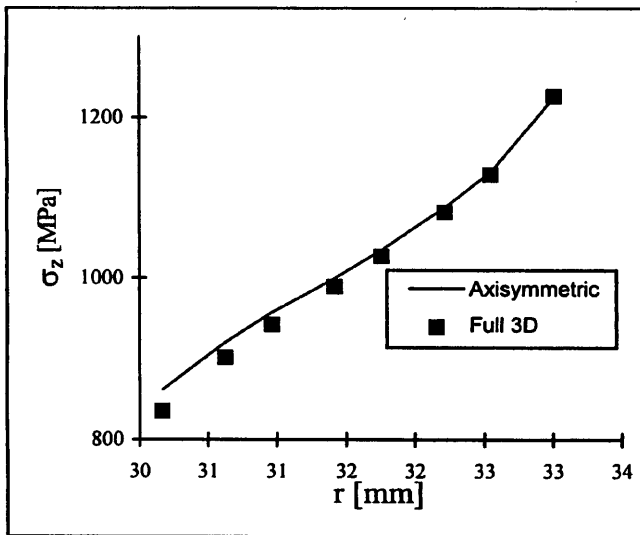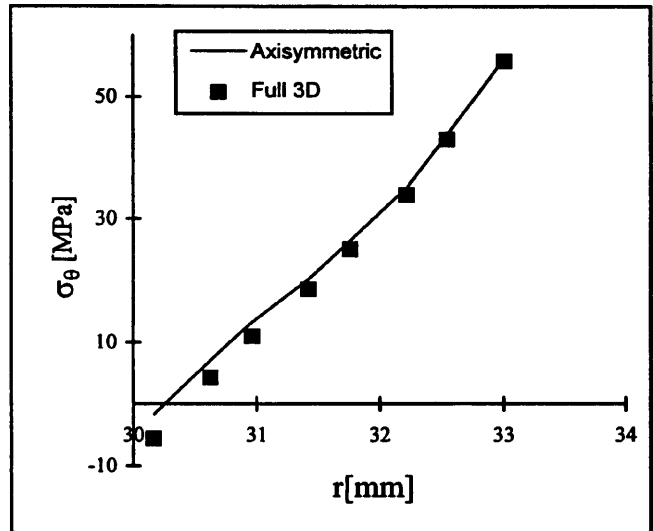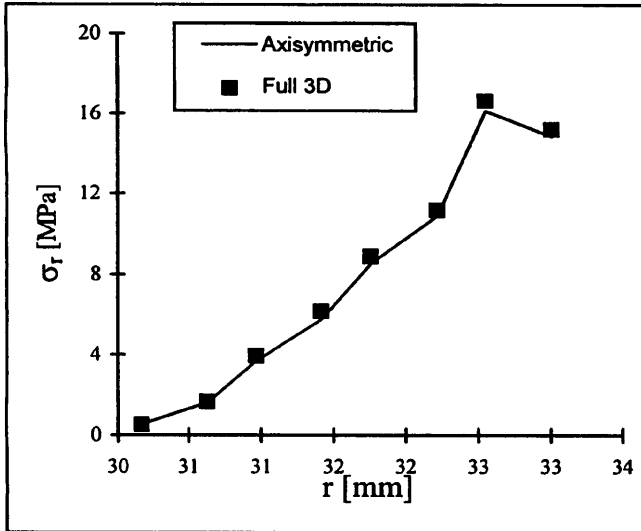
Figure 4.8 Smeared models in bending: full 3D and axisymmetric results, $\theta = 90°$.
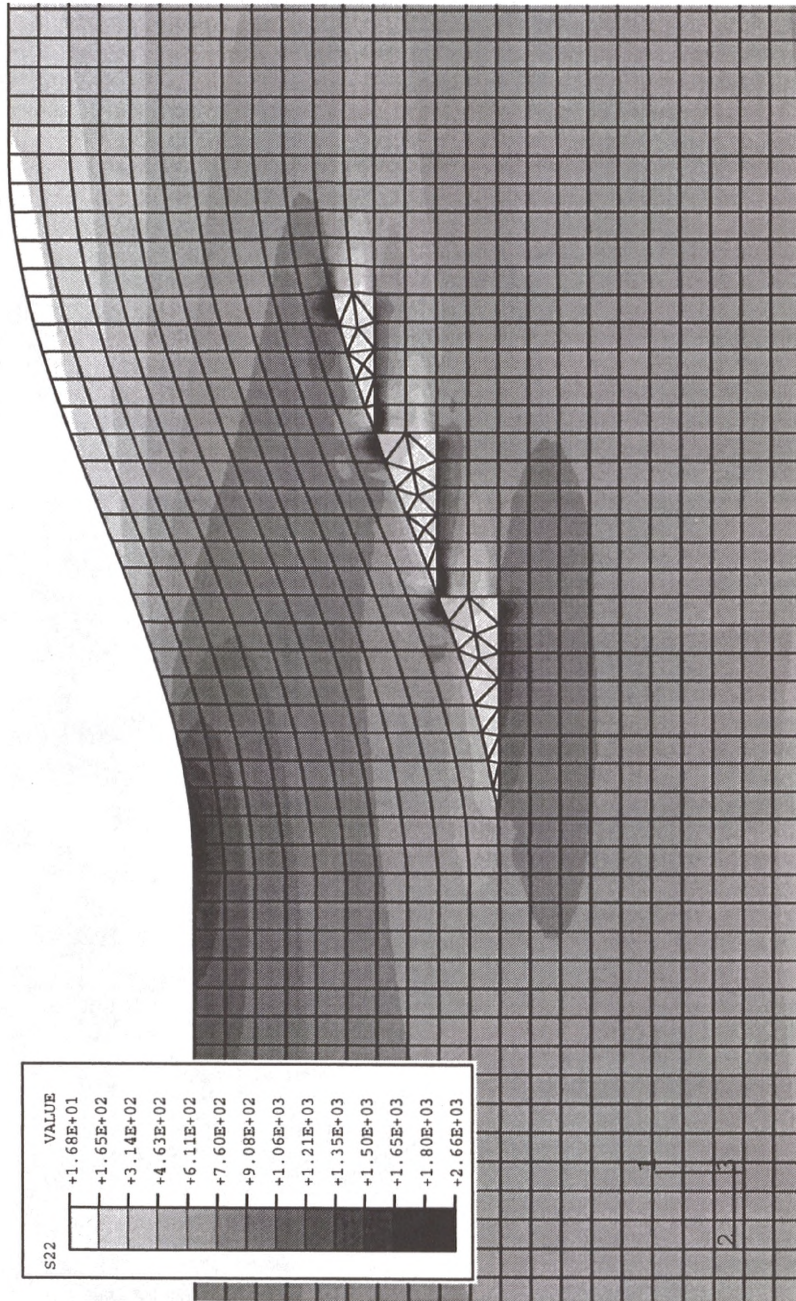
Figure 4.9 Stepped model: FEA mesh and axial stresses.
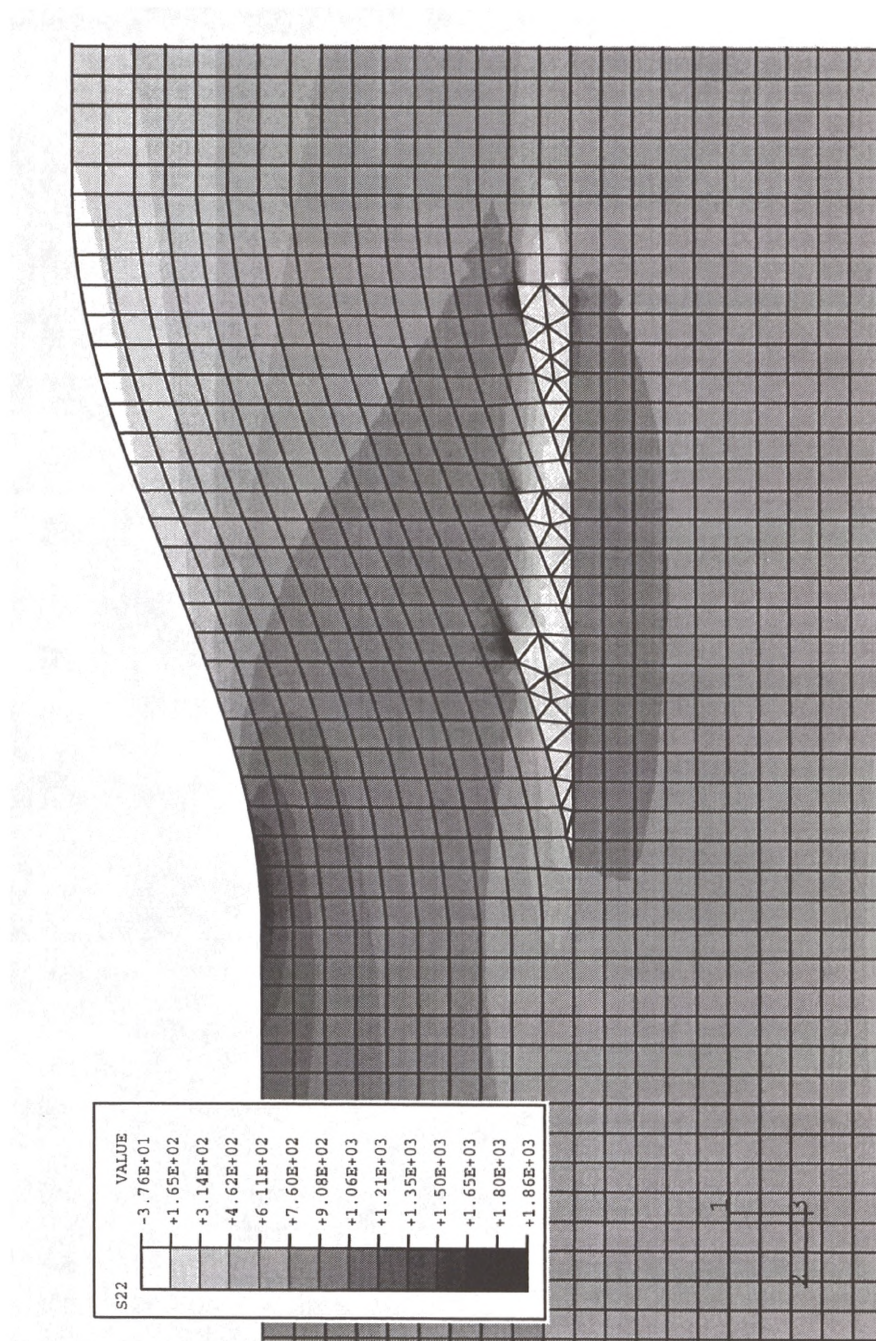
Figure 4.10 Overlapped model: FEA mesh and axial stresses.

171
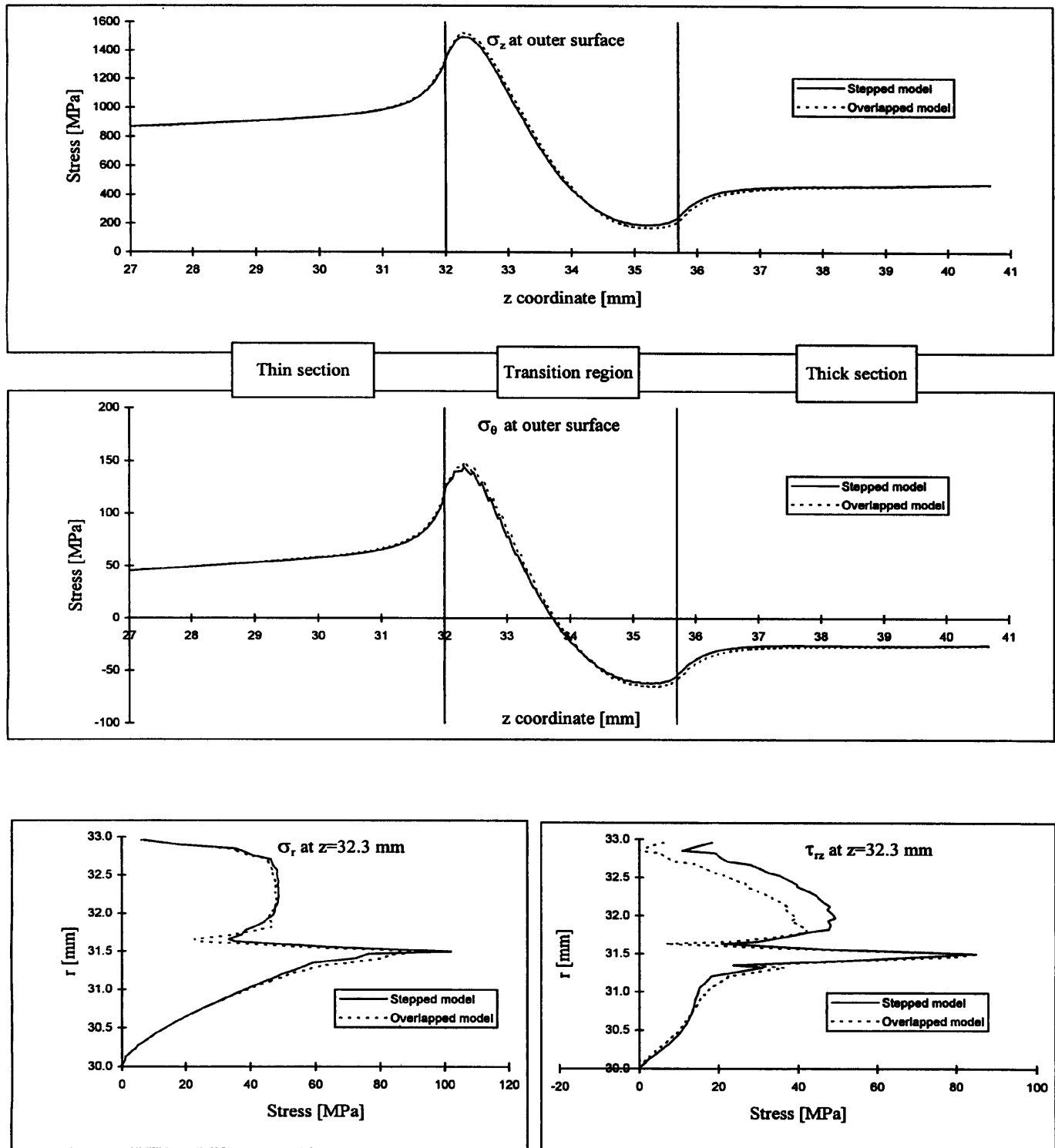
Figure 4.11 Stress fields at the thickness transition region, according to the different models.
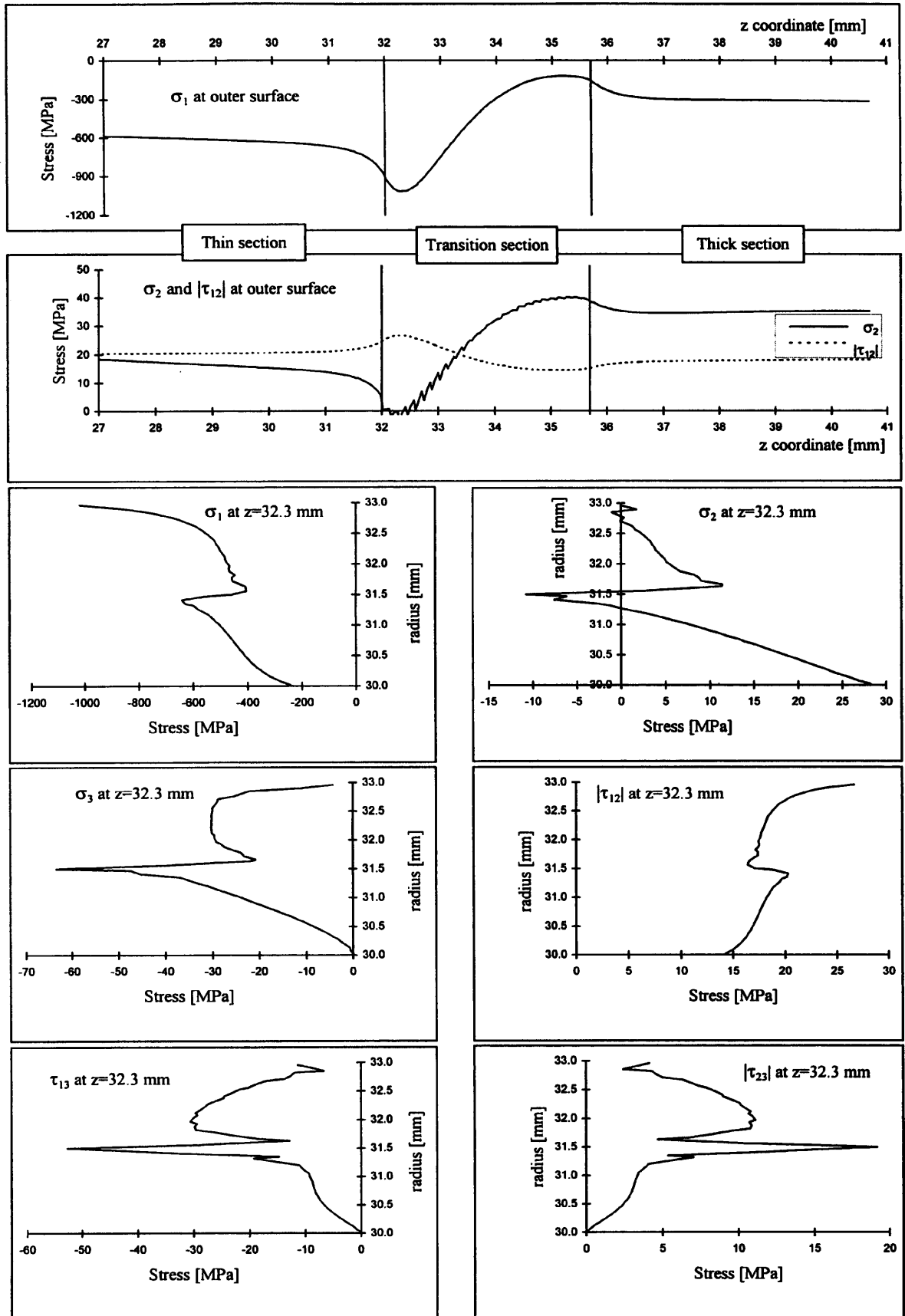
Figure 4.12 Lamina stresses for the stepped model: all-carbon/epoxy tube, bending load, compressed side.
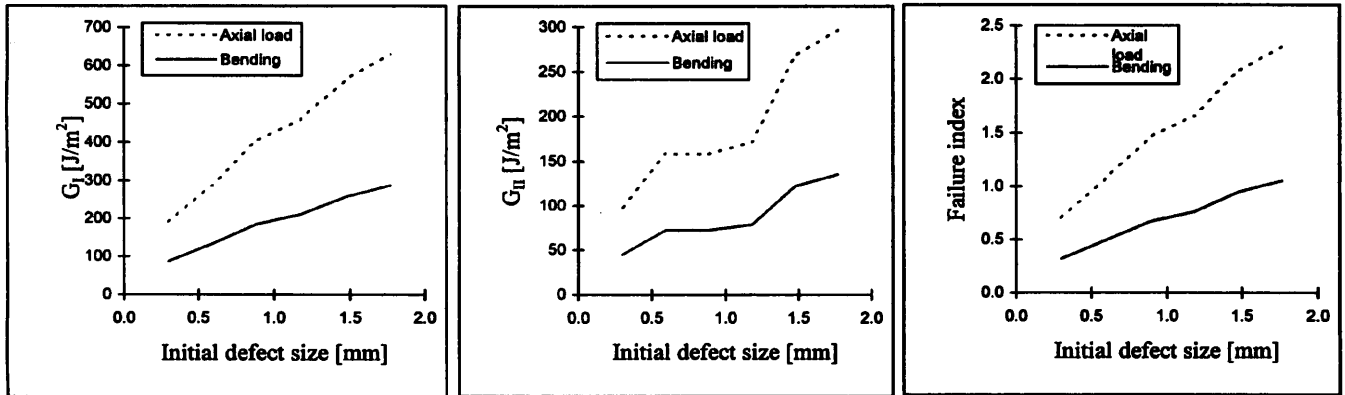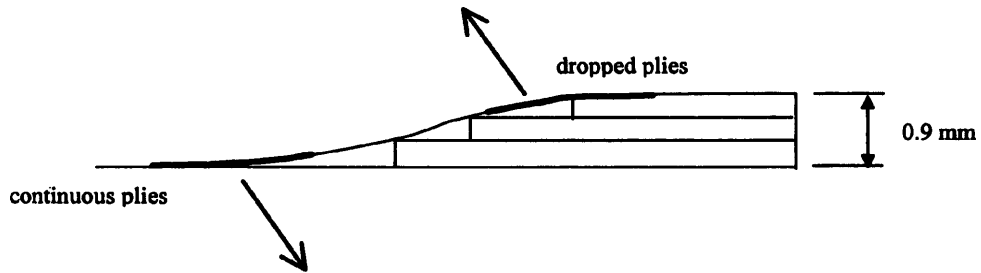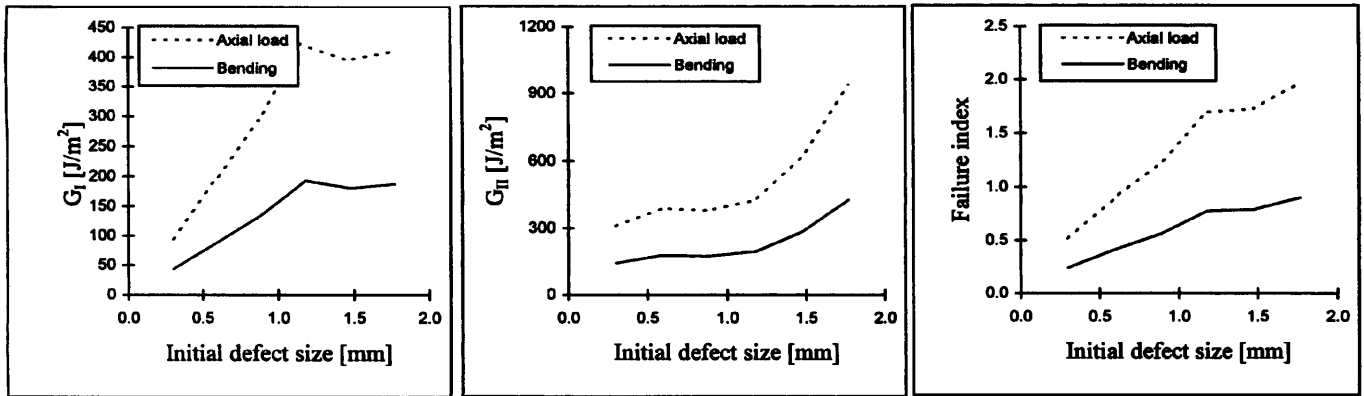
Figure 4.13 Strain energy release rates and failure indices for the all-carbon tube.
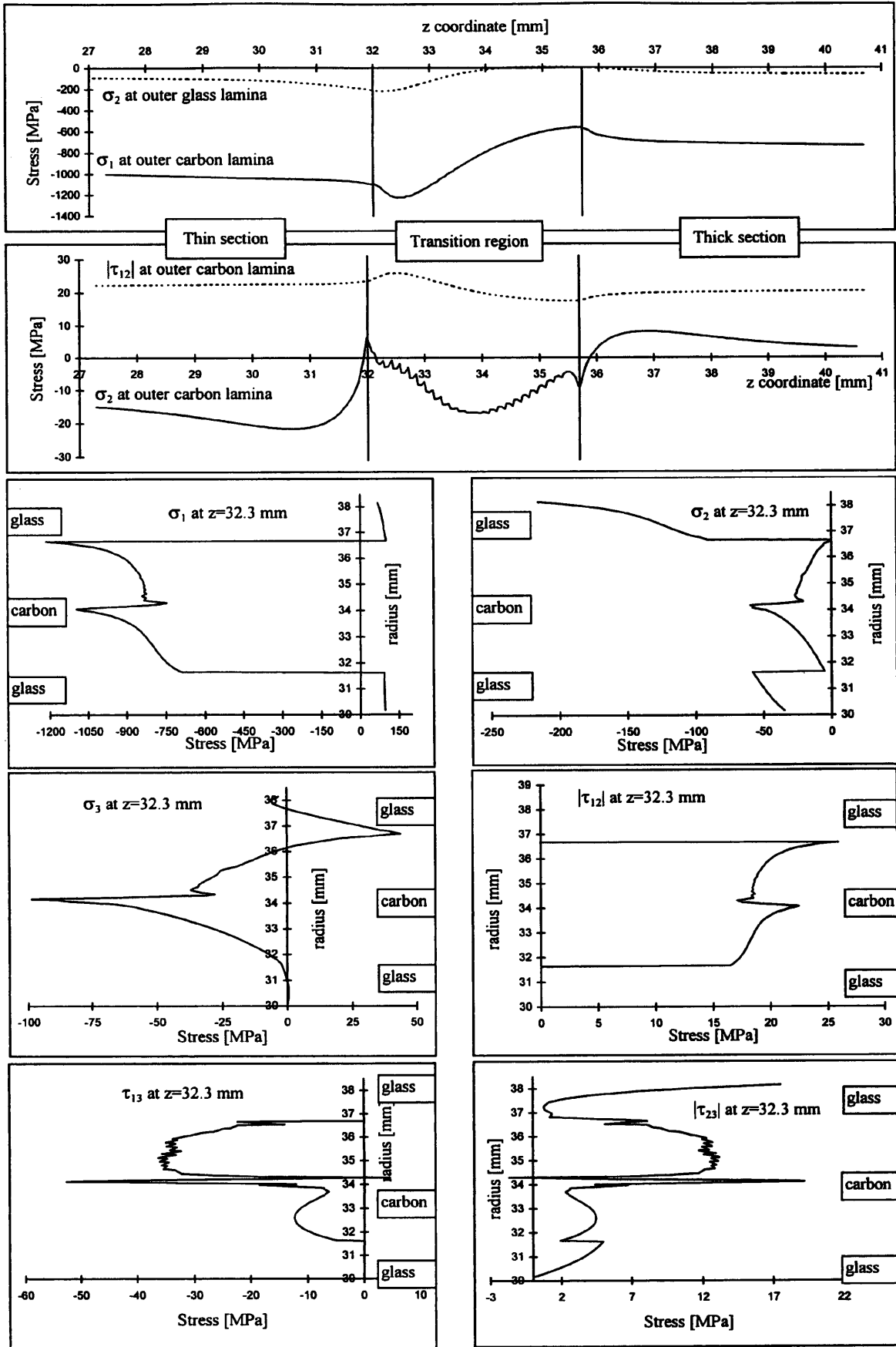
Figure 4.14 Lamina stresses for the hybrid, stepped, +/- 20° carbon tube, bending load, compressed side.

175
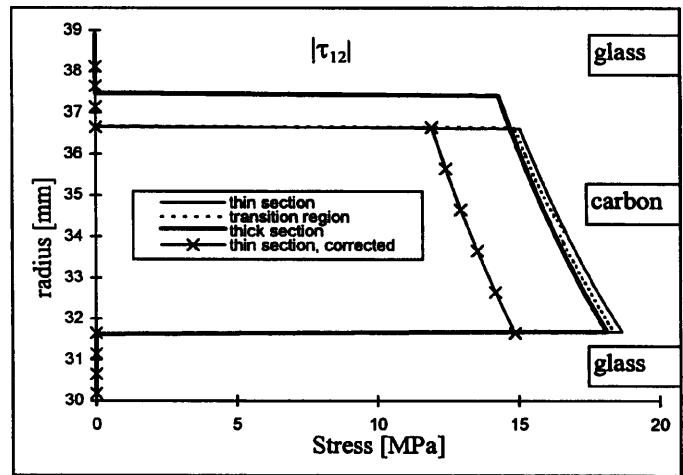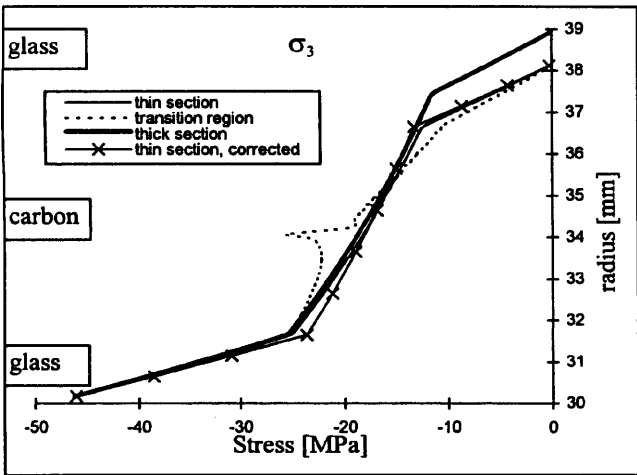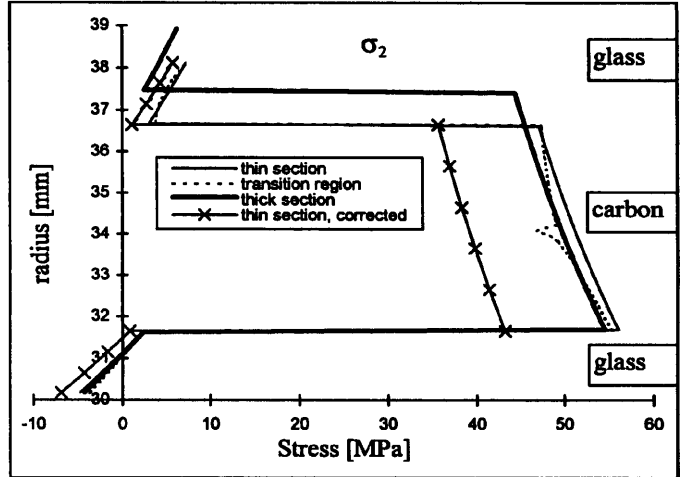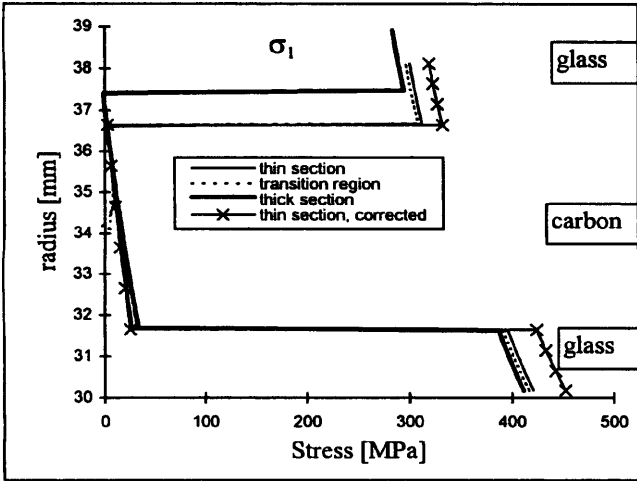
Figure 4.15 Lamina stresses for the hybrid, +/- 20° carbon tube, internal pressure of 46.6 MPa.
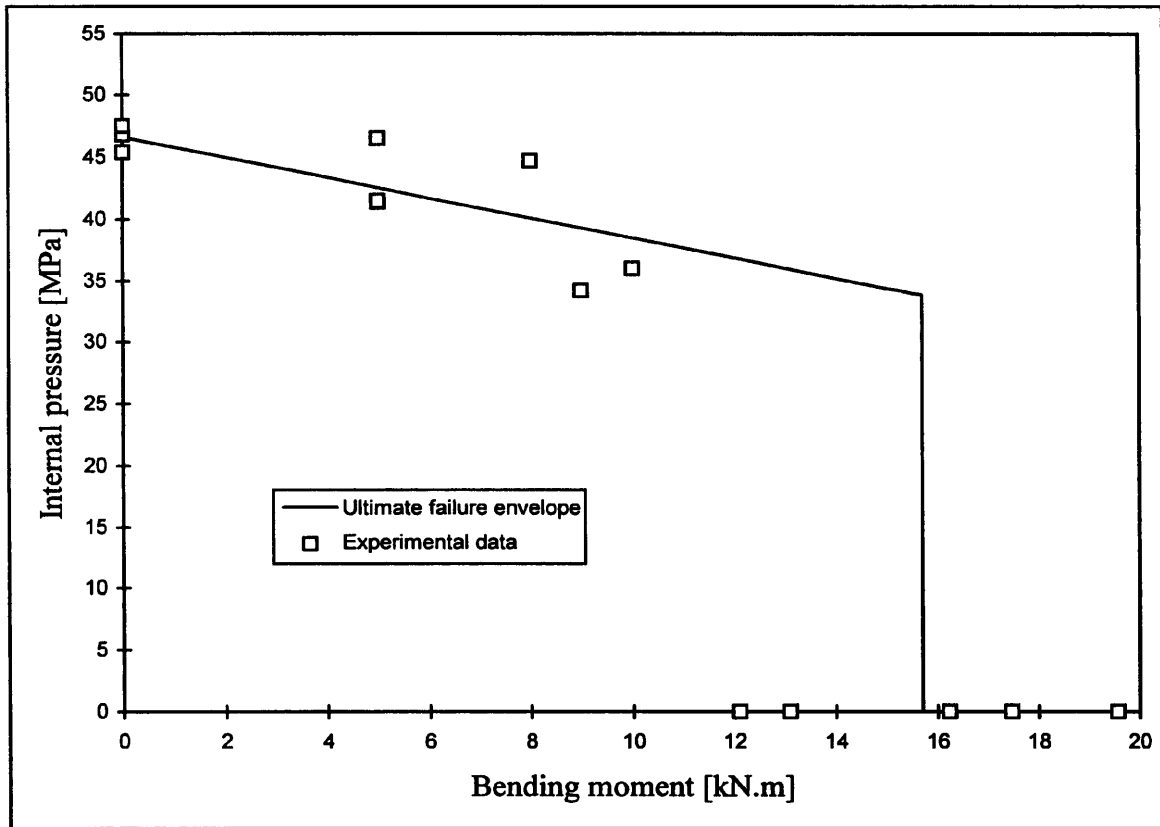
Figure 4.16 Ultimate failure envelope, according to the maximum stress criterion.
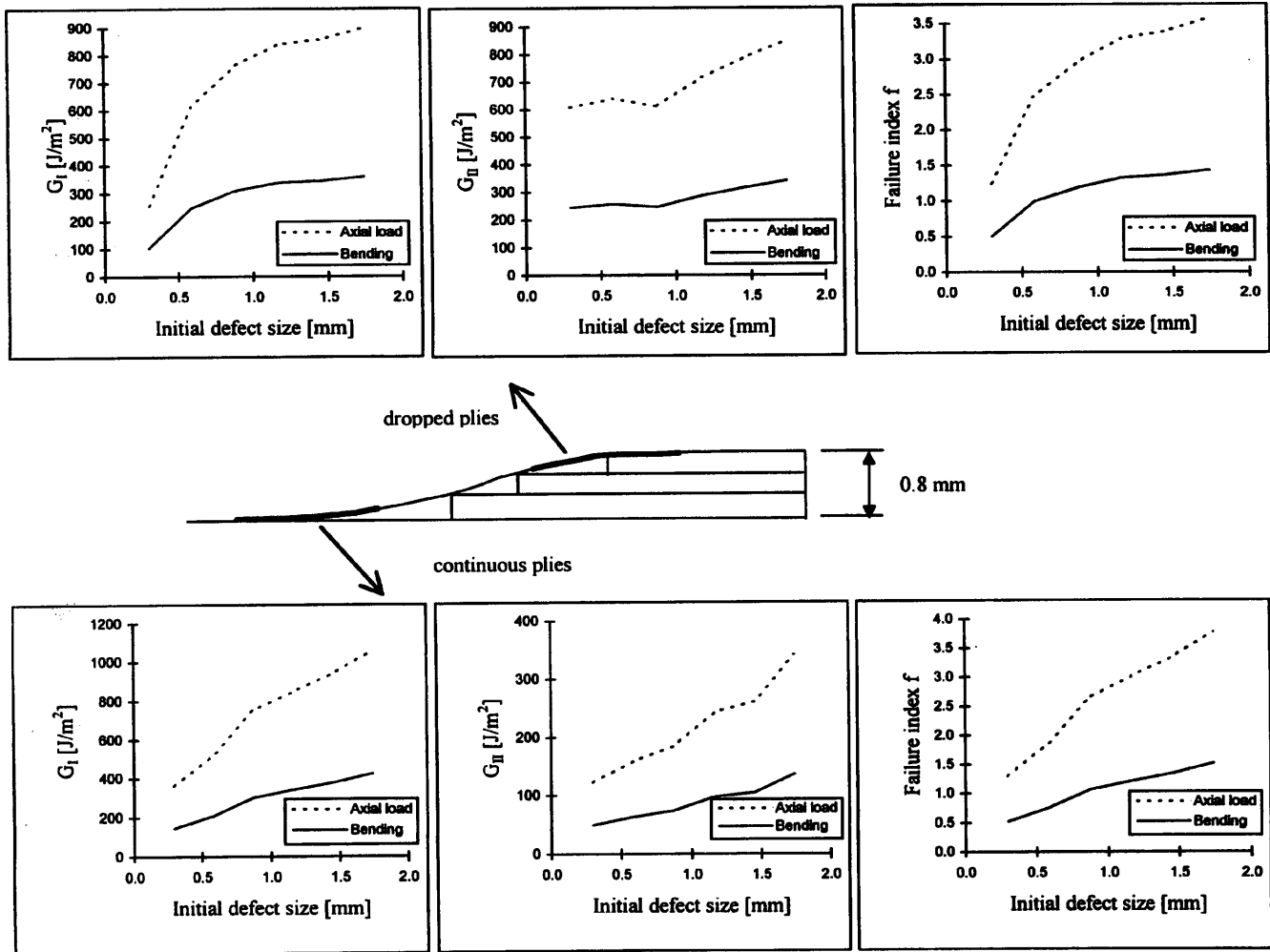
Figure 4.17 Strain energy release rates and failure indices for the hybrid, stepped, +/-20° carbon tube.
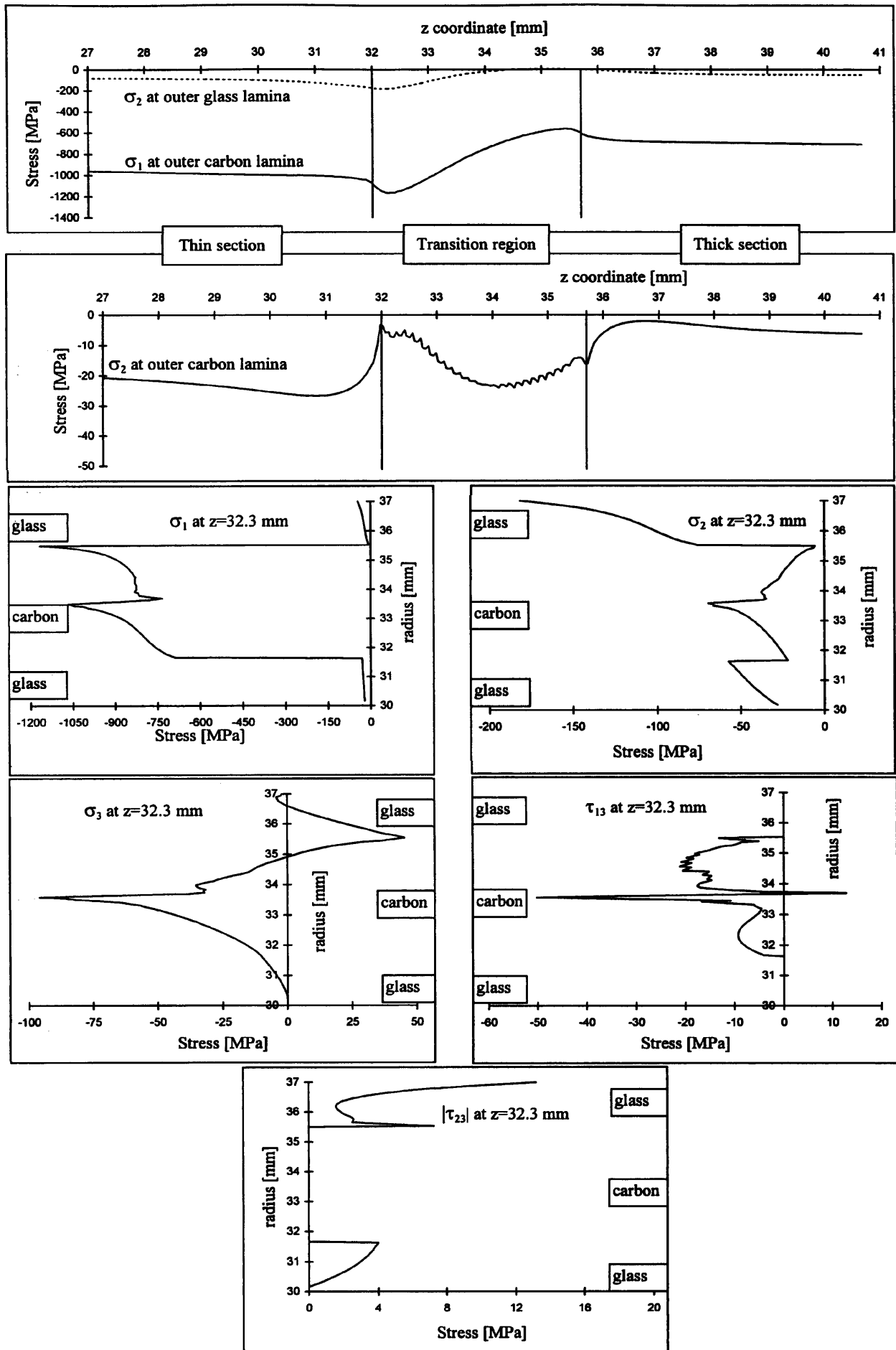
Figure 4.18 Lamina stresses for the hybrid, unidirectional tube, bending load, compressed side.
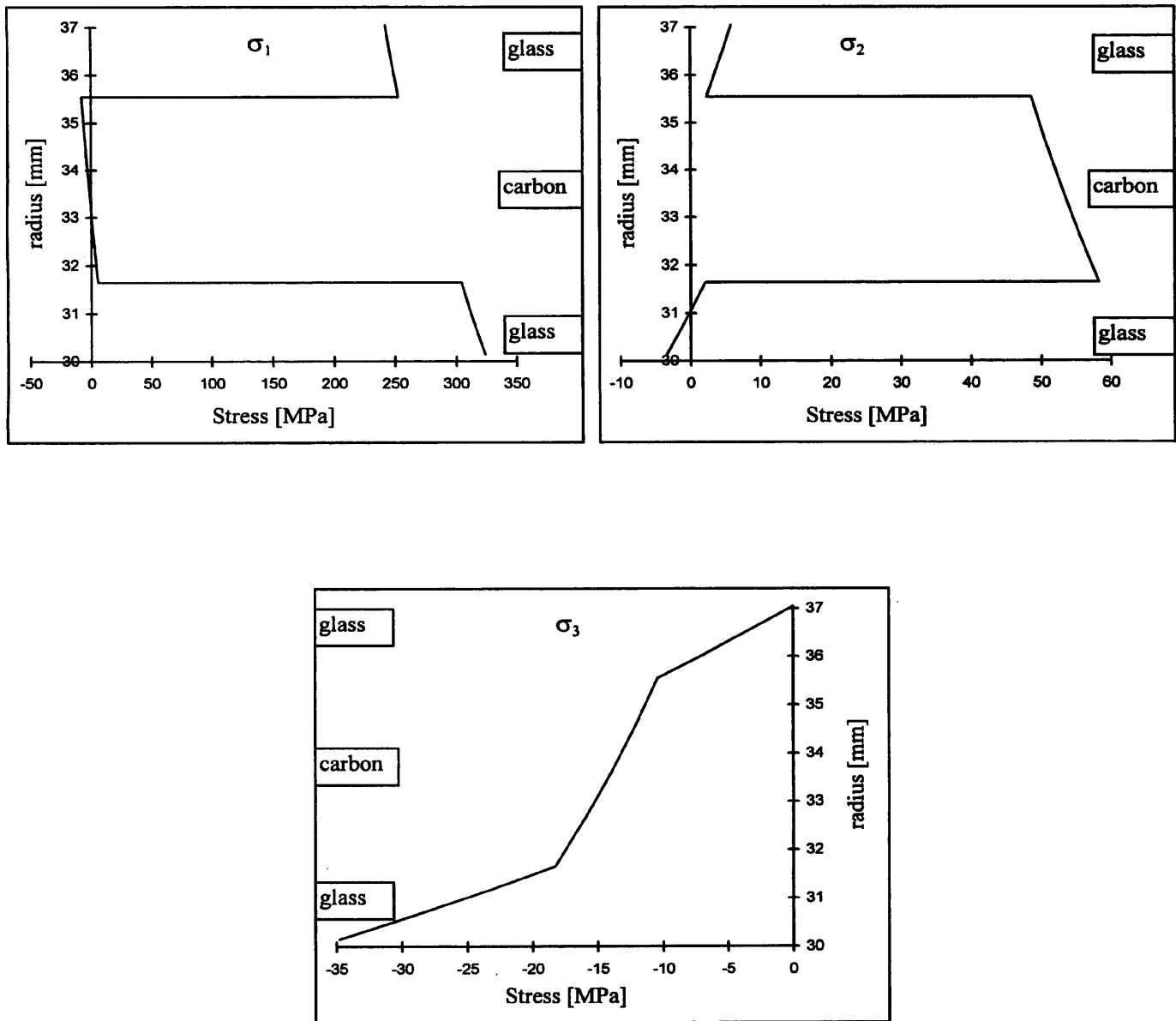
Figure 4.19 Lamina stresses for the hybrid, stepped, 0° carbon tube, internal pressure of 34.8 MPa.
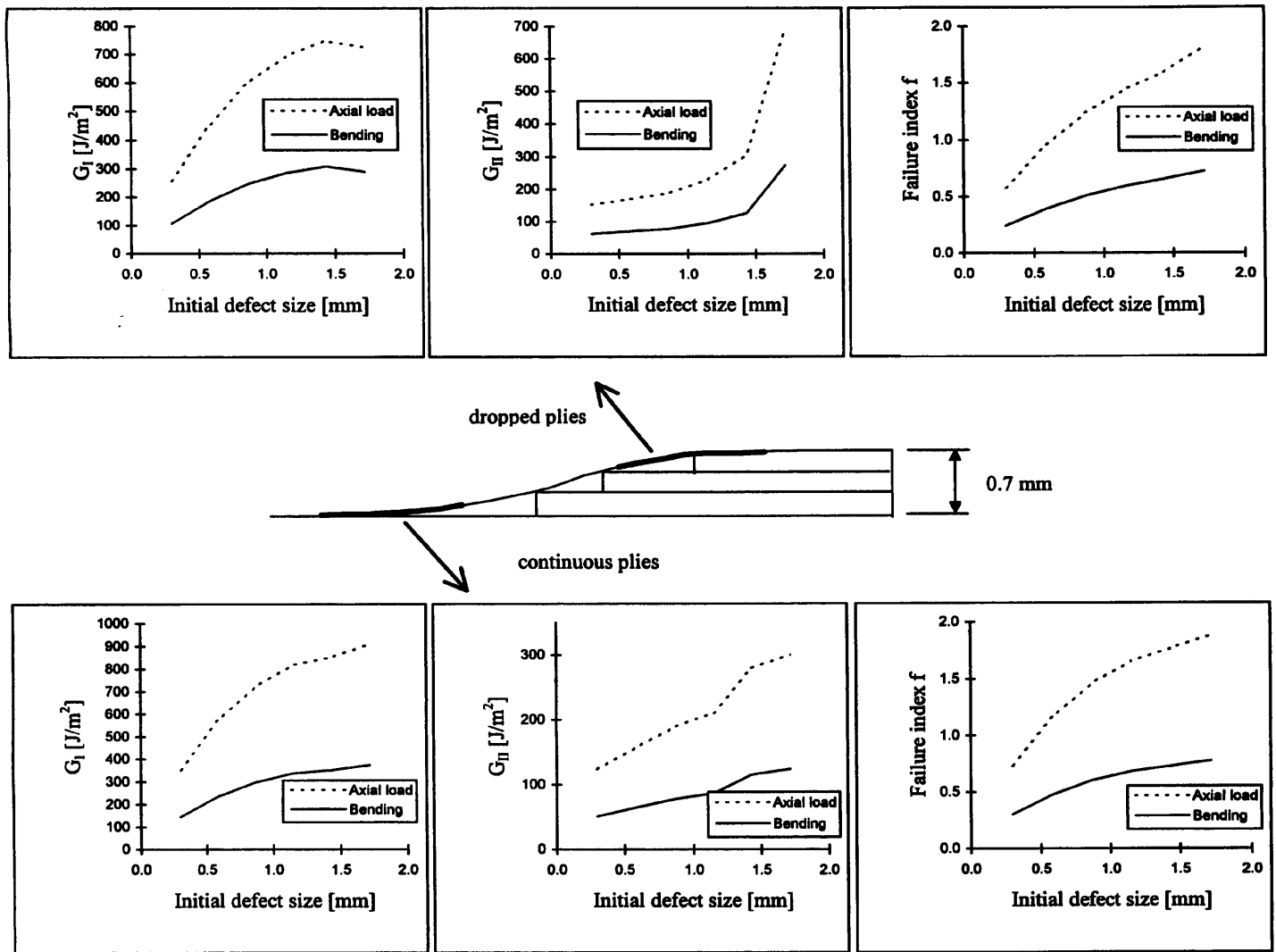
Figure 4.20 Strain energy release rates and failure indices for the hybrid, stepped, $0°$ carbon tube.
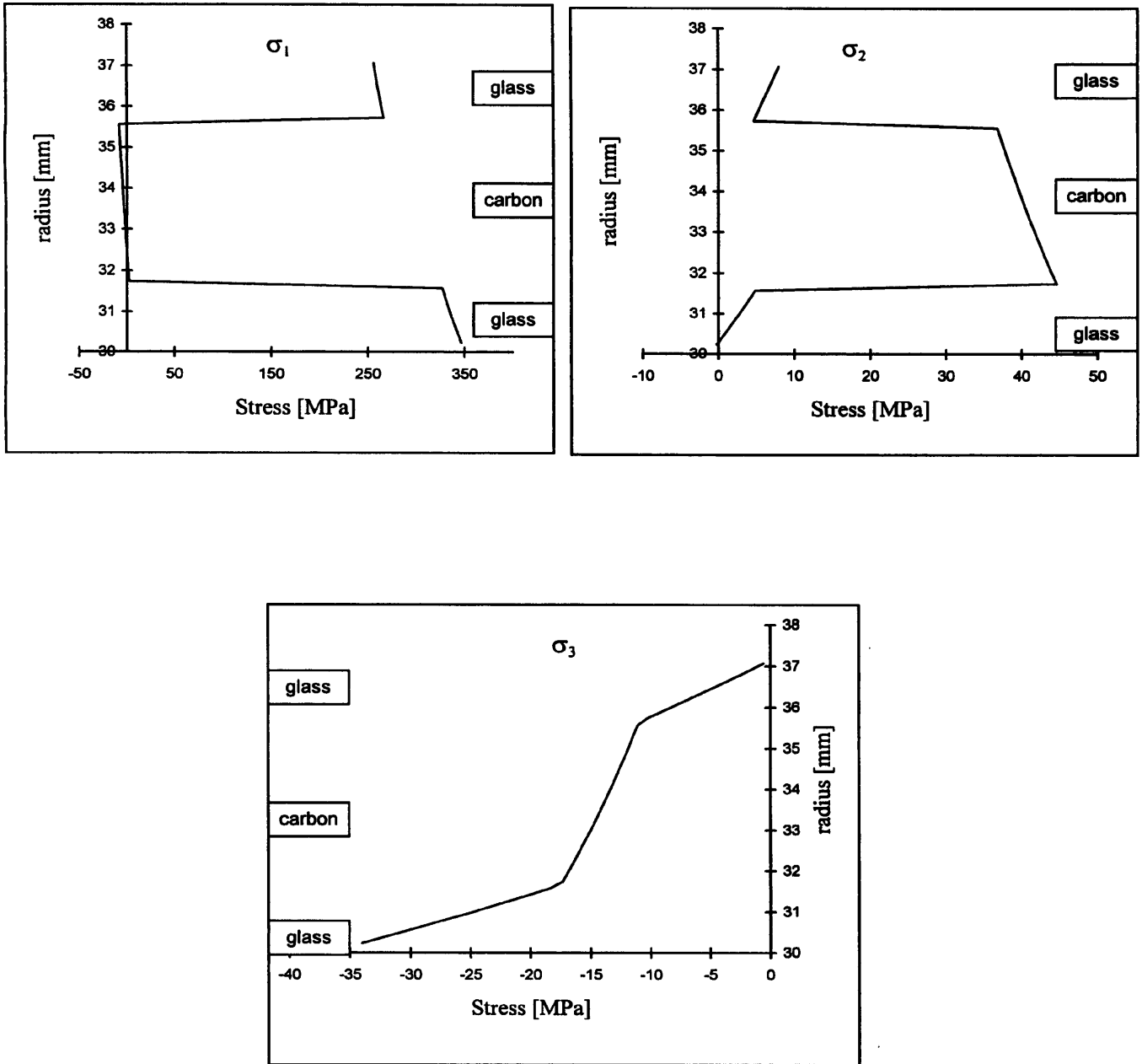
Figure 4.21 Lamina stresses for the hybrid, plain, 0° carbon tubes,internal pressure of 35.1 MPa.

CHAPTER 5 THICK COMPOSITE TUBE MODELS

CHAPTER 5 THICK COMPOSITE TUBE MODELS

5.1 INTRODUCTION

The loads applied to the composite tapered joint are internal or external pressures, axial loads and bending moments. The first three are axisymmetric loads, whilst the relevant results for the last can be obtained from an axisymmetric analysis, as demonstrated in the previous chapter. Thus, if the problem was restricted to the study of a plain tube, one could use simplified, yet three-dimensional, methods.

However, we will have to consider the thickness transition region. This constitutes a stress concentration region for all lamina stresses. We have seen in Chapter 4 that the maximum in-plane stresses (σ_1, σ_2 and τ_{12}) were localised at the inner and outer laminae, for the internal pressure and bending load cases, respectively. The peak out-of-plane stresses (σ_3, τ_{13} and τ_{23}) occurred at the mid-thickness of the carbon sublaminate. Failure by delamination, associated with the out-of-plane stresses, was shown not to prevail over the in-plane types of failure. This held for the two main load cases of a tapered joint, internal pressures and bending moments. The stresses due to internal pressure were not significantly affected by the geometry of the transition region, as one might expect. For the pure bending case, the high fracture toughness values of the carbon/epoxy pre-preg caused the tubes to fail first by axial compressive collapse of the fibres.

The possibility of a preferred occurrence of delamination only existed for pure axial loads, or, at least, for very high axial loads, compared with the bending moments. This condition is unlikely to exist in the tapered joint of a riser, whose specific function is to resist the large bending moments at the base. So, for designing purposes, we have only to take into account the stress concentration due to the difference in thickness affecting the in-plane stresses. The model can be uniform, in the sense that no resin pocket needs to be modelled at all. This introduces a significant simplification to the task, given the variability of the resin pocket lay-out shown in Chapter 3.

The modelling of the composite tapered joint behaviour can then be divided in two parts, related to two distinct regions of the tube. Firstly, a thick laminate model addresses the stress field in the plain portion of the tube, away from the ply drop region. Then, the local geometry of the thickness transition region is considered, aiming to describe the perturbation it causes to the stress fields.

The first model employed the methodology described by Soden [72], related to a special axisymmetric case where the longitudinal strain is considered constant and no shear stress is present. This constant strain state can occur if the length of the tube is large enough. The approach is thus suitable for a plain riser tube or to the portions of a tapered joint sufficiently far from the ply drop-off. The possible load conditions are internal or external pressures and axial forces. The bending moment loading results can be obtained from the axisymmetric ones, as demonstrated earlier. This method was implemented by the author in a FORTRAN programme called TUBEPLAIN.

The second model was based on the variational formulation proposed by Pagano [57]. The problem considered is still axisymmetric, but the axial strain can vary and the out-of-plane shear stress is introduced. Again, all the relevant load cases, including the bending moments, can be considered. The programme that performs the calculations was called TUBEDROP.

The chapter starts with a description of the basic equations that govern the axisymmetric, thick composite tube analysis in general. After the models are discussed, some simulations show the influence of different dropped ply tube configurations on the maximum stresses developed.

5.2 BASIC EQUATIONS

In this section the basic equations for a three-dimensional, small displacement, linear elastic representation of a thick laminated tube are presented. The starting point are the equilibrium equations in cylindrical coordinates, as given by Varadan and Bhaskar [64]. The static equilibrium of an infinitesimal tube element gives the following expressions, ignoring body

185

forces:

$$\frac{\partial \sigma_r}{\partial r} + \frac{1}{r}\frac{\partial \tau_{r\theta}}{\partial \theta} + \frac{\partial \tau_{rz}}{\partial z} + \frac{\sigma_r}{r} - \frac{\sigma_\theta}{r} = 0$$

$$\frac{\partial \tau_{r\theta}}{\partial r} + \frac{1}{r}\frac{\partial \sigma_\theta}{\partial \theta} + \frac{\partial \tau_{\theta z}}{\partial z} + 2\frac{\tau_{r\theta}}{r} = 0 \qquad (5.1)$$

$$\frac{\partial \tau_{rz}}{\partial r} + \frac{1}{r}\frac{\partial \tau_{\theta z}}{\partial \theta} + \frac{\partial \sigma_z}{\partial z} + \frac{\tau_{rz}}{r} = 0$$

The next step is to define the 3D constitutive equations for linear elastic, orthotropic materials. As already shown in Chapter 4, the hybrid tube with balanced angle-ply carbon sublaminate can be considered as made of an equivalent, "smeared", specially orthotropic material. We have the following relations between stresses and strains, given by the rotated stiffness coefficients (expressions 4.8), referred to the cylindrical directions:

$$\begin{Bmatrix} \sigma_r \\ \sigma_\theta \\ \sigma_z \\ \tau_{r\theta} \\ \tau_{rz} \\ \tau_{\theta z} \end{Bmatrix} = \begin{bmatrix} \overline{C}_{11} & \overline{C}_{12} & \overline{C}_{13} & 0 & 0 & 0 \\ \overline{C}_{21} & \overline{C}_{22} & \overline{C}_{23} & 0 & 0 & 0 \\ \overline{C}_{31} & \overline{C}_{32} & \overline{C}_{33} & 0 & 0 & 0 \\ 0 & 0 & 0 & \overline{C}_{44} & 0 & 0 \\ 0 & 0 & 0 & 0 & \overline{C}_{55} & 0 \\ 0 & 0 & 0 & 0 & 0 & \overline{C}_{66} \end{bmatrix} \begin{Bmatrix} \varepsilon_r \\ \varepsilon_\theta \\ \varepsilon_z \\ \gamma_{r\theta} \\ \gamma_{rz} \\ \gamma_{\theta z} \end{Bmatrix} \qquad (4.9)$$

The inverse relation makes use of the rotated compliance matrix, whose terms are given by formulas 4.13 of Chapter 4:

$$\begin{Bmatrix} \varepsilon_r \\ \varepsilon_\theta \\ \varepsilon_z \\ \gamma_{r\theta} \\ \gamma_{rz} \\ \gamma_{\theta z} \end{Bmatrix} = \begin{bmatrix} \overline{S}_{11} & \overline{S}_{12} & \overline{S}_{13} & 0 & 0 & 0 \\ \overline{S}_{21} & \overline{S}_{22} & \overline{S}_{23} & 0 & 0 & 0 \\ \overline{S}_{31} & \overline{S}_{32} & \overline{S}_{33} & 0 & 0 & 0 \\ 0 & 0 & 0 & \overline{S}_{44} & 0 & 0 \\ 0 & 0 & 0 & 0 & \overline{S}_{55} & 0 \\ 0 & 0 & 0 & 0 & 0 & \overline{S}_{66} \end{bmatrix} \begin{Bmatrix} \sigma_r \\ \sigma_\theta \\ \sigma_z \\ \tau_{r\theta} \\ \tau_{rz} \\ \tau_{\theta z} \end{Bmatrix} \qquad (5.2)$$

The 3D strain-displacement relationships in cylindrical coordinates can be written as shown

by Flugge [107] and Fung [108]:

$$\varepsilon_r = \frac{\partial u}{\partial r}, \quad \varepsilon_\theta = \frac{1}{r}\frac{\partial v}{\partial \theta} + \frac{u}{r}, \quad \varepsilon_z = \frac{\partial w}{\partial z}$$

$$\gamma_{r\theta} = \frac{1}{r}\frac{\partial u}{\partial \theta} + \frac{\partial v}{\partial r} - \frac{v}{r}, \quad \gamma_{rz} = \frac{\partial w}{\partial r} + \frac{\partial u}{\partial z}, \quad \gamma_{\theta z} = \frac{\partial v}{\partial z} + \frac{1}{r}\frac{\partial w}{\partial \theta}$$

(5.3)

5.3 AXISYMMETRIC, CONSTANT AXIAL STRAIN MODEL

5.3.1 FORMULATION OF THE MODEL

The basic assumptions in this case are as stated by Soden [72]. In an axisymmetric problem, the shear stresses $\tau_{r\theta}$, $\tau_{\theta z}$ and shear strains $\gamma_{r\theta}$, $\gamma_{\theta z}$ vanish. The tube is long enough to cause a "generalised" constant ε_z plane strain state to exist. Plane sections normal to the axis of the tube remain plane and normal after deformation. Consequently, γ_{rz} and so τ_{rz} - according to expression 4.9 - vanish as well. The equilibrium equations 5.1 are written:

$$\sigma_\theta = \sigma_r + r\frac{\partial \sigma_r}{\partial r}$$

$$\frac{\partial \sigma_z}{\partial z} = 0$$

(5.4)

The strain-displacement (relations 5.3) simplify to:

$$\varepsilon_r = \frac{\partial u}{\partial r}, \quad \varepsilon_\theta = \frac{u}{r}$$

(5.5)

Substituting the second equation into the first yields:

$$\varepsilon_r = \frac{\partial u}{\partial r} = \frac{\partial(\varepsilon_\theta r)}{\partial r} \Rightarrow \varepsilon_r = \varepsilon_\theta + r\frac{\partial \varepsilon_\theta}{\partial r}$$

(5.6)

In the present case it is better to write down the stress-strain equations in terms of the

flexibility matrix. As all shear components vanished, we can refer only to the normal stresses and strains components:

$$
\begin{Bmatrix} \varepsilon_r \\ \varepsilon_\theta \\ \varepsilon_z \end{Bmatrix} = \begin{bmatrix} \overline{S}_{11} & \overline{S}_{12} & \overline{S}_{13} \\ \overline{S}_{21} & \overline{S}_{22} & \overline{S}_{23} \\ \overline{S}_{31} & \overline{S}_{32} & \overline{S}_{33} \end{bmatrix} \begin{Bmatrix} \sigma_r \\ \sigma_\theta \\ \sigma_z \end{Bmatrix}
\tag{5.7}
$$

From the third row of expression we have:

$$
\sigma_z = \frac{1}{\overline{S}_{33}} \left(\varepsilon_z - \overline{S}_{31}\sigma_r - \overline{S}_{32}\sigma_\theta \right)
\tag{5.8}
$$

Substituting σ_z as given above back into the first two rows yields the following two equations:

$$
\varepsilon_r = \left(\overline{S}_{11} - \frac{\overline{S}_{13}^2}{\overline{S}_{33}} \right)\sigma_r + \left(\overline{S}_{12} - \frac{\overline{S}_{13}\overline{S}_{23}}{\overline{S}_{33}} \right)\sigma_\theta + \frac{\overline{S}_{13}}{\overline{S}_{33}}\varepsilon_z
\tag{5.9}
$$

$$
\varepsilon_\theta = \left(\overline{S}_{12} - \frac{\overline{S}_{13}\overline{S}_{23}}{\overline{S}_{33}} \right)\sigma_r + \left(\overline{S}_{22} - \frac{\overline{S}_{23}^2}{\overline{S}_{33}} \right)\sigma_\theta + \frac{\overline{S}_{23}}{\overline{S}_{33}}\varepsilon_z
\tag{5.10}
$$

Now, the expression for σ_θ in 5.4 is used in both equations 5.9 and 5.10:

$$
\varepsilon_r = \left[\overline{S}_{11} + \overline{S}_{12} - \frac{\overline{S}_{13}}{\overline{S}_{33}}\left(\overline{S}_{13} + \overline{S}_{23} \right) \right]\sigma_r + \left(\overline{S}_{12} - \frac{\overline{S}_{13}\overline{S}_{23}}{\overline{S}_{33}} \right)r\frac{\partial\sigma_r}{\partial r} + \frac{\overline{S}_{13}}{\overline{S}_{33}}\varepsilon_z
\tag{5.11}
$$

$$
\varepsilon_\theta = \left[\overline{S}_{12} + \overline{S}_{22} - \frac{\overline{S}_{23}}{\overline{S}_{33}}\left(\overline{S}_{13} + \overline{S}_{23} \right) \right]\sigma_r + \left(\overline{S}_{22} - \frac{\overline{S}_{23}^2}{\overline{S}_{33}} \right)r\frac{\partial\sigma_r}{\partial r} + \frac{\overline{S}_{23}}{\overline{S}_{33}}\varepsilon_z
\tag{5.12}
$$

The differentiation of 5.12 with respect to r, knowing that ε_z is constant, gives:

$$
\frac{\partial\varepsilon_\theta}{\partial r} = \left(\overline{S}_{22} - \frac{\overline{S}_{23}^2}{\overline{S}_{33}} \right)r\frac{\partial^2\sigma_r}{\partial r^2} + \left[\overline{S}_{12} + 2\overline{S}_{22} - \frac{\overline{S}_{23}}{\overline{S}_{33}}\left(\overline{S}_{13} + 2\overline{S}_{23} \right) \right]\frac{\partial\sigma_r}{\partial r}
\tag{5.13}
$$

Finally, expressions 5.11, 5.12 and 5.13 are substituted into the strain-displacements relations

5.6 to deliver the following ordinary differential equation:

$$r^2 \frac{\partial^2 \sigma_r}{\partial r^2} + 3r \frac{\partial \sigma_r}{\partial r} + A_1 \sigma_r = A_2 \varepsilon_z \qquad (5.14)$$

where the constants A_1 and A_2 are:

$$A_1 = 1 - \frac{\left(\overline{S}_{11}\overline{S}_{33} - \overline{S}_{13}^2\right)}{\left(\overline{S}_{22}\overline{S}_{33} - \overline{S}_{23}^2\right)} \quad and \quad A_2 = \frac{\left(\overline{S}_{13} - \overline{S}_{23}\right)}{\left(\overline{S}_{22}\overline{S}_{33} - \overline{S}_{23}^2\right)} \qquad (5.15)$$

A particular solution for 5.14 is simply:

$$\sigma_r = A_3 \varepsilon_z \qquad (5.16)$$

where:

$$A_3 = \begin{cases} \dfrac{A_2}{A_1}, & if \ A_1 \neq 0 \\[3mm] \dfrac{A_2}{2} \ln r, & if \ A_1 = 0 \end{cases}$$

The homogeneous equation

$$r^2 \frac{\partial^2 \sigma_r}{\partial r^2} + 3r \frac{\partial \sigma_r}{\partial r} + A_1 \sigma_r = 0 \qquad (5.17)$$

is the Euler equation, as Zwillinger [109] shows. It is solvable via the following transformation of variables:

$$r = e^t$$
$$\frac{\partial \sigma_r}{\partial r} = e^{-t} \frac{\partial \sigma_t}{\partial t} \qquad (5.18)$$
$$\frac{\partial^2 \sigma_r}{\partial r^2} = e^{-2t} \left(\frac{\partial^2 \sigma_t}{\partial t^2} - \frac{\partial \sigma_t}{\partial t} \right)$$

Equation 5.17 is then written as:

$$\frac{\partial^2 \sigma_t}{\partial t^2} + 2\frac{\partial \sigma_t}{\partial t} + A_1\sigma_t = 0 \qquad (5.19)$$

This is a linear, constant coefficients, ordinary differential equation. Its characteristic equation is:

$$\lambda^2 + 2\lambda + A_1 = 0 \Rightarrow \lambda = -1 \pm \beta, \qquad \beta = \sqrt{1-A_1} \qquad (5.20)$$

So the solution is:

$$\sigma_t = C_1 e^{(-1+\beta)t} + C_2 e^{(-1-\beta)t} \qquad (5.22)$$

Or, using the transformations 5.18:

$$\sigma_r = C_1 r^{(-1+\beta)} + C_2 r^{(-1-\beta)} \qquad (5.23)$$

Finally, the general solution of equation 5.14 is the sum of the complementary solution 5.23 with the particular one, 5.16:

$$\sigma_r = \frac{1}{r}\left(C_1 r^\beta + C_2 r^{-\beta}\right) + A_3\varepsilon_z \qquad (5.24)$$

where C_1, C_2 and ε_z are constants to be determined. From 5.4 it is deduced that:

$$\sigma_\theta = \frac{\beta}{r}\left(C_1 r^\beta - C_2 r^{-\beta}\right) + A_3\varepsilon_z \qquad (5.25)$$

Finally formula 5.8 leads to:

$$\sigma_z = \frac{\left[1 - (\overline{S}_{31} + \overline{S}_{32})A_3\right]}{\overline{S}_{33}}\varepsilon_z - \frac{(\overline{S}_{31} + \overline{S}_{32}\beta)C_1 r^\beta}{\overline{S}_{33}}\frac{1}{r} - \frac{(\overline{S}_{31} - \overline{S}_{32}\beta)C_2 r^{-\beta}}{\overline{S}_{33}}\frac{1}{r} \qquad (5.26)$$

Consider now a laminated tube composed of N layers each with different material properties. The internal radius of the jth layer is r_j, $j=1,2,3,....N$. The thickness of each layer is h_j. The internal pressure, axial force and external pressure are represented by P_i, F and P_e, respectively. One can apply the boundary conditions associated with each layer. Also, for a

given internal layer the boundary conditions represent the continuity constraints at its interfaces. The boundary (or continuity) conditions are:

- At $r = r_1$: $\sigma_r = -P_i$ (1 equation)

- At $r = r_j$: σ_r (layer j-1) = σ_r (layer j) , $j = 2, N$ (N-1 equations)

- At $r = r_j$: u (layer j-1) = u (layer j) , $j = 2, N$ (N-1 equations)

- $\sum_{j=1}^{N} 2\pi \int_{r_j}^{r_j + h_j} \sigma_z r\, dr = F$ (1 equation)

- At $r = r_N + h_N$: $\sigma_r = -P_e$ (1 equation)

There are 2N+1 unknown constants: C_1 and C_2 for each layer plus the overall ε_z, and 2N+1 equations. The resulting system is solved by a FORTRAN programme called TUBEPLAIN, to stress its limited scope to plain, yet thick, composite tubes.

In order to verify the accuracy of the program TUBEPLAIN, the results provided by it were compared to the FEA of specimens HST, at its thinner part, away from the thickness transition region. The load cases considered were the average failure values for those specimens, i.e., an internal pressure of 46.6 MPa and a bending moment of 15.7 kNm. The bending results were obtained from the axisymmetric ones, as demonstrated in Chapter 4.

Figures 5.1 and 5.2 show the comparisons, for the internal pressure and the bending moment cases, respectively. It can be seen that both results compare well. The E_1 longitudinal stiffness considered for the glass/epoxy sublaminate was the original value given by the supplier, 41 GPa. The lamina stresses can be obtained from the stresses referred to the cylindrical directions as shown in Chapter 4 (from expressions 4.16).

5.4 AXISYMMETRIC GENERAL MODEL

5.4.1 DEVELOPMENT OF THE MODEL

This section discusses a more general approach for the analysis of a thick composite tube, now allowing for varying axial strains, nonzero interlaminar shear stress and tapered thickness. It

uses the methodology proposed by Pagano [57], simplified where possible and adapted to our problem. The method is based on the mixed variational theorem introduced by Reissner [110,111].

Consider an axisymmetric elastic body of volume V and external surface S as shown in figure 5.3. The volume is divided into N sub-volumes V_k, with surface S_k each. Pagano applied the variational expression due to Reissner (developed in appendix A) to every subvolume or layer to formulate the elasticity boundary value problem:

$$\delta J_k = \int_{V_k}\left[\left(\frac{u_{i,j}+u_{j,i}}{2}-\frac{\partial U^*}{\partial \sigma_{ij}}\right)\delta\sigma_{ij}-\sigma_{ij,j}\delta u_i\right]^{(k)} dV_k+\int_{S_{k\sigma}}(T_i-\overline{T}_i)^{(k)}\delta u_i^{(k)} dS_k-\int_{S_{ku}}(u_i-\overline{u}_i)^{(k)}\delta T_i^{(k)} dS_k \qquad (5.27)$$

where J_k is an energy functional, U^* is the complementary strain energy density function and T_i are the surface tractions. The bar over a variable means prescribed value. The indices i and j refer to the cylindrical coordinates r, θ and z.

Considering every layer with volume V_k and surface S_k we can state that:

- The bottom of the first layer and the top of the N-th layer are part of S.

- The lateral edges of every layer also belong to S.

- $S_{k\sigma}$ is that portion of S where the tractions are prescribed, S_σ, and S_{ku} is that part of it where the displacements are prescribed, S_u.

- The remaining layer surfaces are the interfaces I_k, common to subvolumes V_k and V_{k+1}. Because they are internal surfaces, it is not possible to prescribe any traction or displacement on them. We can, however apply either traction or displacement continuity conditions between the layer under the interface, V_k and the layer above it, V_{k+1}. In the present analysis, traction continuity conditions were chosen.

Following the previous considerations, the first variation of the functional J is obtained from the summation over the N subvolumes and the N-1 interfaces. The first variation of the functional is then made zero through independent variations of displacements and stresses, to deliver the relations that allow the problem to be solved. Adjacent layers can be made of the same material or different materials. The variational expression reads:

$$\delta J = \sum_{k=1}^{N} \int_{V_k} \left[\left(\frac{u_{i,j} + u_{j,i}}{2} - \frac{\partial U^*}{\partial \sigma_{ij}} \right) \delta \sigma_{ij} - \sigma_{ij,j} \delta u_i \right]^{(k)} dV_k + \int_{S_\sigma} (T_i - \overline{T}_i) \delta u_i \, dS - \int_{S_u} (u_i - \overline{u}_i) \delta T_i \, dS +$$

$$+ \sum_{k=1}^{N-1} \int_{I_k} \left(T_i^{(k)} \delta u_i^{(k)} + T_i^{(k+1)} \delta u_i^{(k+1)} \right) dI_k = 0 \qquad (5.28)$$

The comma in the subscripts means differentiation. As Harrison and Johnson [70] noted, the sub-volumes are taken in the form of layers because this is the most suitable approach to treat laminates. The layers may have curved boundaries and varying thickness. The axial limits of the whole volume are the axial coordinates z_a and z_b as shown by figure 5.3. The figure also shows a generic k-th layer, limited by the functions $r_a^{(k)}(z)$ and $r_b^{(k)}(z)$, that describe the form of its inner and outer boundaries, respectively.

Considering the 3D, axisymmetric geometry of the problem, the boundary S_k of a given subvolume V_k is then composed of the surfaces $r_a^{(k)}(z)$ and $r_b^{(k)}(z)$ and the planes $z=z_a$ and $z=z_b$. The slope of the surface $r_a^{(k)}(z)$, shown in figure 5.3, is given by the angle $\gamma_a^{(k)}(z)$, where:

$$tan\, \gamma_a^{(k)} = \frac{dr_a^{(k)}(z)}{dz} = r_a'^{(k)}(z) \qquad (5.29)$$

The single dash means differentiation with respect to z. Along the cylindrical geratrix described by $r_a^{(k)}(z)$ the infinitesimal curve length is:

$$dS = \sqrt{1 + r_a'^{(k)}}\, dz = \sqrt{1 + tan^2\, \gamma_a^{(k)}}\, dz = sec\, \gamma_a^{(k)} dz \qquad (5.30)$$

The complementary strain energy density function is given by:

$$U^* = \frac{1}{2} (\overline{S}_{ij} \sigma_j) \sigma_i \qquad (5.31)$$

Recalling that in an axisymmetric analysis all the derivatives with respect to the angular coordinate θ are zero, we write the variational expression 5.28 as:

$$\frac{\delta J}{2\pi} = \int_{z_a}^{z_b} \sum_{k=1}^{N} \int_{r_a}^{r_b} \left(u_{,r}\, \delta\sigma_r - \overline{S}_{11}\sigma_r \delta\sigma_r - \overline{S}_{12}\sigma_\theta \delta\sigma_r - \overline{S}_{13}\sigma_z \delta\sigma_r - \frac{\partial\sigma_r}{\partial r}\delta u - \overline{S}_{21}\sigma_r \delta\sigma_\theta - \overline{S}_{22}\sigma_\theta \delta\sigma_\theta \right.$$

$$- \overline{S}_{23}\sigma_z \delta\sigma_\theta + w_{,z}\, \delta\sigma_z - \overline{S}_{31}\sigma_r \delta\sigma_z - \overline{S}_{32}\sigma_\theta \delta\sigma_z - \overline{S}_{33}\sigma_z \delta\sigma_z - \frac{\partial\sigma_z}{\partial z}\delta w - u_{,z}\, \delta\tau_{rz} + w_{,r}\, \delta\tau_{rz}$$

$$\left. + w_{,r}\, \delta\tau_{rz} - \overline{S}_{55}\tau_{rz}\delta\tau_{rz} - \frac{\partial\tau_{rz}}{\partial r}\delta w - \frac{\partial\tau_{rz}}{\partial z}\delta u \right) r\, dr\, dz$$

$$+ \int_{z_a}^{z_b} \left[\left(\tau_{rz}\sin\gamma_a^{(1)} - \sigma_r\cos\gamma_a^{(1)} - P_i\cos\gamma_a^{(1)}\right)\delta u_a^{(1)}\sec\gamma_a^{(1)} r_a^{(1)} + \left(\sigma_z\sin\gamma_a^{(1)} - \tau_{rz}\cos\gamma_a^{(1)}\right) \right.$$

$$- P_i \sin\gamma_a^{(1)}\right)\delta w_a^{(1)}\sec\gamma_a^{(1)} r_a^{(1)} + \left(\tau_{rz}\sin\gamma_b^{(N)} - \sigma_r\cos\gamma_b^{(N)} - P_e\sin\gamma_b^{(N)}\right)\delta u_b^{(N)}\sec\gamma_b^{(N)} r_b^{(N)}$$

$$\left. + \left(\sigma_z\sin\gamma_b^{(N)} - \tau_{rz}\cos\gamma_b^{(N)} - P_e\sin\gamma_b^{(N)}\right)\delta w_b^{(N)}\sec\gamma_b^{(N)} r_b^{(N)} \right] dz \tag{5.32}$$

$$- \sum_{k=1}^{N} \int_{r_a}^{r_b} \left[(u-\overline{u})_{z=z_a}^{(k)}\,\delta\sigma_r + (u-\overline{u})_{z=z_b}^{(k)}\,\delta\sigma_r + (w-\overline{w})_{z=z_a}^{(k)}\,\delta\sigma_z + (w-\overline{w})_{z=z_b}^{(k)}\,\delta\sigma_z \right] r\, dr$$

$$+ \int_{z_a}^{z_b} \sum_{k=1}^{N-1} \left(\sigma_{rb}^{(k)}\delta u_b^{(k)} - \sigma_{ra}^{(k+1)}\delta u_a^{(k+1)} + \tau_{rzb}^{(k)}\delta w_b^{(k)} - \tau_{rza}^{(k+1)}\delta w_a^{(k+1)} \right)\sec\gamma_b r_b^{(k)}\, dz = 0$$

The last integral, that deals with interface conditons, considers the continuity of stresses σ_r and τ_{rz} across any given adjacent layers. The traction boundary conditions at external surfaces $r_a^{(1)}$ and $r_b^{(N)}$ (the second integral) are given by Cauchy's relation:

$$T_i = [\sigma_{ij}].\, \vec{n}_j^T = \begin{bmatrix} \sigma_r & \tau_{rz} \\ \tau_{rz} & \sigma_z \end{bmatrix} \begin{Bmatrix} -\cos\gamma \\ \sin\gamma \end{Bmatrix} \tag{5.33}$$

The relation states that the applied tractions at a given point are equal to the product of the stress tensor (of the relevant stresses) times the surface unit outward normal vector.

The stress field within each layer is approximated, in the form proposed by Pagano [57] by:

$$\sigma_r = \sigma_{r1}(z)f_1^r + \sigma_{r2}(z)f_2^r + \sigma_{r3}(z)f_3^r + \sigma_{r4}(z)f_4^r + \sigma_{r5}(z)f_5^r$$

$$\sigma_\theta = \sigma_{\theta 1}(z)f_1^\theta + \sigma_{\theta 2}(z)f_2^\theta$$

$$\sigma_z = \sigma_{z1}(z)f_1^z + \sigma_{z2}(z)f_2^z$$

$$\tau_{rz} = \tau_{rz1}(z)f_1^{rz} + \tau_{rz2}(z)f_2^{rz} + \tau_{rz3}(z)f_3^{rz}$$

(5.34)

A first simplification is introduced here, as Pagano also considered in his model the shear stresses $\tau_{r\theta}$ anf $\tau_{\theta z}$. In the present analysis it is possible to neglect those stress components, as demonstrated before. The stress functions σ_{rn}, $\sigma_{\theta n}$, σ_{zn} and τ_{rzn} vary only with the z coordinate. The shape functions f_n^r, f_n^θ, f_n^z and f_n^{rz} are direct functions of coordinate r and implicit functions of z, through the curves $r_a(z)$ and $r_b(z)$ that describe the geometry of a given layer. Their expressions are:

$$f_1^r = f_1^\theta = f_1^z = \frac{r_b - r}{r_b - r_a}; \qquad f_2^r = f_2^\theta = f_2^z = \frac{r - r_a}{r_b - r_a}$$

$$f_1^{rz} = \frac{r}{r_a}\frac{r_b - r}{r_b - r_a}; \qquad f_2^{rz} = \frac{r}{r_b}\frac{r - r_a}{r_b - r_a}$$

$$f_3^r = r^3 - (r_a^2 + r_a r_b + r_b^2)r + r_a r_b(r_a + r_b); \qquad f_4^r = r^2 - (r_a + r_b)r + r_a r_b \qquad (5.35)$$

$$f_5^r = \frac{r^2 - (r_a + r_b)r + r_a r_b}{r_a r_b r}$$

$$f_3^{rz} = \frac{(r_a + r_b)r^2 - (r_a^2 + r_a r_b + r_b^2)r}{r_a^2 r_b^2} + \frac{1}{r}$$

The intralaminar stresses σ_θ and σ_z are approximated by linear functions of the coordinate r, whilst the interlaminar stresses σ_r and τ_{rz} are approximated by cubic and parabolic functions respectively. The functions are chosen in these forms to satisfy the equilibrium equations in cylindrical coordinates, expressions 5.1. The shape functions have the properties:

$$f_1^i = 1, \text{ when } r = r_a; \qquad f_1^i = 0, \text{ when } r = r_b$$

$$f_2^i = 0, \text{ when } r = r_a; \qquad f_2^i = 1, \text{ when } r = r_b \qquad (5.36)$$

$$f_3^r = f_3^{rz} = f_4^r = f_5^r = 0, \text{ when } r = r_a \text{ or } r = r_b$$

The approximate expressions for the stresses are then applied to the variational equation 5.32. The integrals over the radial coordinate are solved. The integrals over r that involve derivatives in z of a function $\phi(r,z)$ are solved through the application of the Leibnitz' theorem in the form:

$$\int_{r_a(z)}^{r_b(z)} \frac{\partial \phi(r,z)}{\partial z} dr = \frac{d}{dr} \int_{r_a(z)}^{r_b(z)} \phi(r,z) dr - r_b' \cdot \phi(r_b,z) + r_a' \cdot \phi(r_a,z) \tag{5.37}$$

The variational equation 5.32 then reads:

$$\frac{\delta J}{2\pi} = \int_{z_a}^{z_b} \left\{ \sum_{k=1}^{N} \left[(\mu_{in} + \chi_{in})\delta\sigma_{in} - (F_1\delta U_0 + F_2\delta U_1 + F_3\delta U_2 + F_4\delta U_3 + F_7\delta W_1 + F_8\delta W_2) \right]^{(k)} \right.$$

$$+ \left[(\tau_{rz1} \sin\gamma_a - \sigma_{r1} \cos\gamma_a - P_i \cos\gamma_a)^{(1)} \delta u_a^{(1)} \sec\gamma_a^{(1)} r_a^{(1)} \right.$$

$$+ (\sigma_{z1} \sin\gamma_a - \tau_{rz1} \cos\gamma_a - P_i \sin\gamma_a)^{(1)} \delta w_a^{(1)} \sec\gamma_a^{(1)} r_a^{(1)} \right]$$

$$+ \left[(\tau_{rz2} \sin\gamma_b - \sigma_{r2} \cos\gamma_b - P_e \cos\gamma_b)^{(N)} \delta u_b^{(N)} \sec\gamma_b^{(N)} r_b^{(N)} \right. \tag{5.38}$$

$$+ (\sigma_{z2} \sin\gamma_b - \tau_{rz2} \cos\gamma_b - P_e \sin\gamma_b)^{(N)} \delta w_b^{(N)} \sec\gamma_b^{(N)} r_b^{(N)} \right]$$

$$+ \sum_{k=1}^{N-1} \left[(\sigma_{r2} \sec\gamma_b - r_b' \tau_{rz2})^{(k)} r_b^{(k)} \delta u_b^{(k)} + (r_a' \tau_{rz1} - \sigma_{r1} \sec\gamma_a)^{(k+1)} r_a^{(k+1)} \delta u_a^{(k+1)} \right.$$

$$+ (\tau_{rz2} \sec\gamma_b - r_b' \sigma_{z2})^{(k)} r_b^{(k)} \delta w_b^{(k)} + (r_a' \sigma_{z1} - \tau_{rz1} \sec\gamma_a)^{(k+1)} r_a^{(k+1)} \delta w_a^{(k+1)} \right] \left. \right\} dz$$

$$- \sum_{k=1}^{N} \left[(U_0 - \overline{U}_0)\delta\sigma_{r1} + (U_1 - \overline{U}_1)\delta\sigma_{r2} + (U_2 - \overline{U}_2)\delta\sigma_{r3} + (U_3 - \overline{U}_3)\delta\sigma_{r4} + (W_1 - \overline{W}_1)\delta\sigma_{z1} + (W_2 - \overline{W}_2)\delta\sigma_{z2} \right]^{(k)}_{z=z_a,z_b}$$

New displacement variables are introduced, in the form of weighted integrals of the original displacements over the radial coordinate:

196

$$(U_0, U_1, U_2, U_3) = \int_{r_a}^{r_b} (1, r, r^2, r^3).u \, dr \qquad (5.39)$$

The same sort of relations apply for variables W_1 and W_2, related to the axial displacement w. In expression 5.38, the compatibility equations are obtained from the terms μ_{in}, which are functions of the displacements at the interfaces, and χ_{in}, which are displacement-stress relations. The non-zero terms are:

$$\mu_{r1}^{(k)} = -(r_a u_a)^{(k)} \; ; \quad \mu_{z1}^{(k)} = (r_a r_a' w_a)^{(k)} \; ; \quad \mu_{rz1}^{(k)} = [r_a(r_a' u_a - w_a)]^{(k)}$$

$$\mu_{r2}^{(k)} = (r_b u_b)^{(k)} \; ; \quad \mu_{z2}^{(k)} = -(r_b r_b' w_b)^{(k)} \; ; \quad \mu_{rz2}^{(k)} = [r_b(w_b - r_b' u_b)]^{(k)} \qquad (5.40)$$

and:

$$\chi_{in}^{(k)} = \eta_{in}^{(k)} - \widehat{S}_{ijmn}^{(k)} \sigma_{jm}^{(k)} \; ; \quad \widehat{S}_{ijmn}^{(k)} = \int_{r_a}^{r_b} \overline{S}_{ij}^{(k)} f_n^i f_m^j \, r \, dr \qquad (5.41)$$

The weighted integrals of the compliance coefficients are evaluated analytically. The generalised strains are functions of the weighted displacements:

$$\eta_{r1}^{(k)} = \left(\frac{2U_1 - r_b U_0}{h} \right)^{(k)} \; ; \quad \eta_{r2}^{(k)} = \left(\frac{r_a U_0 - 2U_1}{h} \right)^{(k)} \; ; \quad h^{(k)} = r_b^{(k)} - r_a^{(k)}$$

$$\eta_{r3}^{(k)} = \left[-r_a r_b(r_a + r_b)U_0 + 2(r_a^2 + r_a r_b + r_b^2)U_1 - 4U_3 \right]^{(k)} \; ; \quad \eta_{r4}^{(k)} = \left[-r_a r_b U_0 + 2(r_a + r_b)U_1 - 3U_2 \right]^{(k)}$$

$$\eta_{r5}^{(k)} = \left[\frac{(r_a + r_b)U_0 - 2U_1}{r_a r_b} \right]^{(k)} \qquad (5.42)$$

$$\eta_{\theta 1}^{(k)} = \left(\frac{r_b U_0 - U_1}{h} \right)^{(k)} \; ; \quad \eta_{\theta 2}^{(k)} = \left(\frac{U_1 - r_a U_0}{h} \right)^{(k)}$$

$$\eta_{z1}^{(k)} = \left(\frac{r_b W_1' - W_2'}{h} \right)^{(k)} \; ; \quad \eta_{z2}^{(k)} = \left(\frac{W_2' - r_a W_1'}{h} \right)^{(k)}$$

$$\eta_{rz1}^{(k)} = \left(\frac{3W_2 - 2r_b W_1 + r_b U_2{}' - U_3{}'}{r_a h} \right)^{(k)} \quad ; \quad \eta_{rz2}^{(k)} = \left(\frac{2r_a W_1 - 3W_2 + U_3{}' - r_a U_2{}'}{r_b h} \right)^{(k)}$$

$$\eta_{rz3}^{(k)} = \left[\frac{\left(r_a^2 + r_a r_b + r_b^2 \right)\left(2W_1 - U_2{}' \right) + \left(r_a + r_b \right)\left(U_3{}' - 3W_2 \right) + r_a^2 r_b^2 U_0{}'}{r_a^2 r_b^2} \right]^{(k)}$$

The F_i components are related to the stress equilibrium terms of the energy functional. The original F_5 and F_6 terms from Pagano were not used here because they were related to the $\sigma_{r\theta}$ and $\sigma_{\theta z}$ stresses that are identically zero in the present analysis. The expressions for the remaining terms are:

$$F_1^{(k)} = \left[\frac{r_b \sigma_{r1} - r_a \sigma_{r2}}{h} + r_a r_b \left(r_a + r_b \right)\sigma_{r3} + r_a r_b \sigma_{r4} - \frac{\left(r_a + r_b \right)\sigma_{r5}}{r_a r_b} + \frac{r_a \sigma_{\theta 2} - r_b \sigma_{\theta 1}}{h} + \tau'_{rz3} \right]^{(k)}$$

$$F_2^{(k)} = \left[\frac{2\left(\sigma_{r2} - \sigma_{r1} \right)}{h} - 2\left(r_a^2 + r_a r_b + r_b^2 \right)\sigma_{r3} - 2\left(r_a + r_b \right)\sigma_{r4} + \frac{2\sigma_{r5}}{r_a r_b} + \frac{\sigma_{\theta 1} - \sigma_{\theta 2}}{h} \right]^{(k)}$$

$$F_3^{(k)} = \left\{ 3\sigma_{r4} + \frac{r_b^2 \tau'_{rz1} - r_a^2 \tau'_{rz2}}{r_a r_b h} - \frac{\left(r_a^2 + r_a r_b + r_b^2 \right)\tau'_{rz3}}{r_a^2 r_b^2} + \left[\frac{\left(2r_a - r_b \right)r_b r_a{}' - r_a^2 r_b{}'}{r_a^2 h^2} \right]\tau_{rz1} + \right.$$

$$\left. + \left[\frac{\left(2r_b - r_a \right)r_a r_b{}' - r_b^2 r_a{}'}{r_b^2 h^2} \right]\tau_{rz2} + \left[\frac{r_b^2 r_a{}'\left(r_a + 2r_b \right) + r_a^2 r_b{}'\left(r_b + 2r_a \right)}{r_a^3 r_b^3} \right]\tau_{rz3} \right\}^{(k)} \tag{5.43}$$

$$F_4^{(k)} = \left\{ 4\sigma_{r3} + \frac{r_a \tau'_{rz2} - r_b \tau'_{rz1}}{r_a r_b h} + \frac{\left(r_a + r_b \right)\tau'_{rz3}}{r_a^2 r_b^2} + \left[\frac{r_a r_b{}' - \left(2r_a - r_b \right)r_a{}'}{r_a^2 h^2} \right]\tau_{rz1} + \right.$$

$$\left. + \left[\frac{r_b r_a{}' - \left(2r_b - r_a \right)r_b{}' - r_b^2 r_a{}'}{r_b^2 h^2} \right]\tau_{rz2} - \left[\frac{r_b r_a{}'\left(r_a + 2r_b \right) + r_a r_b{}'\left(r_b + 2r_a \right)}{r_a^3 r_b^3} \right]\tau_{rz3} \right\}^{(k)}$$

$$F_7^{(k)} = \left[\frac{r_b \sigma'_{z1} - r_a \sigma'_{z2}}{h} + \frac{\left(r_b r_a{}' - r_a r_b{}' + r_b^2 \right)\left(\sigma_{z1} - \sigma_{z2} \right)}{h^2} + \frac{2\left(r_b^2 \tau_{rz1} - r_a^2 \tau_{rz2} \right)}{r_a r_b h} - \frac{2\left(r_a^2 + r_a r_b + r_b^2 \right)\tau_{rz3}}{r_a^2 r_b^2} \right]^{(k)}$$

$$F_8^{(k)} = \left[\frac{\sigma'_{z2} - \sigma'_{z1}}{h} + \frac{(r_b' - r_a')(\sigma_{z1} - \sigma_{z2})}{h^2} + \frac{3(r_a \tau_{rz2} - r_b \tau_{rz1})}{r_a r_b h} + \frac{3(r_a + r_b)\tau_{rz3}}{r_a^2 r_b^2} \right]^{(k)}$$

The first variation of the energy functional is equated to zero ($\delta J = 0$), to make it stationary and to provide the equations needed to solve the boundary value problem. There are 18 unknowns per layer: 6 weighted displacements: U_0, U_1, U_2, U_3, W_1 and W_2, and 12 stress functions: σ_{r1}, σ_{r2}, σ_{r3}, σ_{r4}, σ_{r5}, $\sigma_{\theta1}$, $\sigma_{\theta2}$, σ_{z1}, σ_{z1}, τ_{rz1}, τ_{rz2} and τ_{rz3}.

From the geometry of the layered tube and due to the interfacial continuity of displacements (with the same conditions on their variations), we have:

$$r_b^{(k)} = r_a^{(k+1)} \quad ; \quad u_b^{(k)} = u_a^{(k+1)} \quad and \quad w_b^{(k)} = w_a^{(k+1)} \tag{5.44}$$

So, the interfacial continuity terms at the second summation inside the integral in 5.38 for arbitrary variations of the displacements lead to:

$$\left(\sigma_{r2} \, sec\gamma_b - r_b' \, \tau_{rz2} \right)^{(k)} + \left(r_a' \, \tau_{rz1} - \sigma_{r1} \, sec\gamma_a \right)^{(k+1)} = 0 \tag{5.45}$$

$$\left(\tau_{rz2} \, sec\gamma_b - r_b' \, \sigma_{z2} \right)^{(k)} + \left(r_a' \, \sigma_{z1} - \tau_{rz1} \, sec\gamma_a \right)^{(k+1)} = 0 \tag{5.46}$$

From the compatibility terms at the first summation in expression 5.38 we have, for arbitrary variations of stresses $\delta\sigma_{in}$:

$$\left(\mu_{in} + \chi_{in} \right)^{(k)} = -\left(\mu_{in} + \chi_{in} \right)^{(k+1)} = 0$$

$$\left(\mu_{i2} + \chi_{i2} \right)^{(k)} = -\left(\mu_{i1} + \chi_{i1} \right)^{(k+1)} \tag{5.47}$$

And the use of equalities 5.44 in expressions 5.40 provides:

$$\mu_{i2}^{(k)} = -\mu_{i1}^{(k+1)} \tag{5.48}$$

The manipulations above remove the interfacial displacements from the expressions. The final form of equation 5.47 is, then:

$$\chi_{i2}^{(k)} + \chi_{i1}^{(k+1)} = 0 \qquad (5.49)$$

And from expressions 5.40 again, we have, within a given layer:

$$\left(\mu_{z1} + r_a' \mu_{rz1} + r_a'^2 \mu_{r1}\right)^{(k)} = 0 \quad and \quad \left(\mu_{z2} + r_b' \mu_{rz2} + r_b'^2 \mu_{r2}\right)^{(k)} = 0 \qquad (5.50)$$

so:

$$\left(\chi_{z1} + r_a' \chi_{rz1} + r_a'^2 \chi_{r1}\right)^{(k)} = 0 \quad and \quad \left(\chi_{z2} + r_b' \chi_{rz2} + r_b'^2 \chi_{r2}\right)^{(k)} = 0 \qquad (5.51)$$

It is possible now to assembly the system of equations to solve the problem. We start with the inner layer ($k=1$). There are three specific equations for it. The first one comes from expression 5.51 and the other two from the surface conditions in expression 5.38, as the variations in displacements can be made arbitrary:

$$\left(\chi_{z1} + r_a' \chi_{rz1} + r_a'^2 \chi_{r1}\right)^{(1)} = 0$$
$$\left(\tau_{rz1} \sin\gamma_a - \sigma_{r1} \cos\gamma_a\right)^{(1)} = P_i \cos\gamma_a^{(1)}$$
$$\left(\sigma_{z1} \sin\gamma_a - \tau_{rz1} \cos\gamma_a\right)^{(1)} = P_i \sin\gamma_a^{(1)} \qquad (5.52)$$

The next three equations are valid for all layers but the last, and are obtained from 5.49:

$$\chi_{r2}^{(k)} + \chi_{r1}^{(k+1)} = 0$$
$$\chi_{z2}^{(k)} + \chi_{z1}^{(k+1)} = 0$$
$$\chi_{rz2}^{(k)} + \chi_{rz1}^{(k+1)} = 0 \qquad (5.53)$$

The total number of equations to this point is $3(N-1)+3=3N$. Next, we can write, for all the stresses that have zero μ_{in} terms, for given arbitrary $\delta\sigma_{in}$ stress variations in 5.38:

$$\chi_{r3}^{(k)} = 0$$
$$\chi_{r4}^{(k)} = 0$$
$$\chi_{r5}^{(k)} = 0$$
$$\chi_{\theta1}^{(k)} = 0$$
$$\chi_{\theta2}^{(k)} = 0$$
$$\chi_{rz3}^{(k)} = 0 \qquad (5.54)$$

These equations are valid for all layers. Total number of equations: $9N$. From 5.51 comes the following which is applicable to all layers:

$$\left(\chi_{z2} + r_b{}' \chi_{rz2} + r_b{}'^2 \chi_{r2}\right)^{(k)} = 0 \qquad (5.55)$$

Number of equations: $10N$. The equilibrium equations, for arbitrary variations of the displacements, are:

$$\begin{aligned}
F_1^{(k)} &= 0 \\
F_2^{(k)} &= 0 \\
F_3^{(k)} &= 0 \\
F_4^{(k)} &= 0 \\
F_7^{(k)} &= 0 \\
F_8^{(k)} &= 0
\end{aligned} \qquad (5.56)$$

Number of equations so far: $16N$. The last two set of equations is composed of expressions 5.45 and 5.46. They apply to all layers but the last $(k=N)$, where they are replaced by the external surface conditions from 5.38:

$$\left(\sigma_{r2}\, sec\gamma_b - r_b'\, \tau_{rz2}\right)^{(k)} + \left(r_a'\, \tau_{rz1} - \sigma_{r1}\, sec\gamma_a\right)^{(k+1)} = 0$$
$$or$$
$$\left(\tau_{rz2}\, sin\gamma_b - \sigma_{r2}\, cos\gamma_b\right)^{(N)} = P_e\, cos\gamma_b^{(N)}$$

$$\left(\tau_{rz2}\, sec\gamma_b - r_b'\, \sigma_{z2}\right)^{(k)} + \left(r_a'\, \sigma_{z1} - \tau_{rz1}\, sec\gamma_a\right)^{(k+1)} = 0$$
$$or \qquad\qquad\qquad\qquad\qquad\qquad\qquad\qquad\qquad (5.57)$$
$$\left(\sigma_{z2}\, sin\gamma_b - \tau_{rz2}\, cos\gamma_b\right)^{(N)} = P_e\, sin\gamma_b^{(N)}$$

This completes the set of $18N$ equations needed to obtain the $18N$ unknowns of the problem. It can be seen from the expressions shown that derivatives in z of the following variables are involved: U_0, U_2, U_3, W_1, W_2, σ_{z1}, σ_{z2}, τ_{rz1}, τ_{rz2} and τ_{rz3}. The derivatives are replaced by a central finite difference approximation, according to the well-known formula:

$$y_j{}' = \frac{1}{2l}\left(y_{j+1} - y_{j-1}\right) \qquad (5.58)$$

where y represents the variable to be differentiated and l is the step size. The tube is divided into an array of k layers ($k=1$, N) and l segments ($l=1$, M). Figure 5.4 shows the finite difference array for the composite tube with varying thickness.

The basic tube geometry is composed of three sublaminates, each one divided into a number of layers. The second sub-laminate is the one with different thicknesses, as indicated in figure 5.4. It is necessary to transform the compliances, at the regions where the surfaces on which the carbon fibres are inclined by an angle γ to the axis. From Tsai[104], we have:

$$\overline{S}'_{11} = c^4 \overline{S}_{11} + 2c^2 s^2 \overline{S}_{13} + s^4 \overline{S}_{33} + c^2 s^2 \overline{S}_{55}$$

$$\overline{S}'_{12} = c^2 \overline{S}_{12} + s^2 \overline{S}_{23}$$

$$\overline{S}'_{13} = c^2 s^2 \overline{S}_{11} + (c^4 + s^4) \overline{S}_{13} + c^2 s^2 \overline{S}_{33} - c^2 s^2 \overline{S}_{55}$$

$$\overline{S}'_{15} = -2c^3 s \overline{S}_{11} + 2cs(c^2 - s^2) \overline{S}_{13} + 2cs^3 \overline{S}_{33} + cs(c^2 - s^2) \overline{S}_{55}$$

$$\overline{S}'_{22} = \overline{S}_{22}$$

$$\overline{S}'_{23} = s^2 \overline{S}_{12} + c^2 \overline{S}_{23}$$

$$\overline{S}'_{25} = -cs \overline{S}_{12} + cs \overline{S}_{23} \tag{5.59}$$

$$\overline{S}'_{33} = s^4 \overline{S}_{11} + 2c^2 s^2 \overline{S}_{13} + c^4 \overline{S}_{33} + c^2 s^2 \overline{S}_{55}$$

$$\overline{S}'_{35} = -2cs^3 \overline{S}_{11} - 2cs(c^2 - s^2) \overline{S}_{13} + 2c^3 s \overline{S}_{33} - cs(c^2 - s^2) \overline{S}_{55}$$

$$\overline{S}'_{55} = 4c^2 s^2 \overline{S}_{11} + -8c^2 s^2 \overline{S}_{13} + 4c^2 s^2 \overline{S}_{33} + (c^2 - s^2)^2 \overline{S}_{55}$$

where $c = \cos\gamma$; $s = \sin\gamma$

In the following papers, Pagano and Whitford [112] and Pagano [113] addressed the problem of the end conditions, associated to the finite difference algorithm. This is related to the planes at $z=z_a$ and $z=z_b$ on figure 5.4. At those axial limits, expression 5.58 demands values beyond the domain of the analysis. The authors also reported that the number of field equations and boundary conditions differ at those limits. They solved the problem by applying the variational principle to boundaries at the end planes, as well.

In our case, we can make use of the results from the TUBEPLAIN programme. It will provide the necessary displacements and stresses at the axial limits of the model, both for the thin and the thick parts of the dropped ply tube. This approach guarantees the converge to the exact values of a constant thickness tube, sufficiently away from the stress raising detail. The lamina

stresses are obtained from the strains referred to the cylindrical coordinates, as shown in expression 4.16, Chapter 4.

The major drawback of the numerical approach is the size of the system of equations generated. The central finite difference scheme has a truncation error of the order of l^2, and normally small step sizes are needed to capture accurately the high stress gradients. Futhermore, we need to allow the model some "room" to let the stress fall back to its values far from dropped ply, stress raising detail.

Some help comes from the fact that the matrix of the system is banded. There are FORTRAN codes available in the public domain to tackle this special case. This is the case of the Linear Analysis Package (LAPACK) routines [114]. Even so, the problem to solve remained large. In the end, some compromise between problem size and accuracy was needed, as is inherent to most numerical methods. The stress analysis of the composite tube with varying thickness, as proposed above, was implemented by the author in a FORTRAN programme called TUBEDROP. Whilst this programme needs further development to increase its accuracy (see Chapter 7), some examples of its use are presented bellow to illustrate its ability to produce useful results.

5.4.2 CASE STUDIES

Program TUBEDROP was applied to provide the stresses in the all-carbon tubes. The load considered was a bending moment of 4.32 kNm, the average value at failure obtained from the experiments. For the internal and external pressure load cases, it is preferable to use the simpler programme TUBEPLAIN, as it was shown that the dropped plies did not alter the failure process under pure pressure conditions.

Figures 5.5 and 5.6 shows the results, in terms of the stresses referred to the cylindrical coordinates and of the lamina stresses, respectively. The results from TUBEDROP were compared with those from the previous FEA of the all-carbon tubes. The graphs show the stresses at the extreme fibre position, at the compressed side. The agreement was not exact, due to the limitations of the finite difference process. It would require an excessive memory size from the computer to improve the precision further. The process time would also be

considerable.

Nevertheless, TUBEDROP indicated σ_z and σ_1 values very close to the FEA results. The failure of the tube in bending was controlled by σ_1, as was shown in the previous chapters. Consequently, TUBEDROP can give a reasonably accurate provision of the failure load of a dropped ply composite tube in pure bending conditions.

Next, several analysis were performed by TUBEDROP, addressing the effect on the stress concentration factor of the number of +/-α carbon lamina pairs dropped. The analysis considered the geometry of the all-carbon specimens. The SCF was defined as the ratio of the maximum σ_z at the ply drop-off region to its nominal value at the thinner portion of the tube. Figure 5.7 shows the results, ranging from one to four pairs dropped. It is recalled that the specimens tested during the research had three pairs of carbon laminae dropped, with a SCF of about 2. It can be seen from the figure that the relation is fairly linear.

To end the case studies, the hybrid tubes were analysed by TUBEDROP. The geometry of the HST specimens was used for that purpose. The SCF at the outer carbon layer was determined by the programme to be 1.20, compared with a FEA value of 1.22. Programme TUBEDROP lacks some precision, but even so it can provide a good estimate of the most severe stress that will cause the failure of the tube under bending conditions.
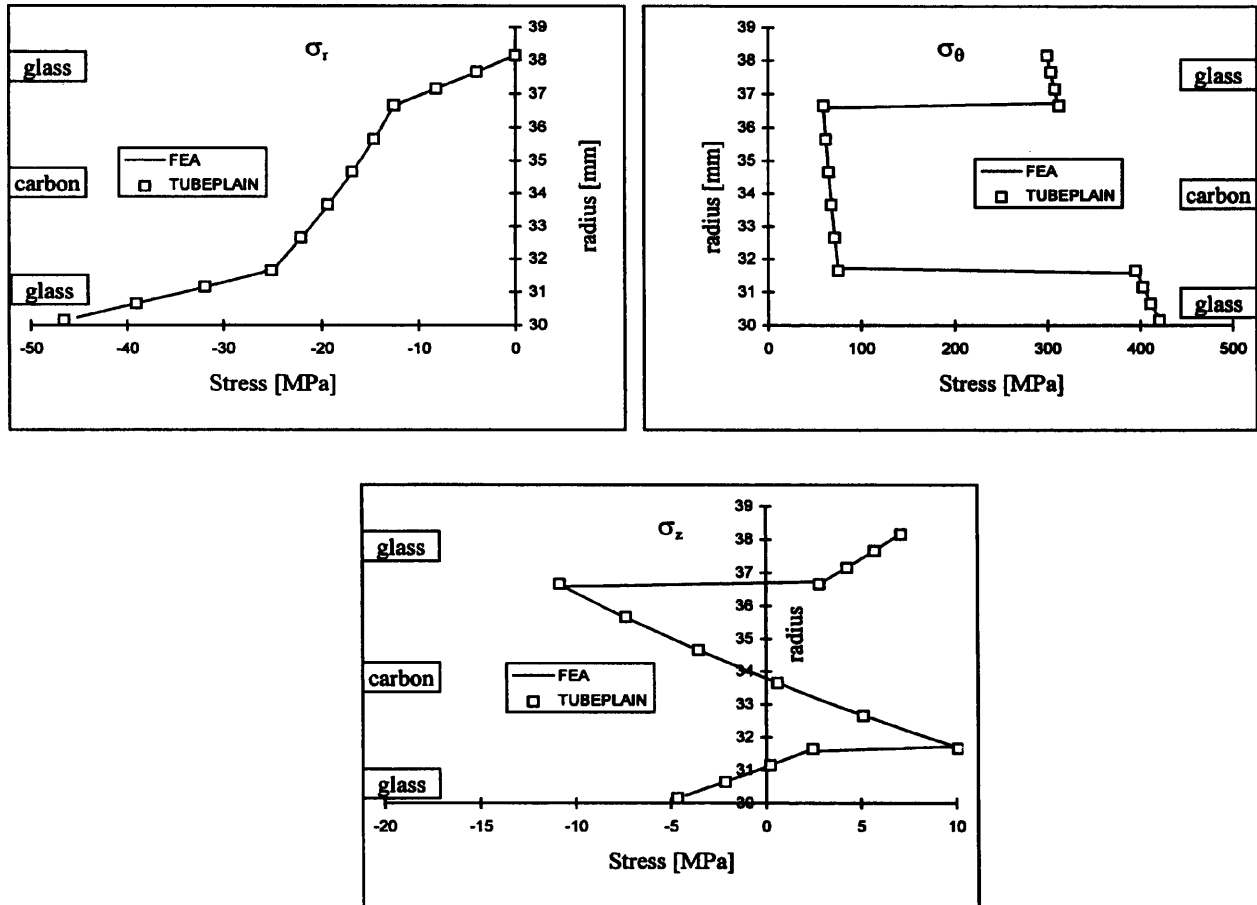
Figure 5.1 Comparison between FEA and TUBEPLAIN results,
thin part of HST tube, internal pressure of 46.6 MPa.
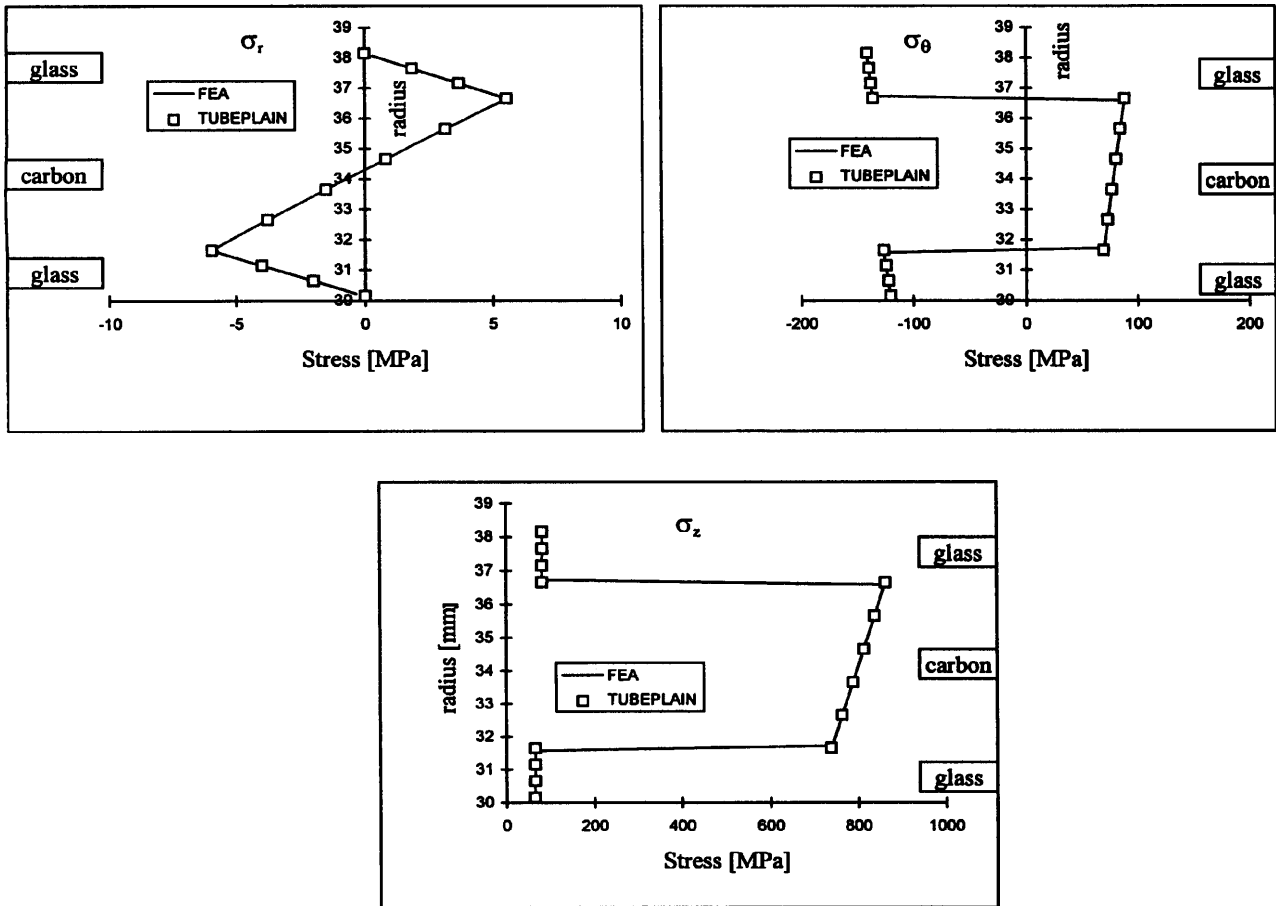
Figure 5.2 Comparison between FEA and TUBEPLAIN results,
thin part of HST tube, bending moment of 15.7 kN.m.
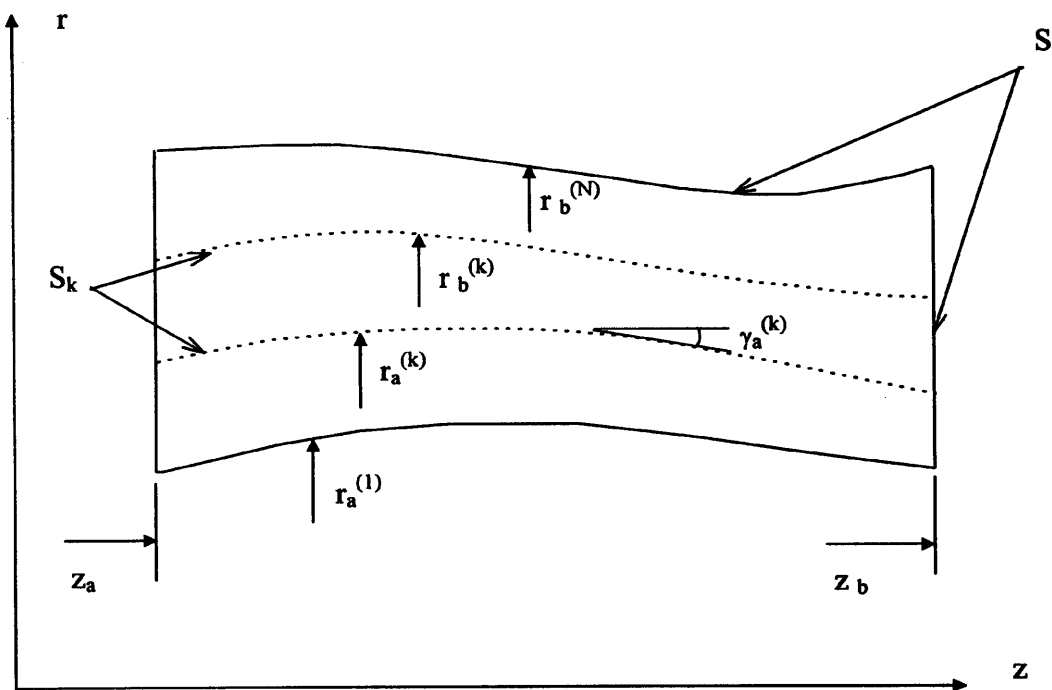
Figure 5.3 Axisymmetric volume V divided into N sub-volumes V_k.
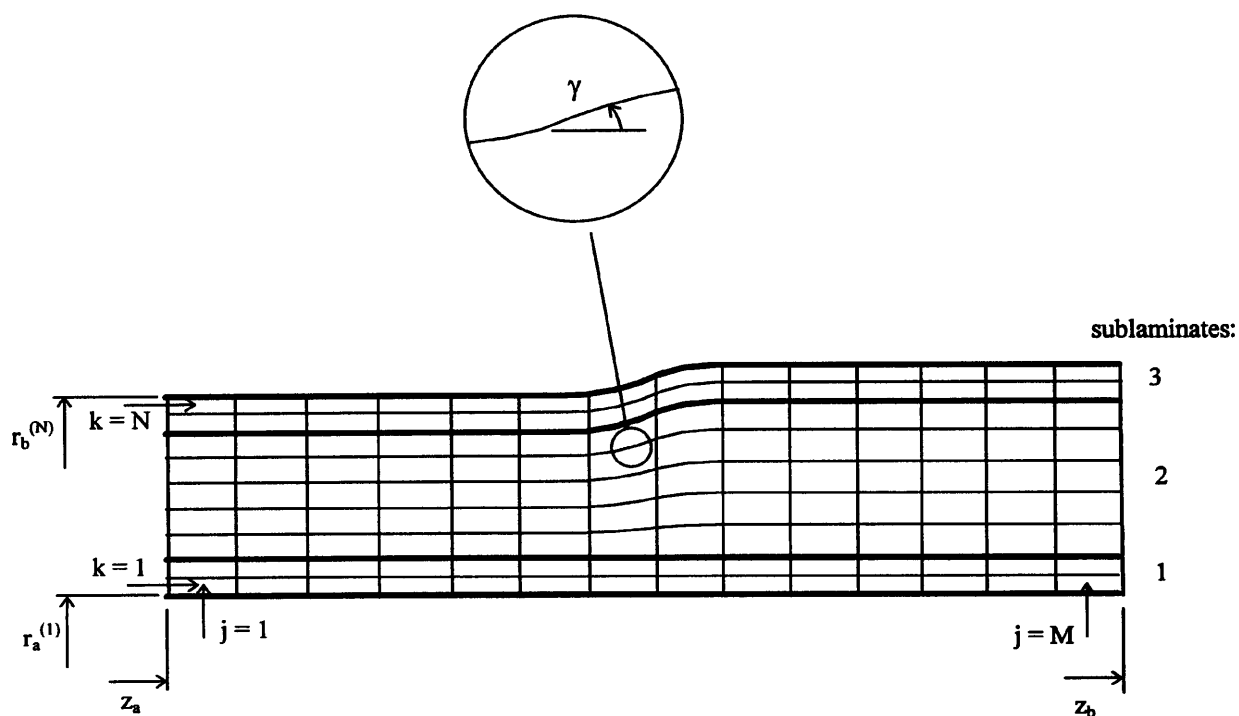
Figure 5.4 Finite difference array for the composite tapered tube.

207
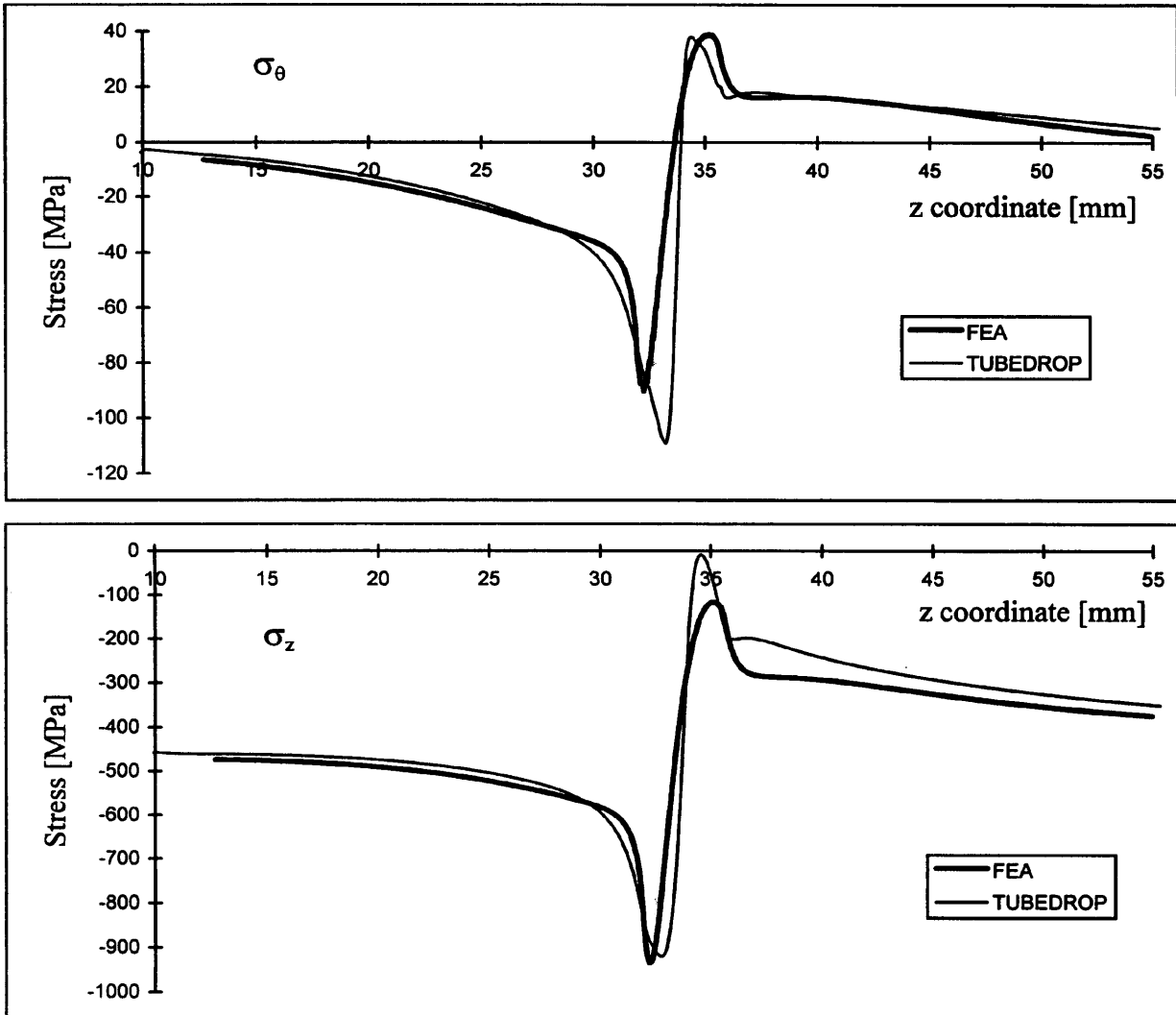
Figure 5.5 Cylindrical stresses: comparison between FEA and TUBEDROP results.
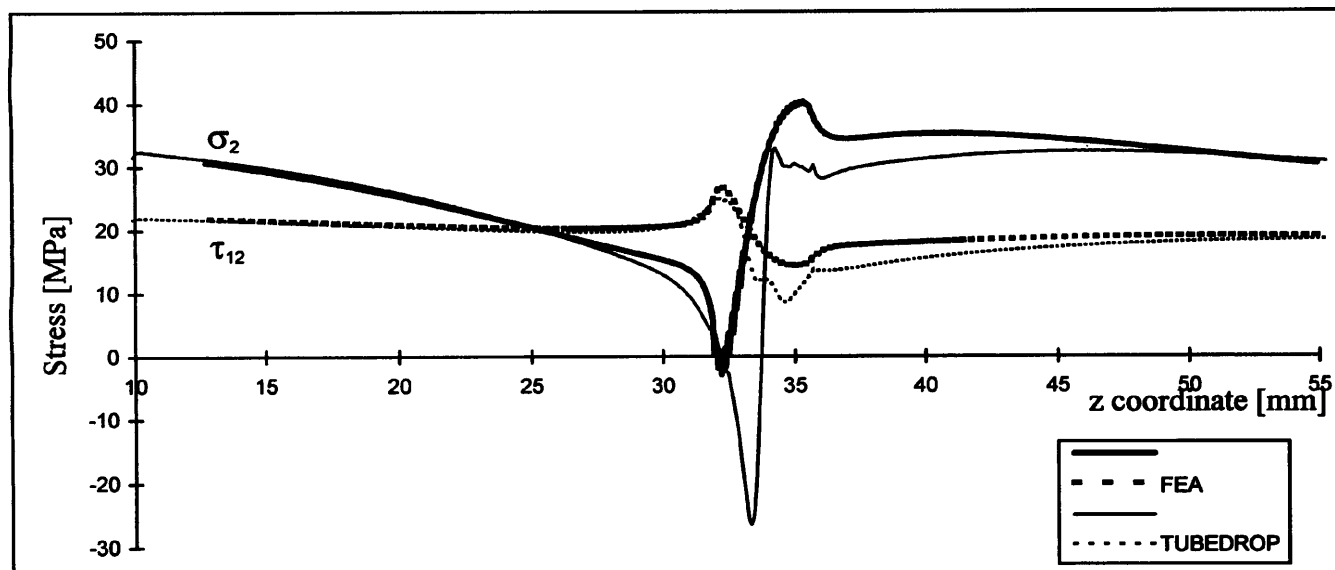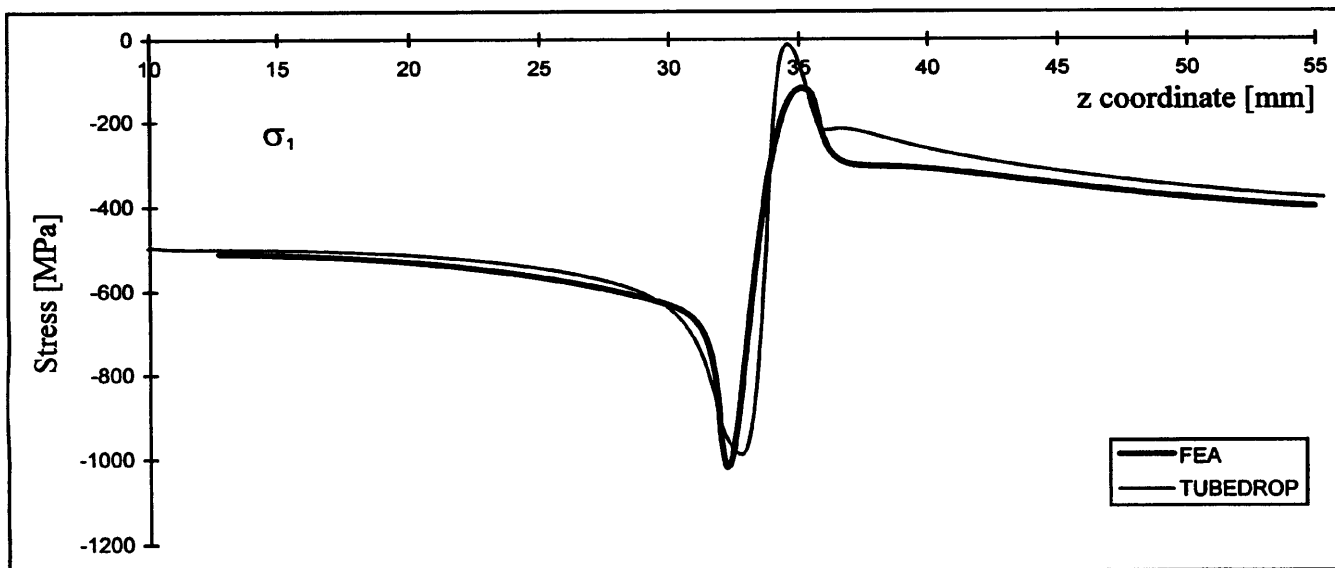
Figure 5.6 Lamina stresses: comparison between FEA and TUBEDROP results.
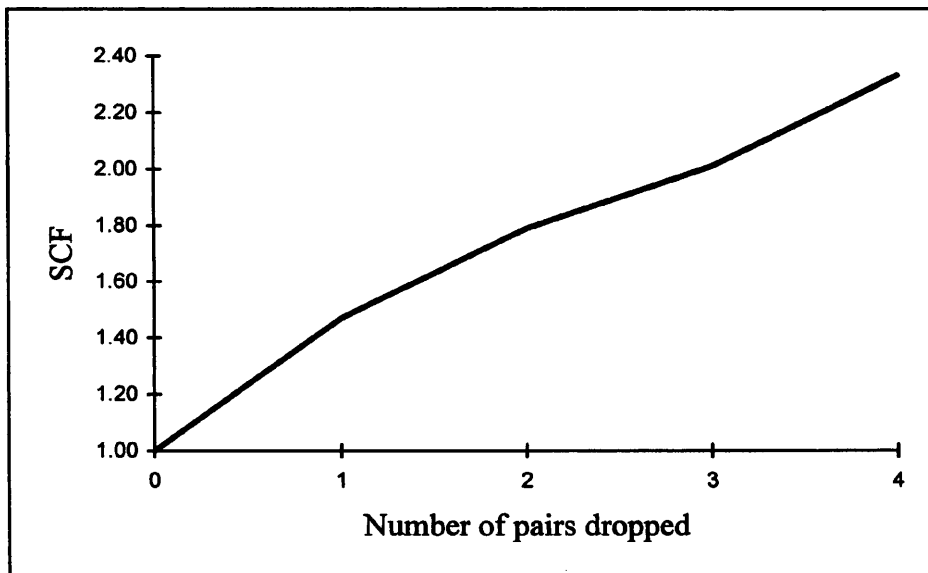
Figure 5.7 Variation of the SCF with the number of carbon layers dropped.

CHAPTER 6 RISER ANALYSIS

CHAPTER 6 RISER ANALYSIS

6.1 INTRODUCTION

In this chapter a comparative analysis is performed of the behaviour of steel and composite production risers for a TLP. The location chosen was the Marlim field, Campos basin, offshore Brazil, in a water depth of 1000 metres. After that, the study is focused on the behaviour of composite tapered (or stress) joints placed at the ends of the riser. The analysis made use of the experimental results and design tools for dropped ply, composite tubes, developed in the present study.

Previous calculations from the author [51] have shown that a composite tapered joint put at the top of the riser would be excessively thick. This was a consequence of the upper support being completely constrained, not allowing the top section of the riser to rotate. To alleviate this situation, the present analysis considered the top section of the riser to be gimballed. This can be obtained by means of flexelements such as those used at the ends of the TLP's tethers described by Stevenson and Harris [115].

Figure 6.1 shows the configuration of such element, which is a composite of elastomer layers bonded to spherical steel shells. The tilting stiffness of the flexelement reduces the bending moments transmitted to the top tapered joint of the riser. These elements also provide some axial flexibility that will slightly abate the axial forces imposed on the riser by the vertical movements of the platform.

Unlike the steel production riser, the composite riser is not supported by tensioners, which brings substantial simplification to the design. The composite riser is anchored to the platform deck under tension, to make sure that no compressive net section force acts along the length of the riser at any time. The analysis concludes with the appraisal of possible causes of change in the pretension, and its implications for the tapered joints design.

6.2 BASIC ASSUMPTIONS FOR RISER ANALYSIS

The comparative study refers to an extreme case associated with a 100-year recurrent storm. The TLP is considered to be installed in the Marlim field, Campos basin, Brazil, at a water depth of 1000 m, where the design specifications for the riser are as given by PETROBRÁS [96]. The environmental conditions and platform motions, related to a 100-year storm, are presented in table 6.1. The ABAQUS/AQUA analysis followed the directives given by the API [98].

The regular wave considered has a height equal to the *significant wave height* H_s at that site, which is 7.8 m. This is defined as the average value of the highest third of all the waves for a given sea state. It is equivalent to the wave height reported in visual observations. The period adopted is 9.4 s, the value of the average *zero up-crossing period* T_z, also obtained from specific oceanographic data. This period is defined as the time lag between two consecutive nil sea surface elevations, when the wave is in the process of rising. An allowance of 2 wave periods - or 18.8 s - is given to assure that the numerical algorithm reached steady state conditions. The time simulation that follows lasts for five wave periods - 47.0 s - with a basic time step of 0.1 s for each interaction.

The analysis is two-dimensional: the platform lateral motions, the wave and current actions are considered to be along the *x*-axis. The sea bottom is taken at a *y* coordinate of -1000 m, with the still water level as the reference. The distance between the top of the riser and the mean sea water level is 18 m.

The data listed in table 6.1 is related to a storm that reaches the platform at a 45° angle in relation to its main horizontal axes. In order to get the maximum lateral motions, the surge and sway responses have to be added vectorially. This results in a mean *static offset* of 66 m, which is the time average value of that lateral motion. Superimposed to this there is a 6.8 m motion amplitude. This lateral movement of the platform varies in a sinusoidal way with time, at the same period as the wave, with a 90° phase angle delay in relation to the wave crest. The platform experiences a *setdown* (mean heave) of 2.3 m. Added to this there is a vertical oscillation with an amplitude of 0.4 m and a period of 3.5 s.

The c_d (drag) and c_m (inertia) coefficients in Morison's hydrodynamic forces equation were estimated before by the author [51], and the following average values resulted:

$$C_d = 0.9 \quad \text{and} \quad C_m = 1.5$$

The coefficients vary with current speeds and wave particle velocities, but the ABAQUS/AQUA program only considers a single value. So, the average values are assumed to hold along the whole length of the riser.

In order to calibrate the ABAQUS/AQUA programme concerning the simulations proposed, one can use the benchmarks provided by the API [98], related to steel risers. The case entitled 1500-20-2D was selected. The water depth in that case is 457 m (1500 ft). The API examples are related to drilling risers, that have a gimbal connection at the seabed. The tube itself has a 533 mm OD (21"), but the diameter for fluid force calculations is 737 mm due to added components. Figure 6.2 shows the results, in terms of the envelope of bending stresses - curves of minimum and maximum values along the length of the riser. The curves shown as dotted lines are the one-standard-deviation envelopes for this case as evaluated by five different designers. The ABAQUS/AQUA results compare well, particularly in the regions with the highest bending stresses near the sea surface and at the seabed, despite some discrepancies at greater depths.

6.3 ANALYSIS OF A STEEL RISER

The first analysis in the present study of production risers considers a steel one, without tensioners or a tapered joint. The tube has a 244 mm (9 5/8") OD and a thickness of 12 mm (0.472"). There are two internal components: one gas lift line with 48 mm (1.9") OD and a thickness of 3.7 mm and one production tubing with 114 mm (4 1/2") OD and a thickness of 6.9 mm. These internal components are suspended from the production head, at the top of the riser. They have telescopic joints at the mud line level, so they do not contribute to the axial stiffness of the riser assembly.

The total bending stiffness is accounted for by adding up each individual bending stiffness, as

the elements of the assembly act as parallel beams:

$$(EI)_{total} = (EI)_{riser} + (EI)_{tubing} + (EI)_{gas\ lift\ line}$$
(6.1)

As all the components are made of steel, the expression above reduces to a sum of the second moments of area of each tube.

The vertical force per unit length is the weight of the riser tube alone, deducting the vertical uplift force in the submerged regions. The density ρ of sea water is 1024 kg/m^3. The cross sectional area of the riser tube is 8.746×10^{-3} m^2. The weight of the tube per unit length, including couplings, is 694 N/m (47.5 lbw/ft). As the height from the top of the riser to the sea surface is 18 m, the apparent weight of the riser is:

$$W_r = 18 \times 694 + 1000 \times (694 - 1024 \times 9.81 \times 8.746 \times 10^{-3}) = 618\ kN$$

In order to prevent negative axial forces in the deepest sections of the riser, at any situation, some pretension is necessary. The pretension is also necessary to avoid interference between two adjacent risers. It is achieved in the present case by pulling the riser while the platform is in the vertical position. This initial tension is 928 kN, at the top of the riser, 1.5 times as high as its apparent weight.

The determination of the total distributed mass of the assembly, for lateral vibration calculations, takes into account every element, including the contained fluids. There is oil of density $\rho = 950$ kg/m^3 inside the tubing, which has an internal cross-sectional area of 7.939×10^{-3} m^2. A completion fluid of $\rho = 1100$ kg/m^3 fills up the annulus, which has an area of 2.592×10^{-2} m^2 The gas lift line contains approximately zero density fluids. The weights of the tubing and the gas lift lines per unit length are 186 N/m (12.75 lbw/ft) and 42 N/m (2.9 lbw/ft) respectively, including couplings. The total mass per unit length is then:

$$m_t = (694 + 186 + 42)/9.81 + 950 \times 7.939 \times 10^{-3} + 1100 \times 2.592 \times 10^{-2} = 130\ kg/m$$

Five hundred and nine beam elements are used, each with 2 m length. The ABAQUS/AQUA analysis does not consider the differential pressure between the annulus and the subsea environment which is due to the different density of the completion fluid compared to sea water.

Figures 6.3 and 6.4 show the output of the analysis, which consists of axial force and bending moments envelope diagrams along the length of the riser. The large axial force variation, of about 2.0 MN, is evident. This is due to the absence of tensioners. The axial force at the seabed varies between 0.19 and 2.16 MN. One can note the high bending moments at the base, from 158 to 394 kNm.

The next analysis considers the use of a tensioner system. Table 6.2 displays its axial properties. It is modelled as an equivalent non-linear spring, based on data provided by Shive [116]. The upstroke displacement is considered negative and its amplitude is less than half that of the downstroke. The zero stroke position provides an axial force equal to 1.5 times the apparent weight of the riser. The top section of the riser is set free to rotate. The results are shown in figures 6.5 and 6.6. The reduction in axial force fluctuation is noticeable, as it falls to about 0.5 MN. A minimum traction of 0.32 MN is obtained near the seabed, the maximum being 0.81 MN. There are also reductions in the maximum value and in the range of bending moments at the base, the extreme values now being 243 and 357 kNm.

The maximum axial stress possible is the sum of the maximum axial (F_s) and bending components (M_s) at the section under consideration because they do not occur in phase. The flexural stiffness of the riser tube is 94% of the flexural stiffness of the whole assembly. The bending moment acting on the riser itself follows the same proportion, relative to the total moment. The cross-sectional area, A_r, of the riser tube is 8.746×10^{-3} m^2 and the second moment of area I_r is 5.900×10^{-5} m^4. The distance between the neutral axis and the extreme fibre equals the external radius of the riser, $R = 122$ mm. The maximum stress in the axial, z direction, at the base of the riser, is then :

$$\sigma_z = \frac{F_s}{A_r} + \frac{M_s.R}{I_r}$$

(6.2)

Entering the numerical values in equation 6.2 results in:

$$\sigma_z = \frac{0.81 \times 10^6}{8.746 \times 10^{-3}} + \frac{0.94 \times 357 \times 10^3 \times 0.122}{5.900 \times 10^{-5}} = 6.94 \times 10^8 = 694 \ MPa$$

The extreme case must take into consideration the possibility of a leakage in the gas lift line,

leading to a high internal pressure in the annulus. This pressure could be up to 20.7 MPa (3000 psi), at the top of the riser. The internal hydrostatic pressure at 1000 m water depth, due to the difference between the densities of the completion fluid and sea water is 0.75 MPa (109 psi), resulting in a total differential internal pressure P of 21.5 MPa in the annulus. The hoop stress is given by:

$$\sigma_\theta = \frac{P r}{t}$$

(6.3)

The riser internal radius r is 110 mm and the thickness t is 12 mm, so

$$\sigma_\theta = \frac{21.5 x 10^6 x 0.110}{0.012} = 1.97 x 10^8 = 197 MPa$$

The axial stress associated with the internal pressure is half the hoop value, or 99 MPa in this case. The three principal stresses at the extreme fibre of the riser tube at the seabed, where the external pressure is 10 MPa (1450 psi), are then:

$$\sigma_r = -10\ MPa\ ;\quad \sigma_\theta = 197\ MPa\quad and\quad \sigma_z = 694 + 99 = 793\ MPa$$

The permissible maximum stress state for this extreme case is given by the API [74]:

$$\frac{\sigma_n}{\alpha\ f_{basic}} \leq 1$$

(6.4)

The net section stress σ_n is the combined von Mises stress at the point of interest. The factor α equals 1.2 for extreme environmental conditions. The allowable stress f_{basic} is the lesser of 2/3 of minimum yield or 1/2 of ultimate strength of the material. For the most common riser material, API steel grade N80, f_{basic} is 345 MPa. The maximum admissible net section stress is then 1.2 x 345 = 414 MPa.

The net section stress is given by:

$$\sigma_n = \sqrt{\frac{(\sigma_r - \sigma_\theta)^2 + (\sigma_r - \sigma_z)^2 + (\sigma_\theta - \sigma_z)^2}{2}}$$

(6.5)

In the present case, expression 6.5 gives a value of 722 MPa for σ_n, 1.7 times as high as the admissible value.

A tapered joint is then introduced, in order to reduce the maximum stress at the base. We consider a 14 m long tapered joint, with 7 different thicknesses varying linearly with the length. After some trials, a tapered joint with thicknesses varying from 15 to 38 mm is considered adequate.

Figures 6.7 and 6.8 show the results. There is a small reduction in the axial forces at the base, the extreme values now being 0.31 and 0.77 MN. The bending moments at the same position have doubled when compared with the previous analysis, because of the greater bending stiffness at seabed. The extreme values are 456 and 715 kNm in this case. The thicker section (t = 38 mm) has an area A_r of 3.080×10^{-2} m^2 and a second moment of area I_r of 2.653×10^{-4} m^4. The net section stress, given by formulas 6.2, 6.3 and 6.5 diminishes to a value of 410 MPa. This is just below the admissible value of 414 MPa, according to the design criterion in expression 6.4. It must be pointed out that the final maximum thickness could be greater than the one determined here when fatigue considerations are included.

6.4 ANALYSIS OF A COMPOSITE RISER

This section deals with the design of plain composite riser tubes. The tapered joints design, that uses the results from the plain tube as an input, is treated in the next section. Programmes ABAQUS/AQUA and TUBEPLAIN are the design tools used here. Some considerations about the choice of materials and manufacturing process are presented first.

The experimental work carried out showed very low T_l strengths for the biased glass/epoxy woven roving used for the hoop layers of the test tubes. It is recalled that the reason for adopting that form of material had to do with the type of glass/epoxy pre-pregs available in the market. For the fabrication of a full scale riser tube, however, there is no reason why the filament winding process could not be used. The 90° glass fibre angle with the axis makes it the method of choice for mass production. As a result, improved strength properties can be considered for the glass/epoxy sublaminates, compared with the woven roving pre-preg

option.

The experimental strengths obtained for the carbon pre-pregs were consistent with the values provided by the suppliers and were also within the boundaries one would expect for this type of material. Furthermore, the specific pre-preg utilised, T300/MTM28, displayed high fracture toughness values that proved crucial for the favourable behaviour of the tapered tubes concerning delamination.

For this reason, that material was chosen to make the carbon sublaminate of the composite riser. The table rolling process, or any similar sheet-by-sheet process, is insensitive to the fibre angle. But, in order to allow high productivity, the winding process was also considered for the assembly of the carbon/epoxy sublaminate of the composite riser. To permit this, without any further complication, the carbon fibre angle for the riser construction was kept at +/- 20°.

Tables 6.3 and 6.4 display respectively the stiffness and strength values for the materials adopted. The carbon /epoxy properties are repeated from Chapter 4, for convenience. The values considered for the glass/epoxy, filament wound hoop layers were all obtained from Tsai [104].

The composite riser tube is considered to behave as a beam-column, for the geometrically non-linear (with string effect) dynamic analysis performed by ABAQUS/AQUA. The sections of the riser are subjected to a force F_s and a bending moment M_s, as figure 6.9 displays. The shear forces, and the stresses it generates, are negligible, as will be shown later in the analysis. The sectional forces are the resultants of the stresses acting in the axial direction of the riser, due to the movements of the platform and to the distributed loads f given by Morison's hydrodynamic equation.

Previous analysis by Meniconi et al. [117], showed that the maximum stress criterion with an incremental approach, as proposed by Hinton et al. [41], worked well for the composite riser configuration. The combined internal pressure and four point bending tests also supported this conclusion, despite the low strengths of the glass/epoxy sub-laminates and the dispersion in the compressive strength values for the carbon/epoxy layers. This second aspect improved as the manufacturing technique for the dropped ply tubes evolved.

The internal diameter of the composite riser is taken equal to that of its steel counterpart, 220 mm. The maximum operational pressure of 20.7 MPa (3000 psi) dictates the total thickness of 12.0 mm for the glass/epoxy sub-laminates, the stresses being obtained from programme TUBEPLAIN. The carbon/epoxy sub-laminate thickness of 10 mm is determined from the ABAQUS/AQUA that provided the maxima of F_s and M_s, and from TUBEPLAIN that supplied the related lamina stresses.

As explained before, the top of the composite riser is connected to the production deck of the platform by means of a flexelement. From Stevenson and Harris [115] it is possible to estimate suitable axial and rotational stiffnesses for that component. The values are 125 kN/mm and 67 kNm/degree, respectively. The flexelement is modelled as two linear springs, to a first approximation. The proposed design methodology for the composite riser is shown in the subsection that follows.

6.4.1 DESIGN METHODOLOGY

Firstly, a design curve was determined, in terms of allowable combinations of pressures and axial loads. Programme TUBEPLAIN is used, together with the maximum stress criterion as discussed above.

For a closed end (2:1) internal pressure case, a first ply failure is detected at a pressure of about 60 MPa, related to transverse matrix cracking of the glass sub-laminates. That pressure is nearly double the value prescribed for the hydrostatic test of the tube, 31 MPa. The elastic constants E_2 and v_{21} are zeroed, as required by the criterion adopted. The pressurisation continues, until the occurrence of a final failure at a pressure of 104 MPa, due to longitudinal rupture of the carbon fibres. The final pressure achieved is 3.3 times as high as the test pressure.

The failure sequence procedure above is repeated for several combinations of internal and external pressures and tensile and compressive axial loads. The results generate two curves, in a pressure *versus* axial force diagram of the composite riser tube. One curve is the first ply failure envelope, the other is the final failure envelope. Both curves are displayed in figure 6.10. A third curve, also displayed, is defined by dividing by three the coordinates of the final

failure curve.

Finally, a design curve was defined, as being the one-third failure curve or the first ply failure surface, whichever gave the smaller values. This implies a safety factor of 3 or the onset of matrix cracking, as the design limit. The design curve, also shown in figure 6.10, corresponds to the first ply failure curve in the majority of the first quadrant and part of the second and to the one-third failure curve in the others.

In the first quadrant the positive axial and hoop loads lead to transverse cracking by tension in both the carbon and glass layers, well before the ultimate load. As both pressure and axial force become compressive, towards the third quadrant, the behaviour of the tube changes. The first ply failure is due to axial compressive collapse in the direction of the fibres and turns out to be the catastrophic one. When the compressive collapse is preceded by matrix cracking, the difference in the loads that cause each failure is small.

After establishing the design curve for the composite tube, the behaviour of a riser made of it can be examined. The analysis starts from the same initial consideration adopted for the steel riser, that is, a riser without tapered joints. The upper section is connected to the production deck of the TLP by means of the flexelement discussed before. The structural tube (not considering the 1 mm thick internal liner), has an ID of 222 mm and a total thickness of 22.0 mm, of which 12.0 mm are made of a 90° glass-epoxy composite, divided into inside and outside laminates. The central layer, with a thickness of 10.0 mm, is made of a $\pm 20^\circ$ carbon-epoxy laminate.

The equivalent axial modulus for the composite tube is easily determined from TUBEPLAIN, if we recall that the longitudinal strain is one of its deliverables. For a given pure axial load case, the determination of E_c is straightforward. The resulting value for the present case is 45.5 GPa.

The second moments of area are 1.265×10^{-4} m^4 and 3.492×10^{-6} m^4 for the riser tube and for the tubing and gas lift line assembly, respectively. The axial modulus for the steel tubing and gas lift pipe is $E_s = 207$ GPa. The total bending stiffness is then:

$$(EI)_{total} = E_c I_{riser} + E_s (I_{tubing} + I_{gas\ lift\ line}) = 45.5 \times 10^9 \times 1.265 \times 10^{-4} + 207 \times 10^9 \times 3.492 \times 10^{-6}$$

$$(EI)_{total} = 6.480x10^6 \ Nm^2$$

Each composite tube joint is considered to have a length of 24 m. This is limited by the tube handling equipment of the platform. The tube length is taken at its maximum possible value, in order to minimise costs and to maximise the weight advantage against steel. Taking the specific gravities of the glass and carbon composite layers as 2120 kg/m^3 and 1520 kg/m^3, respectively, we obtain a density of 1847 kg/m^3 for the total laminate. There is a 1 mm thick internal liner made of Buna-N elastomer, which has a density of 1050 kg/m^3. There is also an external polyethylene coating, 1 mm thick and with a density of 960 kg/m^3.

The total (liner plus structural layers plus coating) cross-sectional area of the composite tube is 1.840x10^{-2} m^2, corresponding to an internal diameter of 220 mm and a total thickness of 24 mm. The dry weight of the riser per unit length is 446 N/m, considering all the materials listed above and two steel couplings weighting 1500 N each every 24 m. The distance between the production deck of the platform and the mean sea level is 18 m. The apparent weight of the riser is then:

$$W_r = 18 \ x \ 446 + 1000 \ x \ (446 - 1024 \ x \ 9.81 \ x \ 1.840x10^{-2}) \ = \ 269 \ kN$$

A pretension of 404 kN - 1.5 times as high as the apparent weight - is applied at the top of the riser. The total distributed mass of the assembly is obtained using the same considerations as before. There is oil of density $\rho = 950$ kg/m^3 inside the tubing, which has an internal transverse area of 7.939x10^{-3} m^2. A completion fluid of $\rho = 1100$ kg/m^3 fills up the annulus, which has a transverse area of 2.592x10^{-2} m^2 The gas lift line contains approximately zero density fluids. The unit weights of the tubing and the gas lift lines are 186 N/m (12.75 lbw/ft) and 42 N/m (2.9 lbw/ft) respectively, including couplings. The total mass per unit length, for the calculation of lateral vibrations, is then:

$$m_t = (446 + 186 + 42)/9.81 + 950 \ x \ 7.939x10^{-3} + 1100 \ x \ 2.592x10^{-2} = 105 \ kg/m$$

Figures 6.11 and 6.12 show the resulting force envelopes, from ABAQUS/AQUA. The absolute values and the ranges of both the axial forces and the bending moments (at the bottom) are reduced in comparison with the steel riser, c.f. figures 6.3 and 6.4. This is because of the smaller axial and bending stiffnesses of the composite riser. The bending moments at

the top of the riser are smaller than those at the bottom due to the action of the flexelement.

The next step is to compare the results obtained with the assumed design curve. In order to do that the concept of equivalent axial force is used. It is recalled that the stresses due to pure bending can be obtained from the axial load case. The equivalent axial force is the force that causes a uniform axial strain equal to the extreme fibre strain in bending, either in tension or compression. There is some conservatism in this concept, because the carbon layers, where the ultimate failure occurs in bending, are not the external sub-laminates. The maximum strain at the outer carbon laminate is slightly smaller than the strain at the outer glass layer, in bending. But, because some first ply failures do occur at the outer glass layers, that definition of equivalent force was retained.

The equivalent forces are then added to the actual section forces, allowing both bending and axial loads to be combined on one axis of the design curve. Because the axial forces and the bending moments are not in phase, the minimum resulting total force can be bounded by taking the sum of the force equivalent to the maximum moment (considered negative, at the compressed side) and the minimum actual section force. Conversely, the maximum total force is bounded by the sum of the force equivalent to the maximum moment (now positive) plus the maximum actual section force.

The maximum curvature of the riser assembly, under a bending moment M_s , is given by the simple equation :

$$\frac{1}{\rho} = \frac{M_s}{(EI)_{total}}$$ (6.6)

and the maximum longitudinal strain ε_z associated with bending, given the external radius of the structural tube, R, is:

$$\varepsilon_x = \frac{R}{\rho}$$ (6.7)

The equivalent axial forces (both tensile and compressive) are obtained from TUBEPLAIN,

for the given uniform axial strain ε_z.

Four sections of the riser are analysed. The top and bottom sections are subjected to the greatest bending moments and so they are liable to the substituted by thicker ones. The section called "near bottom" is just above the height to be reached by a tapered joint 12 metres long at the base ($l = -988$ metres). Figure 6.12 shows that the section at sea level (position 0 metres), is also subjected to a noticeable bending moment, due to wave action. But that region can be reached by the top tapered joint, if the length of it is taken to be 24 metres. The section called "near top" is then just below the last position to be overtaken by top tapered joint ($l = -6$ metres).

The section forces displayed in figures 6.11 and 6.12 are related to a pretension of 1.5 times the apparent weight. As the top of the riser is directly connected to the platform through a flexelement, the pretension is applied by stretching the riser, before anchoring it to the deck. Some loading situations lead to a modification of the riser length and hence of the pretension. These load cases are: astronomical tides, internal pressure acting in the annulus and riser temperature alterations. They are dealt with in the next subsection.

6.4.2 LOAD CASES VERIFICATION

The oceanographic survey stated that the maximum and minimum 100-year return period tides for the Marlim field oceanic area are +1.0 m and -0.9 m, respectively, defining a total tidal variation $\Delta t = 1.9$ m. The platform is anchored to the seabed by 12 tendons, each with a 711 mm (28") OD and 32 mm (1.25") thickness. The length of the tendons in a 1000 m water depth location is 973 m. The total stiffness of the tendons is therefore $K_{tendons} = 1.734 \times 10^8$ N/m. Each composite riser has a stiffness of 7.537×10^5 N/m. Considering 24 risers to be installed, the total axial stiffness of the risers $K_{risers} = 1.809 \times 10^7$ N/m results.

The platform uplift force variation, which is a function of the cross-section area of its columns, is $K_{plat} = 1.046 \times 10^7$ N/m. One can write the following simple equation to find the length variation of the risers due to tidal effects, Δl_{tide}:

$$K_{plat}\left(\Delta t - \Delta l_{tide}\right) = \left(K_{tendons} + K_{risers}\right)\Delta l_{tide} \tag{6.8}$$

By substituting numerical values into the equation, a value of Δl_{tide} = + 98 mm is obtained. That displacement imposes an additional axial force of 73.9 kN on each composite riser.

In the event of a leakage in the gas lift line, there would be a pressure of 20.7 MPa (3000 psi) acting in the annulus between the tubings and the riser, at the top of it. The cross-section area of the annulus is A_{an} = 2.592x10^{-2} m^2. The section force, in the direction of the axis of the tube, resulting from the internal pressure is then:

$$F_s=P.A_{an}=20.7x10^6 x2.592x10^{-2}=536.5 \ kN$$

Programme TUBEPLAIN returned an axial strain ε_z of 1.518x10^{-4} for that pair of internal pressure and axial force values.

At the bottom of the riser the axial force due to pressure is reduced by its apparent weight, being 267.5 kN. The internal pressure there is 21.6 MPa, due to the difference in density between the completion fluid and sea water. The resulting axial strain is -2.222x10^{-4}.

The strains along the axial direction vary linearly with depth, and even change sign, as shown above. The expression of ε_z with respect to depth l is written as:

$$\varepsilon_z(l) = 1.452x10^{-4} +3.667x10^{-7}.l \tag{6.9}$$

The length variation of the composite riser due to internal pressure in the annulus is obtained by:

$$\Delta l= \int_{-1000}^{18} \varepsilon_z(l)\,dl = \left(1.452x10^{-4}l + 1.834x10^{-7}l^2\right)\Big|_{-1000}^{18} = -3.55x10^{-2}m \tag{6.10}$$

The final effect is a shortening of the riser, Δl_{pres} = - 35 mm. This load condition leads to a change not only in riser length, and consequently in its pretension, but also in the hoop stress. That is considered by the pressure coordinate in the design curve graph.

As the platform starts producing oil, the temperature of the riser assembly increases, because the produced fluids emerge hot from the well. The temperature variation of the riser leads to a variation in its length, as well. Typical conditions for the Marlim field are temperatures of

53°C for the oil at the seabed and of 40°C at the arrival on the platform. Ocean temperatures in the area were taken to be of 4°C at the seabed and 10°C at the surface.

A heat transmission calculation was performed, considering every material and fluid in the riser assembly, together with the various heat transmission processes involved. Table 6.5 displays the average temperature rise ΔT resulting, for every layer, at the top and the bottom of the riser.

The coefficients of thermal expansion (CTEs) of the materials, referred to the lamina directions, were obtained from Gibson [10]. They are: $\alpha_1 = 6 \times 10^{-6}$ and $\alpha_2 = 20 \times 10^{-6}$, for the glass/epoxy laminae, and $\alpha_1 = 1 \times 10^{-6}$ and $\alpha_2 = 31 \times 10^{-6}$ for the carbon/epoxy. It is remembered that the CTEs transform like strains:

$$\begin{Bmatrix} \alpha_\theta \\ \alpha_z \\ \alpha_{\theta z} \end{Bmatrix} = \begin{bmatrix} c^2 & s^2 & cs \\ s^2 & c^2 & -cs \\ -2cs & 2cs & c^2-s^2 \end{bmatrix} \begin{Bmatrix} \alpha_2 \\ \alpha_1 \\ 0 \end{Bmatrix} \tag{6.11}$$

Given the fibre angles of 90° (glass) and +/- 20° (carbon), the CTEs referred to the cylindrical directions are:

$$\begin{Bmatrix} \alpha_\theta \\ \alpha_z \\ \alpha_{\theta z} \end{Bmatrix} = \begin{Bmatrix} 6 \\ 20 \\ 0 \end{Bmatrix} x10^{-6} (glass) \quad and \quad \begin{Bmatrix} 27 \\ 5 \\ 19 \end{Bmatrix} x10^{-6} (carbon)$$

It is not possible to use TUBEPLAIN to assess the strains generated by the thermal load, because in this case the external pressures and forces are zero. Nevertheless, a good estimate of the length variation of the riser can be obtained from the classical laminate theory (CLT). The following relation holds, for every k sub-laminate:

$$\{\varepsilon\}_k = [\bar{S}]_k \{\sigma\}_k + \{\alpha\}_k \Delta T_k \tag{6.12}$$

Making the stresses explicit:

$$\{\sigma\}_k = [\bar{Q}]_k (\{\varepsilon\}_k - \{\alpha\}_k \Delta T_k) \tag{6.13}$$

The membrane forces are obtained by adding the product of the stress by the thickness h_k of every sub-laminate:

$$\{N\} = \sum_{k=1}^{n}\{\sigma\}_k h_k = [A]\{\varepsilon\} - \sum_{k=1}^{n}[\bar{Q}]_k h_k \{\alpha\}_k \Delta T_k \qquad (6.14)$$

where [A] is the extensional stiffness matrix, from the CLT. The second term of the equation above are the thermal forces due to temperature changes:

$$\{N^T\} = \sum_{k=1}^{n}[\bar{Q}]_k h_k \{\alpha\}_k \Delta T_k \qquad (6.15)$$

As the external forces {N} are nil in this case, equation 6.14 leads to:

$$\{\varepsilon\} = [A]^{-1}\{N^T\} \qquad (6.16)$$

The axial strains due to the temperature rise, at the top and bottom sections, obtained from 6.16, are 5.959×10^{-5} and 1.106×10^{-4}, respectively. As in the internal pressure case, the axial strains are assumed to vary linearly with the depth, l, and the final riser length alteration is obtained from an integral, as in expression 6.10. The result is an increase in length of the riser, $\Delta l_{temp} = + 87$ mm.

The thermal loading affects the riser not only by modifying its length but also by introducing internal stresses in the sub-laminates, despite the fact that the net membrane forces are zero. The most affected stresses are the σ_1's, along the direction of the fibres. The CLT indicates a maximum σ_1 of 27 MPa for the carbon layers, due to the thermal effect. For the glass/epoxy, the σ_1 values are less than 5 MPa. These are small values, compared with the T_1 strengths of the materials, listed in table 6.4. It is decided to allow some margin between the load results and the design curve to account for these internal thermal stresses.

The displacement applied to the top of the riser prior to anchoring it corresponds to a minimum pretension of 1.5 times its apparent weight. It is a displacement of 536 mm, given the 404 kN pretension and the riser axial stiffness, EA, of 767 MN. This is a situation of low tide, without any pressure in the annulus, but with the riser hot. It is this combination because the tidal rise, the pressurisation of the annulus and the cooling of the riser, all tend to stretch it

further.

The total displacement variation, combining the three effects is $\Delta l_{tide} + \Delta l_{pres} + \Delta l_{temp} = 220$ mm. One more ABAQUS/AQUA analysis is run, with an extra displacement of 220 mm added to the 536 mm original value. A final fact to remember is that, at the bottom of the riser, there could be an external pressure of 10.1 MPa, due to the possibility of the annulus being empty. Figure 6.13 shows the final result, comparing all possible axial forces and pressures combinations with the design curve. As expected, the top and bottom sections load *loci* surpass the design surface. There have to be thicker tube sections there. The thicker sections are provided by the composite tapered joints, whose analysis is performed in the next section. The "near top" and "near bottom" sections are confined inside the design curve, as well as all the sections of the composite riser between them.

Before the composite tapered joints are designed, it was checked whether or not the lower axial stiffness of the composite riser is acceptable, regarding its deformed shape when subjected to the environmental loads. To do that, the deformed shape of a steel riser is compared with that of a composite one. Three different composite risers configurations are analysed, with different carbon fibre angles (namely $35°$, $40°$ and $45°$), resulting in axial stiffnesses (EA) of 600, 480 and 360 MN. There are no tapered joints in any riser. The dimensions adopted for the risers are those given in sections 6.3 and 6.4.1, for the steel and composite cases. A mean pretension of 1.5 times the apparent weight is adopted throughout. The steel riser have the necessary tensioner system and the composite ones are considered to be fully restrained at the top section. An instant of time when the platform is at its most upstream position is chosen for the comparison. Figure 6.14 shows the results.

At depths greater than 300 metres all the composite risers have lateral displacements smaller than those of the steel one. Between that depth and the top, the composite riser with an axial stiffness of 360 MN has displacements noticeably greater. A composite riser with an axial stiffness of 480 MN has lateral displacements only slightly above those of a steel riser, in the shallow region within the top and a depth of 100 metres. Composite risers with an axial stiffness of 600 MN, or higher, have displacements smaller than those of a steel one along their whole length. It must be said that those figures relate to composite risers with external diameters of 268 mm. In conclusion, the present axial stiffness of 767 MN of the riser

geometry adopted is adequate, from the point of view of deformed shape. The reduced lateral displacements of the composite risers, when compared with the steel ones, can lead to a reduction in the distance between the wellheads at the production deck of the platform.

6.5 DESIGN OF THE COMPOSITE TAPERED JOINTS

The design of the tapered joints is performed on a trial and error basis, as the joint geometry affects both the resulting section forces and the design curves. After some trials, a top tapered joint emerged with total thickness varying from 26 to 40 mm, corresponding to carbon layers 14 to 28 mm thick. The total thickness of the glass layers is maintained at 12 mm. Its internal diameter is the same of the composite pipe, 220 mm, and its length equals 24 m, to reach the wave impact zone. The bottom tapered joint has thickness varying from 26 to 60 mm (carbon layers thickness between 14 and 48 mm) with the same ID and glass layers total thickness as the top one. Its length is 12 m, half the length of the top tapered joint. Figures 6.15 and 6.16 show the forces and moments along a composite riser with both tapered joints, for the basic pretension of 1.5 times the apparent weight of the riser. The loading situations that can modify the riser length, and hence its pretension, are addressed the same way as they were for the plain riser tubes.

The increase in weight caused by the tapered joints is compensated for by the increase in axial stiffness. In the end, the amount of vertical displacement to produce the pretension remains the same. The checking of the various loading cases is done for the thinner and thicker sections of each tapered joint. The thickness is reduced by dropping two pairs of $+/-20°$ carbon layers at a time, with a reduction of 0.5 mm in every step. This represents a compromise between the SCF generated by the drop-off detail and the ease of manufacture of the tubes.

Programme TUBEDROP is used to define the SCFs in σ_z for each case, in relation to the value at the thinner portion of the tapered joints. A value of 1.1 resulted, which did not change significantly for the range of total thicknesses involved. Programme TUBEPLAIN is used to define the design curves, with the axial forces multiplied by the SCF. The analysis is performed that way because the design process is on a trial and error basis, with several runs

of the programme required to define a single design curve. To use the time consuming finite difference scheme would be infeasible. Moreover, TUBEDROP lacks accuracy, despite giving a good indication of the SCFs in σ_z. Due to the considerable thickness of the tubes, the SCF for a 0.5 mm ply drop-off remained small, in any case.

Figures 6.17, to 6.19 show the results of the process. The thin part of both joints (figure 6.17) have a good margin between the load loci and the design curve. If it were not for the SCF related to the drop-offs, they could have the same thickness as the plain riser joints. Figure 6.18 shows that the resulting dimensions of the thick portion of the bottom tapered joint are on the design limit, for positive axial forces. In figure 6.19 it is seen that the thick part of the top joint has the same sort of design margin as its thin part. In a real design situation, one more optimisation loop would perhaps be required, but the aim of the present exercise was only to illustrate the feasibility of the process.

The finite element analysis performed in Chapter 4 indicated a length of 20 mm at both sides of a 0.8 mm drop in thickness, where the σ_z values are affected by it. The individual thickness drop of 0.5 mm adopted in the design implies a step at every 176 mm in length of the bottom tapered joint. This is more than enough to avoid any stress concentration interference.

The comparison between the load cases and the design curves showed that the axial loads control the design. The high bending moments at the tapered joints are the major cause of this. They introduce large equivalent axial forces. The margins between the maximum values and the admissible ones are generally smaller for axial loads than they are for to the pressures.

SERR analysis

Next, the possibility of the onset of delamination is investigated for the bottom tapered joint, which is subjected to the highest axial forces (real plus equivalent). Two finite element models are generated, for both extremes of that tapered joint. The dropped plies are considered to end flush, defining a single resin pocket with a height of 0.5 mm. They are placed at the mid-thickness of the carbon/epoxy sub-laminate. Defects with an initial length of 1 mm are supposed to exist at the tip of the resin pockets, which are 3 mm long. The virtual crack closure method of Rybicki and Kanninen [34] is used to calculate the SERRs.

The initial defects are placed at the tip of the resin pockets because it was shown in Chapter 4 that they tend to open under tractive loads, at that position. As the axial section forces are always positive, the tensioned side of the bent tubes displays the highest SERR values. The SERRs are calculated separately for the axial force and for the bending moment components, according to expressions 4.20 and 4.23, respectively. The *axial:bending* σ_z stress fractions are *1:0.81* for the thin part and *1:9.39* for the thick section. The failure indexes are given by formula 4.24, considering the toughness values of 297 J/m^2 for mode I and of 1577 J/m^2 for mode II, obtained experimentally for the +20°/-20° carbon/epoxy angle-ply interfaces. The SERR analysis are related to the maximum operational loads. Figures 6.20 and 6.21 display the results, for the thin and the thick ends of the bottom tapered joint, respectively.

The results show failure indices smaller than 0.3 for the thin part and 0.7 for the thick part of the bottom tapered joint. The axial load component of the SERRs are the most important ones, for the thin part. For the thick part, the bending component is the prevailing one, due to the large bending moments there. Failure indices smaller than one ensure that no delamination occurs at the extreme loading situation, even for severe, circumferential initial defects. This is due mainly to the high fracture toughness of the carbon/epoxy system considered. The graphs in figures 6.20 and 6.21 show, however, that if the delaminations did start, its growth would be unstable, as the derivatives of the SERRs with respect to defect length are negative, in general.

Table 6.6 compares some characteristics of both steel and composite risers. Before the analysis is concluded, one more verification is performed. One of the basic assumptions of the design methodology is that the tubes behave as beam-columns. This is certainly the case for the plain riser tubes, because there are not significant shear forces away from the ends. At the base and the top there are reactive shear forces, however. In Appendix B the shear stresses are evaluated for the thicker part of the bottom tapered joint. The shear stresses are shown to be very small, compared with the stresses introduced by the axial force and the bending moments. As a result, the beam-column behaviour assumption is confirmed

Heave	
mean	- 2.3 m
amplitude	0.4 m
period	3.5 s
Surge and sway	
mean	47 m
amplitude	4.8 m
period	9.4 s
Wave	
Significant heigth H_s	7.8 m
Zero cross period T_z	9.4 s

Current profile	Depth [m]	Speed [m/s]
	0	1.26
	50	1.20
	100	1.10
	140	0.96
	230	1.09
	340	0.97
	415	0.77
	545	0.63
	640	0.61
	750	0.54
	915	0.52
	1000	0.00

Table 6.1 Platform motions and environmental conditions, related to 100-year storm reaching the platform on a 45° angle.

Tensioner force [MN]	Displacement [m]
0.787	- 0.6
0.928	0.0
1.267	1.0
1.687	2.0

Table 6.2 Tensioner characteristics.

Elastic Property	E-Glass/epoxy (v_f=45%) [104]	Carbon/epoxy (v_f=56%)
E_1 [GPa]	39	117
E_2 [GPa]	8	8
G_{12} [GPa]	4	5
v_{12}	0.26	0.34
v_{23}	0.4	0.5

Table 6.3   Lamina stiffness values .

Ultimate Strength [MPa]	E-Glass/epoxy (v_f=45%) [104]	Carbon/epoxy (v_f=56%)
Longitudinal tension T_1	1,062	1,640
Longitudinal compression C_1	610	1,280
Transverse tension T_2	31	80
Transverse compression C_2	118	250
Intralaminar shear S_{12}	72	100

Table 6.4   Lamina ultimate strength values .

Section	Glass, internal	Carbon	Glass, external
Top	10	7	4
Bottom	18	13	8

Table 6.5 Average temperature rise ΔT [°C] .

Characteristic	Steel riser	Composite riser	
Internal diameter [mm]	220	220	
External diameter [mm]	244	268	
Dry weight with connectors [N/m]	694	446	
Wet weight, idem [N/m]	606	261	
Tapered joints	**Bottom**	**Top**	**Bottom**
Length [m]	14	24	12
Smaller thickness [mm]	15	26	26
Greater thickness [mm]	38	40	60

Table 6.6 Some characteristics of the risers.
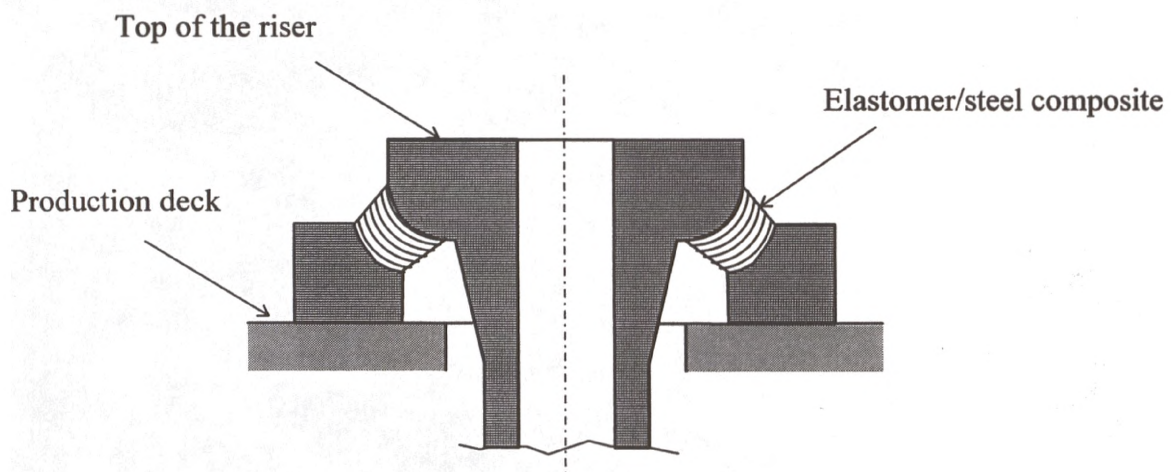
Figure 6.1 Flexelement to be installed at the top of the composite riser.
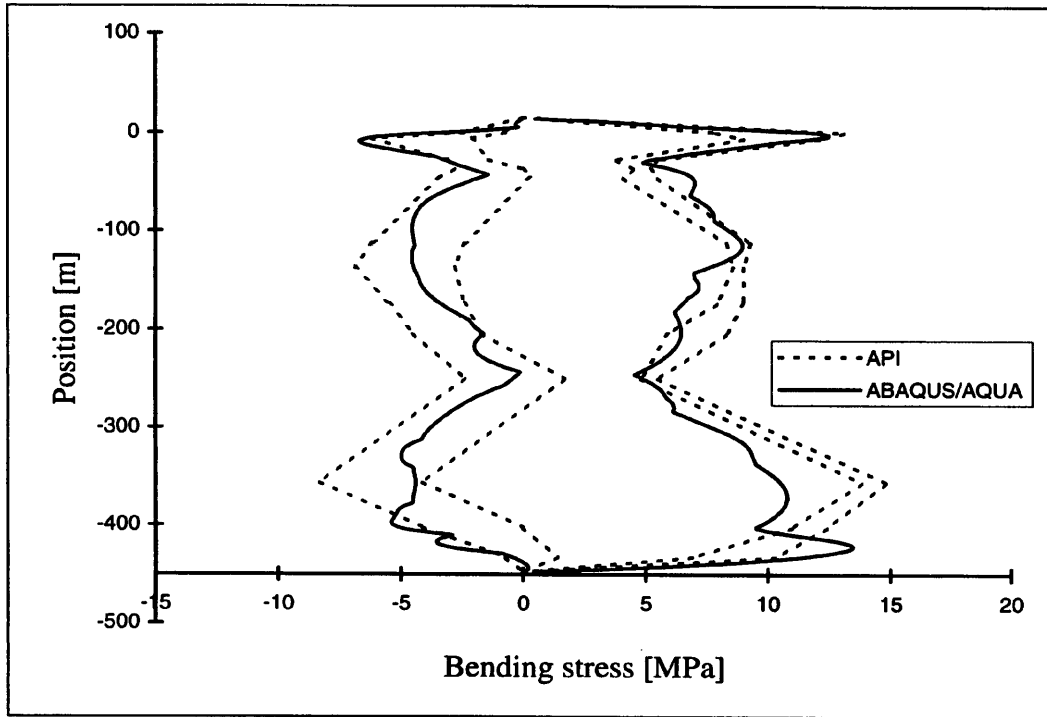
Figure 6.2 Calibration of ABAQUS/AQUA program using API case 1500-20-2-D.
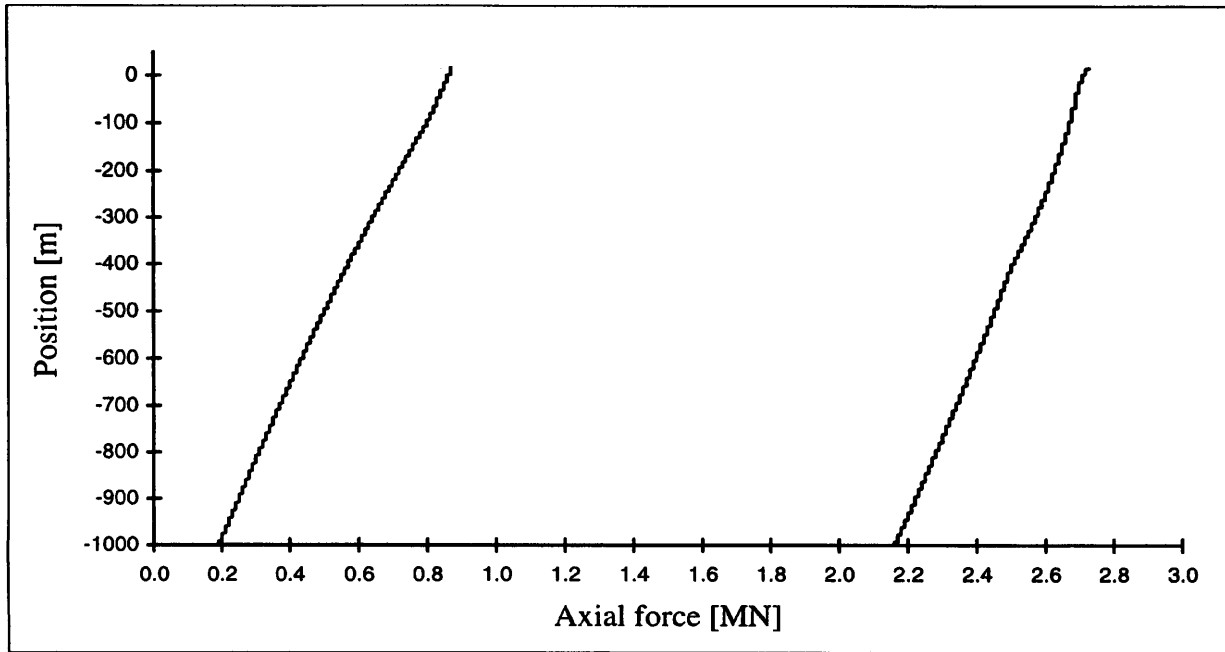
Figure 6.3 Force envelope: steel riser without tapered joint and tensioners.
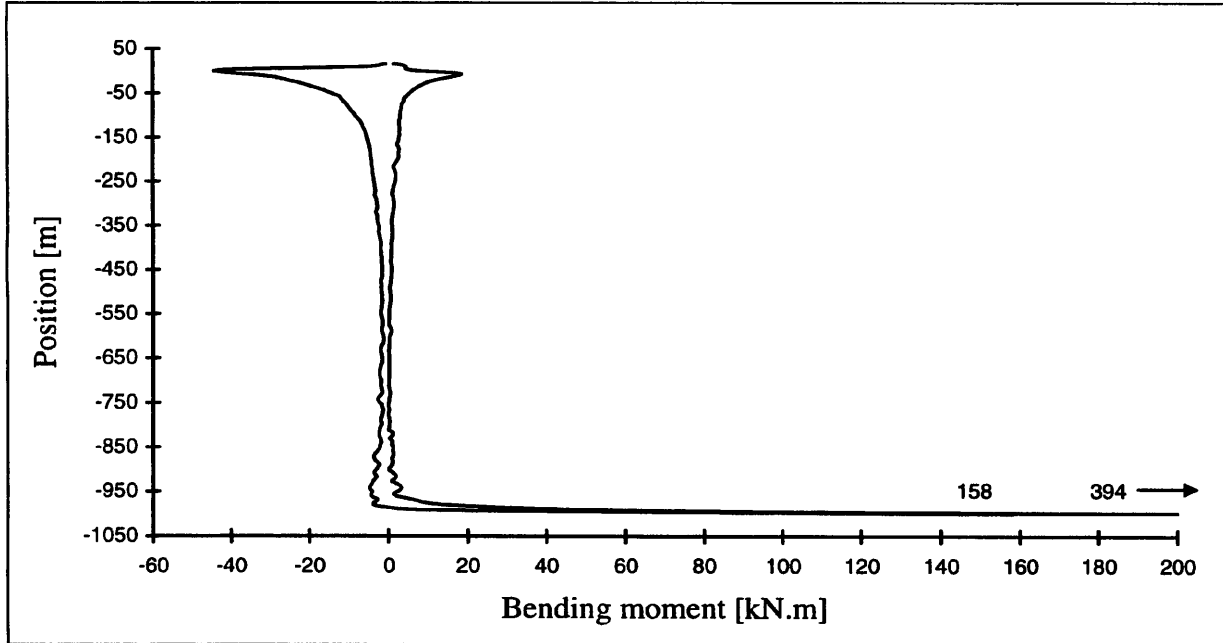

Figure 6.4 Moment envelope: steel riser without tapered joint and tensioners.
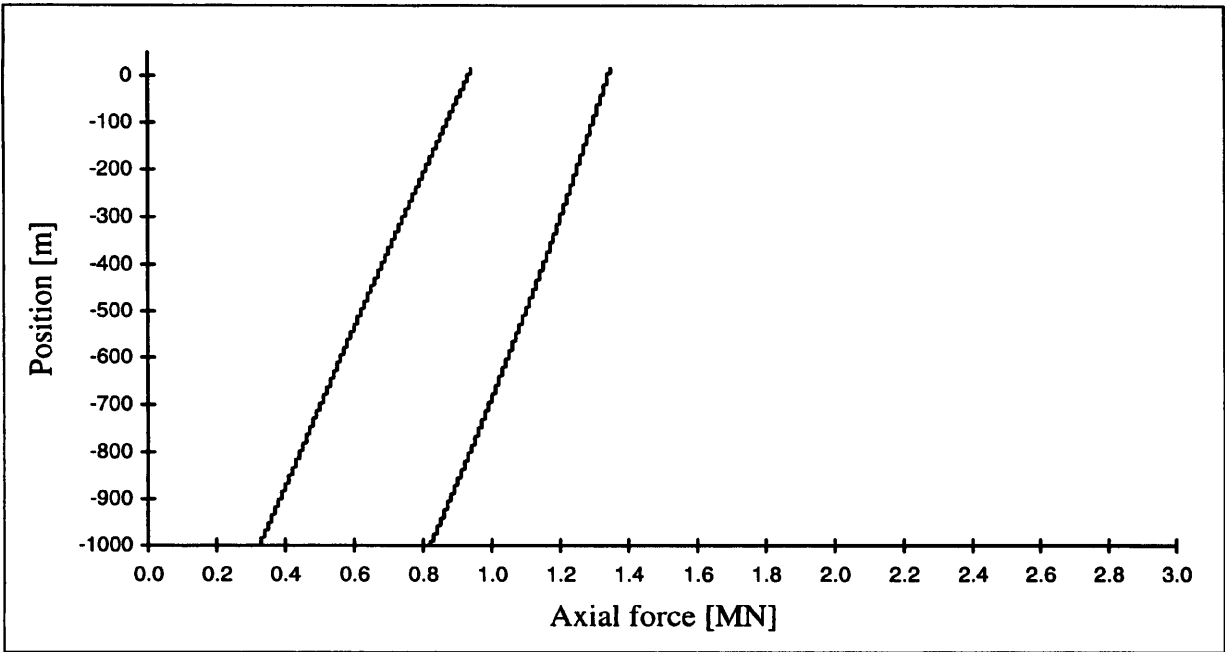
Figure 6.5 Force envelope: steel riser without tapered joint but with tensioners.
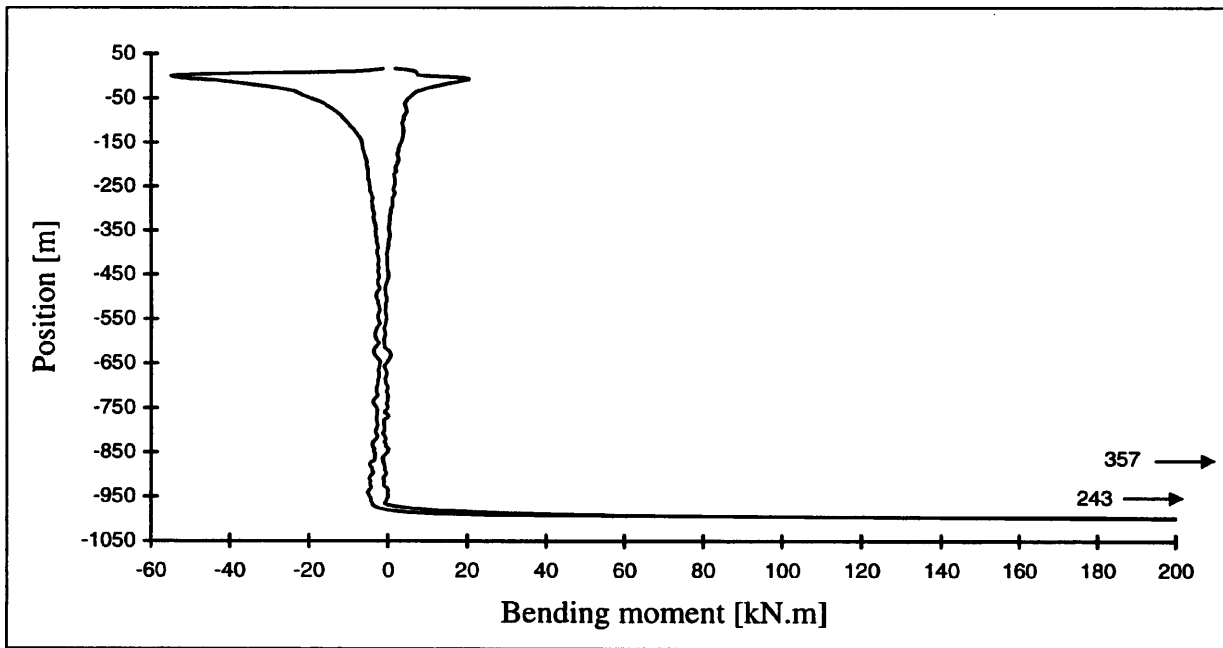
Figure 6.6 Moment envelope: steel riser without tapered joint but with tensioners.

238
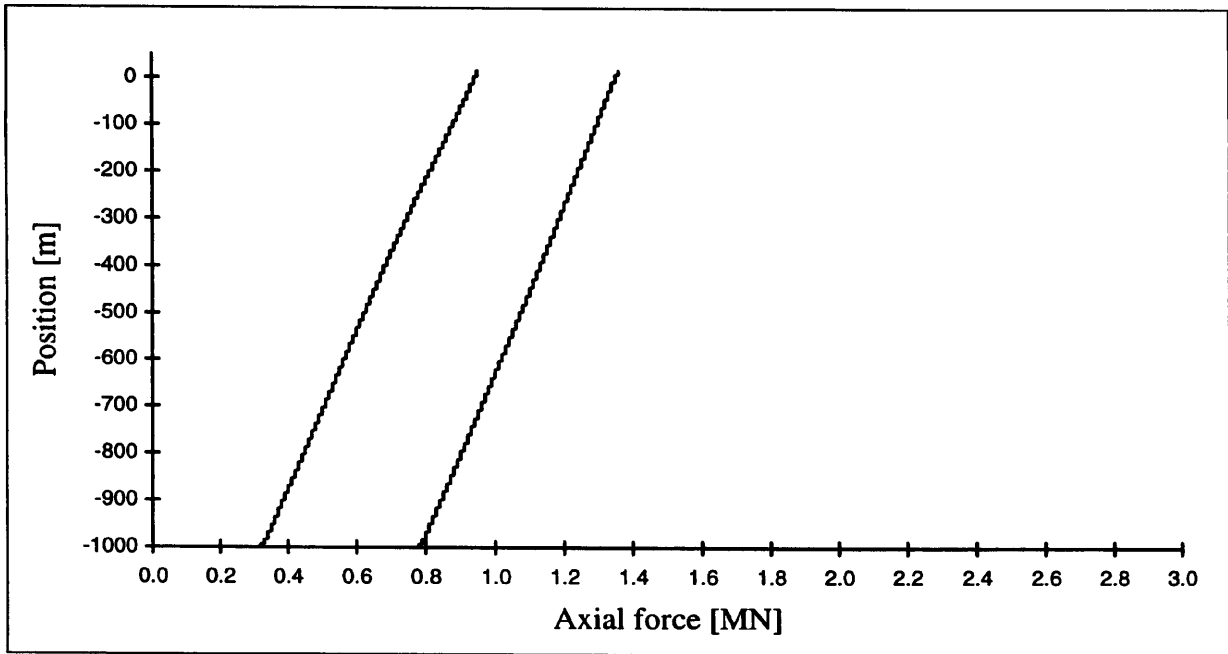
Figure 6.7 Force envelope: steel riser with tapered joint and tensioners.
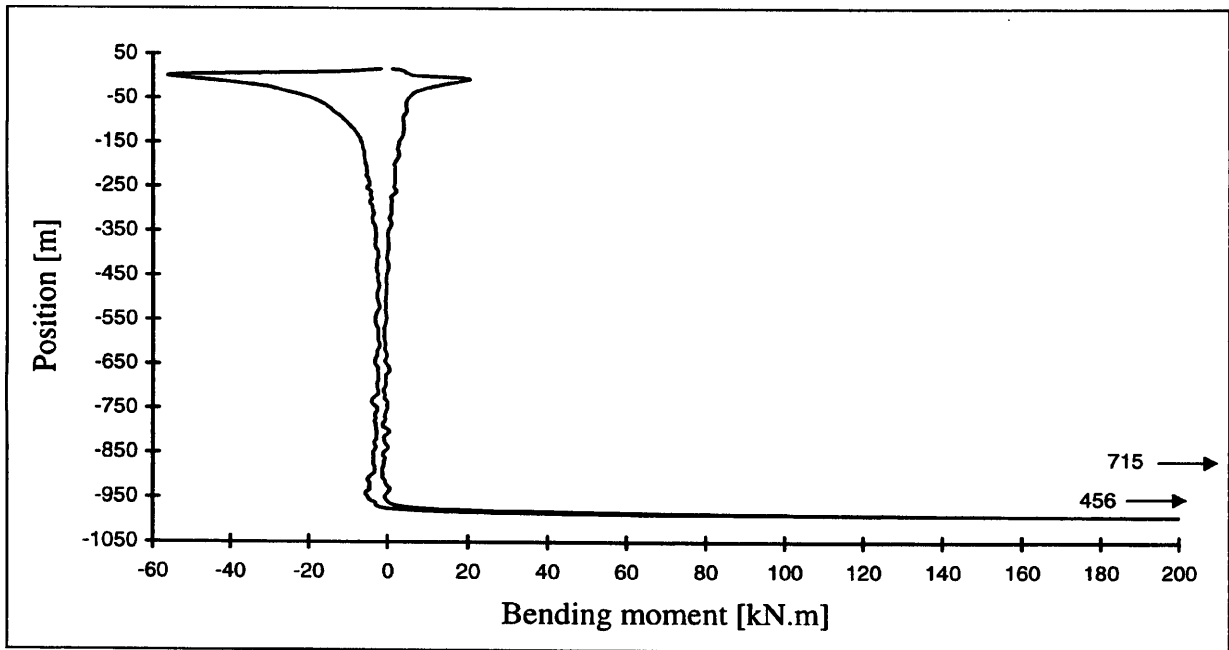
Figure 6.8 Moment envelope: steel riser with tapered joint and tensioners.
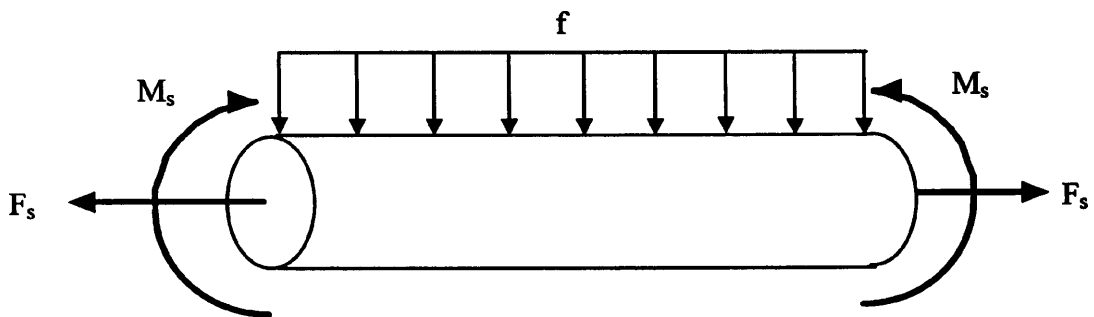
Figure 6.9 Riser tube as a beam-column, showing the loading and section forces.
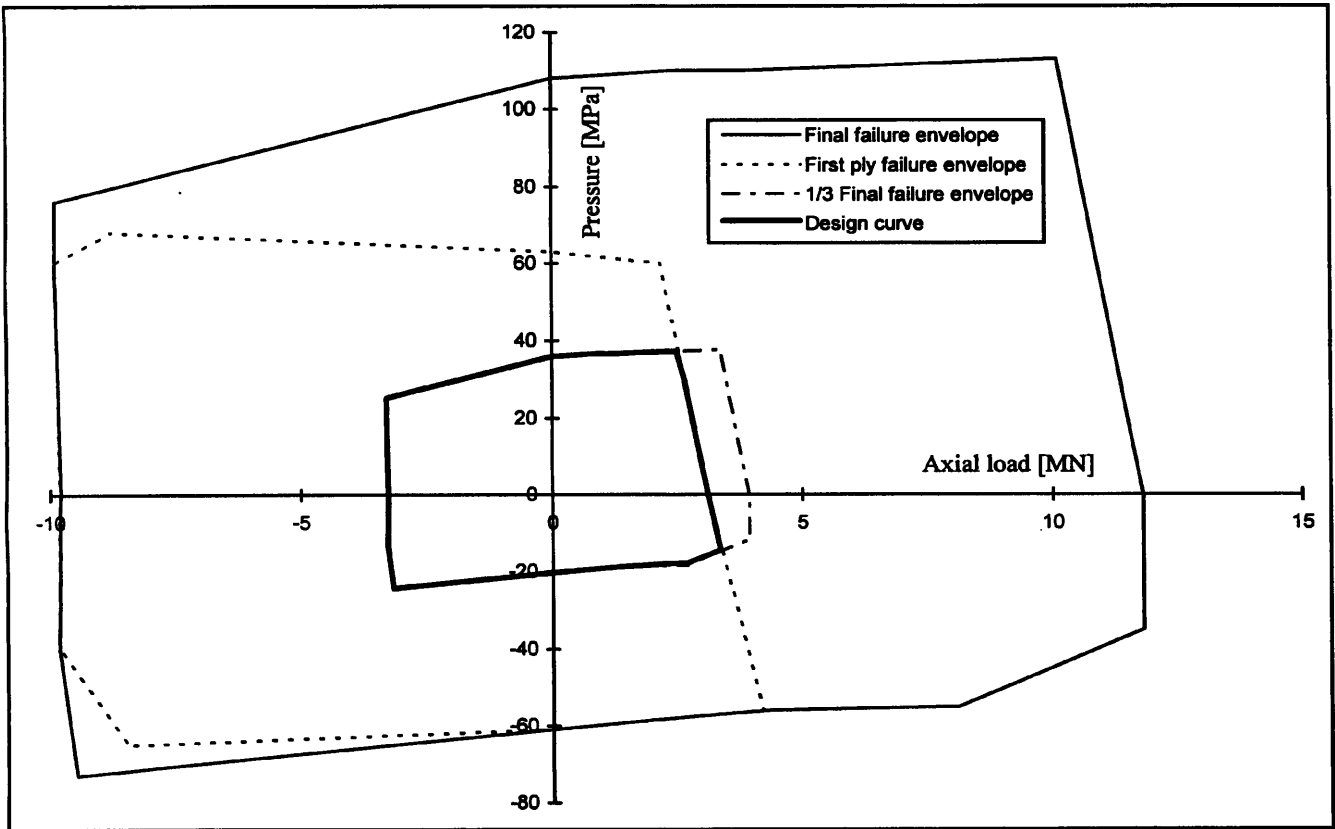
Figure 6.10 Pressure versus axial load curves for the composite riser tube.
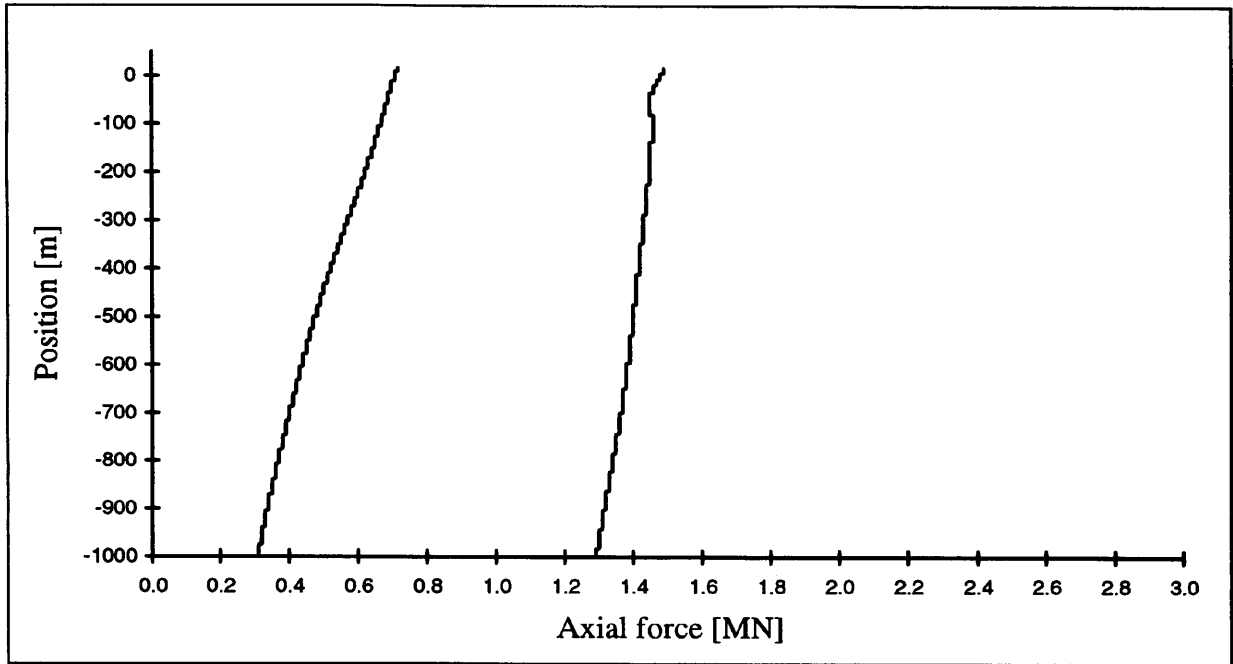
Figure 6.11 Force envelope: composite riser without tapered joints.
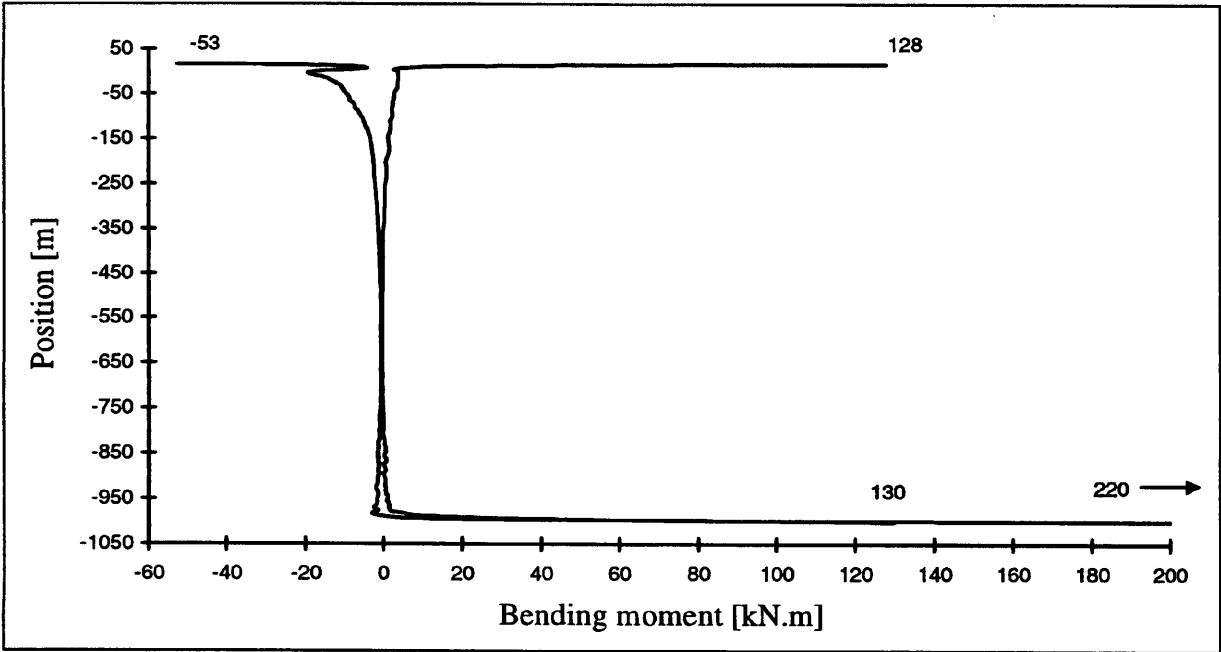
Figure 6.12 Moment envelope: composite riser without tapered joints.
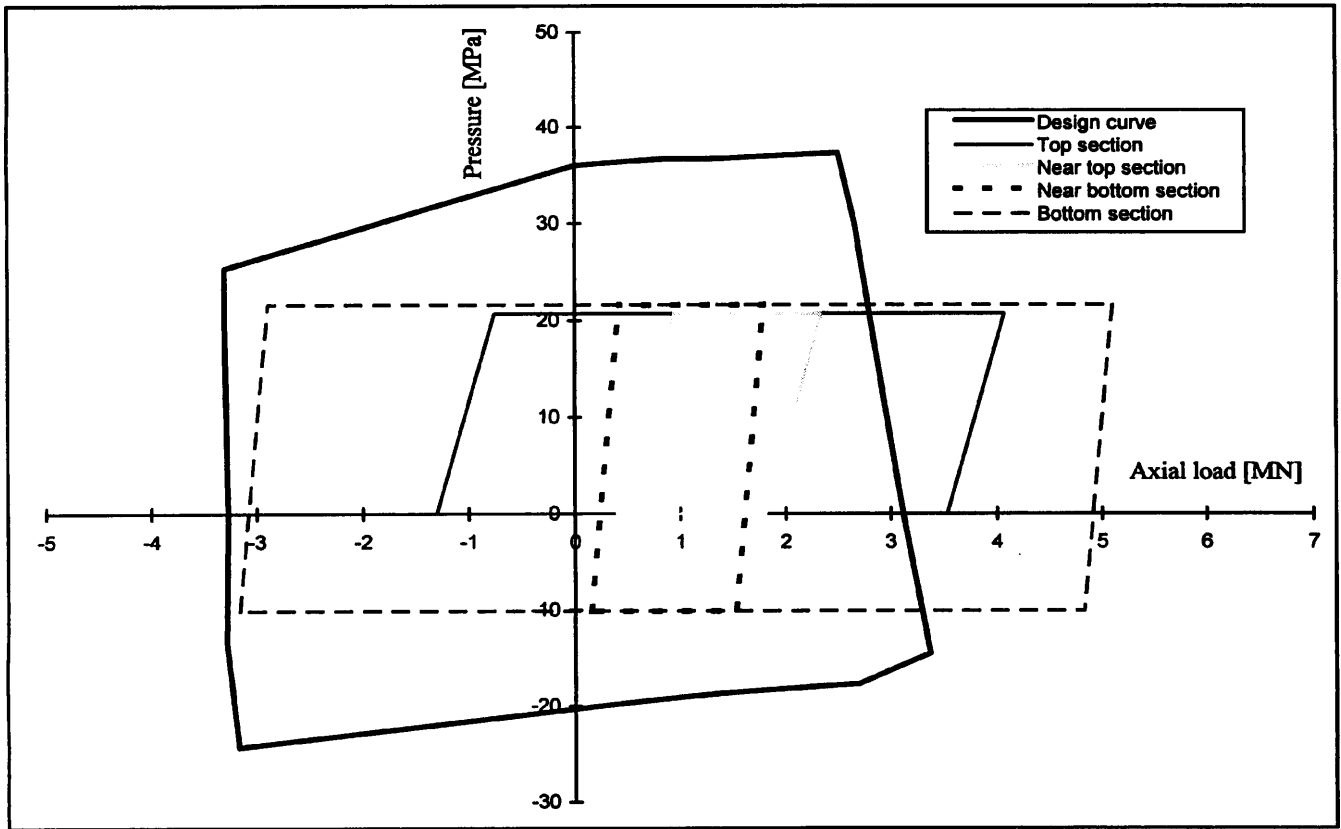
Figure 6.13 Design curve and loading *loci* for the composite riser tube.
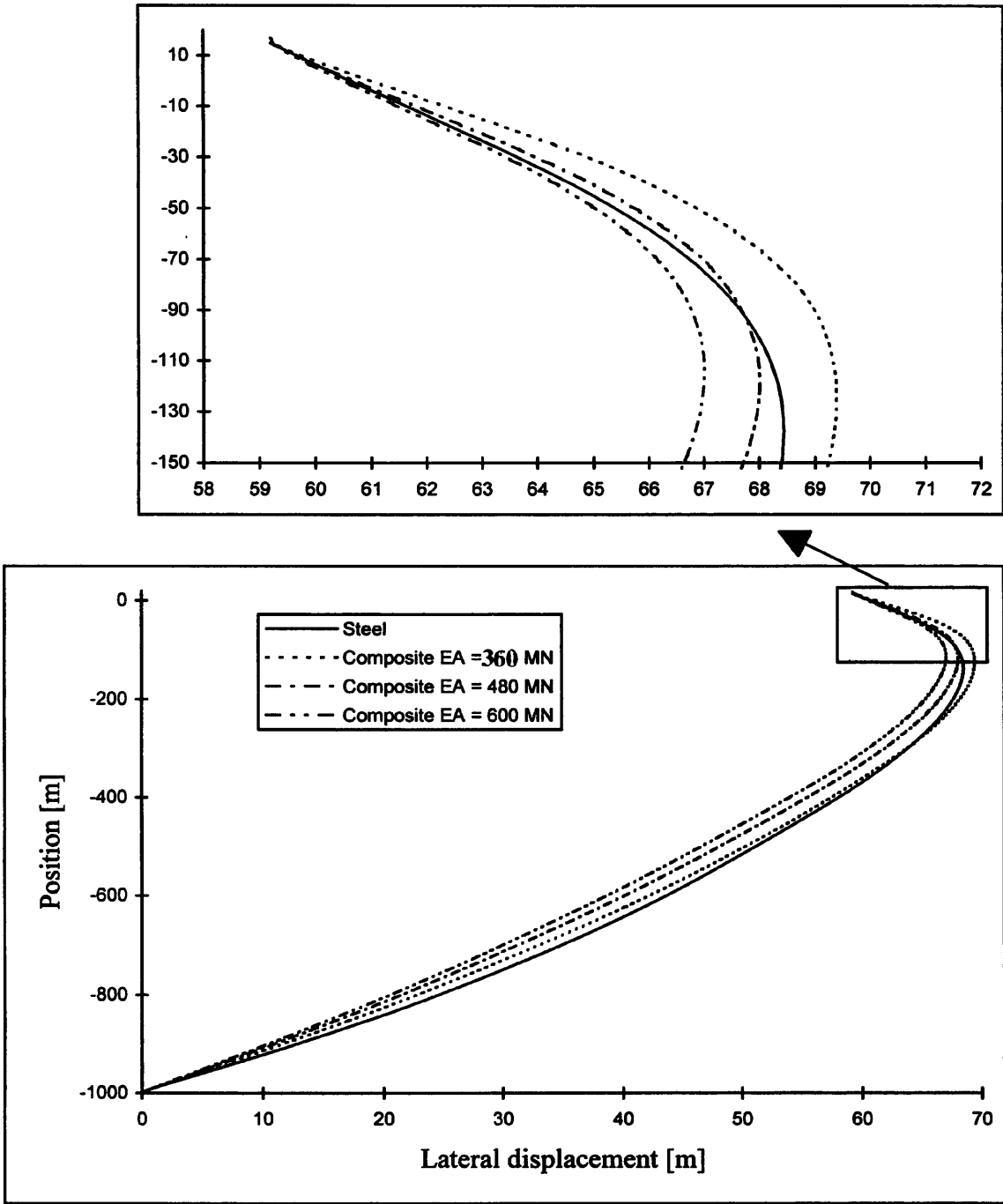
Figure 6.14 Lateral displacements: steel and composite risers.
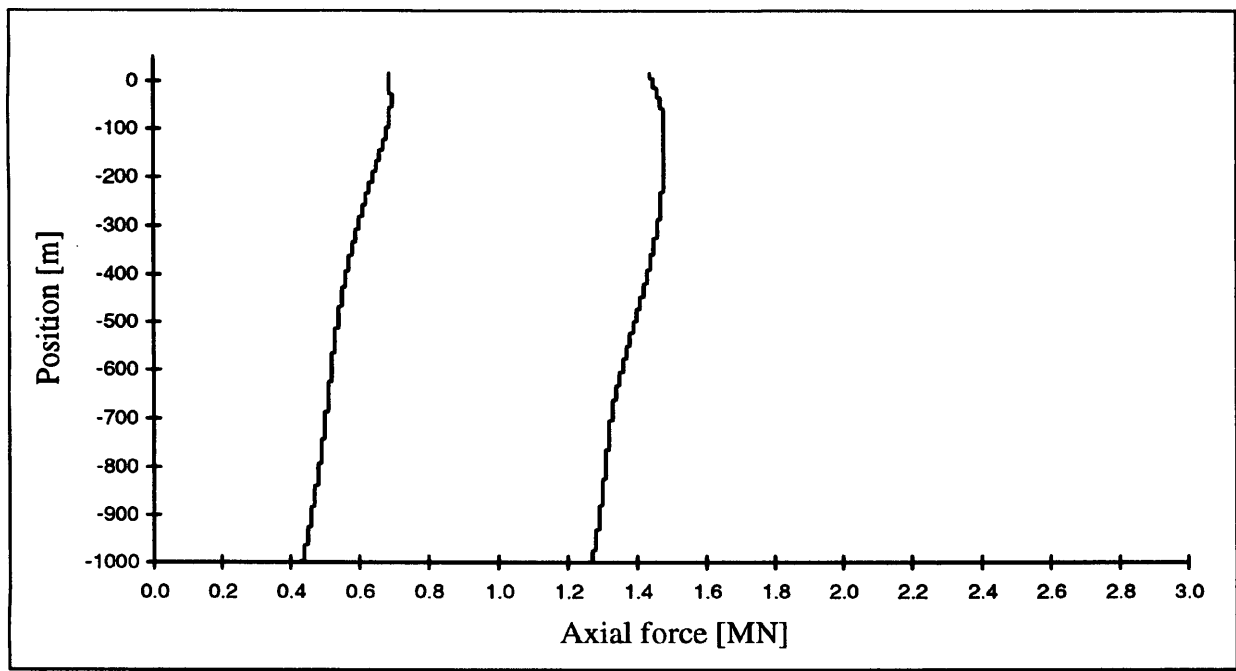
Figure 6.15 Force envelope: composite riser with two tapered joints.
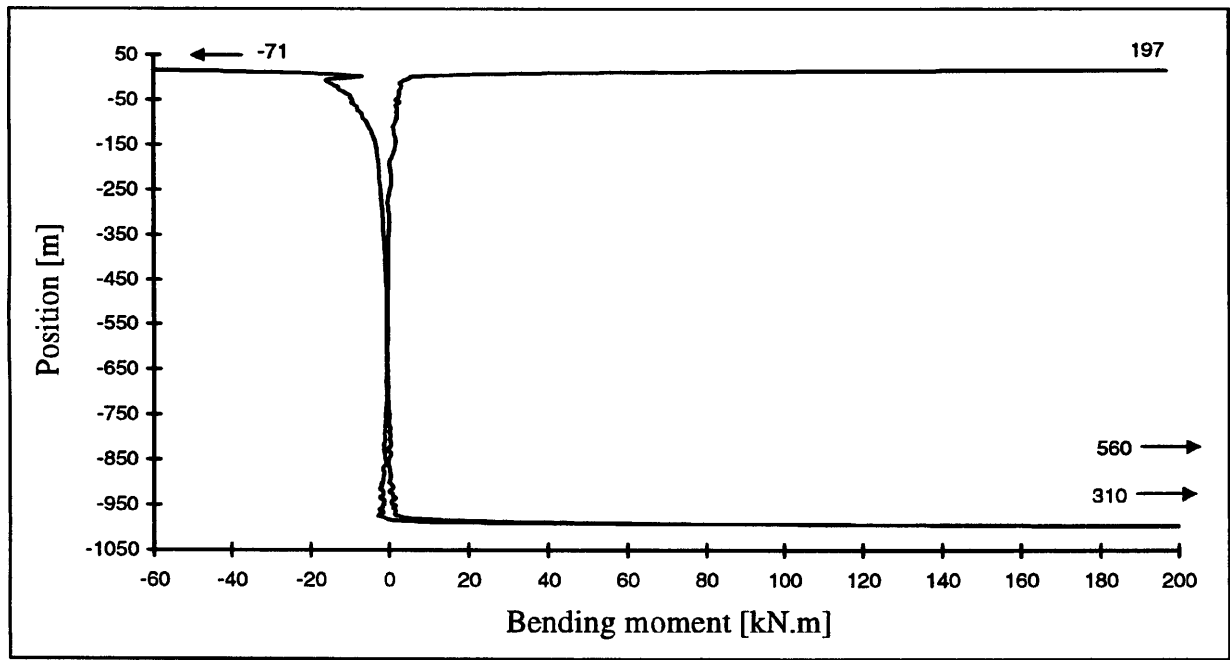
Figure 6.16 Moment envelope: composite riser with two tapered joints.
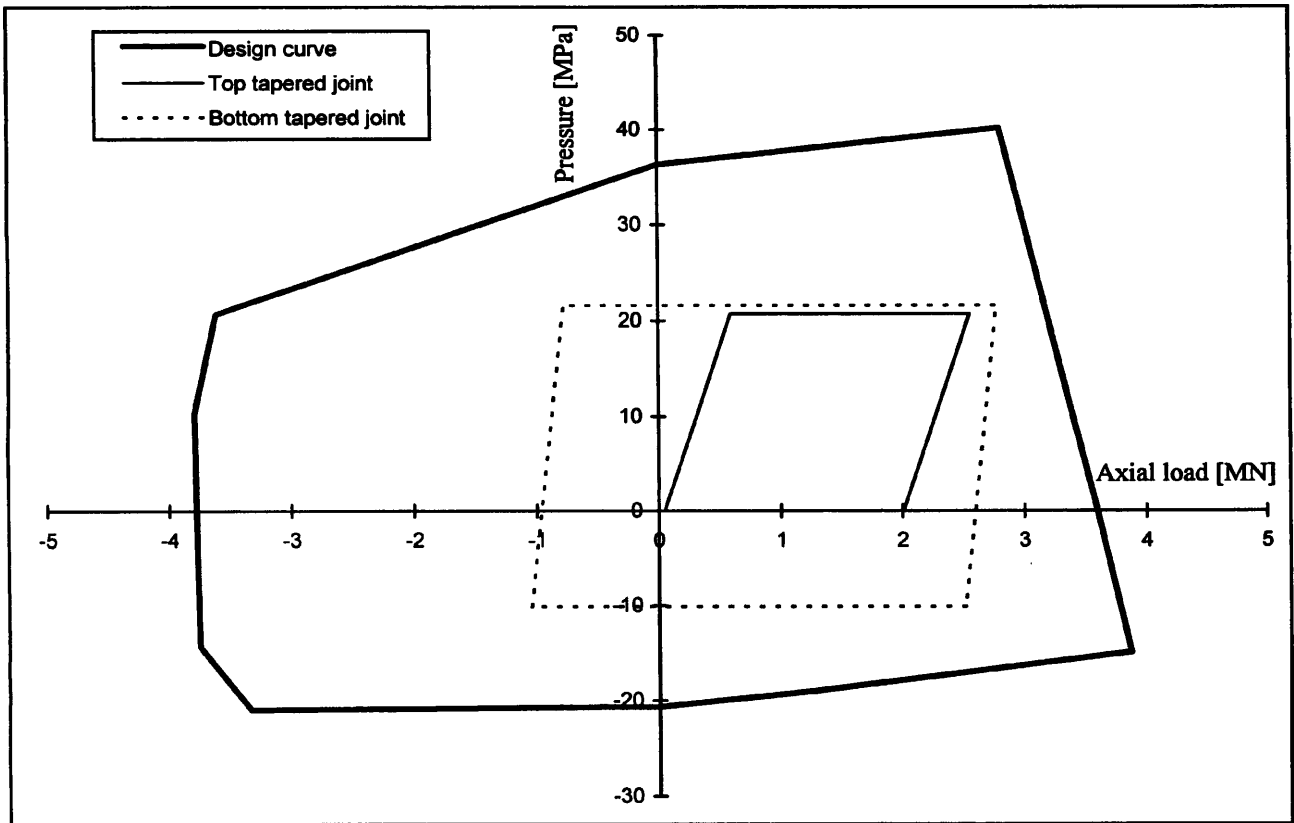
Figure 6.17 Design curve and load *loci* for the composite tapered joints, thin end.
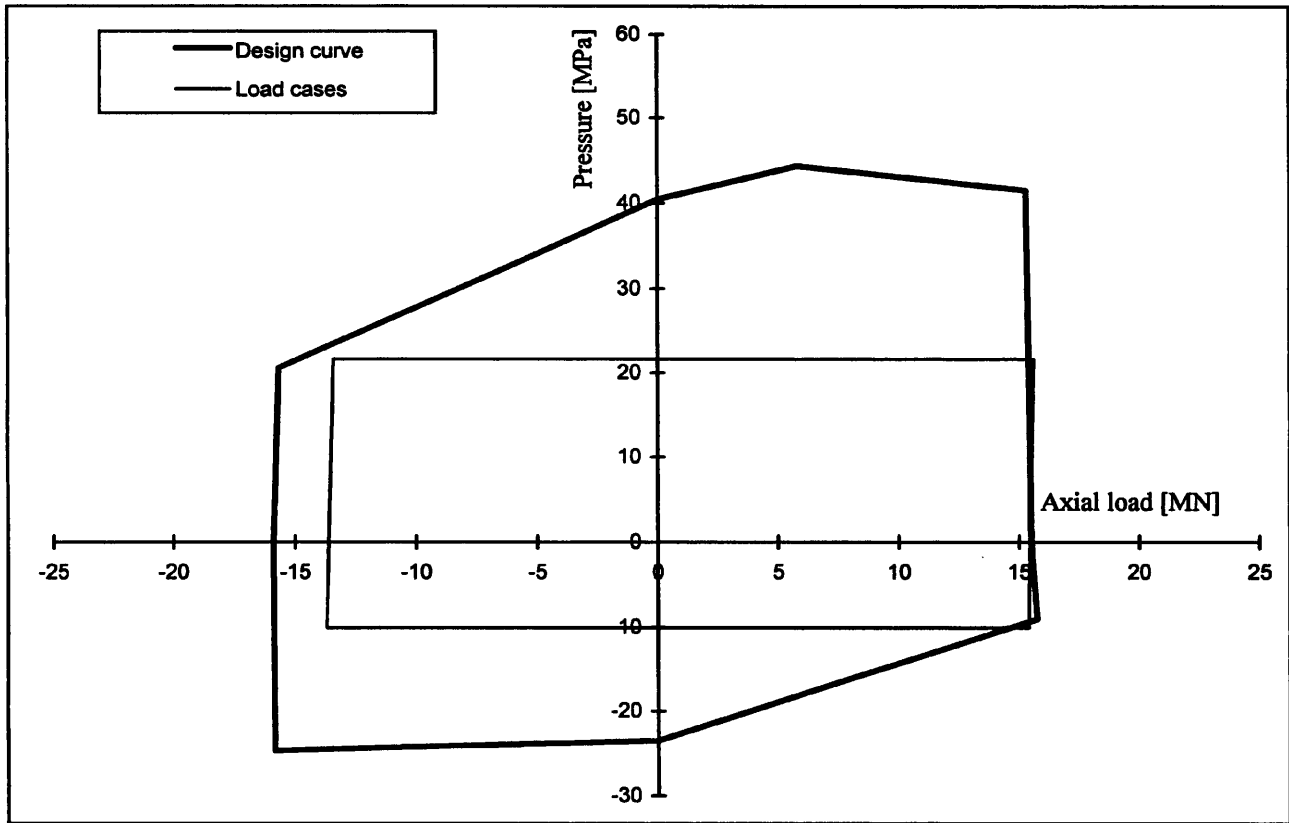
Figure 6.18 Design curve and load *loci* for the bottom composite tapered joint, thick end.
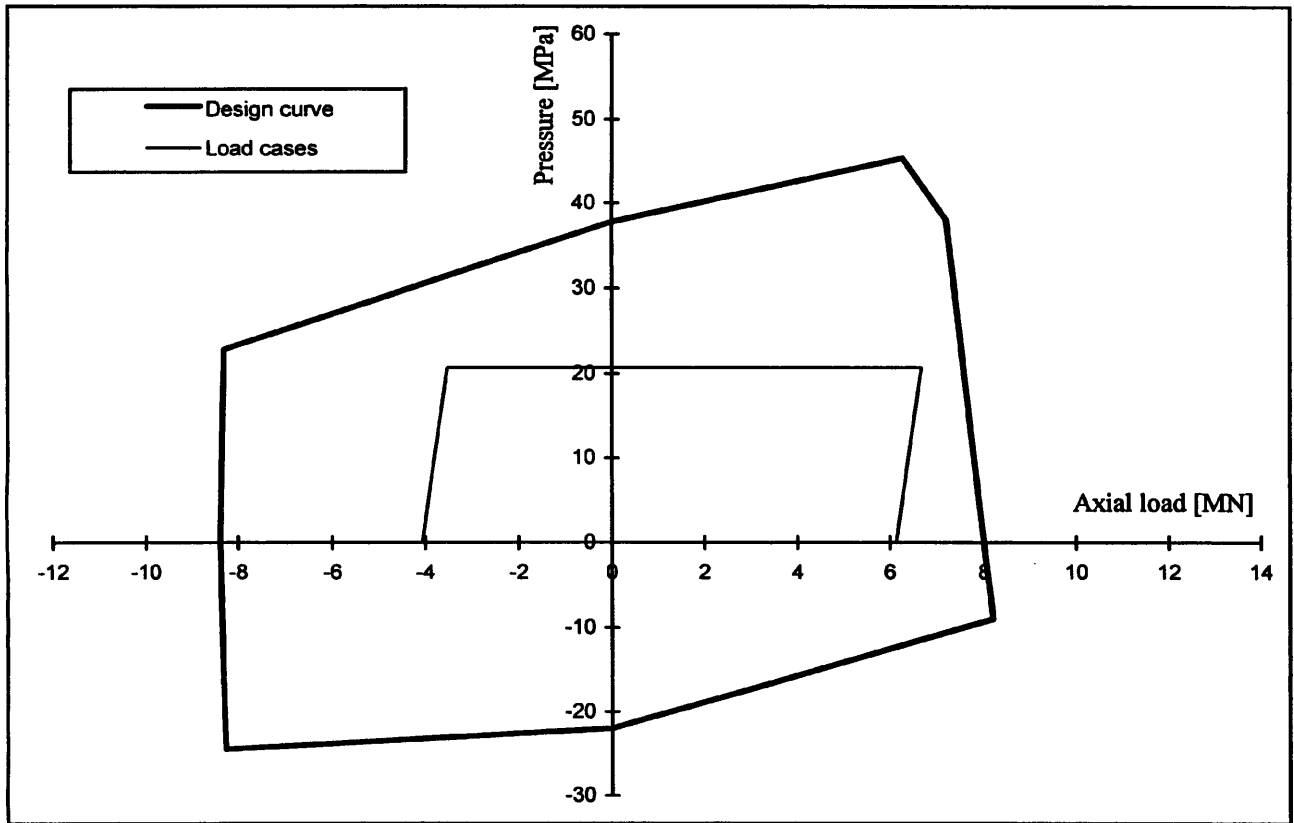
Figure 6.19 Design curve and load *loci* for the top composite tapered joint, thick end.
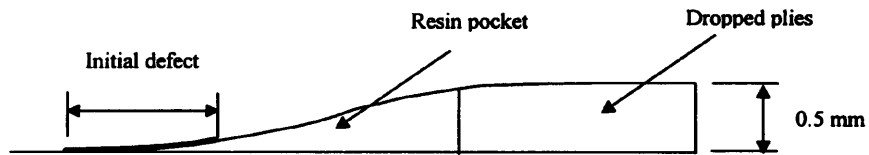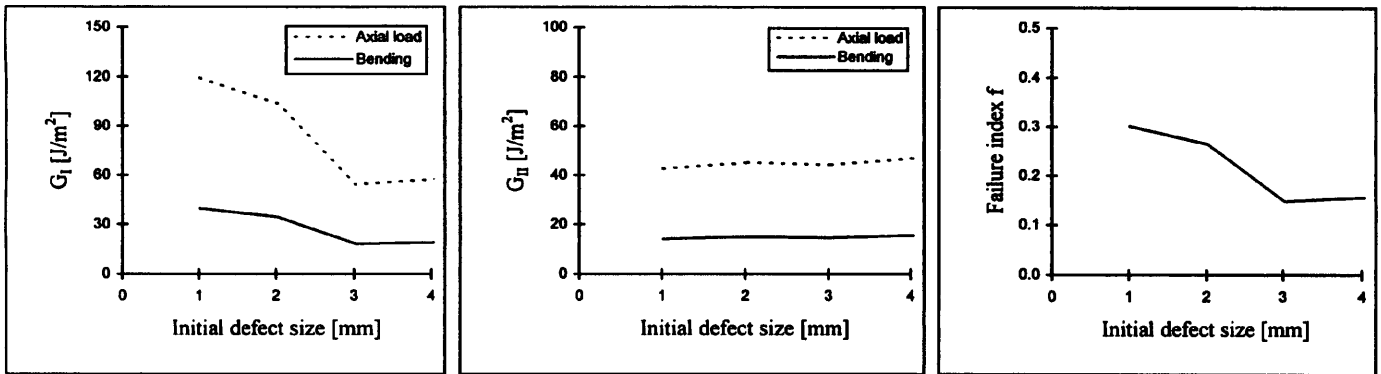
Figure 6.20 Strain energy release rates and failure indices for the thin end of the bottom tapered joint.
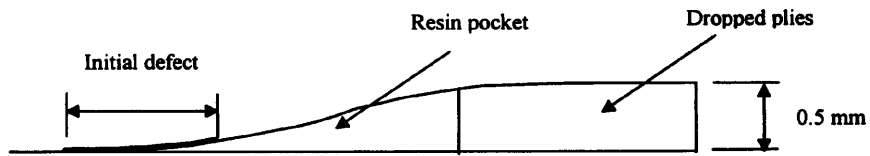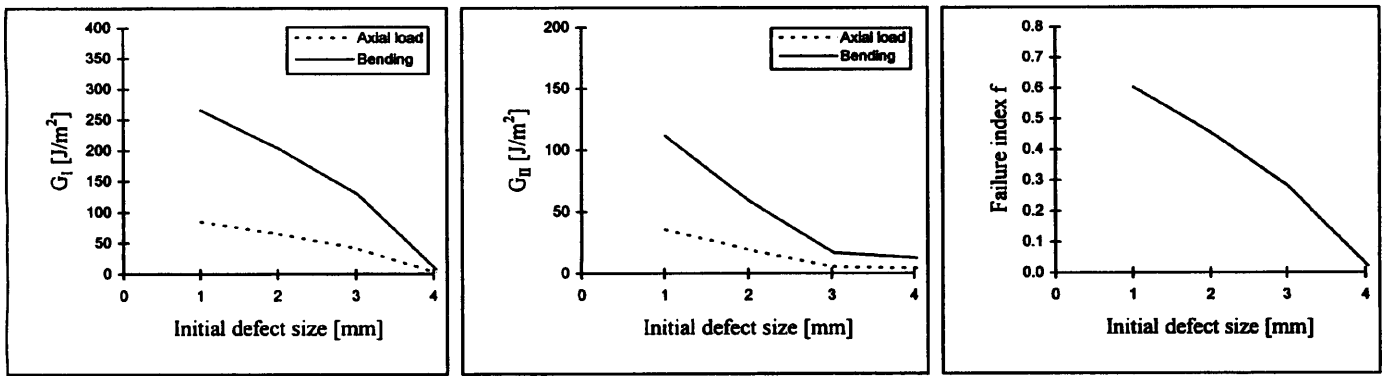
Figure 6.21 Strain energy release rates and failure indices for the thick end of the bottom tapered joint.

CHAPTER 7 CONCLUSIONS

CHAPTER 7 CONCLUSIONS

7.1 EXPERIMENTAL WORK

7.1.1 FRACTURE TOUGHNESS MEASUREMENTS

The preparation of the SERR specimens by hand lay up and the subsequent cure in a controlled temperature press presented little difficulty. The instructions of the carbon/epoxy pre-preg suppliers in terms of curing pressures, temperatures and dwelling times were closely followed. Both test methodologies adopted, i.e., DCB for mode I and ENF for mode II, proved to be simple to apply. The edge Teflon inserts used for the tests of the angle-ply laminates performed well. The cracks remained at the central plane of the specimens.

The toughness values measured were high when compared with published data. The manufacturer of the carbon/epoxy pre-pregs was consulted and confirmed the special formulation of the product to achieve a high toughness performance. This proved to be very important for the behaviour of the dropped ply composite tubes as early delaminations were prevented. Previous research on tapered laminates published in the literature showed that delaminations were a common occurrence for this kind of composite structure.

No trend was observed concerning fibre orientation. Mode I toughness was higher for the unidirectional laminates and smaller for the angle-ply specimens. The scatter in the results was greater for the latter. Both $0°$ and $+/-20°$ carbon fibre SERR values were used in the design analysis of the tapered tubes that followed.

7.1.2 ALL-CARBON, STEPPED TUBE TESTS

Four point bending tests

These were the first specimens to be made and tested. The main objective at that stage was to make sure that the tubes fail at the right spot, the thickness transition region. This proved to be difficult with the all-carbon construction. The part of the tube at the edge of the glass sleeve

presented a stress concentration effect similar to the one caused by the thickness drop. Only two out of five tubes broke at the thickness transition region.

Nevertheless, all of the failures were on the compressed side. This was to be expected, given the lower longitudinal compressive strength of the material when compared with the longitudinal tensile strength. The use of the glass reinforced sleeves to distribute better the bending stresses proved effective in those cases where the failure occurred at the thickness transition region. The steel sleeves utilised to resist the concentrated forces applied by the testing machines performed as expected. There were localised indentations, but the overall dimensions of the steel sleeves remained constant.

One problem in testing opaque materials such as carbon/epoxy laminates is how to know when delaminations are present. There are reports in the literature of changes of behaviour captured by strain gauges, at the onset of delamination. This methodology was tried in the present research. Strain gauges were installed at the thickness transition regions. During the four point bending tests of the all-carbon specimens there was no abrupt changes of slope in the load *versus* strain curves. This indicated the absence of delaminations. After the tests, micrographs taken from two tubes showed no sign of delamination, confirming the indication from the strain gauges.

The micrographs also shown the great concentration of voids in the thickness transition regions due to the poor consolidation there during the cure process. This aspect improved with time as the manufacturer of the tubes perfected the process. The strain measurements made during the all-carbon tubes tests were used later to confirm the E_l modulus of the material and to verify the FEA models proposed.

Fatigue tests

The two screening fatigue tests confirmed the good fatigue behaviour of carbon/epoxy laminates reported in the literature. The fatigue tests were performed in four point bending, in very severe conditions. The tubes were cycled at a stress ratio of 0.1, with a maximum stress of about two thirds the average failure moment. Both tests lasted 500,000 cycles. After the conclusion of the tests, micrographs of samples taken from the thickness transition regions of

the tubes did not show any sign of delamination.

There were some attempts to monitor the fatigue tests by means of strain gauges placed at the thickness transition region. During the tests, some indications of change in behaviour of the tubes were detected by the strain gauges. If there was any fatigue damage, it was not due to delamination at the ply drop-offs.

7.1.3 HYBRID, STEPPED, ANGLE-PLY TUBE TESTS

Four point bending tests

The existence of the hoop glass/epoxy layers in these tubes alleviated the problem of stress concentration at the edge of the glass sleeves. Five out of six failures were at the thickness transition region. All failures were on the compressed side. There was large variation in the values of moment at failure, with a c.v. of 20%. This was due to the variability of the thickness transition region characteristics. There was a large concentration of voids there and the geometry of the ply drop detail changed from one tube to another.

Internal pressure tests

Three tests were performed with a much smaller dispersion in the results at failure compared with the pure bending tests. The graphs of pressure *versus* circumferential strains indicated early damage at pressures of about 80% of the final pressures achieved. The latex membranes used as liners for these tests proved effective in sealing the tubes at the aluminium plugs.

During the test of tube HST04 the latex membrane tore apart, after the initial damage started to show up. The test had to be repeated. This was informative in the sense that the second test clearly indicated the reduction in the hoop stiffness of the tubes due to the damage already present when the membrane burst.

Combined tests

The idea of using a "U" frame to hold the aluminium sealing plugs in position during pressurisation worked well. This allowed the combined tests to be done with a minimum of

extra equipment. There were no additional end fittings needed for the composite tubes and the bending moments were applied by the INSTRON machine.

Safety reasons dictated the need to perform the tests under displacement control. This introduced a little complication in the analysis of the results, because the internal pressure of the tubes played a role in the bending moment applied to the tubes. Nevertheless, the identification of all the forces present permitted the correct interpretation of the results.

The bending moments were applied first, then the tubes were pressurised until burst failure. Two sets of three tests each were executed. In the first one the bending moments corresponded to 66% of the average moment at failure observed during the pure bending tests. The second set of tests were performed at bending moments of 33% of the average moment at failure in pure bending.

There were indications of early damage in all tests, similarly to what happened during the pure internal pressure tests. A general trend was observed that the higher moment corresponded to the lower pressure at failure. The variation in the final pressure results was greater than it was for the pure internal pressure tests. It was smaller, though, than the variation observed in the bending moments at failure during the pure bending tests.

7.1.4 HYBRID, STEPPED, UNIDIRECTIONAL TUBE TESTS

Internal pressure tests

Three tubes were tested under pure (1:0) internal pressure load. Polyethylene replaced latex as the liner material. Because of its lower flexibility, the polyethylene bags made the sealing at the aluminium plugs more difficult. We had to rely on the volumetric capacity of the oil pump to overcome the leakage at the plugs. Even so, the three tests had to be repeated, as the leakages became too volumous at higher pressures. In the end, all of the tubes failed by bursting.

The same early damage detected during the pressure tests of the angle-ply tubes was observed for the unidirectional ones. The average pressure at failure of the hybrid, stepped,

unidirectional carbon tubes was roughly 75% of the average pressure at failure of the hybrid, stepped, angle-ply carbon tubes, for the pure internal pressure condition. The carbon fibre angles were different but the reduction in the pressures at failure appeared to be excessive. The scatter in the three results was also greater than it was for that previous case. The reason for this reduction and scatter probably lies in the lack of quality control the manufacturing process leading to variations in the construction. Unfortunately some time limitations precluded further tests to resolve this issue.

Four point bending tests

Four out of six tubes tested in pure bending displayed failure at the thickness transition region. The scatter in the results (c.v. of 5%) was smaller than the scatter observed for the same tests performed on the hybrid, stepped, angle-ply tubes. This was a sign of improvement in the quality of manufacture of the tubes. Two tubes broke at the edge of the glass reinforcement. Nevertheless, all failures were on the compressed side.

7.1.5 HYBRID, PLAIN, ANGLE-PLY TUBE TESTS

Three tubes were tested in pure bending to address the effect that the transition region had on the strength of the specimens. The carbon sub-laminates of these tubes had the same thickness as the thin portion of the hybrid, stepped, $0°$ carbon tubes. Even though the carbon fibre angles were $+/-20°$ in this case, the resulting moments at failure were 30% on average higher than those related to the previous case. As one would expect, all the failures were on the compressed side, at the edge of the glass reinforcements.

7.1.6 HYBRID, PLAIN, UNIDIRECTIONAL TUBE TESTS

Three tubes with this construction were tested under pure internal pressure. The objective was to confirm the reduction in burst pressure observed from the HST tubes to the HSN tubes. These plain tubes were of the same batch as the HSN ones. The average pressures at failure were of the same magnitude as those for the HSN tubes, confirming the reduction. This result

also shows that the ply drop-off detail does not affect the strength of the tubes under internal pressure once the main stress carriers for this load condition are the glass sub-laminates.

7.2 FINITE ELEMENT MODELS

7.2.1 FEA PARAMETERS

The results from the 3D FEA, provided by the type of element and mesh size adopted, were compared with the results of an exact 3D solution for thick composite tubes available in the literature. Good agreement was obtained.

After the verification of the results provided by the 3D FEA, possible simplifications of the FEA models were sought. In order to apply simpler FEA models, symmetry conditions had to be identified. Symmetry conditions can be assumed if all of the constituent materials of the tubes are specially orthotropic, i.e., their principal directions coincide with the cylindrical directions of the tubes. This was already the case of the glass/epoxy, hoop sub-laminates.

Symmetry conditions were achieved for the carbon/epoxy sub-laminate through the consideration of an equivalent, smeared material. The smeared material was also specially orthotropic. Its elastic properties were obtained by means of an analogy with a simple spring model. The same analogy provided the means of obtaining the stresses referred to the lamina directions back from the smeared material. A comparison between the full 3D and the smeared material FEA models proved the effectiveness of the approach.

The final objective of the analysis was to consider axial symmetry. That allowed the simplest models to be adopted. Among the basic load conditions of the tubes, three are already axisymmetric: the axial loads, the internal and the external pressures. The bending load is not axisymmetric, but from elementary beam theory it was assumed that all the stresses and displacements were proportional to $r \sin\theta$. This assumption allows all the relevant results for the bending case to be obtained from an axisymmetric analysis.

Two FEA models, using the smeared material were run. The first one was a full 3D model of the whole circumference of the tube. The loading condition was a bending moment,

represented by the rotation of one extreme section. The second FEA analysis was an axisymmetric one. Its results were processed based on the proportionality with $r \sin\theta$. The comparison between the two models validated the methodology.

7.2.2 ALL-CARBON TUBES

After the definition of the FEA parameters, the method was applied to evaluate the stresses developed in the tubes tested during the experimental work. The first analysis dealt with the all-carbon specimens. The micrographs taken in Chapter 3 showed two basic geometric configurations of the ply drop-off region: the stepped and the overlapped arrangements. FEA models of both configurations were established.

Four point bending

The models revealed three locations of stress concentration during the bending of the tubes. The first spot was at the outer surface of the tubes, close to the thinner portion where the in-plane stresses were the most affected. The second location was the at tip of the resin pocket where the continuous plies joined again. The third stress concentration regions were the points where the dropped plies touched the continuous ones. This last spots varied in shape, depending on the geometric characteristics of ply drop-off detail. Furthermore, the stresses there were over-estimated by the FEA models, which considered the contact region to be a line, not a surface.

The analysis concentrated on the first two regions, because the stresses there dictated the nature of failure of the tubes. All the failures under pure bending were on the compressed sides. The failures could be either by axial compressive collapse of the outer fibres (where the in-plane stresses were the greatest) or by delamination at the resin pockets (where the out-of-plane stresses prevailed).

Longitudinal collapse of the carbon fibres proved to be the cause of the observed failures. The FEA indicated a minimum longitudinal compressive stress of -1019 MPa at the outer fibres (80% of the strength C_l), for the average moment recorded experimentally at failure. The

absence of delaminations from the micrographs and the results of the FEA models, that showed low SERRs under bending conditions, confirmed this conclusion. The absence of abrupt changes in the curves of strain *versus* load during the four point bending tests also pointed to the fact that delaminations were not present.

7.2.3 HYBRID, STEPPED, ANGLE-PLY TUBES

Four point bending

The FEA results associated to the average moment at failure indicated a minimum compressive stress of -1227 MPa, very close to the corresponding strength of 1280 MPa. There was also an indicated first ply failure by transverse compression of the glass/epoxy sub-laminate. That was confined to the stress concentration spot, at the transition region, close to the thinner portion of the tubes.

The SERR analysis for the pure bending condition resulted in failure indices smaller than one for the average bending moment at failure. It indicated, though, that delamination could be the prevailing failure mode if the load was a compressive axial force.

Internal pressure

The stress results from the FEA indicated that the ply drop-off region does not affect the strength of the tubes under internal pressure loading. The governing stress is the σ_1 stress at the inner glass/epoxy lamina. The σ_1 stress at failure, obtained from the FEA models, indicated a T_1 strength figure lower than that provided by the glass/epoxy woven roving supplier. Even though a correction was applied for the observed E_1 modulus of the material, the stress at failure was still low.

Combined load

A failure envelope was drawn, considering a reduced T_1 strength for the glass/epoxy woven roving. The maximum stress failure criterion was adopted for that purpose. It fitted well the experimental data, showing the reduction in the pressures at failure for increasing bending

moments. The FEA showed that the outer carbon layer failure by longitudinal compression was not affected by the internal pressure. The σ_1 value there was zero, for the pure internal pressure load. This fact is reproduced in the failure envelope by a vertical line passing through the average moment at failure.

7.2.4 HYBRID, STEPPED, UNIDIRECTIONAL TUBES

Four point bending

The FEA indicated a first ply failure by transverse compression at the outer glass/epoxy layer. The minimum compressive σ_1 stress calculated at the outer carbon layer for the average moment at failure was -1172 MPa (92% of the strength C_1). The SERR analysis resulted in failure indices smaller than one, for the side under compression. So, all the indications were that the prevailing failure mode was again by longitudinal compressive collapse of the outer carbon fibres.

Internal pressure

The σ_1 stress at the inner glass layer for the average pressure at failure was even lower than it was for the angle-ply tubes. The unidirectional tubes were made from a different batch of woven roving glass/epoxy pre-pregs. The difference in the stresses at failure pointed to large variations in the properties from one batch to the other. The strength of the pre-pregs, as provided by the supplier, appears to be over-estimated.

7.2.5 HYBRID, PLAIN TUBES

Four point bending

The FEA of the hybrid, plain, angle-ply tubes tested in bending showed a minimum σ_1 stress of -1288 MPa (101% of C_1). The model displayed the stresses at an undisturbed part of the tubes, away from the glass reinforcements. In reality, all tubes broke at the edge of the glass sleeve, as they should. Even so, the FEA results were consistent with the outcome of previous

bending tests and with the tabulated strength of the carbon/epoxy pre-pregs.

Internal pressure

The geometry of the hybrid, plain, unidirectional tubes was the same as the geometry of the thinner portion of the hybrid, stepped, unidirectional tubes. The resulting average pressures at failure of both tubes were practically the same, as were the maximum σ_1 stress at the inner glass layer calculated by the FEA. This confirmed the low actual T_1 strength of the glass/epoxy pre-pregs.

7.3 THICK COMPOSITE TUBE MODELS

The first axisymmetric model considered a generalised plane strain state in which ε_z was assumed to be constant. Only normal stresses were obtained, with reference to the cylindrical coordinates. The model was implemented by the programme TUBEPLAIN. It is suitable for thick laminated tubes without any thickness variations. The basic loads were internal and external pressures, axial loads and bending moments. The results for the bending load case were obtained by some manipulation of the axial load case results, as explained in Chapter 4.

Results from program TUBEPLAIN were compared with the results provided by the FEA for the thin part of tubes HST. The agreement was very good. Programme TUBEPLAIN can also be used for the analysis of the tapered composite tubes under internal and external pressure loads. This is because both the experimental tests and the FEA results have shown that the ply drop-off detail does not influence the failure of the tubes under these loads.

The second axisymmetric model was more general than the first. It allowed variations in ε_z and computed the shear stress τ_{rz}. Programme TUBEDROP permitted the application of the model. A finite difference scheme was applied to represent the derivatives of some of the unknowns present in the system of governing equations. This proved to be the major drawback of the model. The system of equations resulted in huge storage problems, demanding high core allocation and processing time. The system matrix was banded, and the

solver used was suitable for that. Even so, the problem to solve remained considerable.

Programme TUBEDROP was applied to the bending load case of the all-carbon tubes. Several optimisation analyses were run, in the search of the optimum parameters. The final results were similar to those obtained from the FEA of the same tubes. The agreement was not complete though convergence to the FEA values was indicated. Smaller step sizes in the finite difference scheme will render the program very difficult to use. Nevertheless, TUBEDROP is able to calculate SCF values in σ_z very similar to those obtained from the FEA results.

7.4 RISER ANALYSIS

7.4.1 COMPARISON: STEEL *VERSUS* COMPOSITE RISERS

The design of a steel riser demonstrated the influence of the tensioners on the resulting section forces and bending moments along the riser. The need for a tapered joint at the bottom to render acceptable maximum stresses was also demonstrated. The analysis was restricted to the extreme, centenary condition, sufficient for comparison purposes.

The composite riser was considered to be made of the same carbon/epoxy material used for the manufacturing of the specimens tested. This was because of the good properties of the laminate, especially its high fracture toughness. The high fracture toughness proved to be very important in preventing early delaminations. The inclination of the carbon fibres to the axis were maintained at the +/- 20° values. This would allow the high productivity filament winding process to be employed in the making of the carbon sub-laminates, without any additional special manufacturing procedures.

The properties of the glass/epoxy sub-laminates of the composite riser were obtained from the published data related to filament wound glass/epoxy laminates. The assembly of the hoop layers of the riser poses no difficulties for the manufacturing process. The biased woven roving glass/epoxy pre-pregs used in the making of the specimens did not perform up to their stated strength and were mot considered further for the design. Filament wound constructions were preferred.

A design methodology was proposed for the composite riser, expressed in terms of a design curve obtained from the consideration of the maximum stress failure criterion. An incremental approach was used. The design limits implied a safety factor of 3 (in relation to final failure) or the occurrence of first ply failure, whichever resulted in the smaller allowable loads.

The composite riser is not supported by tensioners at its connection with the platform. The riser is installed with a pre-tension of 1.5 times its apparent weight to make sure that the axial forces are always tractive along its length. The design addressed the load cases that can modify the riser pre-tension, namely: astronomical tides, internal pressure and heating.

The composite riser showed lateral displacements smaller than the steel riser at all depths. This should lead to a reduction in the distance between the Christmas trees, leading to a smaller production deck. The wet weight of the composite riser, including metallic end fittings was 43% of the weight of its steel counterpart.

7.4.2 COMPOSITE TAPERED JOINTS

It is proposed that the top of the riser be connected to the production deck by means of a flexelement. The rotational stiffness of the flexelement led to a reduction in the maximum thickness of the top tapered joint. The bottom tapered joint was fixed to provide a smooth transition for the internal tubings from the well to the riser.

The design of the tapered joints is interactive, because their dimensions influence both the design surface and the section forces. Several analyses are needed for a proposed geometry. All combinations of pressures and section forces have to be considered. Programme TUBEDROP is not suitable for this kind of application, given its time requirements for a single solution. The program was however used to define the SCFs in the axial stresses. The axial loads were multiplied by the SCFs, and the design surfaces were obtained by means of TUBEPLAIN. The SCFs were small due to the considerable thickness of the tapered joints.

The thickness reduction was obtained in steps of 0.5 mm, by dropping two pairs of +/- 20° carbon laminae at a time. This is intended to make easier the assembly of the tapered joints by reducing the number of ply drop-offs. Evidently, the minimum step is obtained by terminating

only one lamina. In a real design situation, a good criterion would be to match the SCF occasioned by the ply drop-offs with the SCF introduced by the steel end fittings.

The main conclusion from the research done is that composite production risers are technically feasible. This concerns the whole system, including the stress joints. The main advantage is the effective weight of a composite production riser is less than half the effective weight of its steel counterpart. This leads to a significant reduction on the weight hanging from the platform deck.

The platform itsef can therefore be made smaller, due to the smaller buoyance required. Further reductions in cost and in deck size come from the fact that a composite riser can avoid the use of tensioners. Other fundamental and important advantages of composite risers are their corrosion resistance and their good fatigue performance.

7.5 RECOMMENDATIONS FOR FUTURE WORK

The following are suggested as possible areas for further work to amplify the findings of this thesis:

1) The experimental tests of tapered composite tubes can be extended to external pressures and pure axial loads, to cover the spectrum of operational load cases. More complex experimental apparatus and the design of end fittings are needed for that purpose.

2) Tapered composite tubes made from laminates with brittle epoxy matrix can be used to provide cases where the tube does delaminate before other failure modes are reached. This will provide a verification for the delamination onset criterion.

3) The fatigue behaviour of tapered composite tubes needs to be further investigated, to confirm the favourable behaviour indicated by the screening fatigue tests performed during this research. An experimental technique for the detection of delaminations as the tests are performed needs to be developed. The use of strain gauges has the advantage of simplicity, but data reduction schemes are needed to identify what is really a delamination, from other

264

possible sources of perturbation in the indicated strains.

4) Programme TUBEDROP needs further development to achieve better accuracy and to reduce the computational effort needed for the analysis. More efficient numerical algorithms for the representation of the differential equations can be implemented. Optimised routines for the solution of the system of equations constitute another way forward. They can lead to shorter processing times and smaller core requirements

REFERENCES

1. B.R. TRETHEWEY JR., Mechanics and performance of composite laminates with discontinuous internal plies. *PhD dissertation*, University of Delaware, Newark, USA, 1989.

2. R.B. PIPES AND N. J. PAGANO, Interlaminar stresses in composite laminates under uniform axial extension. *Journal of Composite Materials* 4, 538-548, 1970.

3. W. CUI, M.R. WISNOM and M. JONES, New model to predict static strength of tapered laminates. *Composites* 26.2, 141-146, 1995.

4. K.C. KAIROUZ and R.J. HEATH, Fracture of ply drop-offs in composite structures. *Proceedings of the Seventh European Conference on Composite Materials*, ECCM-7, 2, 79-85, London, United Kingdom, 1996.

5. O.O. OCHOA and W.S. CHAN, Tapered laminates: a study on delamination characterization. *Proceedings of the American Society for Composites Third Technical Conference*, 633-641, Seattle, USA, 1988.

6. C. POON, C. RUIZ and R.P. GREAVES, Analysis of tapered laminated composite, *Rolls-Royce Report PNR92090*, Derby, England, 1995.

7. W. CUI, M.R. WISNOM and M. JONES, Effect of step spacing on delamination of tapered composites. *Composites Science and Technology* 52, 39-46,1994.

8. J.W. GILLESPIE, JR., Damage tolerance of composite structures: the role of interlaminar Fracture Mechanics. *Journal of Offshore Mechanics and Arctic Engineering* 113, 247-252, 1991.

9. A.A. GRIFFITH, The phenomena of rupture and flow in solids. *Philosophical Transactions of the Royal Society* 221A, 163-198, 1920.

10. R. F. GIBSON, *Principles of Composite Materials Mechanics*. McGraw-Hill International Editions, Engineering Mechanics Series, New York, USA, 1994.

11. W.M. WESTERGAARD, Bearing pressures on cracks. *Journal of Applied Mechanics* 61, A49-A53, 1939.

12. E.F. RYBICKI, D.W. SCHMUESER and J.FOX, An energy release rate approach for stable crack growth in the free edge delamination problem. *Journal of Composite Materials* 11, 470-485, 1977.

13. D. BROEK, *Elementary Engineering Fracture Mechanics*. Sijthoff & Noordoff, Alphen aan den Rijn, The Netherlands, 1978.

14. S.J. SONG and A.M. WAAS, Energy-based mechanical model for mixed mode failure of

laminated composites. *AIAA Journal* **33.4**, 739-745, 1995.

15. S.A. SALPEKAR, I.S. RAJU and T.K. O'BRIEN, Strain energy release rate analysis of delamination in a tapered laminate subjected to tension load. *Proceedings of the American Society for Composites Third Technical Conference*, 642-654, Seattle, USA, 1988.

16. S.N. CHATTERJEE, W.A. DICK and R.B. PIPES, Mixed-mode delamination fracture in laminated composites. *Composites Science and Technology* **25**, 49-67, 1986.

17. D.J. WILKINS, A preliminary damage tolerance methodology for composite structures. *Failure Analysis and Mechanisms of Failure of Fibrous Composite Structures, NASA Publication 2278*, Hampton, USA, 1982.

18. P.E.KEARY, L.B. ILCEWICZ, C. SHAAR and J. TROSTLE, Mode I interlaminar fracture toughness of composites using slender double cantileverd beam specimens. *Journal of Composite Materials* **19**, 154-177, 1985.

19. J. IVENS, A.W. VAN VUURE, I. VERPOEST and M. FANTINO, The interlaminar fracture toughness as a means to evaluate the fibre-matrix adhesion in fibre reinforced composites. *Proceedings of the Seventh European Conference on Composite Materials*, ECCM-7, **1**, 99-104, London, United Kingdom, 1996.

20. S. HASHEMI, A.J. KINLOCH and J.G. WILLIAMS, The analysis of interlaminar fracture in uniaxial fibre-polymer composites. *Proceedings of the Royal Society of London A* **427**, 173-199 (1990).

21. S.L. BAZHENOV, Interlaminar and intralaminar fracture modes in 0/90 cross-ply glass/epoxy laminate. *Composites* **26**, 125-133, 1995.

22. P. ROBINSON and D.Q. SONG, A modified DCB specimen for mode I testing of multidirectional laminates. *Journal of Composite Materials* **26(11)**, 1554-1577, 1992.

23. A.J. BRUNNER, P. FLUELER, P. DAVIES, B.R.K. BLACKMAN and J.G. WILLIAMS, Determination of the delamination resistance of fibre-reinforced composites: current scope of test protocols and future potential. *Proceedings of the Seventh European Conference on Composite Materials*, ECCM-7, **2**, 3-8, London, United Kingdom, 1996.

24. AMERICAN SOCIETY FOR TESTING AND MATERIALS, *Standard test Method for Mode I Interlaminar Fracture Toughness of Unidirectional Fibre-reinforced Polymer Matrix Composites*. ASTM D5528, Washington, USA, 1994.

25. EUROPEAN STRUCTURAL INTEGRITY SOCIETY, *Determination of the Mode I Delamination Resistance of Unidirectional Fibre-reinforced Polymer Laminates using The Double Cantilever Beam Specimen (DCB)*. ESIS Technical Committee 4, 1995.

26. P. DAVIES, F. DUCEPT, A.J. BRUNNER, B.R.K. BLACKMAN and A.B. DE MORAIS, Development of a standard mode II shear fracture test. *Proceedings of the Seventh European Conference on Composite Materials*, ECCM-7, **2**, 9-15, London, United

Kingdom, 1996.

27. H. MAKUMA, J.W. GILLESPIE JR. and J.M. WHITNEY, Analysis and experimental characterization of the center notch flexural test specimen for mode II interlaminar fracture. *Journal of Composite Materials* **23**, 756-785, 1989.

28. L.A. CARLSSON and R.B. PIPES, Experimental Characterization of Advanced Composite Materials. Technomic Publishing Co., Inc., Lancaster, USA, 1997.

29. A.J. RUSSEL and K.N. STREET, Moisture and temperature effects on the mixed-mode delamination fracture of unidirectional graphite/epoxy. *Delaminaion and Debonding of Materials, ASTM STP 876*, 349, 1985.

30. Y.B. SHI, D. HULL and J.N. PRICE, Mode II fracture of +θ/-θ angled laminate interfaces. *Composites Science and Technology* **47**, 173-184, 1993.

31. S. FORSTER, P. ROBINSON and J.M. HODGKINSON, An investigation of interlaminar fracture toughness at $0°/θ°$ interfaces in carbon-epoxy laminates. *Proceedings of the 4th International Conference on Deformation and Fracture of Composites*, 231-241, Manchester, England, 1997.

32. H.J. SUE, R.E. JONES and E.I. GARCIA-MEITIN, Fracture behaviour of model toughned composites under mode I and mode II delaminations. *Journal of Materials Science* **28**, 6381-6391, 1993.

33. T. MOHLIN, A.F. BLOM, L.A. CARLSSON and A.I. GUSTAVSSON, Delamination Growth in a Notched Graphite/Epoxy Laminate Under Compression Fatigue Loading. *Delamination and Debonding of Materials, ASTM STP 876*, 168-188, American Society for Testing and Materials, Philadelphia, USA, 1985.

34. E.F. RYBICKI and M.F. KANNINEN, A finite element calculation of stress intensity factors by a modified crack closure integral. *Engineering Fracture Mechanics* **9**, 931-938, 1977.

35. G.B. MURRI, T.K. O'BRIEN and S.A. SALPEKAR, Tension Fatigue of Glass/epoxy and Graphite/Epoxy Tapered Laminates. *Journal of the American Helicopter Society* **38.1**, 29-37, 1993.

36. M. HOJO, S. OCHIAI, C.G. GUSTAFSON and K. TANAKA, Effect of matrix resin on delamination fatigue crack growth in CFRP laminates. *Engineering Fracture Mechanics* **49.1**, 35-47, 1994.

37. C. DAHLEN and G.S. SPRINGER, Delamination Growth in Composites under Cyclic Loads. *Journal of Composite Materials* **28.8**, 732-781, 1994.

38. M.R. WISNOM, M.I. JONES and W. CUI, Failure of Tapered Composites Under Static and Fatigue Tension Loading. *AIAA Journal* **33.5**, 911-918, 1995.

39. M.R. WISNOM, R. DIXON and G. HILL, Delamination in asymmetrically tapered

composites loaded in tension. *Composite Structures* **35**, 309-322, 1996.

40. Z. PETROSSIAN, M.R. WISNOM and M. JONES, Prediction of Delamination Growth at Discontinuous Plies due to Cyclic Loading. *Proceedings of the 4th International Conference on Deformation and Fracture of Composites*, 253-261, Manchester, England, 1997.

41. M.J. HINTON, P.D. SODEN and A.S. KADDOUR, Strength of Composite Laminates under Biaxial Loads. *Applied Composite Materials* **3**, 151-162, 1996.

42. L.J. HART-SMITH, Predicting the strength of fibrous composites by an orthotropic generalization of the maximum-shear-stress (Tresca) criterion. *Proceedings of the Institute of Mechanical Engineers Part G: Journal of Aerospace Engineering* **208**, 9-18, 1994.

43. M.R. PIGGOTT and S.R. RAI, Why Design Criteria for Laminates Are Excessively Conservative. *Proceedings of the American Society for Composites 12th Technical Conference*, 91-98, Dearborn, USA, 1997.

44. D. HULL, *An introduction to composite materials*. Cambridge Solid State Science Series, Cambridge University Press, Cambridge, England, 1993.

45. P.D. EWINS and T.R. POTTER, Some observations on the nature of fibre reinforced plastics and the implications for structural design. *Philosofical Transactions of the Royal Society of London* A **294**, 507-517, 1980.

46. R.R. EFFENDI, J.J. BARRAU and D.G. DEGEORGES, Failure mechanism analysis under compression load of unidirectional carbon/epoxy composites using micromechanical modelling. *Composite Structures* **31**, 87-98, 1995.

47. H.M. HSIAO and I.M. DANIEL, Effect of fibre waviness on stiffness and strengh reduction of unidirectional composites under compressive loading. *Composites Science and Technology* **56**, 581-593, 1996.

48. E.J. BARBERO and J. TOMBLIN, A damage mechanics model for compression strength of composites. *International Journal of Solids and Structures* **33.29**, 4379-4393, 1996.

49. A.K. NOOR and W.S. BURTON, Assessment of computational models for multilayered composite shells. *Applied Mechanics Reviews* **43.4**, 67-96, 1990.

50. J.N. REDDY and D.H. ROBBINS, Theory and computational models for composite laminates. *Applied Mechanics Reviews* **47.6**, 147-169, 1994.

51. L.C.M. MENICONI, Stiffness and strength of tapered composite riser tubes. *First Year Report - PhD by Method A*, University of Mancheter Institute of Science and Technology, 1996.

52. N.J. PAGANO, Exact solutions for composite laminates in cylindrical bending. *Journal of Composite Materials* **3**, 398-411, 1969.

53. J.M. WHITNEY, The effect of transverse shear deformation on the bending of laminated plates. *Journal of Composite Materials* **3**, 534-547, 1969.

54. N.J. PAGANO, Exact solutions for rectangular bidirectional composites and sandwich plates. *Journal of Composite Materials* **4**, 20-34, 1970.

55. S. SRINIVAS, Analysis of laminated, composite, circular cylindrical shells with general boundary conditions. *NASA Report TR R-412*, NASA, Washington, USA, 1974.

56. N.J. PAGANO, Stress fields in composites laminates. *Solids Structures* **14**, 385-400, 1978.

57. N.J. PAGANO, Axisymmetric stress fields in involute bodies of revolution. Adavances in Aerospace Structures and Dynamics AD-06, ASME, 57-64, 1983.

58. J.N. REDDY and C.F. LIU, A higher-order shear deformation theory of laminated elastic shells. *International Journal of Engineering Science* **23-3**, 319-330, 1985.

59. J.G. REN, Exact solutions for laminated cylindrical shells in cylindrical bending. *Composites Science and Technology* **29**, 169-187, 1987.

60. A.K. ROY and S.W. TSAI, Design of thick composite cylinders. *Journal of Pressure Vessel Technology*, **110**, 255-262, 1988.

61. A.K. NOOR and J.M. PETERS, Stress, vibration, and buckling of multilayered cylinders. *Journal of Structural Engineering*, **115**, 69-88, 1989.

62. A.K. NOOR and J.M. PETERS, A posteriori estimates for shear correction factors in multi-layered composite cylinders. *Journal of Engineering Mechanics*, **115**, 1225-1244, 1989.

63. J.G. REN, Analysis of simply-supported laminated circular cylindrical shell roofs. *Composite Structures* **11**, 277-292, 1989.

64. T.K. VARADAN and K.BHASKAR, Bending of laminated orthotropic cylindrical shells - an elasticity approach. *Composite Structures* **17**, 141-156, 1991.

65. K. BHASKAR and T.K. VARADAN, Reissner's new mixed variational principle applied to laminated cylindrical shells. *Journal of Pressure Vessel Technology* **114**, 115-119, 1992.

66. C.P. WU and C.C. LIU, A local high-order deformable theory for thick laminated cylindrical shells. *Composite Structures* **29**, 69-87, 1994.

67. J. YE and K.P. SOLDATOS, Three-dimensional stress analysis of orthotropic and cross-ply laminated hollow cylinders and cylindrical panels. *Computer Methods in Applied Mechanics and Engineering* **117**, 331-351, 1994.

68. J.G. REN, Analysis of laminated circular cylindrical shells under axisymmetric loading. *Composite Structures* **30**, 271-280, 1995.

69. S. DI and H. ROTHERT, A solution of laminated cylindrical shells using an unconstrained third-order theory. *Composite Structures* **32**, 667-680, 1995.

70. P.N. HARRISON and E.R. JOHNSON, A mixed variational formulation for interlaminar stresses in thickness-tapered composite laminates. *Int. J. Solids Structures* **33.16**, 2377-2399, 1996.

71. E.V. IARVE, Spline variational three dimensional stress analysis of laminated composite plates with open holes. *Int. J. Solids Structures* **33.14**, 2095-2118, 1996.

72. P.D. SODEN, Private communication, 1996.

73. D. LIU and X. LI, An overall view of laminate theories based on displacement hypothesis. *Journal of Composite Materials* **30.14**, 1539-1561, 1996.

74. AMERICAN PETROLEUM INSTITUTE, Recommended practice for planning, designing, and constructing tension leg platforms. *API Recommended Practice 2T,* API, Washington, USA, 1987.

75. J.H. DELGADO, P.R. ERB and G. MOE, TLP production risers for 1,200-meter water depth. *Proceedings of the SPE European Offshore Conference,* 299-257, London, United Kingdom, 1986.

76. W.H. PETERSEN, R.W. PATTERSON, J.D. SMITH, D.W. ALLEN, A.G. EKWALL, E.H. PHIFER and YOU SUN LI, Auger TLP well systems. *Proceedings of the 26th Annual Offshore Technology Conference,* paper OTC 7617, 531-540, Houston, USA, 1994.

77. P. ODRU and J.C. GUICHARD, Drilling risers for great water depths: advantage of mass reduction by means of composite materials. *Proceedings of the Deep Offshore Technology Conference,* 1-11, Sorrento, Italy, 1985.

78. C. SPARKS, Lightweight composite production risers for a deep water tension leg platform. *Proceedings of the 5th ASME et al Offshore Mechanics and Arctic Engineering International Symposium* **3**, 86-93, Tokyo, Japan, 1986.

79. P.J.C. TAMARELLE and C. SPARKS, High performance composite tubes for offshore applications. *Proceedings of the 10th Annual Offshore Technology Conference,* paper OTC 5384, 255-259, Houston, USA, 1987.

80. P. ODRU and C. SPARKS, Structures tubulaires minces en materiaux composites - principles de calcul. *Revue de l'Institut Français du Pétrole* **43.1**, 43-51, 1988.

81. C. SPARKS, P. ODRU, H. BONO and G. METIVAUD, High performance composite tubes for TLP production risers. *Proceedings of the 5th Deep Offshore Technology Conference,* 64-74, Marbella, Spain, 1989.

82. C. SPARKS and J. SCHMITT, Optimised composite tubes for riser applications. *Proceedings of the 9th ASME et al Offshore Mechanics and Arctic Engineering*

International Symposium **3**, 1-8, Houston, USA, 1990.

83. C. SPARKS, P. ODRU, G. METIVAUD and M. AUBERON, Composite risers for deepwater applications. *Revue de l'Institut Français du Pétrole* **48.2**, 105-114, 1993.

84. K. KARIVAR-SADRI and O.O. OCHOA, Optimization of composite tubes for offshore applications. *Proceedings of the American Society for Composites 9th Technical Conference* - Offshore Applications, 850-857, Newark,USA,1994.

85. H.A. RASHEED and J.L. TASSOULAS, Strength evaluation of composite risers. *Proceedings of the 27th Annual Offshote Technology Conference*, paper OTC 7826, 215-222, Houston, USA, 1995.

86. F.J. FISCHER, Composite production risers for deepwater offshore structures. *Revue de l'Institut Français du Pétrole* **50.1**, 35-43, 1995.

87. M.M. SALAMA, Advanced composites for the offshore industry: applications and challenges. *Revue de l'Institut Français du Pétrole* **50.1**, 19-26, 1995.

88. LIM, B.V.G. MANNING and O. ALFSTAD, Snorre field TLP rigid riser system: an overview. Proceedings of the Offshore Europe Conference, 475-485, Aberdeen, United Kingdom, 1991.

89. R.J. MYERS and J.H. DELGADO, Jolliet TLWP well systems. *Proceedings of the 22nd Annual Offshore Technology Conference*, paper OTC 6401, 509-515, Houston, USA, 1990.

90. HIN CHIU, Offshore production systems for ultra-deep water in the gulf of Mexico - part I: well systems. *International Journal of Offshore and Polar Engineering* **2.4**, 241-249, 1992.

91. F.J. FISCHER, K.H. LO and S.S. WANG, Material Requiremens for Risers. *Proceedings of the International Workshop on Advanced Materials for Marine Construction*, White Paper No. 2, New Orleans, USA, 1997.

92. D.D. BALDWIN, N.L. NEWHOUSE and K.H. LO, Composite Production Riser Design. *Proceedings of the 29th Annual Offshore Technology Conference*, paper OTC 8431, 11-18, Houston, USA, 1997.

93. D. BALDWIN, N. NEWHOUSE and K.H. LO, Composite production riser development. *Proceedings of the Second International Conference on Composite Materials for Offshore Operations, CMOO-2*, Houston, USA, 1997.

94. R. GOULART and F.E. ROVERI, Analysis methods for production risers. *Private Communication*, Exploitation Projects Division - PETROBRAS Research Centre, Rio de Janeiro, Brazil, 1995.

95. P.P. ROONEY and K.B. ENGEBRETSEN, TLP rigid riser: a case study. *Journal of Petroleum Technology* **March**, 326-331, 1992.

96. PETROBRÁS, Marlim field tension leg platform unit P-29. *Production Riser Technical Specification* **rev 0**, CENPES, Rio de Janeiro, Brazil, 1995.

97. C.P. JOHNSON, Computer aided design for deep water offshore risers. *Proceedings of the 5th Conference of Civil Engineering in the Oceans*, ASCE, 243-257, Houston, USA, 1992.

98. AMERICAN PETROLEUM INSTITUTE, Bulletin on comparison of marine riser analysis. *API Bulletin 16J*, API, Washington, USA, 1992.

99. HIBBIT, KARLSSON AND SORENSEN INC, ABAQUS/Standard version 5.6, *User Manual*, HKS, Pawtucket, USA, 1996.

100. E.M. WOO and K.L. MAO, Interlaminar morphology effects on fracture resistance of amorphous polymer-modified epoxy/carbon fibre composites. *Composites Part A* **27A**, 625-631, 1996.

101. E. SHAHIDI, The Advanced Composites Group, private communication, 1998.

102. C.R. HORGAN, Saint-Venant end effects in composites. *Journal of Composite Materials* **16**, 411-422, 1982.

103. M.F.S. KHALIL and P.D. SODEN, Theorectical Through-thickness Elastic Constants for Filament-wound tubes. *International Journal of Mechanical Sciences*, **36-1**, 49-62, 1994.

104. S.W. TSAI, *Theory of Composites Design*. Think Composites, Dayton, USA, 1992.

105. American Society of Testing and Materials, *Standard Method for Fiber Content of Resin-Matrix Composites by Matrix Digestion*. ASTM D-3171, Washington, USA, 1990.

106. G. ECKOLD, *Design and Manufacture of Composite Structures*. Woodhead Publishing Company Limited, Cambridge, England, 1994.

107. W. FLUGGE, *Stresses in Shells*. Springer Verlag, Berlin, Germany, 1960.

108. Y.C. FUNG, *Foundations of Solid Mechanics*. Prentice-Hall Inc., Englewood Cliffs, USA, 1965.

109. D. ZWILLINGER, *Handbook of Differential Equations*. Academic Press Limited, London, England, 1992.

110. E. REISSNER, On a Certain Mixed Variational Theorem and a Proposed Application. *International Journal of Numerical Methods in Engineering*, **20**, 1366-1368, 1984.

111. M.J. FORRAY, *Variational Calculus in Science and Engineering*. McGraw-Hill, New York, USA, 1968.

112. N.J. PAGANO and L.E. WHITFORD, On the Solution for the Elastic Response of Involute Bodies. *Composites Science and Technology* **22**, 295-317, 1985.

113. N.J. PAGANO, Refined Solutions for the Elastic Response of Involute Bodies. *Composites Science and Technology* **25**, 251-270, 1986.

114. http://www.netlib.org/lapack

115. A. STEVENSON and J.A. HARRIS, Fatigue life estimation of flexelements for TLP structures. *Proceedings of the 11th ASME et al. International Offshore Mechanics and Arctic Engineering Symposium* **3a**, 241-249, Calgary, Canada, 1992.

116. A. SHIVE, Rigid production risers; rigid production riser tensioner; production wellheads and christmas trees. *OMAE and Petroleum Divisions of ASME TLP Design Technoloy Seminar*, Section 10.1 notes, Sugar Land, USA, 1992.

117. L.C.M. MENICONI, S.R. REID and P.D. SODEN, Composite riser tubes - an appraisal. *Proceedings of the 7th International Conference on Fibre Reinforced Composites, FRC'98*, 27-33, Newcastle upon Tyne, England, 1998.

118. S. TIMOSHENKO, *Strength of Materials*. Van Nostrand Reinhold Company, London, England, 1980.

APPENDIX A

REISSNER'S VARIATIONAL THEOREM OF THREE DIMENSIONAL ELASTICITY

This appendix shows the derivation of the energy functional that constitutes the backbone of the methodology proposed by Pagano [57], that was adopted in this work. It refers to a variational theorem introduced by Reissner [110] and also to its development as shown by Forray [111]. The theorem due to Reissner delivers the relationships between stresses and displacements, the equilibrium equations and the boundary conditons, all from one single general expression. It constitutes a generalization of the principle of stationary potential energy, adequate for an approach based on displacements, and the Castigliano's least work theorem, suitable for stress formulations. As Reissner's formulation involves variations both in stresses and displacements, it is also called the mixed theorem.

Consider an elastic body of volume V, with a total surface area of S. The direction cosines of unit outward normal vectors are n_i $(i=x,y,z)$. The portion S_σ of S is where the traction components T_i are prescribed. On the remaining surface, S_u, the displacement vector components u_i $(i=x,y,z)$ are prescribed. U^* is the complementary strain energy density function, written in terms of stresses. In the absence of body forces, we write the following functional, using indicial notation:

$$J = \int_V \left[\sigma_{ij} u_{i,j} - U^* \right] dV - \int_{S_\sigma} u_i \, \overline{T}_i dS - \int_{S_u} \left(u_i - \overline{u}_i \right) T_i dS \qquad (A.1)$$

In the expression above the comma in subscript means partial differentiation in respect to the direction after it. The Reissner's theorem states that *"The equilibrium state of the body is such that $\delta J=0$ for independent variations of u_i and σ_{ij}. From the condition that $\delta J=0$ we deduce the differential equations of equilibirum, boundary conditions, and the stress-displacement relations"*. To demonstrate that, u_i and σ_{ij} are given arbitrary variations δu_i and $\delta \sigma_{ij}$, respectively. The stationary condition of the functional J is achieved by making its first

variation null:

$$\delta J = \int_V \left[\sigma_{ij} \delta u_{i,j} + u_{i,j} \delta \sigma_{ij} - \delta U^* \right] dV - \int_{S_\sigma} \overline{T_i} \delta u_i \; dS - \int_{S_u} \left(u_i - \overline{u_i} \right) \delta T_i dS = 0 \qquad (A.2)$$

But we can write:

$$\sigma_{ij} \delta u_{i,j} = \frac{\partial}{\partial j} \left(\sigma_{ij} \delta u_i \right) - \sigma_{ij,j} \delta u_i \qquad (A.3)$$

The integration of both sides of this last expression over the volume followed by the application of Green's theorem yields:

$$\int_V \sigma_{ij} \delta u_{i,j} \; dV = \int_S \sigma_{ij} n_j \delta u_i \; dS - \int_V \sigma_{ij,j} \delta u_i dV \qquad (A.4)$$

Expression A.4 is substituted in A.2, with the reminder that $\delta u_i = 0$ on S_u, to give:

$$\int_V \left[u_{i,j} \delta \sigma_{ij} - \delta U^* - \sigma_{ij,j} \delta u_i \right] dV + \int_{S_\sigma} \left(\sigma_{ij} n_j - \overline{T_i} \right) \delta u_i \; dS - \int_{S_u} \left(u_i - \overline{u_i} \right) \delta T_i dS = 0 \qquad (A.5)$$

Since both displacement and stress components can be given arbitrary and independent variations, it follows that:

- $\sigma_{ij,j} = 0$ are the equilibrium equations,

- $\sigma_{ij}.n_j - T_i = 0$ on S_σ are the traction boundary conditions,

- $u_i = u_i$ on S_u are the displacement boundary conditions.

And recalling that U^* is a function of the six stress components, the stress-displacement relations are obtained:

$$u_{x,x} = \frac{\partial U^*}{\partial \sigma_x} , \dots \dots \dots \dots , \frac{u_{x,y} + u_{y,x}}{2} = \frac{\partial U^*}{\partial \tau_{xy}} , \dots \dots \dots \qquad (A.6)$$

Using the complementary strain energy term in this last form we write the surface tractions as:

$$T_i = \sigma_{ij} n_j \tag{A.7}$$

And the expression assumes the form that was used by Pagano:

$$\int_V \left[\left(\frac{u_{i,j} + u_{j,i}}{2} - \frac{\partial U^*}{\partial \sigma_{ij}} \right) \partial \sigma_{ij} - \sigma_{ij,j} \delta u_i \right] dV + \int_{S_\sigma} \left(T_i - \overline{T}_i \right) \delta u_i \ dS - \int_{S_u} \left(u_i - \overline{u}_i \right) \delta T_i dS = 0 \tag{A.8}$$

APPENDIX B

VERIFICATION OF THE BEAM-COLUMN BEHAVIOUR OF THE COMPOSITE RISER TAPERED JOINTS

It is necessary to address the relevant stresses present in the tapered joints of a composite riser in operation. This analysis is intended to confirm the validity of the beam-column behaviour assumed for the tapered joints. The object of the study is the bottom tapered joint, i.e. the thicker one. The load case under consideration is the one with the basic pretension of 1.5 times the apparent weight of the riser, displayed in figures 6.15 and 6.16.

The minima and maxima envelopes of the beam section forces at the bottom tapered joint provided the load information needed for the analysis. They are shown in figures B.1(a), B.1(b) and B.1(c) for the section axial forces, shear forces and bending moments, respectively. The values are taken at 6 different locations along the bottom tapered joint length of 12 metres, at 2 metres intervals. Each 2 metre length has a different carbon sub-laminate thickness, ranging from 48 mm at the thicker section at the bottom, to the 14 mm thick section at the top of that tapered joint.

The main conclusion from graphs B.1(a) to B.1(c) is that the shear forces are one order of magnitude lower than the axial forces, even in the section at the support, where the horizontal reactive force is located. The farther from the support is the section analysed, the lower is the shear force.

The study proceeds to calculate the carbon/epoxy lamina stresses, because that sub-laminate is the main one responsible for the beam-column behaviour of the tubes. The axial strain at the extreme fibre is obtained from:

$$\varepsilon_z = \frac{F_s}{EA} + \frac{RM_s}{EI} \tag{B.1}$$

where F_s is the beam section axial force, E is the equivalent elastic modulus of the tube, A is

the cross section area, R is the outer radius of the carbon sub-laminate, M_s is the beam section bending moment and I is the second moment of area of the section. Given the strain ε_z along the axial direction of the tube, the stresses referred to the carbon/epoxy lamina directions are readily obtained from TUBEPLAIN.

From Timoshenko [118] it is possible to derive a formula to give the maximum shear stress for a tubular section:

$$\tau_{\theta z\,max} = \frac{4\,Q}{3\,A}\frac{\left(R^2 + Rr + r^2\right)}{\left(R^2 + r^2\right)} \qquad (B.2)$$

where $\tau_{\theta z\,max}$ is the maximum shear stress, Q is the section shear force and r is the inner radius of the tube. Using the dimensions of the bottom tapered joint, the conclusion reached is that the maximum shear stress there is about 2 times the average value, Q/A. Recalling that the direct and shear stresses are uncoupled for the equivalent, orthotropic, smeared material, it transpires from expressions 4.13 that:

$$\gamma_{\theta z} = \overline{S}_{66}\,\tau_{\theta z} = \frac{\tau_{\theta z}}{\overline{C}_{66}} \qquad (B.3)$$

The analogy with parallel springs implies that both smeared and laminate models share the same strain $\gamma_{\theta z}$. In the laminate model, the shear strain referred to the lamina directions is given by equations 4.16:

$$\gamma_{12} = \left(c^2 - s^2\right)\gamma_{\theta z} \qquad (B.4)$$

and the in-plane shear stress due to the section shear forces are given by expressions 4.3:

$$\tau_{12} = C_{66}\,\gamma_{12} \qquad (B.5)$$

Figure B.1(d) and B.1(e) show the lamina stresses σ_1 and τ_{12} respectively, obtained as above,

for the bottom tapered joint. A more meaningful comparison is obtained by dividing the stresses by their respective strengths ($T_1=1640\ MPa$, $S_{12}=100\ MPa$), listed in table 6.4. This is shown in the graph of figure B.1(f). From it one can deduce that the shear stresses are irrelevant through the whole length of the joint. The location where the stresses are maximum is different, as well. The longitudinal stress is maximum in the bending plane, at the extreme fibres of the carbon sub-laminate. The maximum shear stress is located at the neutral plane. The result allows the adoption of the equivalent axial force concept and the testing of the tubes in a pure bending mode.
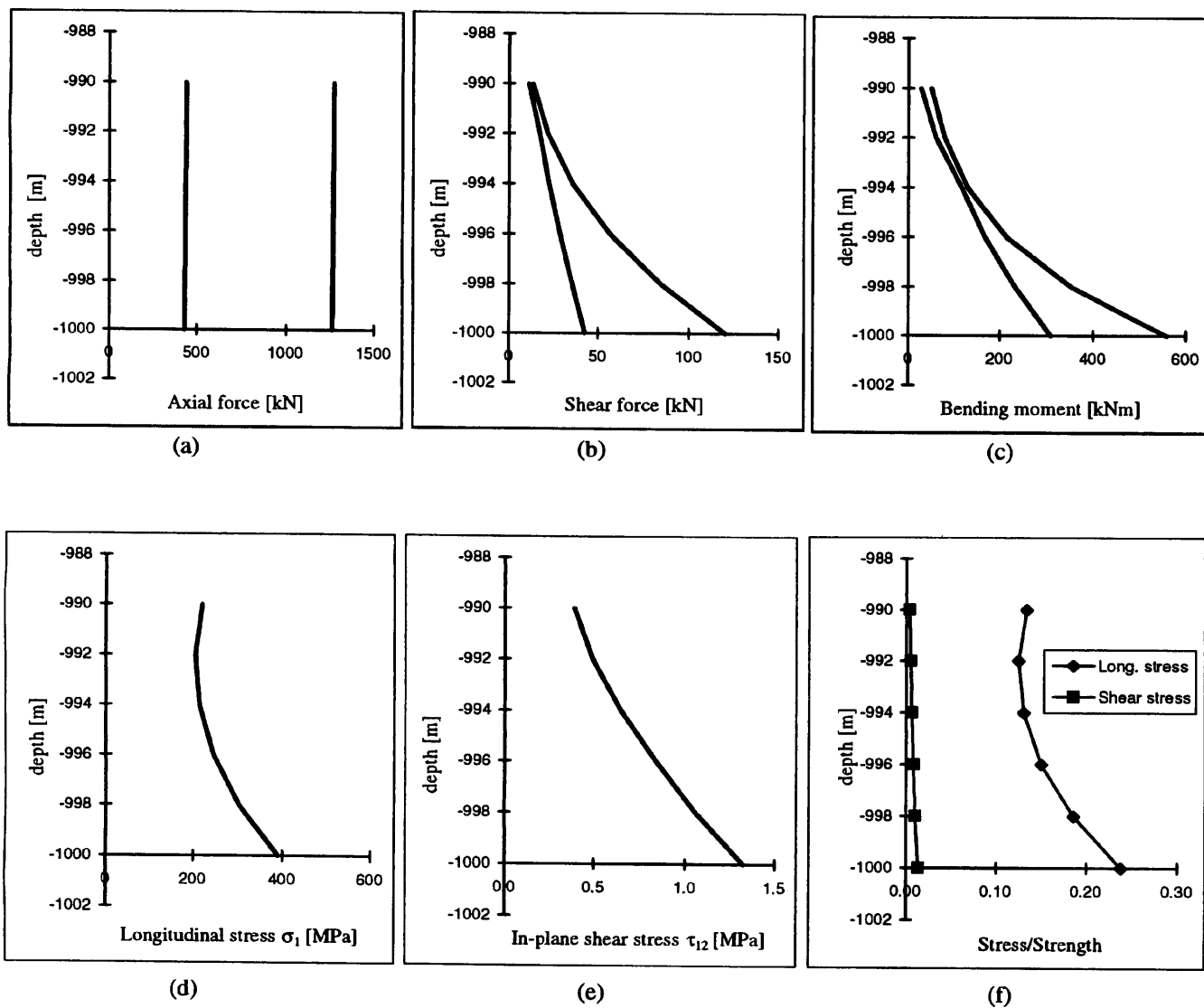
Figure B.1 Section forces and maximum carbon lamina stresses at the bottom tapered joint.